



DEGREE PROJECT IN CIVIL ENGINEERING AND URBAN
MANAGEMENT,
SECOND CYCLE, 30 CREDITS
STOCKHOLM, SWEDEN 2021

Long-term deformation of balanced cantilever bridges due to non-uniform creep and shrinkage

SIDRA AKBAR

MATHIAS CARLIE



**KTH ROYAL INSTITUTE OF TECHNOLOGY
SCHOOL OF ARCHITECTURE AND THE BUILT ENVIRONMENT**



**KTH Architecture and
the Built Environment**

Long-term deformation of balanced cantilever bridges due to uneven creep and shrinkage

MATHIAS CARLIE & SIDRA AKBAR

Master of Science Thesis
Stockholm, Sweden 2021

Master Thesis June 2021
TRITA-ABE-MBT-21382
ISBN: 978-91-7873-951-6

KTH School of ABE
SE-100 44 Stockholm
SWEDEN

© Mathias Carlie & Sidra Akbar 2021
KTH Royal Institute of Technology
Department of Civil and Architectural Engineering
Division of Concrete Structures

Abstract

Balanced cantilever bridges have historically experienced excessive deformations. Previous research suggests that the cause may be due to differential thickness in the box girder cross-section and underestimation of creep and shrinkage. In this project, the long-term deformation of balanced cantilever bridges due to non-uniform creep and shrinkage have been investigated. The non-uniform creep and shrinkage are caused by variations in drying rates for the different parts of the box-girder cross-sections. A finite element model was created in the program Abaqus as a case study of the Alvik bridge. The finite element model was used to evaluate the difference between non-uniform and uniform creep and shrinkage with Eurocode 2. Further, a comparison between Eurocode 2 and Bažant's B4 model was conducted for non-uniform creep and shrinkage. The comparison aimed to evaluate the difference between industry and research specific calculation models, for the effect of creep and shrinkage on deformations. A parameter study was also conducted to discern the effect of parameters: ballast load, water-cement ratio and conditions related to drying of concrete (relative humidity and perimeter exposed to air). A comparison with the deformation measurements of the Alvik bridge was conducted to validate the results from the model.

The results showed that there was a significant difference in the calculated deformation of the bridge during the first ten years between analyses based on non-uniform and uniform distribution of creep and shrinkage, respectively. The non-uniform analysis gave larger deformations. However, only minor differences between the two approaches could be detected in the final deformation after 120 years. The main reason for the differences in the early behaviour is primarily caused by the differences in shrinkage rate between the top and bottom flanges. In these analyses, the top flange was assumed to not dry out from the top. Thereby, the shrinkage rate of the top flange caused by one-way drying was similar to the bottom flange that was assumed to be exposed for two-way drying. The B4 model gave larger deformations compared to Eurocode 2. This may be due to difference in the definition of perimeter and surface. Eurocode 2 considers the perimeter exposed to air. The B4 model instead considers the entire surface area of the part. The B4 model and Eurocode 2 show similar results as the measurements. However, the B4 model gave results more consistent with the measurements. In the parameter study, lower relative humidity gave smaller deformations, since concrete shrinks quicker in dry ambient air. Varying the water-cement ratio did not affect the deformations noticeably. Higher ballast height gave significantly larger deformations. The height of the ballast was an uncertain factor due to varying heights in the structural drawings of the case study. Accurate height of ballast is therefore important.

Keywords: Balanced cantilever bridges, box girder cross-section, concrete, non-uniform creep and shrinkage, Bažant's B4 model, Eurocode 2, long-term deformations, finite element analysis

Sammanfattning

Freivorbau broar har historiskt sett haft problem med kraftiga deformationer. Tidigare forskning föreslår att detta har orsakats av tjockleksskillnader i lådtvärsnitt och underskattning av krypning och krympning. Denna studie har undersökt effekten av ojämn krypning och krympning på freivorbau broars långtidsdeformationer. Den ojämn krypningen och krympningen orsakas av skillnader i uttorkningshastigheter för lådtvärsnittets olika delar. En finita elementmodell definierades i programmet Abaqus som en fallstudie på Alviksbron. Modellen användes för att utvärdera skillnaden mellan ojämn och jämn krypning och krympning med Eurokod 2. En jämförelse mellan Eurokod 2 och Bažant's B4 modell genomfördes med hänsyn till ojämn krypning och krympning. Syftet med jämförelsen var att utvärdera skillnader mellan byggnormer och forskningsmodeller med hänsyn till deformationer orsakade av ojämn krypning och krympning. Vidare genomfördes en parameterstudie för att urskilja effekten av parametrarna: ballast last, vatten-cement-tal och förhållanden relaterade till betongens uttorkning (relativ fuktighet och omkrets utsatt för luft). Deformationerna från finita elementmodellen jämfördes med uppmätta deformationer av Alviksbron.

Resultaten visade att det fanns en signifikant skillnad i beräknad deformation under de första tio åren mellan ojämn och jämn krypning och krympning. Ojämn krypning och krympning gav större deformationer. Mindre deformationsskillnad gavs dock i slutgiltig deformation efter 120 år. Den främsta anledningen till skillnaderna i deformation under de första tio åren är orsakat av skillnader i krympningens hastighet mellan övre- och undre fläns. I analyserna antogs det att övre flänsen inte torkade ut från dess övre del. Därmed var krympningens hastighet likartad för övre flänsen som torkade ut åt ett håll, och undre flänsen som torkade ut åt två håll. B4 modellen gav större deformationer jämfört med Eurokod 2. En möjlig förklaring för detta är definieringen av omkrets gentemot ytans area. Eurokod 2 definierar en omkrets utsatt för luft. B4 modellen definierar i stället arean av en yta, utan att ta hänsyn till om den är utsatt för luft. Även om B4 modellen och Eurokod 2 ger likartade deformationer, ger B4 modellen oftare deformationer som stämmer bättre överens med deformationsmätningarna av Alviksbron. Lägre relativ fuktighet gav mindre deformationer, eftersom betong krymper fortare i torrt klimat. Ändring av vattencementtal gav inte någon märkbar ändring i deformationer. Högre ballasthöjd gav betydligt större deformationer. Höjden på ballast var en osäker faktor på grund av varierande höjder i Alviksbrons konstruktionsritningar. Noggrann höjdbestämmelse av ballasten är därför viktigt.

Nyckelord: Freivorbau broar, lådtvärsnitt, betong, ojämn krypning och krympning, Bažants B4 modell, Eurokod 2, långtidsdeformationer, finita element analys

Preface

The MSc thesis was conducted from January to May 2021 at the Division of Concrete Structures, Department of Civil and Architectural Engineering at the Royal Institute of Technology. The research was initiated by Dr Richard Malm who was also our supervisor.

First and foremost, we would like to thank Dr Richard Malm for his continuous support and guidance throughout this thesis. We are tremendously grateful for Dr Richard Malm, due to his ability in providing an educational and encouraging atmosphere despite it being another year with Covid-19.

To express our gratitude to our loved ones, we have divided our messages below.

Sidra: I would like to thank my parents who have brought me to Sweden from Pakistan. Your hardships and strength have given me the opportunity to follow my dreams. Thank you for believing in me when I cannot believe in myself. I am forever grateful. I would like to thank my siblings for always listening and being present with a hug whenever times have been hard. I would like to thank my friends for always creating an environment for me to laugh and thrive. I would like to thank my family and friends for being there for me and forgiving me when I was not able to be there.

Mathias: I would like to thank my family and friends for their encouragement throughout my studies at KTH. A special thanks to my parents, who have always encouraged me to learn more, which has helped me throughout my studies.

Stockholm, June 2021

Mathias Carlie & Sidra Akbar

Contents

Abstract	i
Sammanfattning	ii
Preface	iii
Contents.....	iv
1 Introduction	1
1.1 Background.....	1
1.2 Aim and scope of the thesis	2
1.3 The layout of the thesis	3
2 Long-term behaviour of concrete	5
2.1 Non-linear behaviour of concrete	5
2.2 Concrete creep.....	7
2.3 Concrete shrinkage.....	10
2.4 Relaxation of prestressed tendons in concrete.....	11
2.5 Models for calculating long-term behaviour of concrete	13
2.5.1 B4 model	13
2.5.2 Eurocode	26
3 Material input in Abaqus for long-term behaviour of concrete	33
3.1 Concrete creep.....	33
3.2 Concrete shrinkage.....	37
3.3 Relaxation of prestressed tendons in concrete.....	37
4 Benchmark models	39
4.1 General	39
4.2 Concrete creep test.....	40
4.2.1 Cube and cylinder model	43
4.3 Steel relaxation test.....	45
4.3.1 Prestressed tendon.....	46
4.4 Concrete shrinkage test	47
4.4.1 Simplified bridge span	49

5	Case study - the Alvik bridge	50
5.1	Geometry and general description	50
5.2	Material properties.....	53
5.3	Construction phase.....	54
5.4	Loads	54
5.5	Cracking and strengthening.....	57
5.6	Measurement observation of the Alvik bridge.....	58
6	Modelling of the Alvik bridge	61
6.1	Model construction.....	61
6.2	Material properties.....	64
6.3	Construction phase.....	69
6.4	Considered loads	71
6.5	Parameter study.....	72
6.6	Service life	73
6.7	Mesh control test.....	73
7	Results from finite element analyses	75
7.1	General	76
7.2	Effect of calculation models	77
7.2.1	Deformation along the bridge span	77
7.2.2	Deformation over time at midspan	83
7.2.3	Influence of creep versus shrinkage	86
7.3	Parameter study for non-uniform creep and shrinkage	87
7.3.1	Influence of relative humidity	87
7.3.2	Influence of the water-cement ratio.....	90
7.3.3	Influence of ballast.....	91
7.3.4	Influence of cross-section perimeter exposed to air	93
7.4	Stress state.....	93
8	Discussion and Conclusion	95
8.1	Effect of non-uniform versus uniform creep and shrinkage.....	95
8.2	Difference in deformation behaviour between B4 model and Eurocode 2 ...	96
8.3	Influence of parameters on deformation	97
8.4	Validity of numerical analysis	98
8.5	Further research.....	98
	Bibliography.....	100

A	Material input.....	102
A.1	Creep coefficient variation for each segment	102
A.2	Shrinkage strain variation for each segment	117
A.3	Relaxation data for tendons	131
B	Drawings.....	133
B.1	Instrumentation	133
B.2	Structural Drawings.....	135

Chapter 1

Introduction

1.1 Background

Balanced concrete cantilever bridges have become popular throughout the years due to their slender structures and ability to span over lengths of 200 - 300 meters. Due to their construction method, balanced cantilever bridges do not require the need for falsework. This is advantageous when the bridge span is located at a high elevation or if the bridge spans over a large body of water (Takács, 2002).

Balanced cantilever bridges can be constructed in two ways, namely: precast or cast in-situ, using the balanced cantilever method. The general process of the balanced cantilever method is that segments are cast symmetrically. Casting originates from a fixed starting point, such as the bridge pier and adjoining in the midspan from the other side of the pier, as illustrated in Figure 1.1. As a segment is cast, it is then used as a support for a form traveller to deliver the formwork for a new segment and continue the casting process for the subsequent segment. The bridges are designed to have an initial upward camber; a planned upward deflection, erected during the construction phase. This measure is taken to counter the deformation during the construction phase and ensure that the spans meet at the same level when the connecting segment is cast (Malm & Sundquist, 2010).

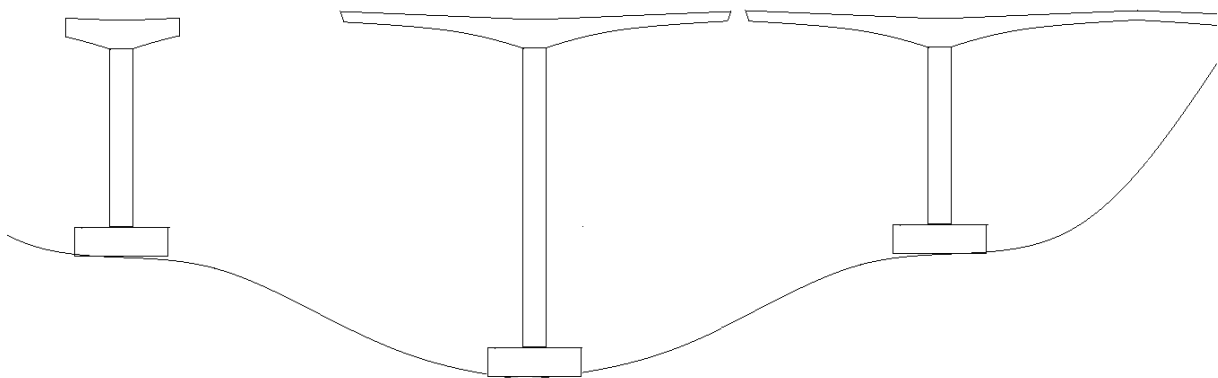


Figure 1.1 Construction process of cast in-situ balanced cantilever bridge.

When designing these bridges, the box-girder cross-sections are often designed with varying thickness, both in the thickness of the cross-section depending on where in the span the cross-section is located, and that the webs, top flange, and bottom flange of the cross-section have different thicknesses.

Many balanced cantilever bridges have experienced excessive long-term deformations (Krístek et al., 2006). Research on these issues has been conducted by for example Krístek et al. (2006) where it was concluded that the long-term deformations could be caused by the difference in thickness of the top and bottom slab of the bridge span cross-section. This meant that the shrinkage and drying creep varied between the top and bottom slab and caused excessive deflections. Underestimation of creep and shrinkage may be a contributing factor to the deformation and long-term behaviour of the balanced concrete cantilever bridges (Malm & Sundquist, 2010).

The issues with the bridges have historically meant that some have not been able to meet the requirements for the serviceability limit state. There has also been a case where a bridge did not satisfy the ultimate limit state requirements and suffered structural failure (Bažant et al., 2015). It is therefore important to investigate the cause of the issues these bridges encountered.

1.2 Aim and scope of the thesis

This study aimed to investigate the effect of differing thickness in box girder cross-sections on deformation, due to creep and shrinkage, in balanced cantilever bridges.

Three research questions were formulated to achieve the aim of the study:

1. What is the effect of calculating with non-uniform compared to uniform creep and shrinkage on the deformation?
2. What is the difference in resulting deformation between industry- and research specific calculation models for non-uniform creep and shrinkage?
3. What is the influence of dominant parameters on the magnitude of deformation caused by creep and shrinkage?

To answer the research questions, a finite element model was created based on a case study of the Alvik bridge. Three benchmark models were created to verify the implementation of the material behaviour in the case study model.

The deformation behaviour of the case study model was analysed for non-uniform and uniform creep and shrinkage. The primary method used to analyse the difference between non-uniform and uniform creep and shrinkage was the industry-specific model, namely Eurocode 2.

A comparison between an industry specific calculation model and a research specific calculation model was conducted. The material behaviour and resulting deformation behaviour for the case study model were used for the comparison.

The chosen parameters were ballast load, water-cement ratio and conditions related to drying of concrete (relative humidity and perimeter exposed to air). The parameters were tested with varying values to investigate their effect on creep and shrinkage.

The material data used in the analyses in this thesis were either taken from design codes, such as Eurocode, or information given in structural drawings for the case study.

The finite element model for the case study was not intended to be a replica of the real-life structure. The purpose of the analysis was instead to use the model as an example of the type of bridges this thesis aims to investigate.

The material behaviour of the concrete in this thesis is assumed as linear elastic. The effects of cracks in the concrete are not considered.

1.3 The layout of the thesis

Chapter 1 - Introduction

In this chapter, a description of the issue of long-term deformations in cantilever bridges is presented. A background is given on conclusions from previous research to present a clearer problem description. The aim and scope of the thesis are also provided, where three research questions are presented as the focus of the thesis. Thereafter the scope and layout of the thesis are presented.

Chapter 2 - Non-linear behaviour of concrete

In this chapter, an overview of the long-term behaviour of concrete is presented. Thereafter, theoretical background from literature for long-term behaviour such as creep and shrinkage of the concrete, as well as relaxation of the prestressed steel tendons is described. Finally, methods for calculating the material behaviour of creep, shrinkage and relaxation are presented.

Chapter 3 - Material input in Abaqus for long-term behaviour of concrete

This chapter discusses the finite element application in Abaqus for the theory described in Chapter 2.

Chapter 4 - Benchmark models

This chapter describes the analysis of simpler benchmark models for verification of the material properties used in the analysis of the more complex case study model. The verification models were the cube and cylinder models; which were used to verify the concrete creep behaviour, the prestressing bar model; which was used to verify the steel relaxation behaviour and the simplified bridge span model; which was used to principally study if non-uniform shrinkage would cause larger deformations compared to uniform shrinkage.

Chapter 5 - Case study - the Alvik bridge

A description of the studied bridge is given in this chapter where geometry, material properties and loads are described. The construction phase and service life are also described to give insight into the deformation behaviour of the bridge during construction and its service life.

Chapter 6 - Modelling of the Alvik bridge

In this chapter, the information presented in Chapter 5 was used to develop a finite element model in Abaqus. The defined geometry is described as well as input data used for the material behaviour and the applied loads are presented. The analysis of the construction phase and service life are presented. An explanation is also provided on which basis the mesh size for the case study model was chosen, with a mesh control analysis.

Chapter 7 - Result from finite element analysis

This chapter shows the results of the analysis of the case study model. The results are divided into two parts. The first part shows the difference between the effect of non-uniform and uniform analysis on deformation behaviour. The first part also shows the difference between Eurocode 2 and the B4 model with non-uniform analysis. The second part shows the result from the parameter study.

Chapter 8 - Discussion and conclusion

This chapter is divided into five parts. The first three parts discuss and conclude the defined research questions. The fourth part discusses the validity of the numerical analysis. The fifth part discusses what further research could be performed.

Chapter 2

Long-term behaviour of concrete

2.1 Non-linear behaviour of concrete

When a load is applied to a material such as concrete, stresses will develop due to the deformation of the concrete. The change in deformation from before and after the load is applied can be measured as the strain. Since the strength of concrete is based on the stress capacity, as well as the allowed deformation being of significance, the stress-strain relationship is of considerable importance. When testing concrete, the relationship between the stress and strain is often illustrated graphically as the stress-strain curve (Ansell et.al, 2014). An example of this illustration is given in Figure 2.1.

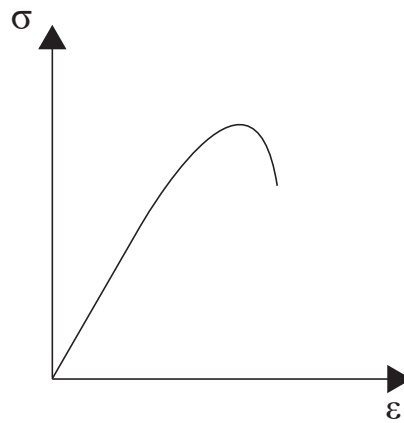


Figure 2.1: Illustration of a stress-strain curve (Ansell et. al, 2014).

When a compressive load is initially applied on concrete, the response will be an approximately linear relationship between the stress and strain. However, as the stresses increase, so do the number of micro-cracks in the concrete. When enough micro-cracks appear, the strain in the concrete will increase without a corresponding linear increase of the stress. When visualized in the stress-strain curve, the curve will start to level out and eventually cracks will be large enough that the concrete will no longer be able to carry any amount of load (Ansell et.al, 2014).

According to Engström (2007), the maximum stress capacity of the concrete is usually taken as the stress-strain curve's maximum stress value. As an approximation, the linearity of the stress-strain curve is usually considered up to 0.5 to 0.6 times the maximum compressive stress capacity. After this value, the stress-strain curve can no longer be considered linear.

An aspect of concrete non-linear behaviour that pertains to the rate of loading is that the stress capacity of concrete, as well as its non-linearity, will differ depending on the loading rate (Engström, 2007). A load applied quickly, e.g., for a few seconds, will result in a steeper and a more linear stress-strain curve. Comparatively, a load applied slowly, e.g., for a few months, will result in a more levelled out and non-linear stress-strain curve, as illustrated in Figure 2.2.

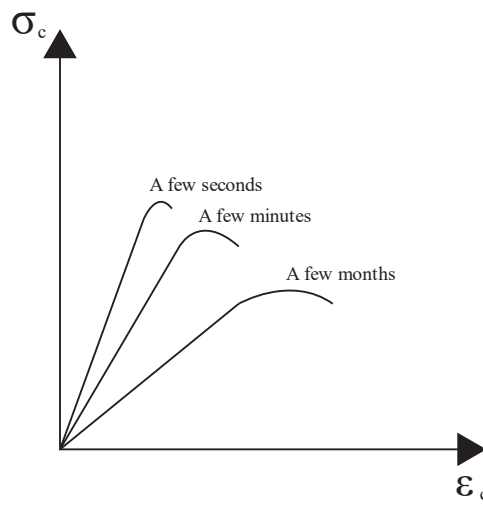


Figure 2.2: Illustration of the behaviour of stress-strain curve concerning short- and long-term loading (Engström, 2007).

The non-linearity of the stress-strain curve is an important factor when considering long term behaviour such as creep deformations. At the linear section of the stress-strain curve, linear creep is assumed. However, in the non-linear section, a risk for creep failure exists, despite the structure not reaching the design load (Engström, 2007).

2.2 Concrete creep

According to Ansell et.al (2014), the phenomenon of creep occurs when a structure is subjected to increasing long-term deformation despite constant stress. Furthermore, the phenomenon of creep occurs when the constant stress applied to the structure results in the formation of microcracks which in turn result in further strain. Creep recovery is described as the process when the material returns towards its normal state after the momentary elastic recovery happens once the load is removed. Figure 2.3 illustrates the relationship of strain over time to further illustrate the phenomenon (Ansell et.al, 2014).

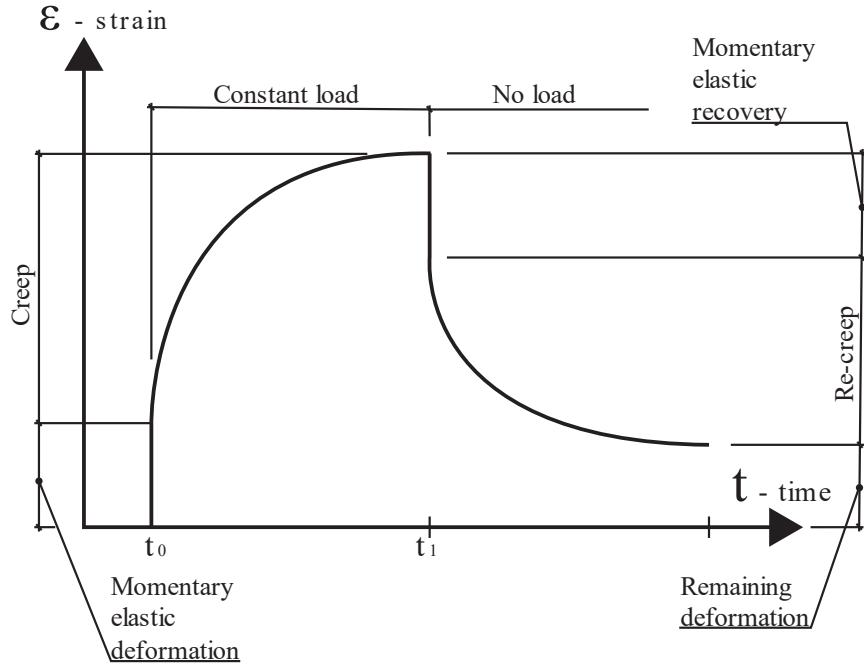


Figure 2.3: Time-dependent strain development due to creep and the recovery caused by unloading (Ansell et.al, 2014).

The phenomena can further be described with the help of rheological models, such as The Maxwell and The Kelvin (Voigt) Model. The Maxwell Model consists of a series connection between a spring and a damper, both having individual systems of describing their material properties of elasticity and viscoelasticity respectively as well as strain and stress. The Kelvin (Voigt) model on the other hand also consists of a spring and damper but has a parallel connection, see Figure 2.4. The spring is used to describe the elastic behaviour of the material whereas the damper is used to describe the restrained behaviour or the viscosity of the material (Kelly, 2013).

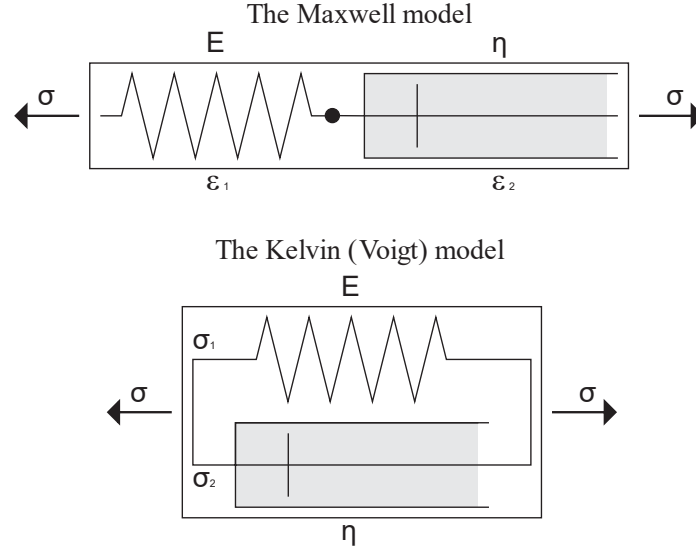


Figure 2.4: Illustration of the Maxwell and Kelvin (Voigt) model, respectively (Kelly, 2013).

The strain in the Maxwell model can be described as the sum of the strain from the spring and the damper, whereas in the Kelvin (Voigt) model the relationship that can be analysed is that the total stress is the sum of the stress in the spring and the damper, respectively. The stress-strain relationship is described in Eq. (2.1) and Eq. (2.2) for the spring and damper, respectively (Kelly, 2013).

$$\varepsilon_{spring} = \frac{\sigma_{spring}}{E} \quad (2.1)$$

$$\varepsilon_{damper} = \frac{\sigma_{damper}}{\eta} \quad (2.2)$$

where,

$\varepsilon_{spring}, \varepsilon_{damper}$	strain in the spring and damper, respectively. [-]
$\sigma_{spring}, \sigma_{damper}$	applied stress in the spring and damper, respectively [Pa]
E	elastic modulus [Pa]
η	viscosity [Pa-s].

By combining Eq. (2.1) and Eq. (2.2) for the relationships described for the model, the Maxwell model can be described by Eq. (2.3) and the Kelvin (Voigt) model can be described by Eq. (2.4) (Kelly, 2013).

$$\sigma_{damper} + \frac{\eta}{E} \cdot \dot{\sigma}_{damper} = \eta \cdot \dot{\varepsilon} \quad (2.3)$$

$$E \cdot \varepsilon_{spring} + \eta \cdot \dot{\varepsilon}_{damper} = \sigma \quad (2.4)$$

To analyse the creep from the models, one has to analyse the response of the models from when the load is applied. In the Maxwell model, a load will cause the spring to have an initial elastic strain. The long-term behaviour can be described as the integration of the initial strain for time, with Eq. (2.5) (Kelly, 2013).

$$\varepsilon(t) = \sigma_0 \cdot \left(\frac{t - t_0}{\eta} + \frac{1}{E} \right) \quad (2.5)$$

where,

t	time [s]
t_0	time at loading [s].

Similarly in the Kelvin (Voigt) model, when a load is applied the spring will be restrained by the damper, while the springs natural response is to deform. The initial slope is therefore the initial stress divided by the viscosity. This is then followed by a secondary slope given as the stress in the damper divided by the viscosity of the material. Considering the condition that the initial strain is zero, the time-dependent strain is described as shown in Eq. (2.6) (Kelly, 2013).

$$\varepsilon(t) = \frac{\sigma_0}{E} \cdot \left(1 - e^{-\left(\frac{E}{\eta}(t-t_0)\right)} \right) \quad (2.6)$$

where,

σ_0	the initial stress [Pa].
------------	--------------------------

The difference between the models, as illustrated in Figure 2.5, is that the Maxwell model gives the elastic response and permanent strain but not the decreasing strain rate. The Kelvin (Voigt) model instead gives the inelastic recovery but not the elastic response and permanent strain (Kelly, 2013).

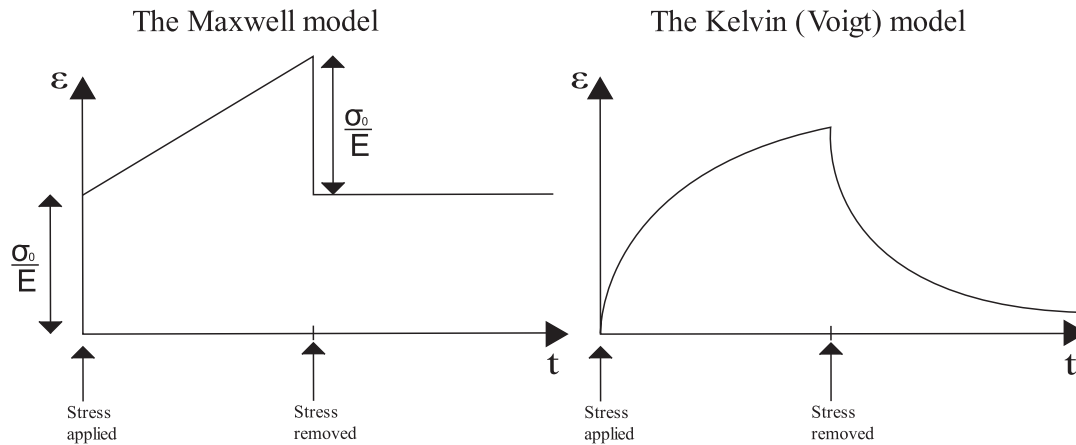


Figure 2.5: Difference in behaviour prediction in the Maxwell and Kelvin model (Kelly, 2013).

Different combinations of the model can be used to describe different properties of the material such as linear elasticity, linear viscosity as well as further development of non-linear models. The viscoelastic behaviour of concrete can be described by either of the models depending on the purpose of the analysis. For creep calculations, the Kelvin Chain model is recommended as it is based on a creep function (Takács, 2002).

2.3 Concrete shrinkage

In its most rudimentary form, concrete shrinkage is the phenomenon of water evaporating during the concrete curing process. The evaporation of the water from the concrete mixture means that the volume of the concrete will be reduced. The term concrete shrinkage is often synonymously used when referring to drying shrinkage. However, the meaning of concrete shrinkage entails more than just the evaporation of water during the curing process. The total shrinkage can be divided up into four different categories: the drying shrinkage, plastic shrinkage, autogenous shrinkage, and carbonation shrinkage. The two primary categories are drying shrinkage and autogenous shrinkage (Ansell et al, 2014).

Drying shrinkage is the process of excess water evaporation from the concrete mixture in exchange with its ambient environment. The excess water in the concrete mixture's pores has not reacted with the cement paste. Autogenous shrinkage is the loss of water due to the hydration process, where the hydration process is the chemical reaction between water and cement paste that occurs when the concrete hardens. The drying shrinkage will for the majority of concrete mixtures cause the most amount of shrinkage. The autogenous shrinkage will however have a larger impact on the amount of shrinkage on concrete with a water-cement ratio lower than around 0.5-0.55 (Silfwerbrand, 2017). Since the shrinkage of the concrete leads to a reduction of the volume, a strain will occur

if the boundary conditions restrain the concrete from reducing its volume (Ansell et al, 2014).

According to Engström (2007), the following five primary variables affect the amount of concrete shrinkage.

The first primary variable is the composition of the ingredients in the concrete. The composition is an important factor since of the most essential ingredients in the concrete, which are water, cement, and aggregates, only the aggregates are free from shrinkage. Therefore, the amount of water and cement content i.e., cement paste content used in the concrete mixture will affect the amount of shrinkage. A larger amount of water and/or cement content will lead to a larger amount of shrinkage (Ansell et al, 2014).

The second primary variable is the treatment of the concrete mixture. If the concrete is not mixed sufficiently, then the concrete composition may shrink inhomogeneously, which can lead to additional stresses developing in the concrete. Insufficient mixing can also lead to larger pores, where water will gather, without being able to react with the cement mixture and ultimately evaporate (Ansell et al, 2014).

The third primary variable is the concrete's exposure to the environment. The amount of shrinkage due to environmental causes depends on the relative humidity. The concrete mixture will have a larger drying shrinkage in an environment with low relative humidity in comparison to an environment with high relative humidity (Engström, 2007).

The fourth primary variable is the geometry and placement of the sample, i.e., the size of the surface, its thickness and exposure to ambient conditions. A larger surface area exposed to the environment leads to more shrinkage and a thinner concrete sample will shrink quicker than a thicker concrete sample. Since concrete as a material has low permeability, the thickness will represent an important factor when calculating how long time it will take for the concrete mixture to dry out. An example of this is given in Engström (2007), where it will take one year for a 0.1 m thick slab of concrete to achieve 80% of its final shrinkage. In comparison, if the slab is 0.4 m it will take around 10 years and if the slab is 1.0 m thick then it will take more than 100 years.

The fifth primary variable is the age of the concrete mixture from when the curing began. Since concrete shrinkage is a process of evaporation and chemical reactions it is also a process that is time-dependent.

2.4 Relaxation of prestressed tendons in concrete

Prestressing systems can either follow principles of pre-tensioning or post-tension, where the latter is most common in the case of cast in-situ. The post-tensioned reinforcement can either be bonded or unbonded. Losses can occur in the prestressed tendons due to locking and de-tensioning, friction as well as time-dependent loss such as relaxation of the reinforcement (Ansell et al, 2014).

The phenomenon of relaxation occurs when the stress in steel decreases at constant strain. This phenomenon is similar to the creep of the concrete where the prestressing tendons creep because of high stress and thereby result in tendons experiencing

relaxation (Borbolla & Mazzola, 2003). The phenomenon can also be described with the help of the rheological models mentioned in Chapter 2.2. From the Maxwell model, the stress-strain relationship that can be used to describe stress relaxation, $\sigma(t)$, is given by Eq. (2.7).

$$\sigma(t) = \varepsilon_0 \cdot E \cdot e^{\frac{-t}{t_R}} ; t_R = \frac{\eta}{E} \quad (2.7)$$

where,

ε_0	constant strain [-]
t	time [days]
t_R	time required for relaxation to occur, also known as relaxation time [days].

In the Kelvin (Voigt) model, the spring is still restrained by the damper resulting in difficulty for instantaneous stress to occur unless the stress is infinite. That is since the damper's response or strain is not instant when the stress is applied. Therefore, the spring absorbs the stress resulting in no stress relaxation over time. Therefore, for calculations regarding relaxation, it is recommended to use the Maxwell model since the Kelvin (Voigt) model is not sufficient for describing the phenomenon (Kelly, 2013).

This recommendation can be understood further with the help of illustrations as shown in Figure 2.6, where in the Maxwell model the relaxation over time can be analysed. As illustrated, the Kelvin (Voigt) model cannot describe relaxation over time as the initial stress is directly represented by the stress in the spring. Therefore, over time, the analysis cannot be performed (Takács, 2002).

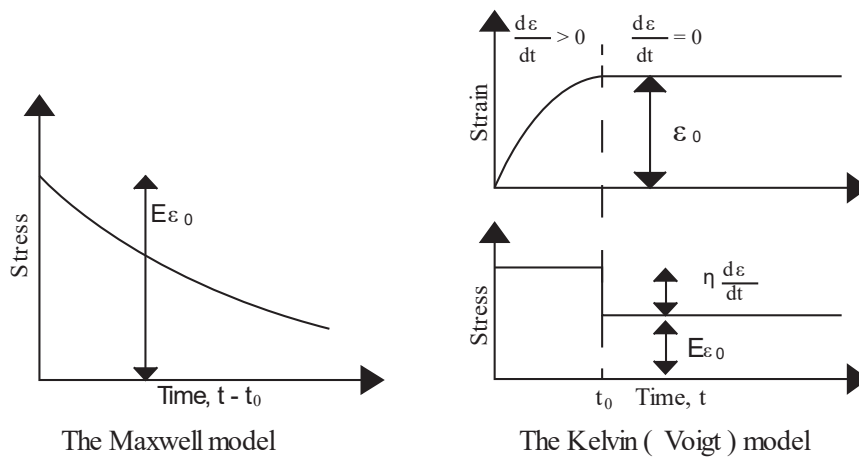


Figure 2.6: Relaxation in the Maxwell and Kelvin (Voigt) model respectively (Takács, 2002).

2.5 Models for calculating long-term behaviour of concrete

Several models can be used to calculate the long-term behaviour of concrete. However, this thesis focused on two methods, the B4 model (Bažant et al., 2015) and Eurocode 2 (EC2, 2008). Eurocode 2 was chosen as the industry-specific model. Eurocode is a developed standard of construction by the European Committee for Standardization. The B4 model was chosen as the research specific model. It is an improved version of the previous B3 model (Bažant & Baweja, 2001) recommended by RILEM from 1996. The B4 model was developed by researchers looking to further improve on the current design codes in use (Bažant et al., 2015). Applying both models can give the study a broader understanding as similarities and differences between research and industry can be analysed.

The variables, coefficients and parameters presented in Chapter 2.5.1 and Chapter 2.5.2 only apply to their respective chapter.

2.5.1 B4 model

Bažant et al. (2015) present five levels of structures considering their sensitivity to creep and shrinkage. Examples of structures for the five levels are:

1. Reinforced concrete beams with spans smaller than 20 m and heights less than 30 m.
2. Prestressed concrete beams with spans up to 20 m.
3. Box-girder bridges with spans up to 80 m.
4. Long-span prestressed box-girder bridges
5. Unique, cutting edge structures such as bridges with record-breaking spans.

The B4 model is recommended for structures in level four and five. (Bažant et al., 2015)

Bažant et al. (2015) present a flow chart that illustrates the calculation procedure for the B4 model in Figure 2.7.

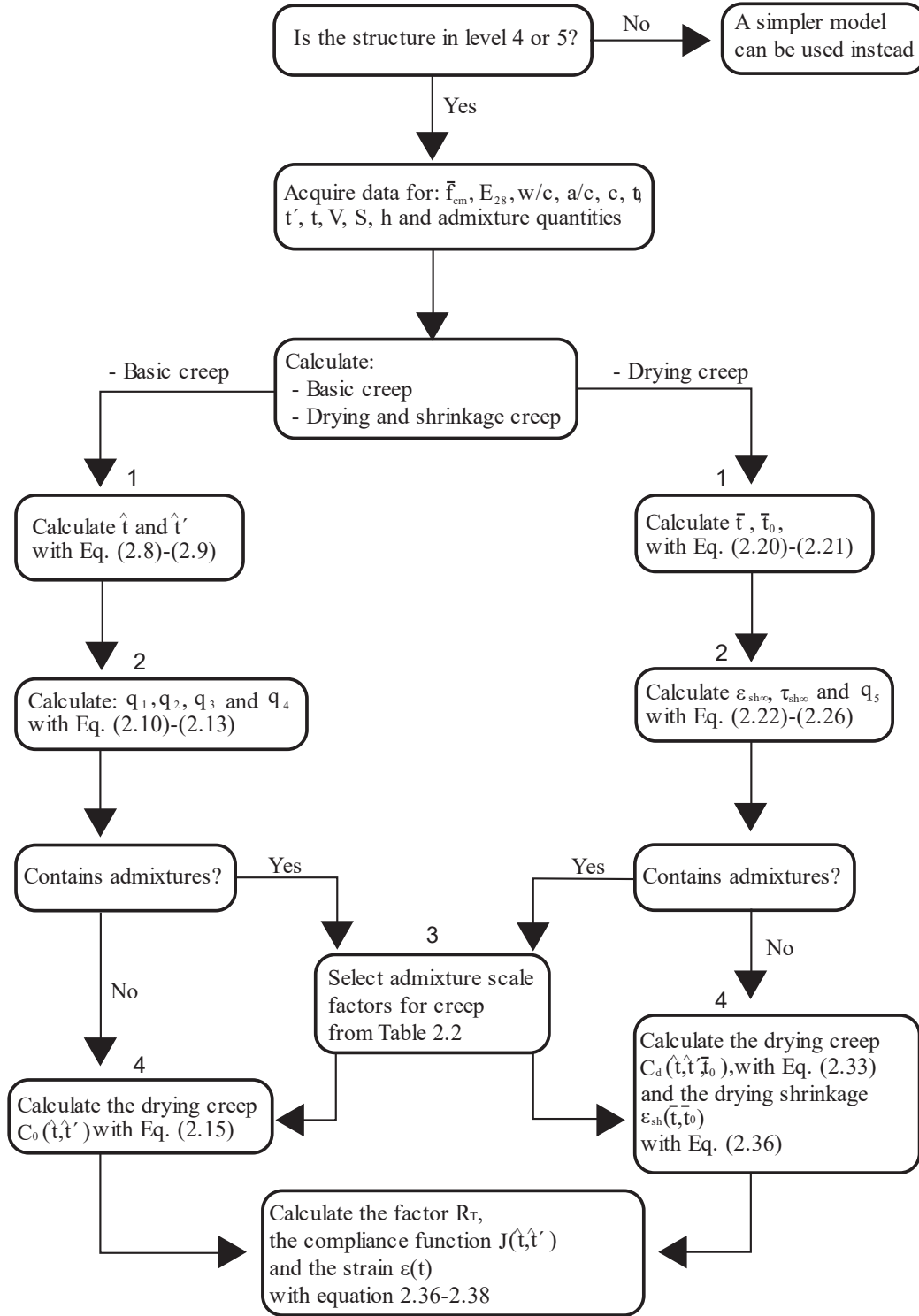


Figure 2.7: Flow chart for the implementation of the B4 model calculation based on (Bažant et al., 2015).

The calculation procedure for the basic creep and the shrinkage/drying creep is divided into four steps each, as illustrated in Figure 2.7. The combination of the basic creep and the shrinkage/drying creep is needed for the prediction of the creep and shrinkage model.

Basic creep

The first step of calculating basic creep is to calculate:

\hat{t}' temperature corrected age at loading [days],
given by Eq. (2.8)

\hat{t} temperature corrected current age [days],
given by Eq. (2.9)

$$\hat{t}' = t_0 \cdot e^{\beta_{Th}} + (t' - t_0) \cdot e^{\beta_{Ts}} \quad (2.8)$$

$$\hat{t} = \hat{t}' + (t - t') \cdot e^{\beta_{Tc}} \quad (2.9)$$

where,

$\beta_{Th}, \beta_{Ts}, \beta_{Tc}$ are variables used to simplify equations and have the relationship between the following variables,

$$\beta_{Th} = e^{\left(\frac{U_h}{R_g} \left(\frac{1}{293} - \frac{1}{T_{cur} + 273}\right)\right)}$$

$$\beta_{Ts} = e^{\left(\frac{U_s}{R_g} \left(\frac{1}{293} - \frac{1}{T_{cur} + 273}\right)\right)}$$

$$\beta_{Tc} = e^{\left(\frac{U_c}{R_g} \left(\frac{1}{293} - \frac{1}{T_{cur} + 273}\right)\right)}$$

t_0 age where the concrete is first exposed to the environment [days].

t' age of the concrete at the time of loading [days].

t time from start of concrete curing to the current time [days].

U_h, U_s, U_c activation energy for hydration (h), drying shrinkage (s) and creep (c) [J/mol].

R_g gas constant [J×K/mol].

T_{cur} temperature at curing [°C], $20\text{ °C} \leq T_{cur} \leq 30\text{ °C}$.

T average environmental temperature before and after loading [°C], $-25\text{ °C} \leq T \leq 75\text{ °C}$.

For the activation energies U_c , U_h and U_s , Bažant et al. (2015) state that they can be given the value of $\frac{U_c}{R_g} = \frac{U_h}{R_g} = \frac{U_s}{R_g} = 4\,000\text{ K}$.

When the temperature is at 20°C , then the temperature corrected age reduces to the actual ages, i.e., $\hat{t}' = t'$ and $\hat{t} = t$.

The second step of calculating basic creep is to calculate:

- q_1 instantaneous compliance $[1/\text{Pa}]$, given by Eq. (2.10).
- q_2 ageing viscoelastic creep $[1/\text{Pa}]$, given by Eq. (2.11).
- q_3 non-ageing viscoelastic creep $[1/\text{Pa}]$, given by Eq. (2.12).
- q_4 flow $[1/\text{Pa}]$, given by Eq. (2.13).

$$q_1 = \frac{p_1}{E_{28}} \quad (2.10)$$

$$q_2 = \frac{p_2}{1 \cdot 10^9} \cdot \left(\frac{w/c}{0.38}\right)^{p_{2w}} \quad (2.11)$$

$$q_3 = p_3 \cdot q_2 \cdot \left(\frac{a/c}{6.0}\right)^{p_{3a}} \cdot \left(\frac{w/c}{0.38}\right)^{p_{3w}} \quad (2.12)$$

$$q_4 = \frac{p_4}{1 \cdot 10^9} \cdot \left(\frac{a/c}{6.0}\right)^{p_{4a}} \cdot \left(\frac{w/c}{0.38}\right)^{p_{4w}} \quad (2.13)$$

where,

w/c water-cement ratio $[-]$, $0.22 \leq w/c \leq 0.87$.

a/c aggregate-cement ratio $[-]$, $1.0 \leq a/c \leq 13.2$.

$p_1, p_2, p_{2w}, p_3, p_{3a}, p_{3w}, p_4, p_{4a}, p_{4w}$ are creep factors corresponding to the cement type and are presented in Table 2.1 (Bažant et al., 2015).

Three cement types are given: R – regular cement, RS – Rapid hardening cement and SL – slow hardening cement.

The 28-day elastic modulus E_{28} $[\text{Pa}]$, is given by Eq. (2.14).

$$E_{28} = 4734 \cdot 10^6 \cdot \sqrt{\frac{\bar{f}_c}{1 \cdot 10^6}} \quad (2.14)$$

where,

\bar{f}_c

Mean cylinder strength at 28 days [MPa],
 $15 \text{ MPa} \leq \bar{f}_c \leq 70 \text{ MPa}$.

Table 2.1: Creep factor depending on the cement type (Bažant et al., 2015).

Parameter	R	RS	SL	Parameter	R	RS	SL
p_1	0.70	0.60	0.80	p_{2w}	3.00	3.00	3.00
p_2	$58 \cdot 10^{-3}$	$17.4 \cdot 10^{-3}$	$40.5 \cdot 10^{-3}$	p_{3a}	-1.10	-1.10	-1.10
p_3	$39.3 \cdot 10^{-3}$	$39.3 \cdot 10^{-3}$	$39.3 \cdot 10^{-3}$	p_{3w}	0.40	0.40	0.40
p_4	$3.4 \cdot 10^{-3}$	$3.4 \cdot 10^{-3}$	$3.4 \cdot 10^{-3}$	p_{4a}	-0.90	-0.90	-0.90
p_5	$777 \cdot 10^{-6}$	$94.6 \cdot 10^{-6}$	$496 \cdot 10^{-6}$	p_{4w}	2.45	2.45	2.45
p_{5H}	8.00	1.00	8.00*	$p_{5\epsilon}$	-0.85	-0.85	-0.85
p_{5w}	0.78	0.78	0.78	p_{5a}	-1.00	-1.00	-1.00
* - lacking data or assumed							

The third step for calculating basic creep is to consider the influence of admixtures in the concrete. Bažant et al. (2015) define the following as admixtures: retarder, fly ash, super plasticizer, silica fume, air-entraining agent and water reducer. These are considered as affecting the creep and shrinkage by multiplication with the factors corresponding to the cement type, presented in Table 2.1. In Table 2.2, the multiplication factors corresponding to admixtures from Bažant et al. (2015) are presented.

Table 2.2: Multiplication factors depending on the admixture (Bažant et al., 2015).

Admixture class (% of c)	·p2	·p3	·p4	·p5
Retarder (≤ 0.5)	0.31	7.14	1.35	0.48
Fly ash (≤ 15)				
Retarder (> 0.5)	1.43	0.58	0.90	0.46
Fly ash (≤ 15)				
Fly ash (≥ 15)	0.37	2.33	0.63	1.60
Super plasticizer (≥ 0)	0.72	2.19	1.72	0.48
Silica fume (≥ 0)	1.12	3.11	0.51	0.61
Air entraining agent (≥ 0)	0.90	3.17	1.00	0.10
Water reducer (≤ 2)	1.00	2.10	1.68	0.45
Water reducer ($> 2, \leq 3$)	1.41	0.72	1.76	0.60
Water reducer (> 3)	1.28	2.58	0.73	1.10

The fourth and final step in calculating the basic creep is to calculate the basic creep compliance, $C_0(\hat{t}, \hat{t}')$, given by Eq. (2.15). The basic creep compliance considers the effect of creep where no moisture exchange occurs with the environment.

$$C_0(\hat{t}, \hat{t}') = q_2 \cdot Q(\hat{t}, \hat{t}') + q_3 \cdot \ln(1 + (\hat{t} - \hat{t}')^{0.1}) + q_4 \cdot \ln\left(\frac{\hat{t}}{\hat{t}'}\right) \quad (2.15)$$

where,

the binomial integral $Q(\hat{t}, \hat{t}')$ is approximated by Eq. (2.16).

$$Q(\hat{t}, \hat{t}') = Q_f(\hat{t}') \cdot \left(1 + \left(\frac{Q_f(\hat{t}')}{Z(\hat{t}, \hat{t}')} r(\hat{t}')\right)^{-\frac{1}{r(\hat{t}')}}\right) \quad (2.16)$$

where,

$Q_f(\hat{t}')$ is given by Eq. (2.17).

$Z(\hat{t}, \hat{t}')$ is given by Eq. (2.18).

$r(\hat{t}')$ is given by Eq. (2.19).

$$Q_f(\hat{t}') = \left(0.086 \cdot \hat{t}'^{\frac{2}{9}} + 1.21 \cdot \hat{t}'^{\frac{4}{9}}\right)^{-1} \quad (2.17)$$

$$Z(\hat{t}, \hat{t}') = \hat{t}'^{-0.5} \cdot \ln(1 + (\hat{t} - \hat{t}')^{0.1}) \quad (2.18)$$

$$r(\hat{t}') = 1.7 \cdot \hat{t}'^{0.12} + 8 \quad (2.19)$$

Shrinkage/drying creep

The first step for calculating the shrinkage/drying creep according to Bazant et al. (2015) is to calculate the time variables:

\bar{t} temperature corrected exposure age [days], given by Eq. (2.20)

$$\bar{t} = (t' - t_0) \cdot e^{\beta_{Ts}} \quad (2.20)$$

\bar{t}_0 temperature corrected age from when the concrete is first exposed to the environment [days], given by Eq. (2.21).

$$\bar{t}_0 = t_0 \cdot e^{\beta_{Th}} \quad (2.21)$$

When the temperature is at 20 °C, the temperature corrected age reduces to the actual ages, i.e., $\bar{t} = t - t_0$ and $\bar{t}_0 = t_0$.

The second step for calculating the shrinkage/drying creep is to calculate:

The halftime for drying shrinkage, τ_{sh} [days], given by Eq. (2.22).

$$\tau_{sh} = \tau_0 \cdot k_{\tau a} \cdot \left(k_s \cdot \frac{2V}{S} \right)^2 \quad (2.22)$$

where,

$k_{\tau a}$ shrinkage factor based on the type of aggregate [-], given by Table 2.3

k_s geometry dependent shape factor where,
 $k_s = 1.00$ (infinite slab)
 $k_s = 1.15$ (infinite cylinder)
 $k_s = 1.30$ (sphere)
 $k_s = 1.55$ (cube)

V volume of the model [mm^3], $12 \text{ mm} < V / S < 120 \text{ mm}$.

S surface area of the model [mm^2]. $12 \text{ mm} < V / S < 120 \text{ mm}$.

The interval V / S is given from a typical range of applicability for the B4 model.

Ultimate shrinkage time, τ_0 [days], is given by Eq. (2.23).

$$\tau_0 = \tau_{cem} \cdot \left(\frac{a/c}{6.0} \right)^{p_{\tau a}} \cdot \left(\frac{w/c}{0.38} \right)^{p_{\tau w}} \cdot \left(\frac{6.5 \cdot c}{\rho} \right)^{p_{\tau c}} \quad (2.23)$$

where,

τ_{cem}	shrinkage parameter dependent on cement type [days], given in Table 2.4.
$p_{\tau a}$	shrinkage parameter dependent on cement type [-], given in Table 2.4.
$p_{\tau c}$	shrinkage parameter dependent on cement type [-], given in Table 2.4.
c	cement content $\left[\frac{\text{kg}}{\text{m}^3}\right]$, $200 \frac{\text{kg}}{\text{m}^3} \leq c \leq 1500 \frac{\text{kg}}{\text{m}^3}$.
ρ	concrete density $\left[\frac{\text{kg}}{\text{m}^3}\right]$.

The ultimate shrinkage strain, $\varepsilon_{sh\infty}(\bar{t}_0)$ [-], is given by Eq. (2.24).

$$\varepsilon_{sh\infty}(\bar{t}_0) = -\varepsilon_0 \cdot k_{\varepsilon a} \cdot \frac{E(7 \cdot \beta_{Th} + 600 \cdot \beta_{Ts})}{E(\bar{t}_0 + \tau_{sh} \cdot \beta_{Ts})} \quad (2.24)$$

where,

$k_{\varepsilon a}$	shrinkage factor based on the type of aggregate [-], given by Table 2.3.
ε_0	Ultimate drying shrinkage strain, given by Eq. (2.25).

$$\varepsilon_0 = \varepsilon_{cem} \cdot \left(\frac{a/c}{6.0}\right)^{p_{\varepsilon a}} \cdot \left(\frac{w/c}{0.38}\right)^{p_{\varepsilon w}} \cdot \left(\frac{6.5 \cdot c}{\rho}\right)^{p_{\varepsilon c}} \quad (2.25)$$

where,

$p_{\varepsilon a}, p_{\varepsilon w}, p_{\varepsilon c}, \varepsilon_{cem}$	shrinkage parameters dependent on the type of cement [-], presented in Table 2.4.
--	---

The drying creep, q_5 [1/Pa], is given by Eq. (2.26).

$$q_5 = \frac{p_5}{1 \times 10^9} \cdot \left(\frac{a/c}{6.0}\right)^{p_{5a}} \cdot \left(\frac{w/c}{0.38}\right)^{p_{5w}} |k_h \cdot \varepsilon_{sh\infty}(\bar{t}_0)|^{p_{5\varepsilon}} \quad (2.26)$$

where,

$p_5, p_{5a}, p_{5w}, p_{5\varepsilon}$ creep factors corresponding to the cement type [-], presented in Table 2.1.

k_h humidity factor [-], given by Eq. (2.27).

$$k_h = \begin{cases} 1 - h^3, & h \leq 98 \% \\ 12.94 \cdot (1 - h) - 0.2, & 98 \% < h \leq 100 \% \end{cases} \quad (2.27)$$

where,

h relative humidity of the environment [%].

Table 2.3: Factors for shrinkage based on the type of aggregate (Bažant et al., 2015).

Aggregate type	$k_{\tau a}$	$k_{\varepsilon a}$	Young's modulus E_{agg} (GPa)	Density ρ_{agg} (g/cm ³)
Diabase	0.06*	0.76*	70-90	2.8-3.0
Quartzite	0.59	0.71	50-90	2.5-2.8
Limestone	1.80	0.95	10-70	1.8-2.9
Sandstone	2.30	1.60	10-50	2.0-2.8
Granite	4.00	1.05	30-70	2.5-2.8
Quartz Diorite	15.0*	2.20*	50-100	2.7-3.1
* Denotes uncertain fitted parameters				

Table 2.4: Parameters given by the cement types rate of hardening (Bažant et al., 2015).

Parameter	R	RS	SL
τ_{cem} (days)	0.016	0.080	0.010
$p_{\tau a}$	-0.33	-0.33	-0.33
$p_{\tau w}$	-0.06	-2.40	3.55
$p_{\tau c}$	-0.10	-2.70	3.80
ε_{cem}	$360 \cdot 10^{-6}$	$860 \cdot 10^{-6}$	$410 \cdot 10^{-6}$
$p_{\varepsilon a}$	-0.80	-0.80	-0.80
$p_{\varepsilon w}$	1.10	-0.27	1.00
$p_{\varepsilon c}$	0.11	0.11	0.11

The third step for calculating shrinkage/drying creep is to consider the influence of admixtures in the concrete. Admixtures such as retarder, fly ash, super plasticizer, silica fume, air-entraining agent or water reducer are considered as affecting the creep and shrinkage by multiplication with the factors corresponding to the cement type, presented in Table 2.2. The multiplication factors for different admixtures can be found in Bažant et al. (2015).

The fourth and final step of determining the shrinkage/drying creep is to calculate:

Autogenous shrinkage strain, $\varepsilon_{au}(\bar{t}, \bar{t}_0)$ [-], given by Eq. (2.28).

$$\varepsilon_{au}(\bar{t}, \bar{t}_0) = \varepsilon_{au\infty} \cdot \left(1 + \left(\frac{\tau_{au}}{\bar{t} - \bar{t}_0} \right)^{\alpha_{sh}} \right)^{r_t} \quad (2.28)$$

where,

α_{sh} is a variable used to simplify Eq. (2.28) and has the relationship between the following variables,

$$\alpha_{sh} = r_{\alpha} \cdot \left(\frac{w/c}{0.38} \right)$$

r_t autogenous shrinkage parameter depending on the type of cement [-], presented in Table 2.5.

$\varepsilon_{au\infty}$ final autogenous shrinkage strain [-], given by Eq. (2.29).

$$\varepsilon_{au\infty} = -\varepsilon_{au,cem} \cdot \left(\frac{a/c}{6} \right)^{r_{ea}} \cdot \left(\frac{w/c}{0.38} \right)^{r_{ew}} \quad (2.29)$$

where,

$\varepsilon_{au,cem}, r_{\varepsilon a}, r_{\varepsilon w}$ autogenous shrinkage parameters given by the cement types rate of hardening, presented in Table 2.5.

τ_{au} autogenous shrinkage halftime [days], given by Eq. (2.30).

$$\tau_{au} = \tau_{au,cem} \cdot \left(\frac{w/c}{0.38} \right)^{r_{\tau w}} \quad (2.30)$$

where,

$\tau_{au,cem}, r_{\tau w}$ autogenous shrinkage parameters given by the cement types rate of hardening, presented in Table 2.5.

$\varepsilon_{sh}(\bar{t}, \bar{t}_0)$ drying shrinkage strain [-], given by Eq. (2.31).

$$\varepsilon_{sh}(\bar{t}, \bar{t}_0) = \varepsilon_{sh\infty}(\bar{t}_0) \cdot k_h \cdot S(\bar{t}) \quad (2.31)$$

where,

$S(\bar{t})$ time curve [-], given by Eq. (2.32).

$$S(\bar{t}) = \tanh \sqrt{\frac{\bar{t}}{\tau_{sh}}} \quad (2.32)$$

The compliance factor for drying creep, $C_d(\hat{t}, \hat{t}', \bar{t}_0)$, [1/Pa], is given by Eq. (2.33).

$$C_d(\hat{t}, \hat{t}', \bar{t}_0) = q_5 \cdot \left(e^{(-P_{5H} \cdot H(\hat{t}, \bar{t}_0))} - e^{(-P_{5H} \cdot H_c(\hat{t}', \bar{t}_0))} \right)^{0.5} \quad (2.33)$$

where,

p_{5H} creep parameter dependent on cement type, presented in Table 2.1.

$H(\hat{t}, \hat{t}_0)$ parameter, given by Eq. (2.34).

$$H(\hat{t}, \hat{t}_0) = 1 - (1 - h) \cdot \tanh \sqrt{\frac{\hat{t} - \bar{t}_0}{\tau_{sh}}} \quad (2.34)$$

$H_c(\hat{t}', \hat{t}_0)$ parameter, given by Eq. (2.35).

$$H_c(\hat{t}', \hat{t}_0) = 1 - (1 - h) \cdot \tanh \sqrt{\frac{\hat{t}' - \bar{t}_0}{\tau_{sh}}} \quad (2.35)$$

Table 2.5: Parameters for autogenous shrinkage given by the cement types rate of hardening (Bažant et al., 2015).

Parameter	R	RS	SL
$\tau_{au, cem}$ (days)	1.00	41.0	1.00
$r_{\tau w}$	3.00	3.00	3.00
r_t	-4.50	-4.50	-4.50
r_α	1.00	1.40	1.00
$\epsilon_{au, cem}$	$210 \cdot 10^{-6}$	$-84 \cdot 10^{-6}$	0
$r_{\epsilon a}$	-0.75	-0.75	-0.75
$r_{\epsilon w}$	-3.50	-3.50	-3.50

Subsequently, the drying shrinkage and autogenous shrinkage are added together as the total shrinkage strain $\epsilon_{sh, tot}(\bar{t}, \bar{t}_0)$, given by Eq. (2.36).

$$\epsilon_{sh, tot}(\bar{t}, \bar{t}_0) = \epsilon_{au}(\bar{t}, \bar{t}_0) + \epsilon_{sh}(\bar{t}, \bar{t}_0) \quad (2.36)$$

When the basic creep and the shrinkage/drying creep are calculated, the compliance function for ultimate creep, $J(\hat{t}, \hat{t}') [1/\text{Pa}]$ can be calculated with Eq. (2.37).

$$J(\hat{t}, \hat{t}') = q_1 + R_T \cdot C_0(\hat{t}, \hat{t}') + C_d(\hat{t}, \hat{t}', \bar{t}_0) \quad (2.37)$$

where,

R_T vertical scale factor for the temperature [-], given by Eq. (2.38).

$$R_T = e^{\beta T_c} \quad (2.38)$$

Subsequently, the final strain, $\varepsilon(t)$ [-], can be calculated with Eq. (2.39).

$$\varepsilon(t) = J(\hat{t}, \hat{t}') \cdot \sigma + \varepsilon_{sh,tot}(\bar{t}, \bar{t}_0) + \alpha_T \cdot \Delta T \quad (2.39)$$

where,

α_T coefficient of thermal expansion [$1/^\circ\text{C}$].

ΔT difference in temperature from the reference temperature to the temperature at the time t [$^\circ\text{C}$].

σ applied stress [Pa].

It is further possible to use the compliance function, $J(\hat{t}, \hat{t}')$, to calculate an equivalent creep coefficient $\varphi(t, t')$, given by Eq. (2.40).

$$\varphi(t, t') = E_c(t') \cdot J(\hat{t}, \hat{t}') - 1 \quad (2.40)$$

where,

$E_c(t')$ the elastic modulus at the time of loading [Pa], given by Eq. (2.41).

$$E_c(t') = \frac{1}{J(t' + \Delta t, t')} \quad (2.41)$$

where,

$J(t' + \Delta t, t')$ value of the compliance function after one time step.

Δt the duration of the time step, dependent on the method used for applying the load on the concrete specimens where $0.1 \text{ s} \leq \Delta t \leq 0.1 \text{ days}$.

2.5.2 Eurocode

According to EC2 (2008), for calculating the time-dependent behaviour of concrete, the types of analysis are divided into four sections:

1. General and incremental step-by-step method.
2. Methods based on the theorems of linear viscoelasticity.
3. The ageing coefficient method.
4. Simplified coefficient method.

Certain initial conditions and assumptions apply to all the methods, wherein:

- Creep and shrinkage are considered independent of each other.
- The average creep and shrinkage properties are used in each section where minor differences at different locations are neglected.
- The total deformation caused by actions at different ages can be assessed with the help of the principle of superposition.

From the methods, one and two are typically used for cantilever construction. General and incremental step-by-step method can be applied to all structures. It is recommended for verification of transitional construction phases, as done in cantilever construction since the properties vary along the length. The *Simplified coefficient method* is applied to structures whose support conditions vary, such as in span-to-span or free cantilever construction.

To perform a general analysis, the general method with an incremental step-by-step approach was further analysed. The method assumes the following conditions:

- The reinforcing steel behaves linearly under instantaneous loads.
 - Varying deformation and relaxation should be considered when the stress in prestressing steel is greater than $\frac{f_{p,max}}{2}$, where $f_{p,max}$ is the pre-stressed reinforcements ultimate strength [Pa].
 - A perfect bond between concrete and reinforcement is assumed.
 - Equilibrium and compatibility are maintained.
- Plane sections are assumed, before and after deformation, in the case of linear elements.

Creep:

The creep coefficient, $\varphi(t, t_0)$ [-], is given by Eq. (2.42).

$$\varphi(t, t_0) = \varphi_0 \cdot \beta_c(t, t_0) \quad (2.42)$$

where,

t age of concrete at considered time [days].

t_0 age of concrete at the time of load application [days].

The nominal creep coefficient, φ_0 [-], is given by Eq. (2.43).

$$\varphi_0 = \varphi_{RH} \cdot \beta(f_{cm}) \cdot \beta(t_0) \quad (2.43)$$

where,

φ_{RH} factor considering the impact of relative humidity [-], given by Eq. (2.44).

$$\varphi_{RH} = \begin{cases} 1 + \frac{1 - \frac{RH}{100}}{0.1 \cdot \sqrt[3]{h_0}} & \text{for } f_{cm} \leq 35\text{MPa} \\ \left(1 + \frac{1 - \frac{RH}{100}}{0.1 \cdot \sqrt[3]{h_0}} \cdot \alpha_1\right) \cdot \alpha_2 & \text{for } f_{cm} > 35\text{MPa} \end{cases} \quad (2.44)$$

where,

RH relative humidity of the ambient environment [%]

h_0 equivalent thickness [mm], given by Eq. (2.45).

$$h_0 = \frac{2A_c}{u} \quad (2.45)$$

where,

A_c cross-section area [m^2].

u perimeter of the cross-section in contact with air [m].

The factor considering the impact of the concrete strength, $\beta(f_{cm})$ [-], is given by Eq. (2.46).

$$\beta(f_{cm}) = \frac{16.8}{\sqrt{f_{cm}}} \quad (2.46)$$

where,

f_{cm} mean value of the concrete's strength after 28-days [Pa].

The factor considering the impact of the concrete's age at load application, $\beta(t_0)$ is given by Eq. (2.47).

$$\beta(t_0) = \frac{1}{0.1 + t_0^{0.20}} \quad (2.47)$$

The coefficient for creep development with time, after load application, $\beta_c(t, t_0)$ [-], is given by Eq. (2.48).

$$\beta_c(t, t_0) = \left(\frac{t - t_0}{\beta_H + t - t_0} \right)^{0.3} \quad (2.48)$$

where,

β_H factor considering the impact of relative humidity and equivalent thickness [-], given by Eq. (2.49).

$$\beta_H = \begin{cases} 1.5 \cdot (1 + (0.012 \cdot RH)^{18}) \cdot h_0 + 250 \leq 1500 & \text{for } f_{cm} \leq 35 \text{ MPa} \\ 1.5 \cdot (1 + (0.012 \cdot RH)^{18}) \cdot h_0 + 250 \cdot \alpha_3 \leq 1500 \cdot \alpha_3 & \text{for } f_{cm} > 35 \text{ MPa} \end{cases} \quad (2.49)$$

where,

$\alpha_1, \alpha_2, \alpha_3$ coefficients considering the impact of the concretes strength [-], given by Eq. (2.50), Eq. (2.51) and (2.52) respectively.

$$\alpha_1 = \left(\frac{35}{f_{cm}} \right)^{0.7} \quad (2.50)$$

$$\alpha_2 = \left(\frac{35}{f_{cm}} \right)^{0.2} \quad (2.51)$$

$$\alpha_3 = \left(\frac{35}{f_{cm}} \right)^{0.5} \quad (2.52)$$

Shrinkage:

The total concrete shrinkage strain, ε_{cs} , given by Eq. (2.53).

$$\varepsilon_{cs} = \varepsilon_{cd} + \varepsilon_{ca} \quad (2.53)$$

where,

ε_{cd} drying shrinkage strain [-], given by Eq. (2.54).

$$\varepsilon_{cd} = \beta_{ds}(t, t_s) \cdot k_h \cdot \varepsilon_{cd,0} \quad (2.54)$$

where,

k_h coefficient dependent on the equivalent thickness [-], presented in Table 2.6.

$\beta_{ds}(t, t_s)$ coefficient for drying shrinkage [-], given by Eq. (2.55).

$$\beta_{ds}(t, t_s) = \frac{t - t_s}{(t - t_s) + 0.04 \cdot \sqrt{h_0^3}} \quad (2.55)$$

where,

t_s age of concrete at the start of drying shrinkage [days]. Usually at the end of post-processing.

The nominal value for unrestrained shrinkage, $\varepsilon_{cd,0}$ [-], is given by Eq. (2.56).

$$\varepsilon_{cd,0} = 0.85 \cdot \left((220 + 110 \cdot \alpha_{ds1}) \cdot e^{-\alpha_{ds2} \frac{f_{cm}}{f_{cm0}}} \right) \cdot \beta_{RH} \cdot 10^{-6} \quad (2.56)$$

where,

$\alpha_{ds1}, \alpha_{ds2}$ coefficients dependent on cement type, presented in Table 2.7.

$f_{cm0} = 10 \text{ MPa}$

β_{RH} coefficient dependent on the ambient relative humidity, given by Eq. (2.57).

$$\beta_{RH} = 1.55 \cdot \left(1 - \left(\frac{RH}{RH_0} \right)^3 \right) \quad (2.57)$$

where,

$$RH_0 = 100\%$$

The autogenous shrinkage strain, ε_{ca} [-], is given by Eq. (2.58).

$$\varepsilon_{ca}(t) = \beta_{as}(t) \cdot \varepsilon_{ca}(\infty) \quad (2.58)$$

where,

$\beta_{as}(t)$ autogenous shrinkage coefficient [-], given by Eq. (2.59).

$$\beta_{as}(t) = 1 - e^{-0.2 \cdot t^{0.5}} \quad (2.59)$$

$\varepsilon_{ca}(\infty)$ final autogenous shrinkage strain [-], given by Eq. (2.60).

$$\varepsilon_{ca}(\infty) = 2.5 \cdot (f_{ck} - 10) \cdot 10^{-6} \quad (2.60)$$

where,

f_{ck} characteristic concrete strength, at 28 days [Pa].

Table 2.6: Values for k_h with regard to h_0 .

h_0	k_h
100	1.0
200	0.85
300	0.75
≥ 500	0.70

Table 2.7: Shrinkage coefficients dependent on cement type.

Cement type	α_{ds1}	α_{ds2}	s
S	3	0.13	0.38
N	4	0.12	0.25
R	6	0.11	0.20

Relaxation:

EC2 (2008) states that reinforcement must be designed according to its given relaxation class. The relaxation classes are divided into three classes:

Class 1: Thread or line with normal relaxation.

Class 2: Thread or line with low relaxation.

Class 3: Hot-rolled and cold-rolled bars.

The relaxation loss is usually given as the relation between the absolute value of the tension lost during relaxation and the initial relaxation loss, $\frac{\Delta\sigma_{pr}}{\sigma_{pi}}$ [-]. The relaxation loss is given for class 1, 2 and 3 with Eq. (2.61), Eq. (2.62) and Eq. (2.63), respectively.

Class 1

$$\frac{\Delta\sigma_{pr}}{\sigma_{pi}} = 5.39 \cdot \rho_{1000} \cdot e^{6.7 \cdot \frac{\sigma_{pi}}{f_{pk}}} \cdot \left(\frac{t_i}{1000}\right)^{0.75 \cdot \left(1 - \frac{\sigma_{pi}}{f_{pk}}\right)} \cdot 10^{-5} \quad (2.61)$$

Class 2

$$\frac{\Delta\sigma_{pr}}{\sigma_{pi}} = 0.66 \cdot \rho_{1000} \cdot e^{9.1 \cdot \frac{\sigma_{pi}}{f_{pk}}} \cdot \left(\frac{t_i}{1000}\right)^{0.75 \cdot \left(1 - \frac{\sigma_{pi}}{f_{pk}}\right)} \cdot 10^{-5} \quad (2.62)$$

Class 3

$$\frac{\Delta\sigma_{pr}}{\sigma_{pi}} = 1.98 \cdot \rho_{1000} \cdot e^{8 \cdot \frac{\sigma_{pi}}{f_{pk}}} \cdot \left(\frac{t_i}{1000}\right)^{0.75 \cdot \left(1 - \frac{\sigma_{pi}}{f_{pk}}\right)} \cdot 10^{-5} \quad (2.63)$$

where,

$\Delta\sigma_{pr}$ absolute value of relaxation loss [Pa].

σ_{pi} initially applied stress [Pa].

ρ_{1000} relaxation loss after 1000 hours with an ambient temperature of 20 °C [%], where,

$\rho_{1000} = 8 \%$ - (Class 1)

$\rho_{1000} = 2.5 \%$ - (Class 2)

$\rho_{1000} = 4 \%$ - (Class 3)

f_{pk} characteristic value for the pre-stressed reinforcements ultimate strength [Pa].

t_i time after application of initial stress [hours].

The long-term values for losses due to relaxation are recommended to be calculated for 57 years, namely $t = 500\,000$ hours.

Elastic modulus

The development of the elastic modulus for concrete, $E_{cm}(t)$ [Pa], is given by Eq. (2.64).

$$E_{cm}(t) = \left(\frac{f_{cm}(t)}{f_{cm}} \right)^{0.3} \cdot E_{cm} \quad (2.64)$$

where,

$f_{cm}(t)$ mean value of concrete strength at time t [Pa], given by Eq. (2.65).

f_{cm} mean concrete strength at 28 days [Pa].

E_{cm} mean concrete elastic modulus at 28 days [Pa].

$$f_{cm}(t) = e^{s \cdot \left(1 - \sqrt{\frac{28}{t}}\right)} \cdot f_{cm} \quad (2.65)$$

where,

s coefficient dependent on cement type [Pa], presented in Table 2.7.

Chapter 3

Material input in Abaqus for long-term behaviour of concrete

3.1 Concrete creep

To model creep in Abaqus, viscoelastic behaviour is required in the input property. In Abaqus, the creep property can either be given by *creep* under material specification or visco-elastic under the time-domain *visco-elastic* description (Malm & Sundquist, 2010).

Previous studies, such as Canovic & Goncalves (2005) have compared the options *creep* and *visco-elastic* to determine the appropriate option for cases with varying stress.

The option *creep* allows two options of laws to calculate from, namely, power-law and the hyperbolic-sine law. Canovic & Goncalves (2005) concluded that hyperbolic sine law is too complicated, and power law is inappropriate with applied stress variation. Therefore, the material specification using *creep* was not investigated further and was disregarded as it was not relevant to the scope of this thesis.

The option *visco-elastic* allows the user to input the viscoelastic behaviour with respect to time through four options (Malm & Sundquist, 2010):

1. Prony series specification
2. Creep data input
3. Relaxation data input
4. Frequency-dependent data input

Prony series specification

Prony series requires input data for the following material specifications:

g_i^p	The modulus ratio in the i^{th} term in the prony series expansion of the shear traction relaxation modulus.
k_i^p	The modulus ratio in the i^{th} term in the prony series expansion of the normal traction relaxation modulus.

τ_i The relaxation time for the i^{th} term in the prony series expansion.

The number of i terms can be specified according to available data and user preference (Canovic & Goncalves, 2005).

Creep data input

Creep data requires input data for the following material specifications:

$j_S(t)$ The normalized shear compliance, given by Eq. (3.1).

$j_K(t)$ The normalized bulk compliance, given by Eq. (3.2).

$$j_S(t) = G_0 \cdot J_S(t) \quad (3.1)$$

$$j_K(t) = K_0 \cdot J_K(t) \quad (3.2)$$

where,

G_0 instantaneous shear modulus, given by Eq. (3.3)

K_0 instantaneous bulk modulus, given by Eq. (3.4)

$J_S(t)$ shear compliance, given by Eq. (3.5)

$J_K(t)$ bulk compliance, given by Eq. (3.6).

$$G_0 = \frac{E_0}{2 \cdot (1 + \nu_0)} \quad (3.3)$$

$$K_0 = \frac{E_0}{3 \cdot (1 + \nu_0)} \quad (3.4)$$

where,

E_0 instantaneous elastic modulus [Pa]

ν_0 Poisson's ratio [-].

$$J_S(t) = \frac{\gamma(t)}{\tau_0} \quad (3.5)$$

where,

$\gamma(t)$ total shear strain [-].

τ_0 constant applied stress [Pa].

$$J_K(t) = \frac{\varepsilon^{vol}(t)}{p_0} \quad (3.6)$$

where,

$\varepsilon^{vol}(t)$ total volumetric strain [-].

p_0 constantly applied pressure [Pa].

Abaqus converts the creep test data to relaxation data. The relaxation data is used to calculate the prony series parameters through nonlinear least-squares fit (Canovic & Goncalves, 2005).

The nonlinear least-square-fit procedure minimizes relative error in stress which is used by Abaqus when experimental data is used to determine material constants (Dassault Systemes, 2020).

Relaxation data input

Relaxation data requires data input for the following material specifications:

$g_r(t)$ Normalized shear modulus, given by Eq. (3.7).

$k_r(t)$ Normalized bulk modulus, given by Eq. (3.8).

$$g_r(t) = \frac{G_R(t)}{G_0} = \frac{1}{1 + \varphi(t, t_0)} \quad (3.7)$$

$$k_r(t) = \frac{K_R(t)}{K_0} = \frac{1}{1 + \varphi(t, t_0)} \quad (3.8)$$

where,

$G_R(t)$ shear relaxation modulus, given by Eq. (3.9)

$K_R(t)$ bulk relaxation modulus, given by Eq. (3.10).

$$G_R(t) = \frac{E_0}{2 \cdot (1 + \nu_0) \cdot (1 + \varphi(t, t_0))} \quad (3.9)$$

$$K_R(t) = \frac{K_0}{3 \cdot (1 - 2\nu_0) \cdot (1 + \varphi(t, t_0))} \quad (3.10)$$

where,

$\varphi(t, t_0)$ creep coefficient [-]

Similar to Creep data input, Abaqus uses the Relaxation data input to calculate the Prony series parameters through nonlinear least-squares fit (Canovic & Goncalves, 2005).

Frequency-dependent data input.

The frequency-dependent data is given through sinusoidal oscillation experiments. Further investigations of this were not conducted since it was not necessary to achieve the aim of this thesis.

3.2 Concrete shrinkage

One option according to Malm (2016) for simulating concrete shrinkage in finite element analysis, is to apply a temperature change to the model. In Abaqus, this is done by using the *Predefined Field Manager* tool. By applying a temperature change to the model, the model will shrink if a negative temperature difference is applied and vice versa for a positive temperature. Concrete shrinkage constitutes a reduction of volume. Therefore, a negative temperature change should be applied. To simulate non-uniform shrinkage, it is possible to apply different temperature changes to each segment and part of the model. As previously mentioned in Chapter 2.3, the amount of volume reduction depends on the material properties, geometry, and environment. A segment will have a larger relative volume reduction if it has a smaller thickness and larger exposed surface area. To simulate this, a larger temperature change needs to be applied to segments with a larger surface area to thickness ratio.

An important detail is then to calculate the equivalent change in temperature caused by shrinkage. According to Zhuoya et al. (2018), the applied temperature change, ΔT , is dependent on the thermal coefficient and the total shrinkage strain. The temperature change is given by Eq. (3.11).

$$\Delta T = \frac{\varepsilon_{cs}}{\alpha} \quad (3.11)$$

where,

ε_{cs}	total shrinkage strain [-]
α	thermal coefficient of expansion [1/°C].

3.3 Relaxation of prestressed tendons in concrete

According to Malm & Sundquist (2010), the relaxation of prestressed tendons can be implemented into Abaqus analogously to the way creep is implemented with relaxation data. The relaxation data is calculated according to Chapter 2.5.2 and implemented according to the method presented in Chapter 3.1.

The ratio of relaxation losses and initial prestress, as given in Chapter 2.5.2, needs to be converted to the normalized shear moduli $g_r(t)$ and normalized bulk moduli $k_r(t)$ according to Eq. (3.12) and Eq. (3.13).

$$g_r(t) = 1 - \frac{\Delta\sigma_{pr}}{\sigma_{pi}} \quad (3.12)$$

$$k_r(t) = 1 - \frac{\Delta\sigma_{pr}}{\sigma_{pi}} \quad (3.13)$$

where,

$\Delta\sigma_{pr}$ absolute value of relaxation loss [Pa]

σ_{pi} initially applied stress [Pa].

Chapter 4

Benchmark models

4.1 General

A common understanding while performing finite element analyses is that errors are harder to solve when encountered in a complicated model. Therefore, certain verification and validation models are often used to verify or validate certain aspects of the whole model by creating simpler models. The simpler models can be tested for their sensitivity to certain parameters to have a general understanding of the influence of said parameters. The recommended validation points are the Basic material test, Structural test, and Mesh sensitivity tests. A Basic material test is performed to ensure that the influence of geometry and boundary conditions do not influence the analysis in a way that compromises its validity. In this test, the theoretical relations are validated, and it is ensured that the analysed result focuses on the researched parameters. A Structural test ensures that the structural behaviour of the material is correctly modelled which can be seen by the structural response of the model. Mesh sensitivity is another form of verification to see the influence of mesh on the result of the model, more of this was discussed in Chapter 6.7 (Malm 2016).

In this MSc project, the following verification models were analysed:

1. Concrete creep test
2. Steel relaxation test
3. Concrete shrinkage test

In the concrete creep test, the general behaviour of concrete with regards to creep was analysed by creating a cube and a cylinder model, respectively. The analysis was divided into two models, one based on Eurocode 2 and the other according to the B4 model.

The purpose of the steel relaxation test was to analyse the general behaviour of steel with regards to relaxation according to Eurocode 2 through finite element calculations. This analysis was conducted with a prestressing bar model.

The concrete shrinkage test was used to investigate the difference in vertical deformation with uniform compared to non-uniform shrinkage. This test was conducted on a simplified bridge span model.

In general, the benchmark models followed the same sign convention and direction specification to ensure consistency.

4.2 Concrete creep test

A cube and a cylinder model were used to confirm that models representing creep behaviour accurately correspond to experiments and background theory, as mentioned in Chapter 2. The cube model's creep behaviour was constructed with the B4 model and Eurocode 2. A previous creep experiment with a cylinder was compared with analytical calculations by the B4 model and Eurocode 2 to ensure the correct implementation of the B4 model and Eurocode 2.

For modelling the cube, a *solid* element part with dimensions 1x1x1 m was created with properties representing the viscoelastic behaviour of concrete, as shown in Figure 4.1.

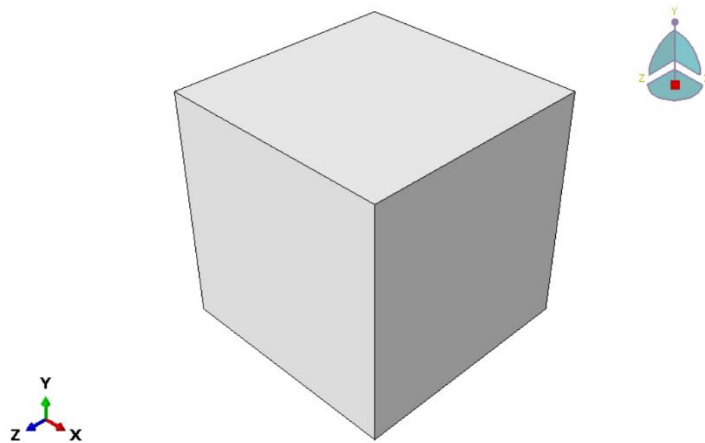


Figure 4.1: Cube model with dimensions 1x1x1 m.

The viscoelastic properties were defined through material specification or *visco-elastic*. The general properties of the cube were chosen as described in Table 4.1.

Table 4.1: Material properties for the cube model.

Material	Density [kg/m ³]	Young's modulus [GPa]	Poisson's Ratio [-]	Expansion Coefficient [1/°C]
Concrete	2400	33	0.2	$1 \cdot 10^{-5}$

Further, the creep input data was calculated with relaxation data input where $g_r(t)$ and $k_r(t)$ were calculated with Eq. (3.7) and Eq. (3.8). The creep coefficient, $\varphi(t, t_0)$ was calculated using Eq. (2.40) for the B4 model and Eq. (2.42) for Eurocode 2.

Three steps were defined to simulate the complete creep phenomenon, namely: “Initial”, “loading” and “unloading”. Another aspect of modelling the loading step was to define the Step as *visco* to analyse the creep effects. Creep modelling requires time-dependent material behaviour where the *visco* step gives a short-term static response in the analysis.

To ensure that the creep behaviour was captured without effects from other loads, loads such as self-weight were not modelled. The only modelled load was a uniform load on top of the surface of the cube, as illustrated in Figure 4.2.

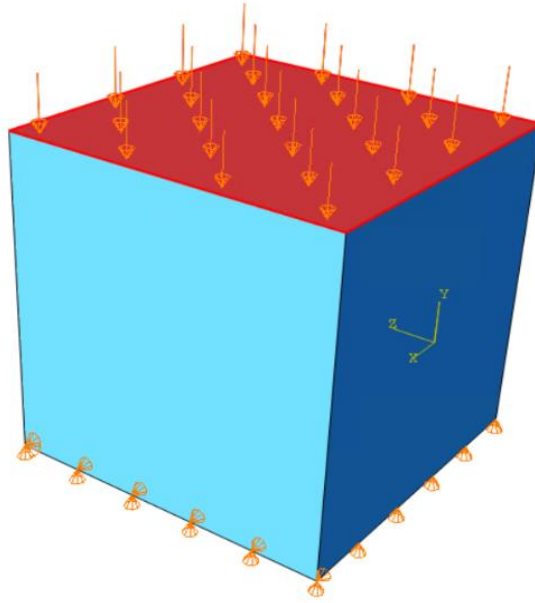


Figure 4.2: Uniform load on the surface of the cube.

The boundary conditions were chosen as the bottom surface being restrained in the vertical direction (y-axis) to ensure that the cube is affected by the axial compressive load. To restrict movement in horizontal directions, one of the sides of the cube was restrained in the horizontal directions, one in the x-axis and one in the z-axis, as illustrated in Figure 4.3.

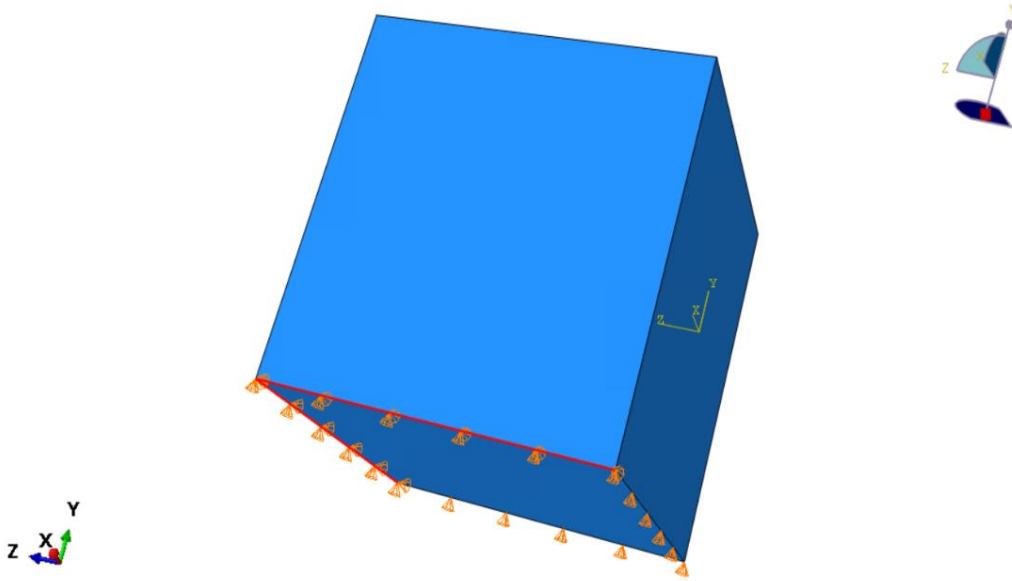


Figure 4.3: Chosen boundary conditions of the cube.

The chosen mesh size was 0.1 m for the cube model. The cube model was analysed with material curves based on the B4 model or Eurocode 2 with one day as the time interval and unloading after 1000 days. The obtained results are presented in Chapter 4.2.1.

As the analysis of creep was fundamental to the analysis of this thesis, an additional analytical test was conducted. The test used input data from an experiment by Weil (1959) to analyse the similarities and differences in creep coefficient. This could give a better understanding of the analytical and FEM model as well as relevant differences. An Abaqus model was created using input data from the experiment by Weil (1959). Apart from the time at unloading and geometry, the modelling process was similar to the aforementioned process for the cube model. The time at unloading was 767 days, as this was the time used by Weil (1959). The geometry was a cylinder with a radius of 50 mm and a height of 400 mm as used in Weil (1959). The chosen boundary conditions were the same as the cube model. The corresponding results, using the B4 model and Eurocode 2, were compared with results from the experiment by Weil (1959) as described in Chapter 4.2.1.

4.2.1 Cube and cylinder model

The results from the cube model through Abaqus with Eurocode 2 and the B4 model are illustrated in Figure 4.4 as the creep strain over time.

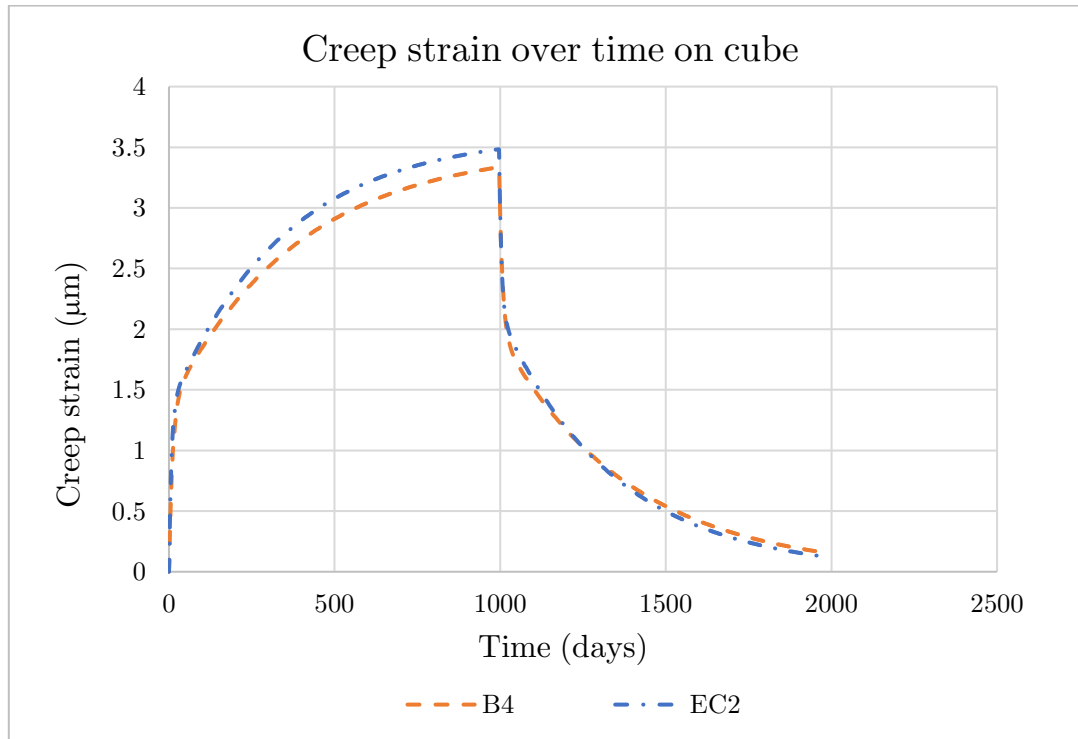


Figure 4.4: Creep strain over time with Eurocode 2 and B4 model.

The creep coefficient over time of cylinder experiment from Weil (1959) as a comparison with B4 model and Eurocode 2 is illustrated in Figure 4.5. The resulting creep strain of the cylinder experiments from modelling in Abaqus is shown in Figure 4.6.

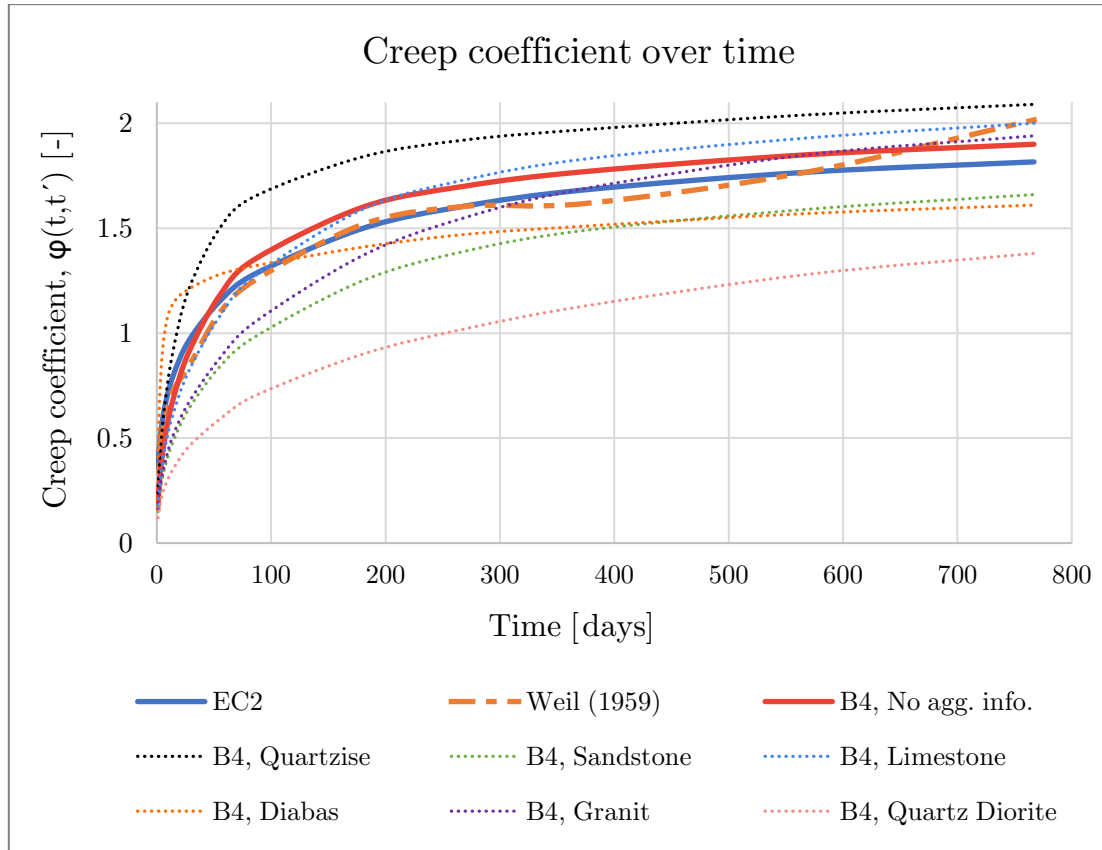


Figure 4.5: Creep coefficient over time with Weil 1959, Eurocode 2 and B4 model.

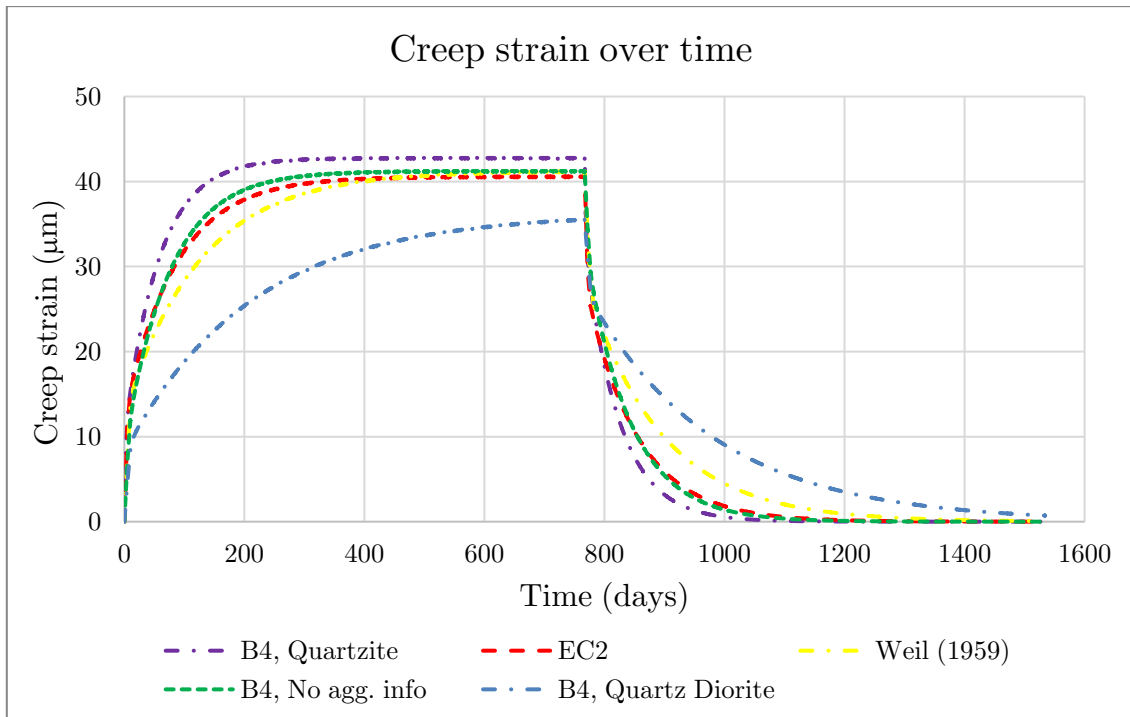


Figure 4.6: Creep strain over time with Weil 1959, Eurocode 2 and B4 model.

The analysis from the cube model indicated that the behaviour of creep strain was similar with minor differences in the peak value, which is expected as the models are different. The cylinder model shows that the value of creep coefficient varies considerably when using the B4 model, depending on which aggregate was chosen. The creep coefficient modelled with Eurocode 2 and the B4 model when no aggregate type was specified, were similar to the experiment by Weil (1959). This observation was also true when creep strain was calculated from Abaqus. Therefore, to improve the accuracy of creep strain values, in cases when aggregate is not known, it is appropriate to use a non-specified value of the aggregate instead of assuming it. Choosing the wrong aggregate type in the B4 model may result in significant changes in the result and therefore should be calculated with caution. Eurocode 2 on the other hand, gives relatively accurate values compared to Weil (1959), despite being a simpler model in comparison with the B4 model.

4.3 Steel relaxation test

To verify the losses due to relaxation of prestressing steel tendons with a finite element model, a simple 2D version of a prestressing steel tendon was defined and the stress loss due to relaxation was calculated according to Eurocode 2 as described in Chapter 2.5.2.

The tendon was modelled as a truss in Abaqus with fully restrained boundary conditions, as illustrated in Figure 4.7. The material and geometrical properties are presented in Table 4.2.

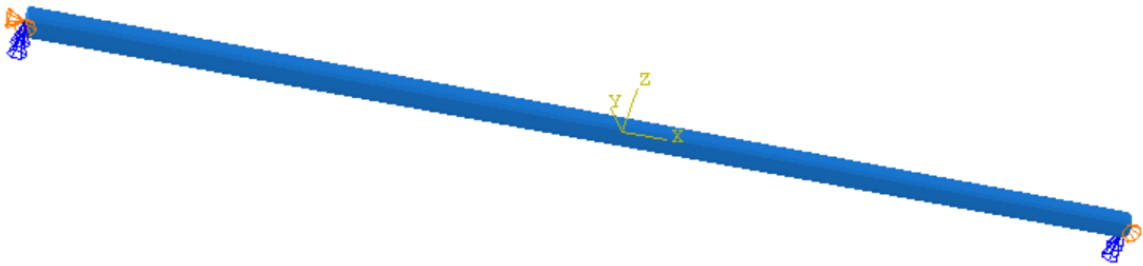


Figure 4.7: 2D prestressing rebar tendon model with boundary conditions.

Table 4.2: Material and geometrical properties of steel prestressing tendons

Density (kN/m ³)	Young's Modulus (GPa)	Poisson's ratio [-]	Length (mm)	Cross-sectional area (mm ²)
7700	210	0.3	1000	462

To simulate the losses in stress due to relaxation of the steel, the tendon was modelled as a viscoelastic material, where relaxation data was incorporated with Eq. (3.12) and Eq. (3.13).

To isolate the effect of stress loss due to relaxation, the only load applied on the prestressing tendon was an initial stress of 1450 MPa. In Abaqus, this was applied as a *Predefined field* load over the whole tendon.

The tendon was simulated with a period of 57 years (500 000 hours) as per the recommended period described in Chapter 2.5.2. The chosen mesh size was 10 mm.

The result from the finite element model was compared with the theoretical value of stress relaxation from Eurocode 2, where the theoretical stress relaxation was calculated with Eq. (2.63) and Eq. (3.12). The obtained results are presented in Chapter 4.3.1.

4.3.1 Prestressed tendon

The stress relaxation of the tendon is presented in Figure 4.8. The results show that the stress relaxation curvature behaviour from the finite element model was similar to the theoretical behaviour, as described by the Maxwell model, in Figure 2.6. The comparison between the theoretical stress relaxation with EC2 and finite element value showed that they have similar behaviour. However, the finite element seems to overestimate the relaxation during the first 30 years.

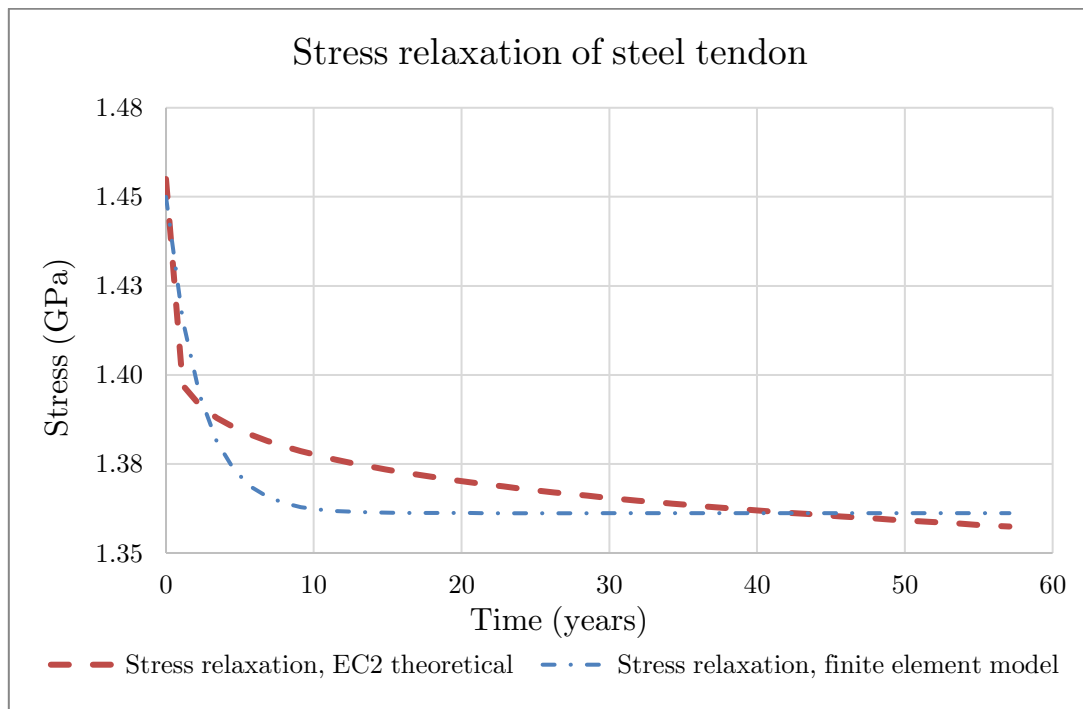


Figure 4.8: Stress relaxation in the steel tendon.

4.4 Concrete shrinkage test

The simplified bridge span was based on a simplified description of the main span of the Alvik bridge. A cross-section of the Alvik bridge near pier 4, as illustrated in Figure 4.9, was chosen as the cross-section for the whole simplified bridge span model. The length of the span for the simplified bridge span model was chosen as 140 m, which is the length of the main span of the Alvik bridge as illustrated in Figure 5.1.

The model was used to principally show if non-uniform shrinkage of the box-girder cross-section would lead to larger deformations, compared to a cross-section with uniform shrinkage. The simplified bridge span was then modelled in Abaqus, as illustrated in Figure 4.10 and with material properties given in Table 4.3.

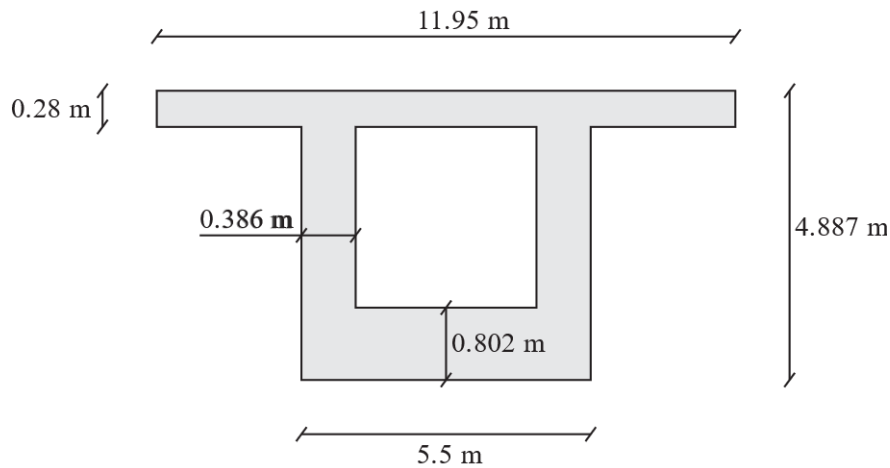


Figure 4.9: Cross-section of the Alvik bridge near pier 4.

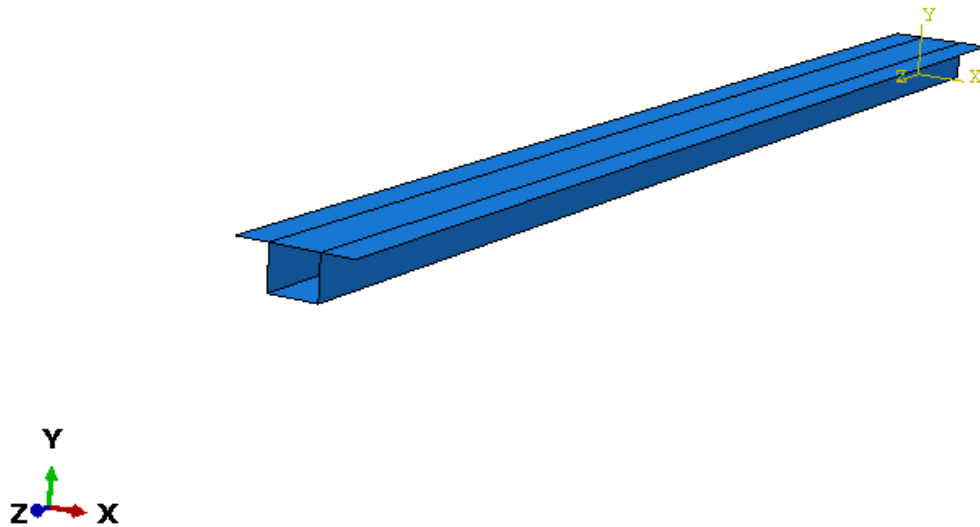


Figure 4.10: Simplified bridge span model assembly in Abaqus.

Table 4.3: Material properties for Simplified bridge span model.

Material	Density [kg/m^3]	Young's modulus [GPa]	Poisson's Ratio [-]	Expansion Coefficient [$1/^\circ\text{C}$]
Concrete	2400	33	0.2	$1 \cdot 10^{-5}$

Since the main span of the Alvik bridge is connected to a pillar and box girder spans on each side, the boundary conditions for the simplified bridge span model were given as a coupling connected to a reference point at the cross-section's centre of gravity, as illustrated in Figure 4.11.

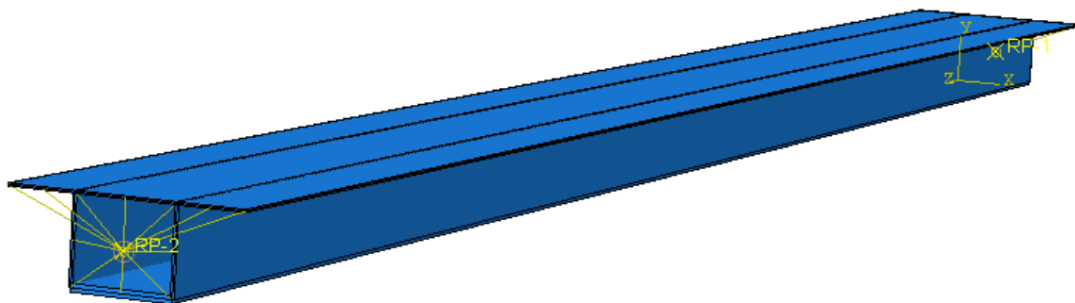


Figure 4.11: Boundary conditions applied to the model.

To establish shrinkage in a finite element model, equivalent temperature loads as described in Chapter 3.2 were implemented. To analyse non-uniform shrinkage, the model was subjected to different temperature loads depending on the thickness of each part of the cross-section. The applied temperature change was chosen to correspond with the thickness of each respective cross-section part. Thinner cross-section segments have larger shrinkage strains compared to thicker cross-section segments. Therefore, the temperature change should be larger in thin cross-section segments compared to thicker cross-section segments. The bottom slab was given a temperature change of 10 °C. The webs, which had roughly 50 % of the thickness of the bottom slab were given a temperature change of 20 °C. The top slab which had roughly 35% of the thickness of the bottom slab was given a temperature change of 40 °C. The change in temperature applied to the cross-section with uniform shrinkage was chosen by applying a constant temperature change over the cross-section. Therefore, a temperature change of 25 °C was applied to all parts of the cross-section. In Abaqus, the temperature loads were applied with the tool *predefined field*. The chosen mesh size was 3 m since a detailed analysis was not required. Only the general behaviour of the model was analysed. The obtained results are presented in Chapter 4.4.1.

4.4.1 Simplified bridge span

The deformation due to non-uniform and uniform shrinkage is presented in Figure 4.12. The difference in displacement indicated that non-uniform shrinkage does result in larger deformations, in comparison with uniform shrinkage. The results show that it is important to consider non-uniform shrinkage. However, the equivalent temperature changes for this simplified model were not based on shrinkage strain values normally occurring in concrete. This means that the size of the difference in deformation may not be entirely representative.

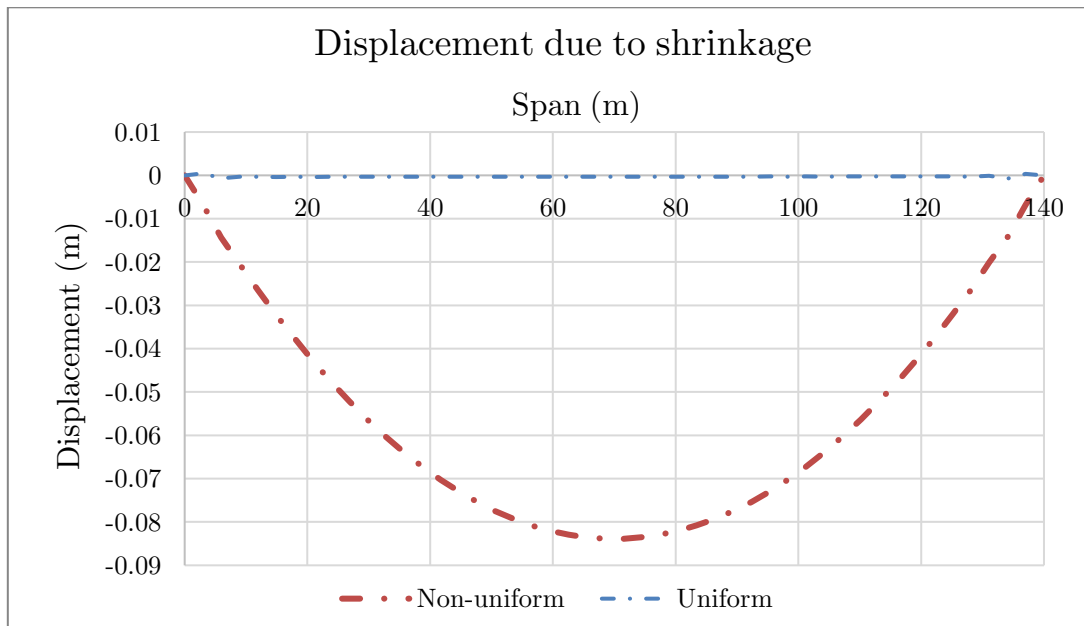


Figure 4.12: Displacement due to non-uniform and uniform shrinkage.

Chapter 5

Case study - the Alvik bridge

5.1 Geometry and general description

The case study used in this thesis was based on the Alvik bridge. It is located in central Stockholm, connecting Stora Essingen with Alvik. The bridge was taken into traffic in the year 2000 and is used as a means of travelling for pedestrians, cyclists, and light rail traffic. The bridge consists of 7 supports that carry the 6 spans, as illustrated in Figure 5.1. The length of the spans varies from 33 m, between supports 1 and 2, to 140 m at the midspan between supports 4 and 5. The total length of the bridge is 430 m, and the width is 13 m (Ericsson et. al, 2002).

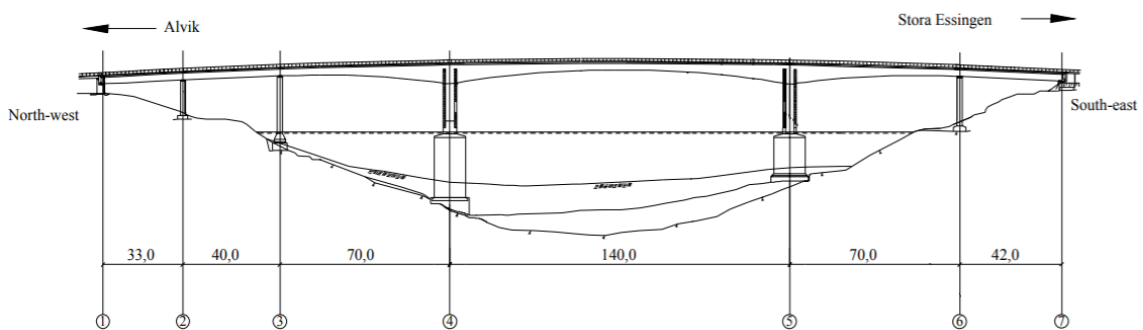


Figure 5.1: Spans and piers of the Alvik bridge. (Appendix B.1).

The cross-section of the bridge is a box girder section with roughly $\frac{2}{3}$ of the bridge's width used by light rail traffic and $\frac{1}{3}$ by pedestrians and cyclists. The cross-section has different thicknesses between the top and bottom flange, as illustrated in Figure 5.2. The thickness and height of the cross-section also varies in the spans where balanced cantilevering construction was used, namely between support 3 to 4, 4 to 5 and 5 to 6.

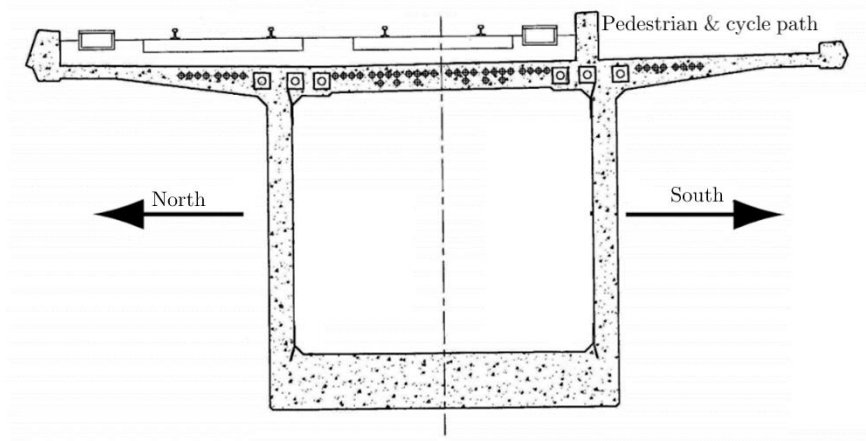


Figure 5.2: Box girder cross-section of The Alvik bridge (Appendix B.1).

The variation of the span lengths, the thickness of the top and bottom flanges, thickness of the web as well as height of the cross-section is presented in Table 5.1, which were acquired from the original structural drawings of the bridge (Appendix B.2). The values for thickness and height of the cross-section are largest near the supports and decrease gradually with the lowest values at midspans. Balanced cantilever construction was not used for spans between support 1 to 3 and 6 to 7. However, they also have box girder cross-sections, where the cross-section is constant throughout the spans.

Table 5.1: Summary of the variation of the span lengths, thickness and height of the cross-section.

Between supports	Span length [m]	Maximum thickness top flange [m]	Thickness bottom flange [m]	Total height of cross-section [m]	Thickness of web [m]
3 - 4	70	0.305 - 0.240	1.35 - 0.384	8.017 - 3.202	0.386
4 - 5	140	0.305 - 0.240	1.35 - 0.384	8.017 - 3.202	0.386
5 - 6	70	0.305 - 0.240	1.35 - 0.384	8.017 - 3.202	0.386

An important aspect of the bridge structure is the prestressed tendons. During the construction phase, tendons are prestressed in the top flange to create an upwards camber. When the construction phase is complete and the centre segment has been cast, tendons in the bottom flanges are post-tensioned. The arrangement and number of tendons in the top flange is illustrated in Figure 5.3, where the numbers are the amount of tendons on one side of the bridge, over support number 5. The arrangement and

number of tendons in the bottom flange is illustrated in Figure 5.4, where the numbers are the amount of tendons on one side of the bridge.

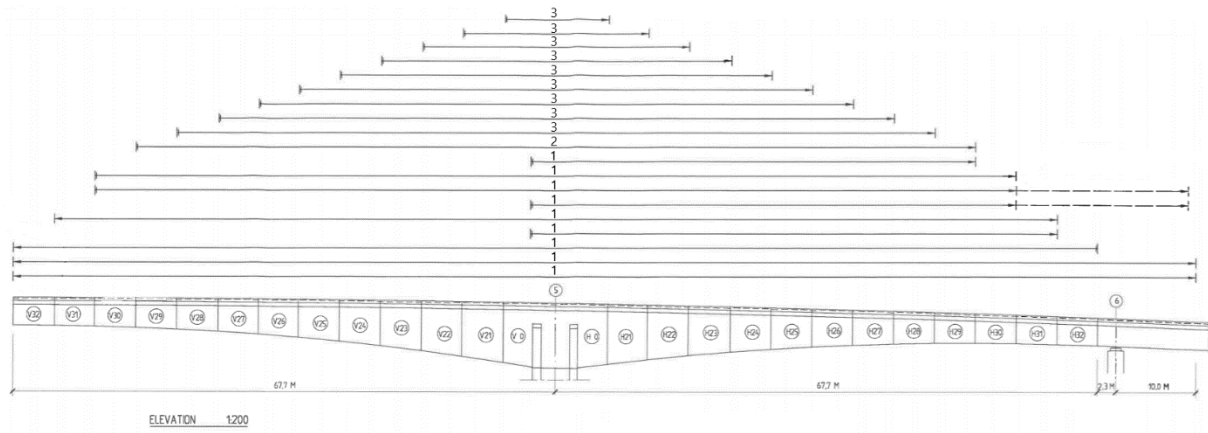


Figure 5.3: Arrangement and number of tendons in the top flange (Appendix B.2).

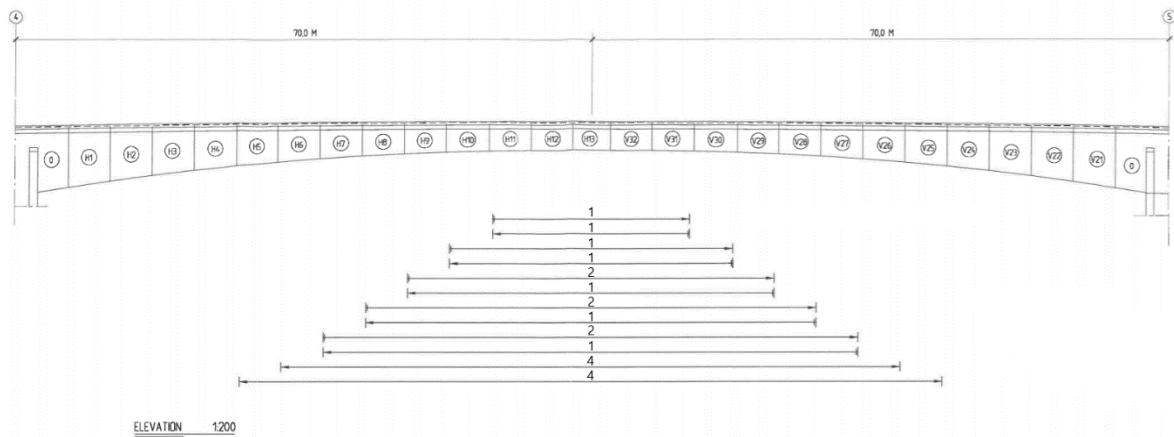


Figure 5.4: Arrangement and number of tendons in the bottom flange (Appendix B.2).

Each tendon consists of 16 wires, where a wire has a diameter of 12 mm. The tendons are placed throughout the cross-section of the top flange and bottom flange, as illustrated in Figure 5.2 for the tendons in the top flange.

The main supports 4 and 5 are constructed on moraine (Appendix B.2). The two main cantilevering supports 4 and 5, have two pillars at each support, as illustrated in Figure 5.5. The individual pillars have dimensions of 1x6 m. The pillars have a height of 25 m above the waterline (Appendix B.2).

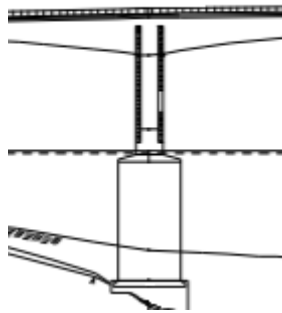


Figure 5.5: Illustration of the twin pillars at support 4 (Appendix B.1).

5.2 Material properties

In general, the Alvik bridge consists of two main materials which comprise the structural components: concrete and steel. The properties of the concrete and steel are presented in and Table 5.2 and Table 5.3, respectively.

The majority of the Alvik bridge was constructed with concrete strength class K45, where some segments were constructed with K50 and K55 (Appendix B.2). To simplify the analysis, only strength class K45 was used. According to Malm & Sundquist (2010), concrete strength class C35/45 is equivalent to K45. The values for concrete presented in Table 5.2 are the 28-day values for concrete strength class C35/45.

Table 5.2: Concrete material properties

Parameter	Value	Unit	Source
Density (Reinforcement included)	2500	kg/m ³	(Eurocode 2, 2002)
Poisson's ratio	0.2	—	(Eurocode 2, 2008)
Elastic modulus	34	GPa	(Eurocode 2, 2008)
Mean cylinder compressive strength	43	MPa	(Eurocode 2, 2008)
Water-cement ratio	0.45	—	(Appendix B.2)

Table 5.3: Prestressed steel material properties.

Parameter	Value	Unit	Source
Density	7850	kg/m ³	(Eurocode 2, 2008)
Poisson's ratio	0.3	—	(Eurocode 2, 2008)
Elastic modulus	195	GPa	(Eurocode 2, 2008)
Relaxation class	2	—	(Appendix B.2)

5.3 Construction phase

The Alvik bridge was built according to the cast in-situ balanced cantilevering method. The bridge span was segmentally and symmetrically cast, from piers 4 and 5, towards the centre of the spans. Each segment was cast with the help of a form traveller. The newly cast concrete was allowed to harden for roughly one week, where the form traveller was subsequently moved forward to cast the next segment (Ericsson, 2002). As each segment was cast, the cantilevered bridge segments were given an upward camber with the help of the prestressed steel tendons. Between segment H12 and V32, the connecting segment, H13, was cast which created a continuous span between pier 4 and 5. All the segments are 5.1 m long, except for the connecting segment, which is 4.6 m, and the segments at the supports, which are 6.5 m. The tendons in the bottom slab were post-tensioned after the connecting segment had been cast (Malm & Sundqvist, 2010).

5.4 Loads

Self-weight

The effect of the self-weight is applied due to the density of the materials in the Alvik bridge. The gravitational acceleration was assumed as 9.82 m/s^2 .

Ballast and asphalt

The ballast and asphalt are applied on the bridge deck after the completion of the construction phase. The ballast and asphalt are applied to different parts of the bridge, where the ballast is applied on the area reserved for the light rail and the asphalt is applied on the area reserved for the pedestrian and cycle path, as illustrated in Figure 5.2.

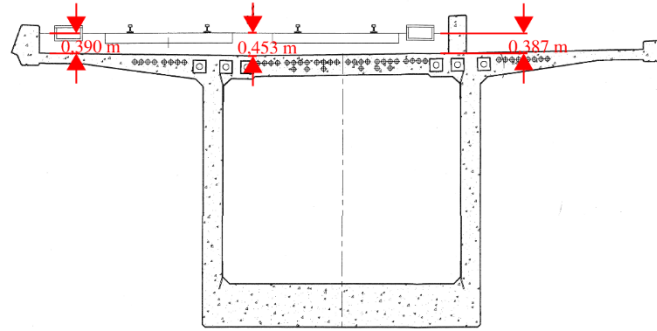


Figure 5.6: Railway and pedestrian & cycle path area, as well as the height of ballast (Appendix B.2).

The magnitude of the load for ballast and asphalt is determined by the density and height of the material, see Table 5.4. The height of the ballast was measured from the drawing illustrated in Figure 5.6. The average height of the ballast, from the measurements in Figure 5.6, was 0.41 m. Therefore 0.41 m was chosen as the height of the ballast on the bridge deck.

Table 5.4: Ballast and asphalt load properties.

	Density [kg/m^3]	Height [m]	Equivalent load [kN/m^2]	Source
Ballast	2600	0.41	10.7	Eurocode 2 (2002)
Asphalt	2200	0.1	2.20	(Appendix B.2)

Form traveller

According to Malm & Sundqvist (2010), the load from the form traveller is 480 kN. The load was given by the design company for a similarly constructed bridge. Therefore, the same load magnitude was assumed for the Alvik bridge.

The form traveller load acts on the most recently cast segment. The four spans constructed with balanced cantilever construction method each have an equivalent form traveller load, during the construction phase.

Prestress

The tendons were tensioned with different loads. Where, the arrangement, loads and equivalent stress are presented in Table 5.5 for the top tendons and Table 5.6 for the

bottom tendons. The numbers describing the placement of the tendons, from segment to segment, corresponding to the numbers in Figure 5.3 and Figure 5.4.

Table 5.5: Placement, applied force, and equivalent stress for the tendons in the top flange (Appendix B.2).

Placement (segment to segment)	Force applied on each cable [kN]	Equivalent stress [MPa]
V0-H0	2242	929
V21-H21	2294	950
V22-H22	2345	972
V23-H23	2377	985
V24-H24	2377	985
V25-H25	2377	985
V26-H26	2377	985
V27-H27	2377	985
V28-H28	2377	985
V29-H29	2377	985
V0-H29	2377	985
V30-H10	2377	985
V30-H10	2377	985
V0-H30	2377	985
V31-H31	2377	985
V0-H31	2377	985
V32-H32	2377	985
V32-H32	2377	985
V32-H32	2377	985

Table 5.6: Placement, applied force, and equivalent stress for the tendons in the bottom flange (Appendix B.2).

Placement (segment to segment)	Force applied on each cable [kN]	Equivalent stress [MPa]
V25-H25	2377	985
V26-H6	2377	985
V27-H27	2377	985
V28-H28	2377	985
V29-H29	2377	985
V30-H30	2377	985
V31-H31	2313	958

5.5 Cracking and strengthening

About two years after the Alvik bridge was constructed, significant crack propagation was noticed in the webs of the bridge, as illustrated in Figure 5.7 (Malm & Sundqvist, 2010).

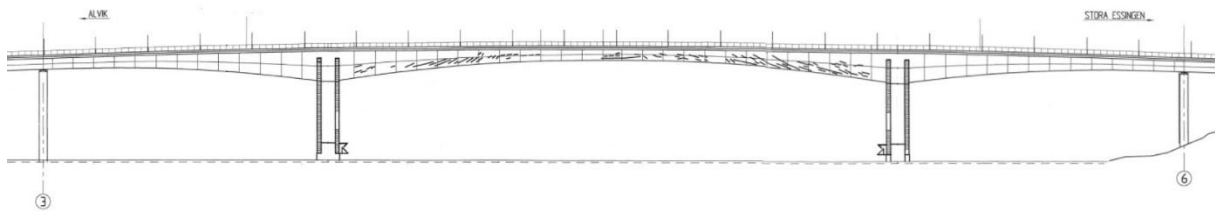


Figure 5.7: Cracks on the Alvik bridge (Appendix B.1).

To ensure that further crack propagation was stopped, strengthening procedures were conducted. The strengthening was conducted during 2003 by Skanska Teknik AB according to the design instructions by Luleå Technical University. The strengthening was performed as described in SBUF (n.d.), see Figure 5.8. Smaller cracks were taped with strips of carbon fibre laminate glued perpendicular to them. Larger cracks were treated by drilling tie rods through the web inside the box girder (SBUF, n.d.). Certain cracks were filled after the strengthening work.

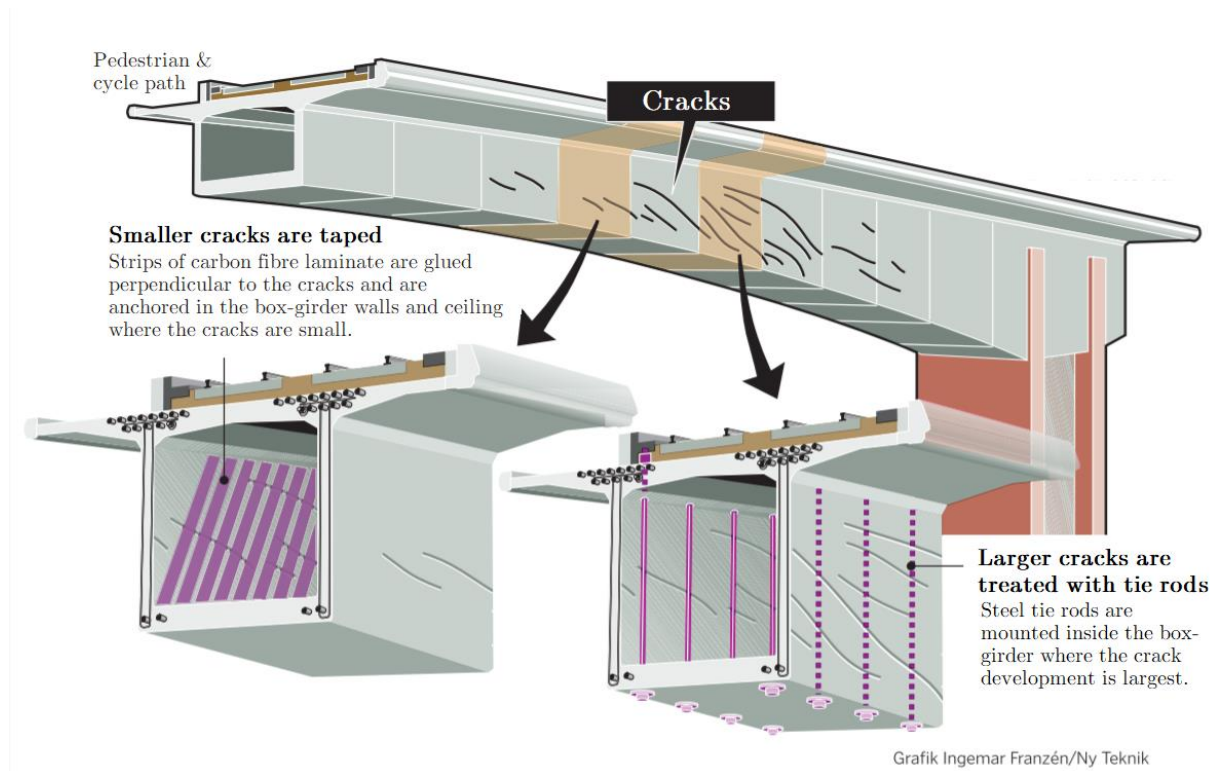


Figure 5.8: Strengthening of the Alvik bridge (SBUF, n.d.).

According to Malm & Sundqvist (2010), cracks and creep cannot be modelled simultaneously in Abaqus. Malm & Sundqvist (2010) also mention that ignoring the effects of creep could have a large impact on the final deformation. For the Alvik bridge, cracks were found in the webs meaning that webs should either consider cracking or creep in the modelling for this thesis. According to Malm & Ansell (2009), only minor differences in deformation were obtained when cracking in webs was regarded compared to disregarded. Therefore, this thesis only focused on modelling with creep and disregarded the contribution of cracking.

5.6 Measurement observation of the Alvik bridge

After discovering cracks on the Alvik bridge, the owners, Stockholm Public Transport (SL), decided to monitor the bridge deformation over time to determine if the strengthening solutions were sufficient. The dynamic measurement of the variation in crack width was conducted by Malm et.al. (2006). The monitoring of the bridge was conducted by Bro och Stålkontroll (2020) starting in March 2002. As illustrated in Figure 5.9, the long-term deformation measurements were obtained along several points along the bridge from Bro och Stålkontroll, BSK (2020). The numbers corresponding to the points along the bridge correspond to the numbers along the horizontal axis in Figure 5.10. Figure 5.10 illustrates the measured displacement over time along the northern and southern edge of the Alvik bridge.

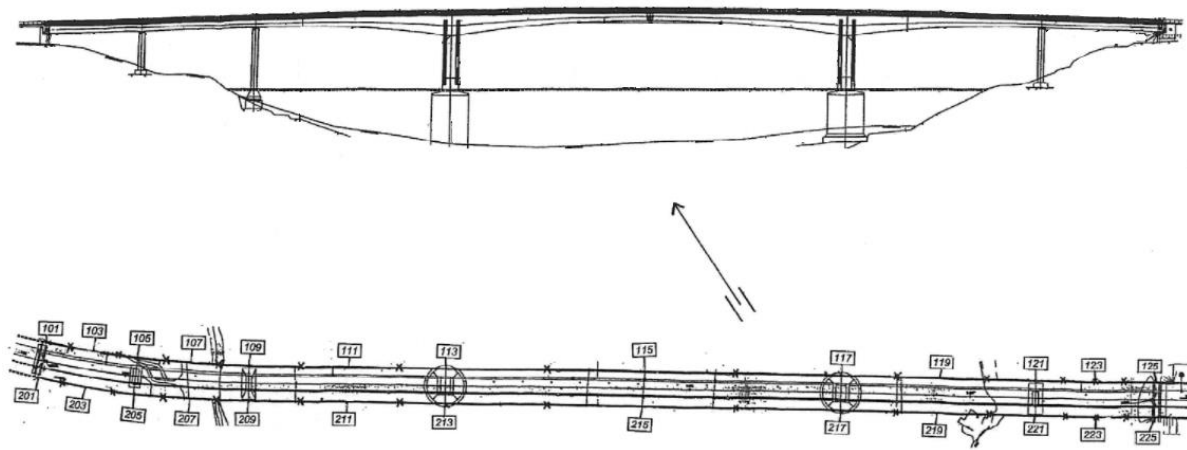


Figure 5.9: Measurement points along the Alvik bridge Bro och Stålkontroll (2020).

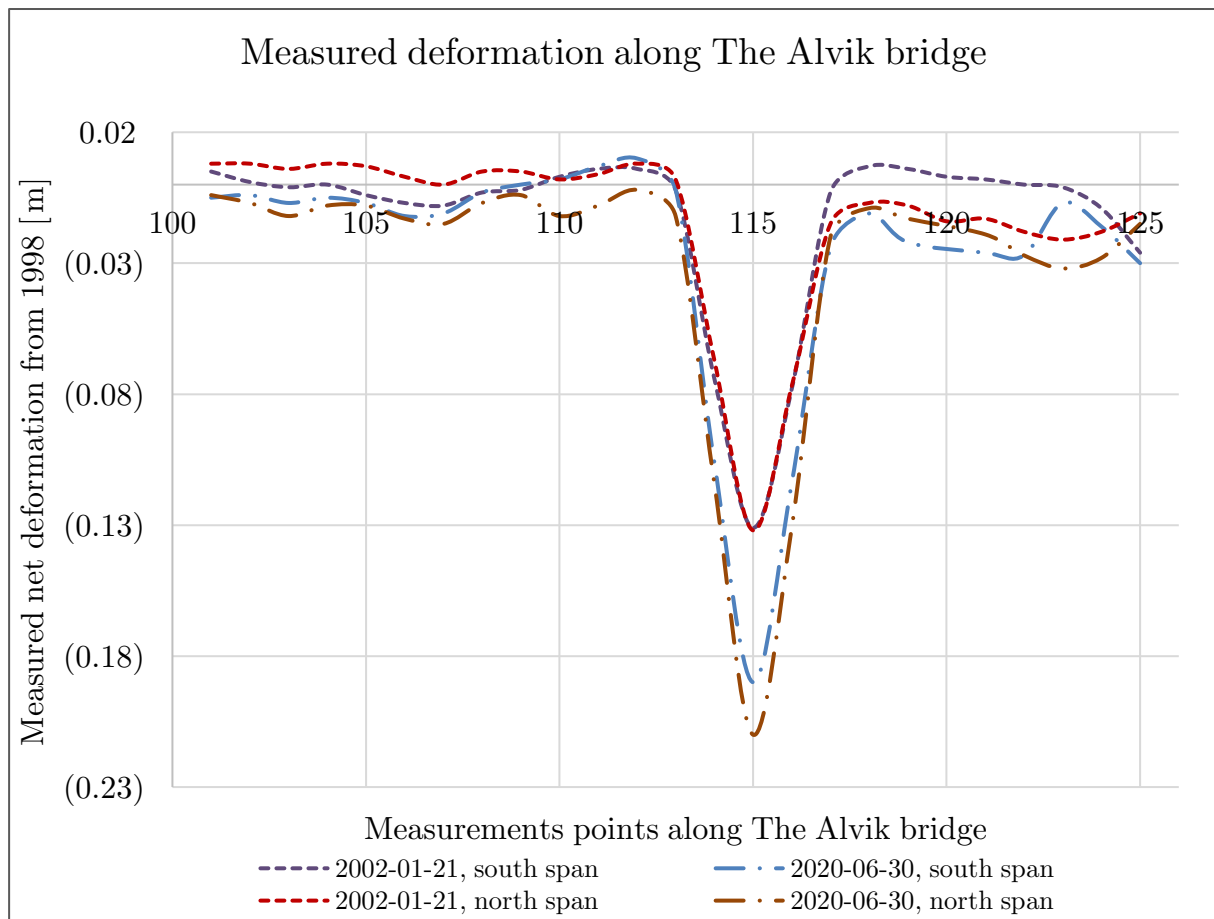


Figure 5.10: Displacement along the north and south edge of the bridge span from 2002 and 2020 (Bro och Stålkontroll, 2020).

The measured deformations illustrated in Figure 5.10 shows deformation in 2002 and 2020 compared to the original measurements from 1998: by subtracting the measured height in 2002 and 2020 from the measured height in 1998. This was implemented to acquire a net deformation that would be simpler to compare with the results from Abaqus. Similarly, the behaviour of net deformation from the year 1998 to 2020 for midspan, is illustrated in Figure 5.11.

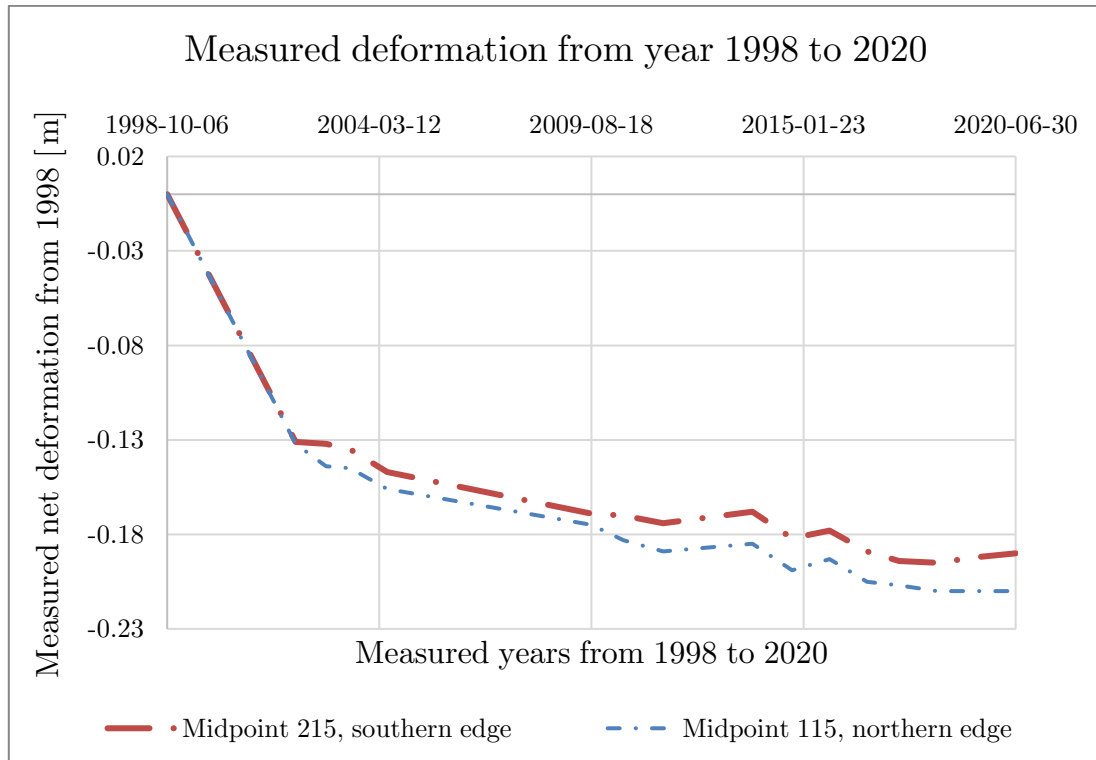


Figure 5.11: Measured deformation for southern and northern midspan from the year 1998 to 2020 (Bro och Stålkontrol, 2020).

Chapter 6

Modelling of the Alvik bridge

6.1 Model construction

The Abaqus model of the Alvik bridge was defined with three different element types:

1. Shell elements to represent the box girder segments of the span between supports 3 to 4, 4 to 5 and 5 to 6.
2. Beam elements to represent the piers at supports 4 and 5, as well as the box girder segments of spans between supports 1 to 2, 2 to 3 and 6 to 7.
3. Truss elements represent the tendons in the top and bottom flanges.

The shell element segments were simplified from the structural drawings by disregarding curves, simplifying edges and assuming a constant thickness in the web and flanges along each segment. The edges were simplified by disregarding the edge beams. The edge beams do not need to be considered when assessing the structural capacity of the bridge (Trafikverket, 2019). An example of simplification is given in comparison between Figure 6.1 and Figure 6.2.

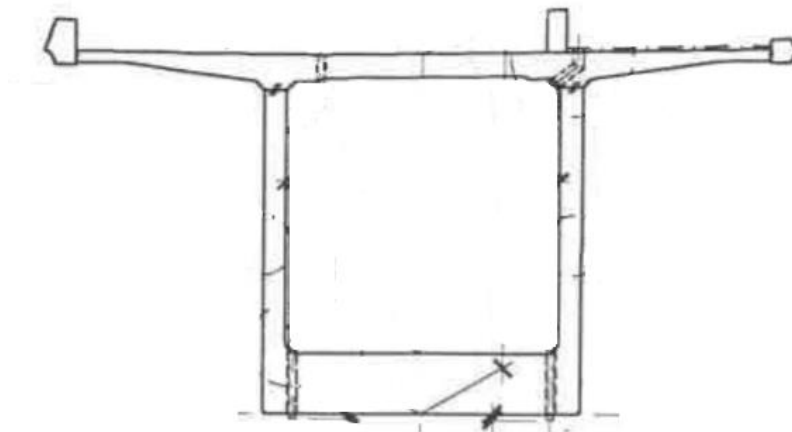


Figure 6.1: Example of cross-section before simplification (Appendix B.2).

The modelled cross-sections had different length, height and thickness depending on their placement in the bridge span. The variation in geometry is illustrated in Figure 6.2. The cross-section on the right represents segment H0/V0 (above the supports), while the left represents segment H13 (the connecting segment), where the numbering is illustrated in Figure 5.3 and Figure 5.4.

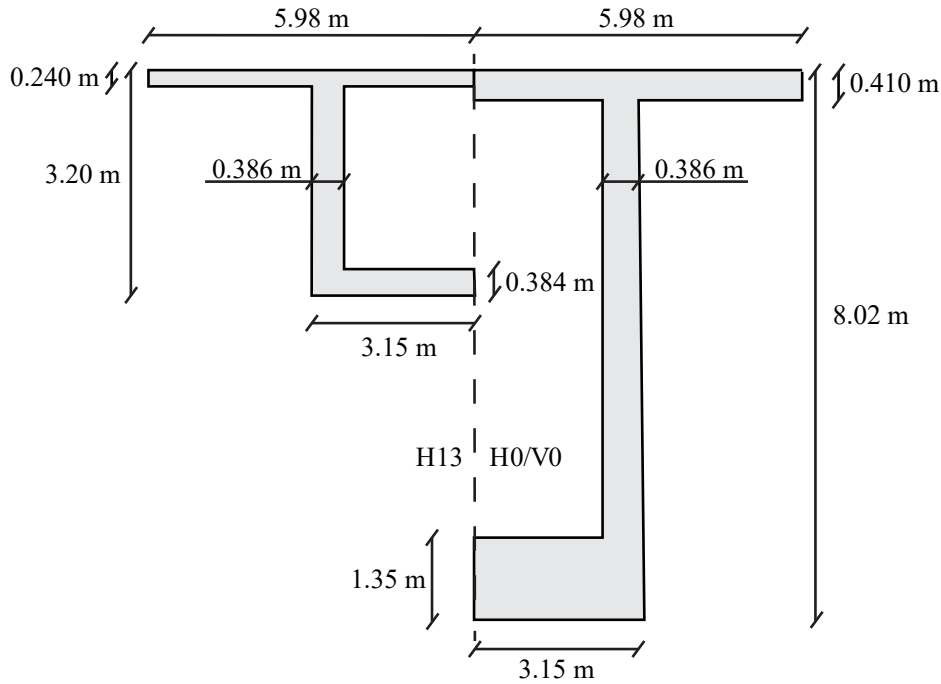


Figure 6.2: Cross-section of segment H13 (left) and H0/V0 (right).

Each segment was divided into three parts: top flange, web, and bottom flange, as illustrated in Figure 6.3. All the segments, except for the segments above the supports and the connecting segment, were given a length of 5.1 m. The segments above the supports were given a length of 6.5 m. The connecting segment was given a length of 4.6 m.

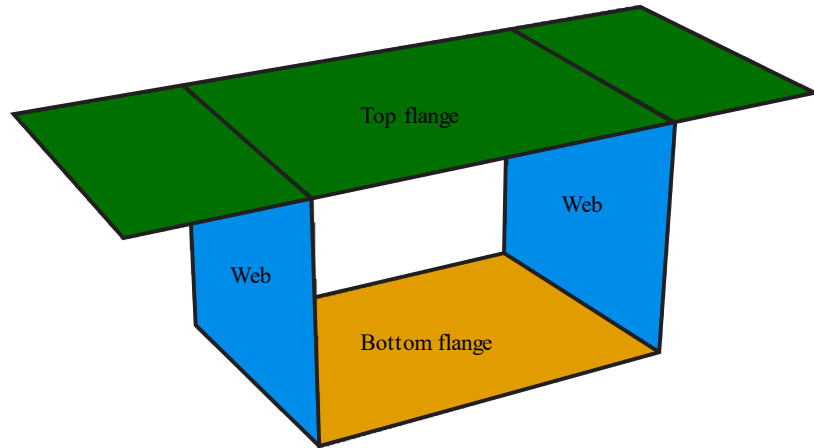


Figure 6.3: The different parts of a bridge segment.

To represent the box girder spans between supports 1 to 2, 2 to 3 and 6 to 7, an equivalent I-profile was assigned to the beams, as illustrated in Figure 6.4. The piers at supports 4 and 5, were modelled as beams with equivalent twin pillars, as illustrated in Figure 6.4.

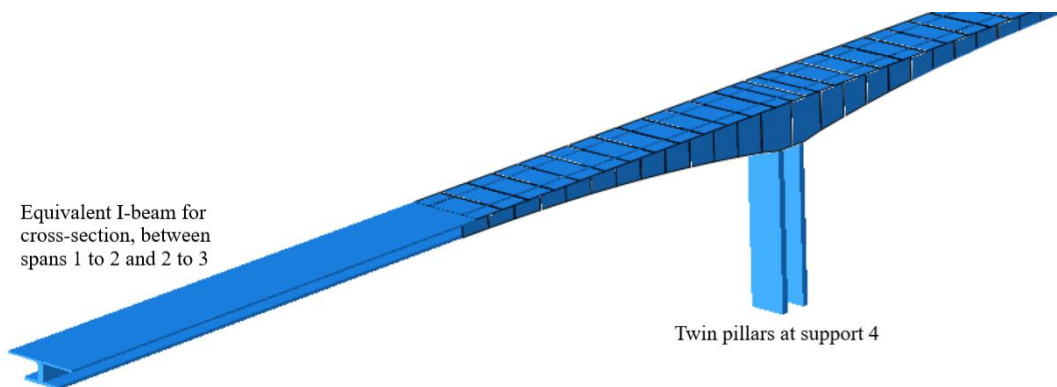


Figure 6.4: Beam profiles for span and support at the northwest end of the Alvik bridge.

The geometry of the truss elements representing the tendons was modelled according to Figure 5.3 and Figure 5.4. The trusses were assigned an equivalent cross-section area corresponding to the number of tendons in each truss. The placement of tendons was simplified by placing the tendons at the intersection of top flange and web for the top tendons, and at the intersection of bottom flange and web for bottom tendons.

Interactions

Tie constraints were used to connect the box girder cross-sections and to connect the tendons to the box girder segments.

Coupling constraints were used to connect the box girder cross-sections to the piers at support 4 and 5. Coupling constraints were also used to connect the box girder cross-sections to the spans between supports 1 to 2, 2 to 3 and 6 to 7.

Boundary conditions

The boundary conditions between the piers and the soil foundation were modelled as fully restrained in rotation and translation.

The boundary conditions at piers 1, 2, 3, 6 and 7 allowed rotations. Translation in the direction of the span was not allowed until the spans were joined with the cantilever sections. After the spans were joined, translation along the span was allowed at piers 1, 2, 3, 6, and 7.

6.2 Material properties

Concrete

The piers at supports 4 and 5, as well as the box girder segments of spans between supports 1 to 2, 2 to 3 and 6 to 7, were assigned concrete material values according to Table 2.1. The rest of the values used are presented in Table 6.1.

Table 6.1: Material input data for concrete used in Abaqus.

Parameter	Value	Unit
Cement type	-	N (EC2) R (B4)
Aggregate-cement ratio	5.03	-

Other input variables used in the calculations were relative humidity, which was set to 70% and water-cement ratio, which was set to 0.45. The material property values from Table 6.1 were also assigned to the shell element box girder segments. However, the shell element box girder sections were assigned an elastic modulus with a developing strength over time, where the concrete reached a strength of 34 GPa after 28 days. As mentioned in Chapter 5.3, the load was applied on the box girder segments after seven days. It was therefore important to capture the strength of the concrete from seven days. The concrete strength will continue to develop after 28 days, and this development was also

captured and implemented as a material property. The development of the elastic modulus was calculated with Eq. (2.64) and is presented in Figure 6.5.

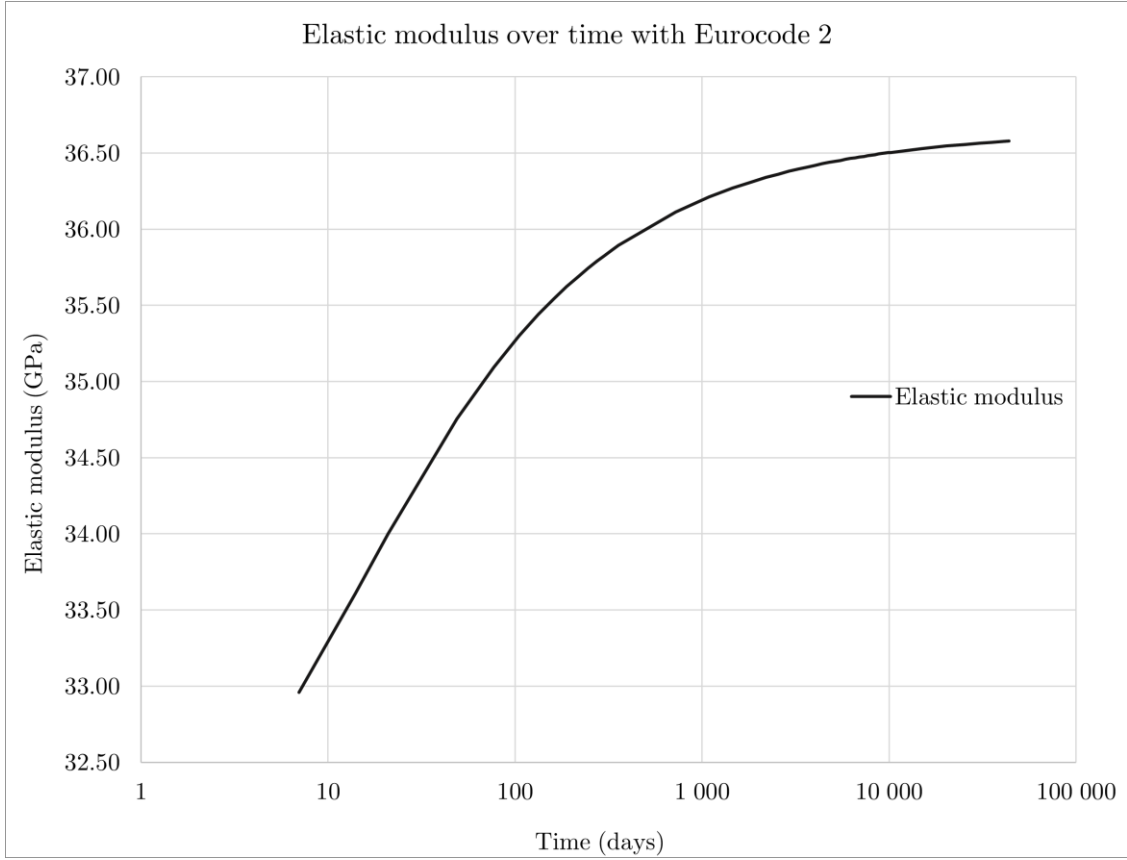


Figure 6.5: Development of elastic modulus over time.

To simulate non-uniform creep and shrinkage, each of the respective segment's parts were given individual relaxation data curves and temperature changes. Each segment was divided into three parts: top flange, bottom flange, and webs, as illustrated in Figure 6.3.

To simulate uniform creep and shrinkage, each bridge segment was analysed as one whole part, where the whole segment was given an individual relaxation curve. This allows the entire cross-section to have the same behaviour regarding creep and shrinkage and disregards the effect of the geometry of the segment's individual parts.

Relaxation data input was implemented in Abaqus to capture the viscoelastic creep behaviour for the shell element box girder sections. Relaxation data was implemented with the normalized shear modulus and normalized bulk modulus, using Eq. (3.7) and Eq. (3.8) respectively. The creep coefficient used in Eq. (3.7) and Eq. (3.8) was either calculated with Eq. (2.40) when the B4 model was used or by Eq. (2.42) when Eurocode 2 was used.

As a representation of the relaxation data input, the average value of the creep coefficient overtime for all the segments and parts is given in Figure 6.6 and Figure 6.7. Detailed values for each segment and part are given in Appendix A.1.

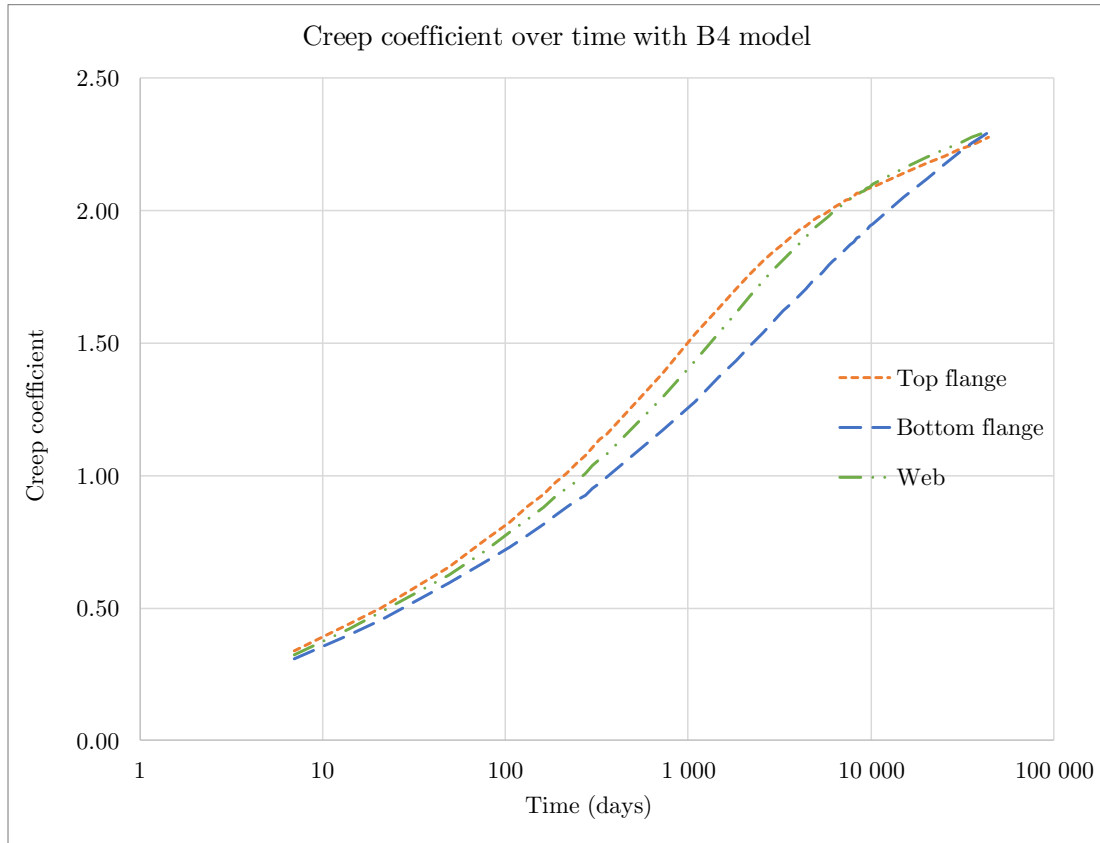


Figure 6.6: Creep coefficient value as an average between all segments, with B4 model.

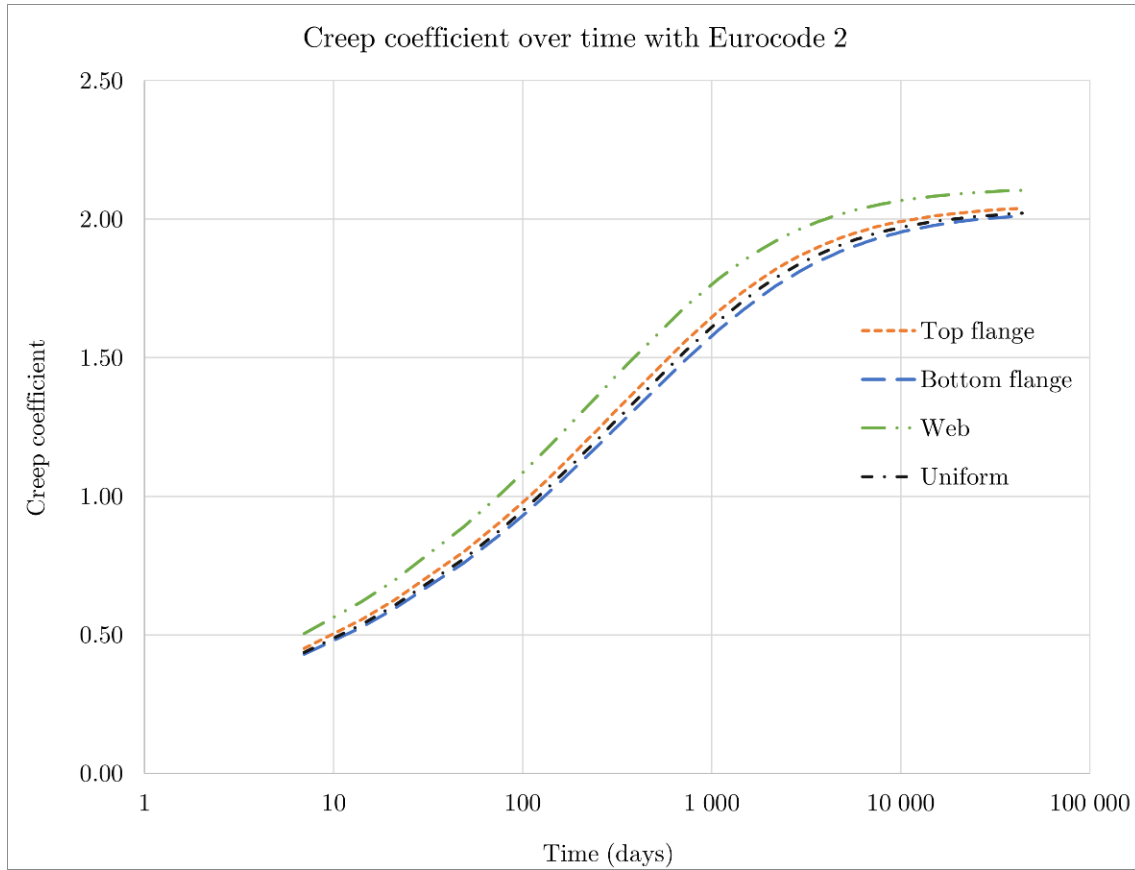


Figure 6.7: Creep coefficient value as an average between all segments, with Eurocode 2.

Shrinkage was implemented in Abaqus as a temperature change over time. The temperature change was implemented with the Abaqus tool *predefined field*. The temperature change was calculated with Eq. (3.11), where the total shrinkage strain was either calculated with Eq. (2.36) when the B4 model was used or by Eq. (2.53) when Eurocode 2 was used.

As a representation of the temperature change, the average value of the shrinkage strain overtime for all the segments and parts is given in Figure 6.8 and Figure 6.9. Detailed values for each segment and part are given in Appendix A.2.

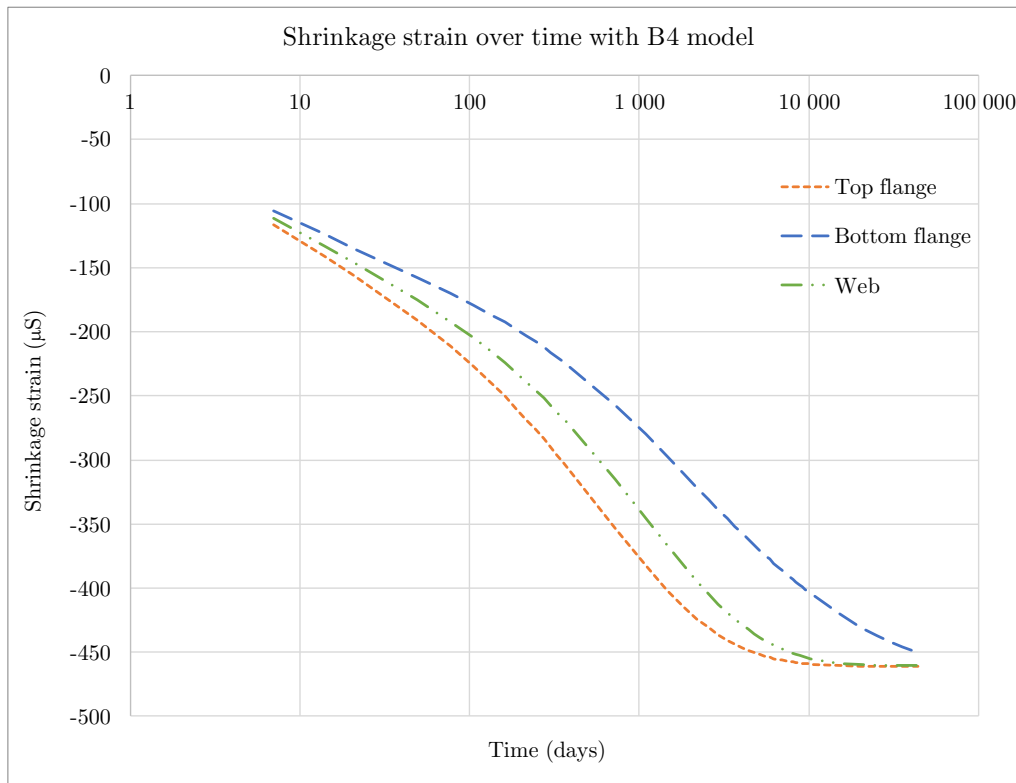


Figure 6.8: Shrinkage strain value over time value as an average between all segments, with B4 model.

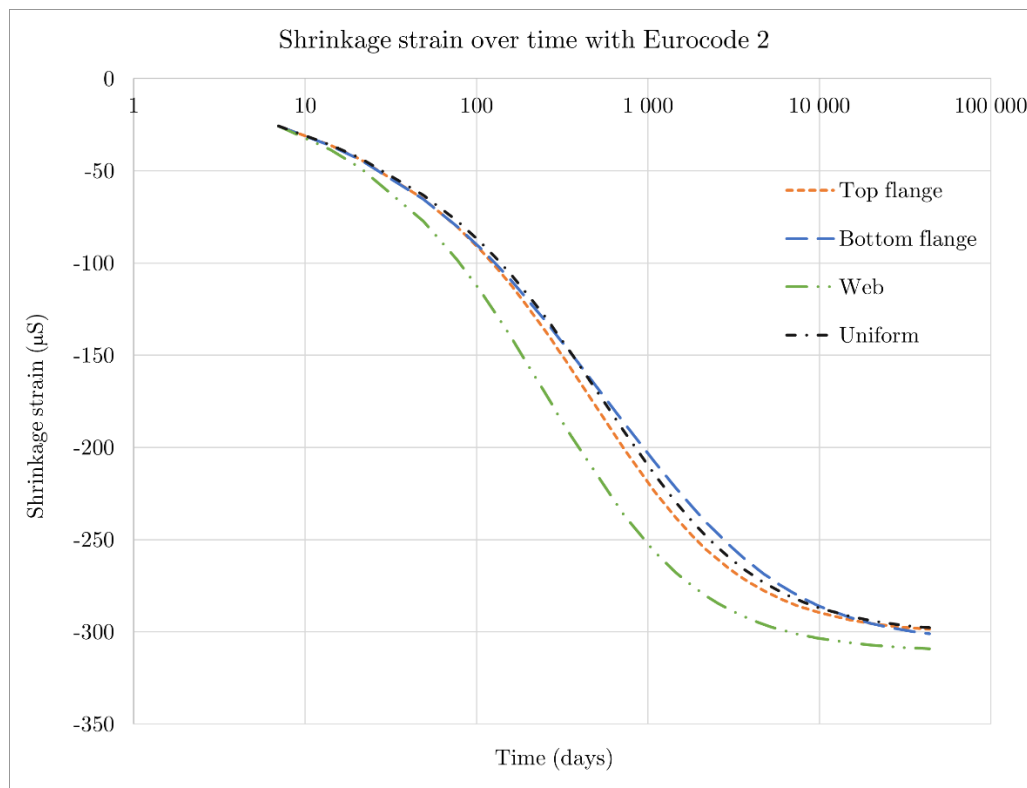


Figure 6.9: Shrinkage strain value over time value as an average between all segments, with Eurocode 2.

Steel

The tendons in the top and bottom flange were assigned steel material values according to Table 5.3. Relaxation data input was implemented in Abaqus to capture the relaxation behaviour of the tendons. Relaxation data was implemented with the normalized shear modulus and normalized bulk modulus, using Eq. (3.12) and Eq. (3.13) respectively. The absolute value of relaxation loss and initially applied stress used in Eq. (3.12) and Eq. (3.13) was calculated with Eq. (2.62). Detailed values of the relaxation data input for the tendons are given in Appendix A.3.

6.3 Construction phase

The Abaqus tool *model change* was used to simulate the construction phase of the balanced cantilever method. In the initial stage, all the bridge parts were deactivated from the analysis. Parts of the bridge were then activated and included in the analysis following the plans given in the structural drawings. The description of when each part was included is presented in Table 6.2. Each change in stage represents one week. The segments described in Table 6.2 represent the subsequent segment included in each stage, where segment 0 is the segment directly above the pier and segment 1 is the subsequently cast segment. When the segments were included in the analysis, their starting age was seven days. Therefore, the tendons were included and stressed in the same stage as their respective segments were included.

Table 6.2: Inclusion of parts for the bridge construction.

Stage	Included part
Initial (0)	All parts deactivated
1	Piers 4 and 5 Segment 0, Tendons for segment 0
2	Segment 1 Tendons for segment 1
3	Segment 2 Tendons for segment 2
4	Segment 3 Tendons for segment 3
5	Segment 4 Tendons for segment 4
6	Segment 5 Tendons for segment 5
7	Segment 6 Tendons for segment 6
8	Segment 7 Tendons for segment 7
9	Segment 8 Tendons for segment 8
10	Segment 9 Tendons for segment 9
11	Segment 10 Tendons for segment 10
12	Segment 11 Tendons for segment 11
13	Segment 12 Tendons for segment 12
14	Connecting segment 13 All bottom tendons. Spans between supports 1 to 3 and 6 to 7
15	Long-term analysis, see Chapter 6.6

An example of the age difference for the segments during the construction is presented in Figure 6.10. The presented values are given in weeks.

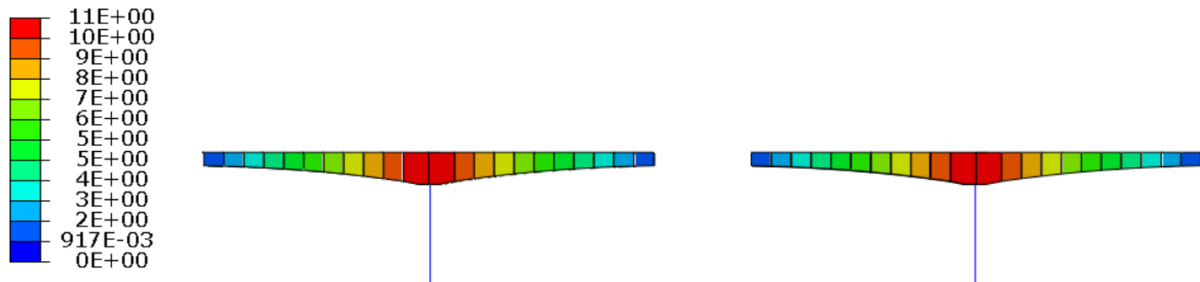


Figure 6.10: Age difference of the segments during the construction phase. Values are given in weeks.

6.4 Considered loads

Self-weight

The self-weight load was modelled as a *gravity* load in Abaqus. The load was therefore applied to all the parts of the model, where the magnitude of the load is dependent on the geometry and density of the part, as well as the gravitational acceleration.

Ballast and asphalt

The ballast and asphalt load were applied in Abaqus as a *pressure* load on the bridge deck for spans 3 to 4, 4 to 5 and 5 to 6. The remaining spans, which were modelled as beams had an equivalent *line load* applied on them. The magnitude of the line load was the pressure load multiplied by the width of the bridge deck. The load was applied after the completion of the construction phase. The magnitude of the loads from ballast and asphalt are described in Table 6.3.

Table 6.3: Magnitude of load for ballast and asphalt.

Parameter	Pressure load [kN/m ²]	Line load [kN/m]
Ballast	10.7	97.3
Asphalt	2.20	6.22

Form traveller

The form traveller load was applied as a *concentrated load* in Abaqus. As described in Chapter 5.4, the total load of the form traveller was 480 kN. The load was divided into four concentrated loads, each load had a magnitude of 120 kN. Two of the loads were applied at the intersection of the top flange and web. The other two loads were applied at the intersection of the bottom flange and web.

Prestress

The stress applied on the tendons was applied as *predefined field stress* in Abaqus. The stress was applied in the longitudinal direction of the tendon. The magnitude of the stress applied to the tendons is given in Table 5.5 and Table 5.6.

6.5 Parameter study

To achieve a greater understanding of how different parameters affect the long-term deformations due to creep and shrinkage influenced the bridge, a parametric study was performed. The influence of four parameters was investigated regarding their effect on creep and shrinkage: relative humidity, the height of ballast, water-cement ratio and considered cross-section perimeter.

The influence of relative humidity was based on testing one value lower and one value higher than the original value. The values were chosen from relative humidity data acquired from SMHI (Swedish Meteorological and Hydrological Institute). According to SMHI (2020), the average relative humidity in the bridge's geographical area between 1996 and 2020 is around 60-70 % in July, and 85-95 % in January. The chosen values for the parameter study were then 60% and 90 %, as well as comparing with the original value of 70 %, used in the main analysis.

The influence from the water-cement ratio was investigated based on three different values, representing one higher and one lower than the original value. The chosen values for the parameter study were a water-cement ratio of 0.4 and 0.5 in comparison to the value of 0.45 used in the main analysis. The B4 model uses water-cement ratio as an input variable for creep and shrinkage, Eurocode 2 does not. Therefore, the water-cement ratio parameter study was only conducted with the B4 model.

The influence of the load from the ballast on the long-term deformation was studied for different ballast heights. The height depended on the information given from the structural drawings. As illustrated in Figure 5.2, the ballast may vary from 0.39 m to 0.45 m. The height of 0.41 m corresponds to the calculated average value of the measured value from the structural drawings, as illustrated in Figure 5.2. According to Malm (2020), the height of ballast on a bridge constructed with the same method as the Alvik bridge had a ballast height of 0.30 m. The chosen values for the parameter study were a ballast height of 0.30 m and 0.45 m.

The size of the cross-section perimeter is a variable presented in Eurocode 2. The perimeter was described as the part of the cross-section in contact with air. As illustrated

in Figure 5.2, the bridge deck was covered with ballast by the railway, and with asphalt mastic on the pedestrian path-way. The parameter study for the cross-section perimeter was then conducted to investigate the effect of including the bridge deck in the perimeter. The summary of the tested parameter values is presented in Table 6.4: Tested values of the parameter study.

Table 6.4: Tested values of the parameter study.

Relative humidity (%)	Water-cement ratio	Ballast			
		Self-weight [kN/m^3]	Height [m]	Pressure [kN/m^2]	Line load [kN/m]
60	0.45	26	0.45	11.8	108
70	0.5	26	0.41	10.7	97.2
90	0.4	26	0.30	7.80	71.2

6.6 Service life

According to Trafikverket (2019), the bridge should be designed with a service life of 120 years. This requirement is defined for all bridges where potential maintenance, repairs or replacement of the bridge would influence the railway traffic. The period used in the Abaqus analysis was therefore defined as 120 years to investigate the behaviour of the deformations throughout the technical lifetime of the bridge.

6.7 Mesh control test

As mentioned in Takács (2002), analysis should be performed to reduce the possibility or error due to element size. According to Malm (2016), a mesh control with the following rule should be performed to ensure verification of accurate results from a finite element model: an increase in element size should only lead to a marginal difference in the result. The Alvik bridge was then tested according to this rule. An element size of 1.5 m and 0.75 m were tested. The results are illustrated in Figure 6.11.

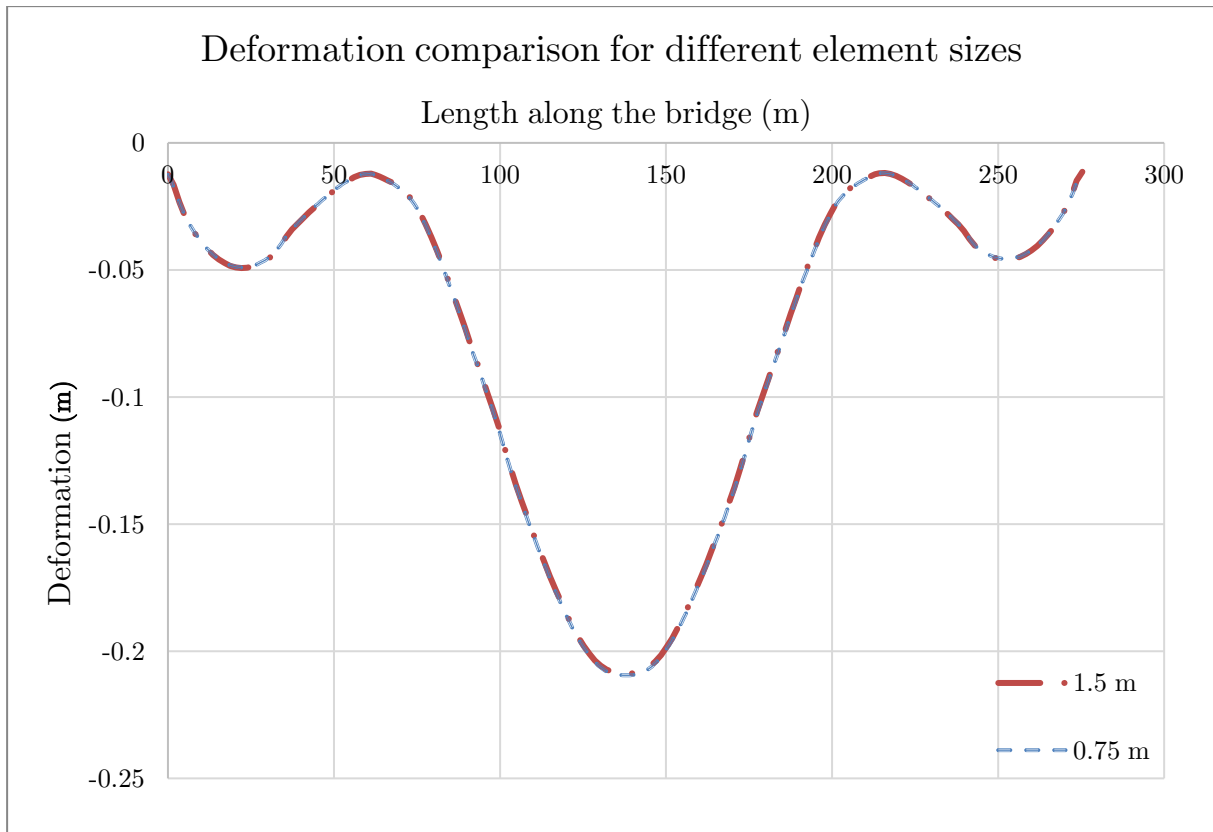


Figure 6.11: Result of mesh control test.

The result from the mesh control test shows that there was not any noticeable difference in deformation when using an element size of 1.5 m and 0.75 m. Therefore, an element size of 1.5 m was used for all the analyses with the Alvik bridge model.

Chapter 7

Results from finite element analyses

This chapter summarizes the results obtained from the modelled bridge. The results are divided into four parts:

1. General
2. Effect of calculation models
3. Parameter study for non-uniform creep and shrinkage
4. Stress state

The first part shows the general deformation obtained from the model. The purpose is to show the overall deformation of the bridge after 120 years. Here a comparison is shown for the deformation on the north and south edges as well as the deformation along with the span.

The second part compares the resulting deformation when using the calculation models: Eurocode 2 with a non-uniform and uniform approach as well as the B4 model with a non-uniform approach. Comparisons are also drawn between the resulting values from the model and the measured deformations. The results are divided into two approaches: deformation along with the span and deformation over time at midspan. The deformation along the span is only shown for the parts of the bridge that are built with the cantilever construction method. The horizontal axis value from 0 to 70 m refers to the span between pier 3 and 4. The horizontal axis value from 70 to 210 m refers to the span between pier 4 and 5, whereas the value from 210 to 280 m refers to the span between pier 5 and 6. Results from different periods are also shown to analyse the behaviour change over time. This part also compares how much influence creep and shrinkage individually have on the resulting deformation with the different calculation models.

The third part compares the results from the parameter study. In this part, the B4 model and Eurocode 2 are compared with a non-uniform approach. Similar to the second part, the results are also divided into two approaches: formation along the span and deformation over time at midspan. The period is 120 years for the representation of results.

The fourth part compares the stress state acquired from the different calculation models such as Eurocode 2 with a non-uniform and uniform approach as well as the B4 model

with a non-uniform approach. The stress state is shown after 3 years from which the first measurement was taken on the Alvik bridge. The purpose of this was to compare what difference the approaches have on the expected stress state and conclude the effect it could have on cracking.

7.1 General

The general behaviour of the deformation after 120 years with Eurocode 2 and a non-uniform approach, is illustrated in Figure 7.1. The figure shows that the north edge had larger deformation compared to the south edge. The maximum deformation occurred at the midspan of the bridge. The final deformation at midspan on the north edge had about 0.21 m deformation at midspan, whereas the south edge had 0.19 m deformation at midspan.

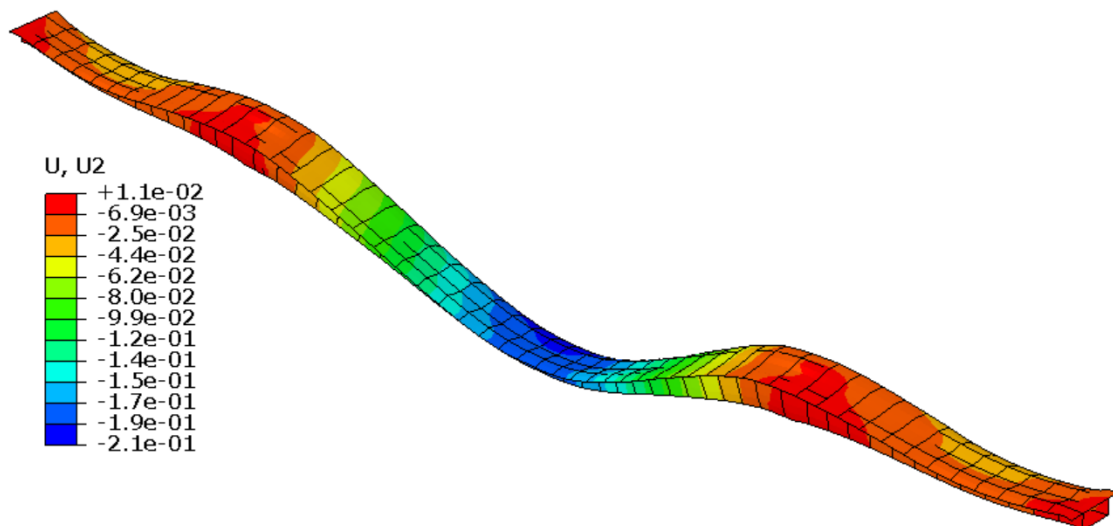


Figure 7.1: General behaviour of the deformation after 120 years with Eurocode 2, non-uniform approach. The measurements are given in meters, where U is the vertical displacement.

7.2 Effect of calculation models

7.2.1 Deformation along the bridge span

The total deformation along the bridge span was plotted after 3 years, 22 years and 120 years. These timespans were chosen in consideration of the measured deformation and the lifespan of the bridge. The first deformation measurement was recorded about 3 years after the construction of the Alvik bridge. The latest recorded deformation was in the year 2020 which is about 22 years after the Alvik bridge was constructed. The period of 120 years was chosen since that is the expected lifespan of the bridge.

The deformation along the bridge span at the north edge after around 3 years is illustrated in Figure 7.2, for non-uniform and uniform analysis with Eurocode 2, and non-uniform analysis with the B4 model. Figure 7.2 shows that deformation midspan varied between the different calculation models. The simulation showed higher deformations at midspan compared to the measured deformation. The measured deformation at midspan was 0.132 m, whereas the midspan deformation calculated with the B4 model was 0.165 m. The midspan deformation for Eurocode 2 was 0.153 m and 0.161 m with the uniform and non-uniform approach, respectively. The shape of the simulated deformation was not an accurate resemblance to the measured deformation.

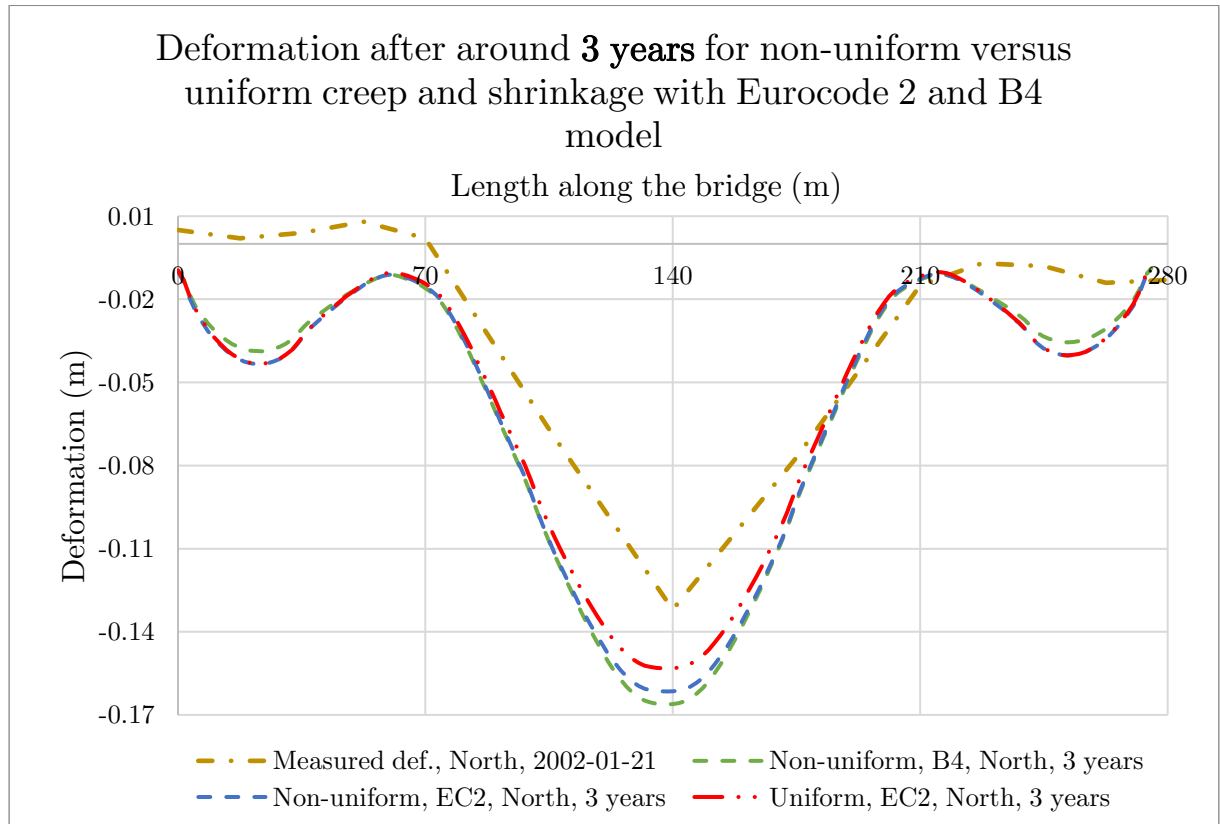


Figure 7.2: Deformation after around 3 years for non-uniform and uniform analysis with Eurocode 2, and non-uniform analysis with B4 model.

The deformation along the bridge span at the south edge after around 3 years is illustrated in Figure 7.3, for non-uniform and uniform analysis with Eurocode 2, and non-uniform analysis with the B4 model. Figure 7.3 shows that the deformation results varied between the different calculation models. The simulation showed larger deformations at midspan compared to the measured deformation. The measured deformation at midspan was 0.131 m, whereas the midspan deformation calculated with the B4 model was 0.142 m. The midspan deformation for Eurocode 2 was 0.130 m and 0.137 m with the uniform and non-uniform approach, respectively. The shape of the simulated deformation is not an accurate resemblance to the measured deformation.

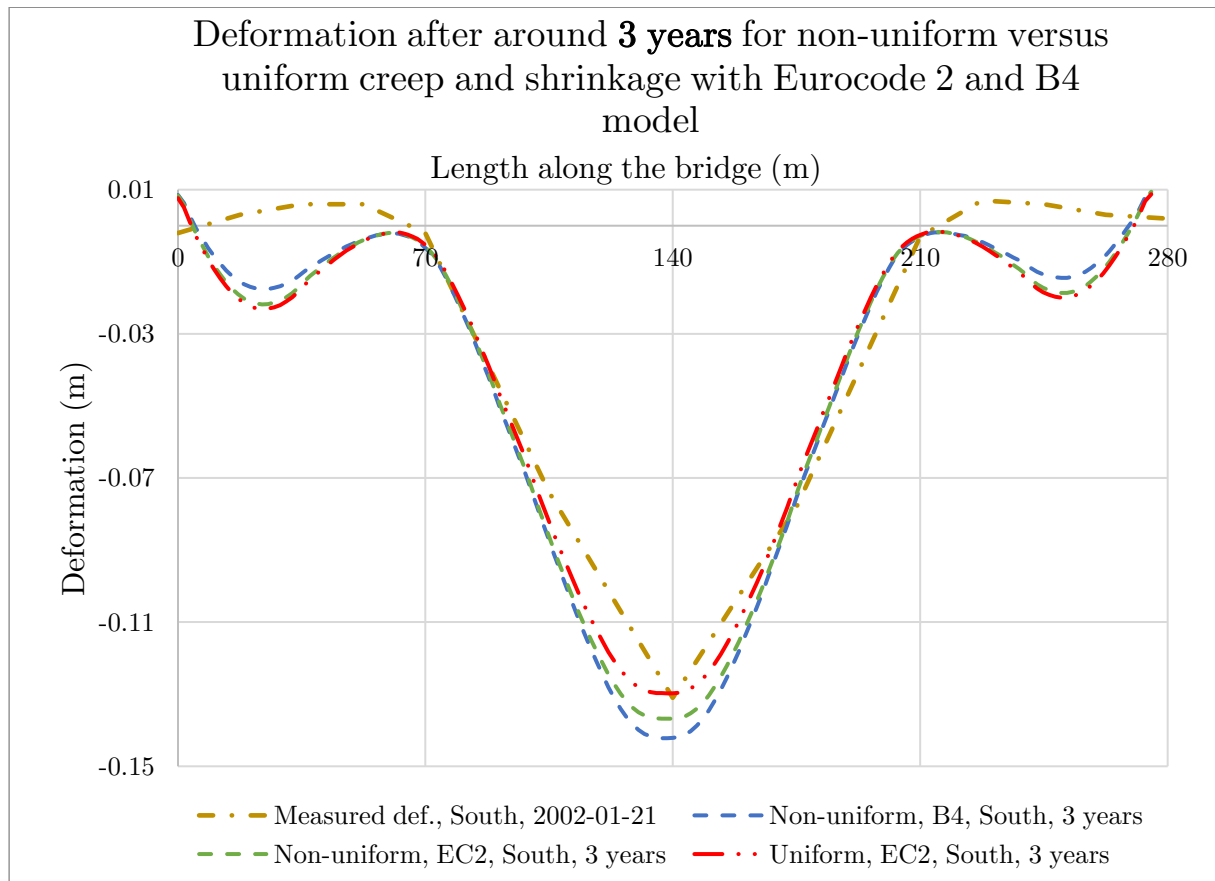


Figure 7.3: Deformation after around 3 years for non-uniform versus uniform creep and shrinkage with Eurocode 2 and B4 model.

The deformation along the bridge span at the north edge after around 22 years is illustrated in Figure 7.4 for non-uniform and uniform analysis with Eurocode 2, and non-uniform analysis with the B4 model. The value of the measured deformation at midspan was in between the deformation values from the simulated models. The measured deformation at midspan was 0.210 m, whereas the midspan deformation calculated with the B4 model was 0.216 m. The midspan deformation for Eurocode 2 was 0.202 m and 0.203 m with the uniform and non-uniform approach, respectively.

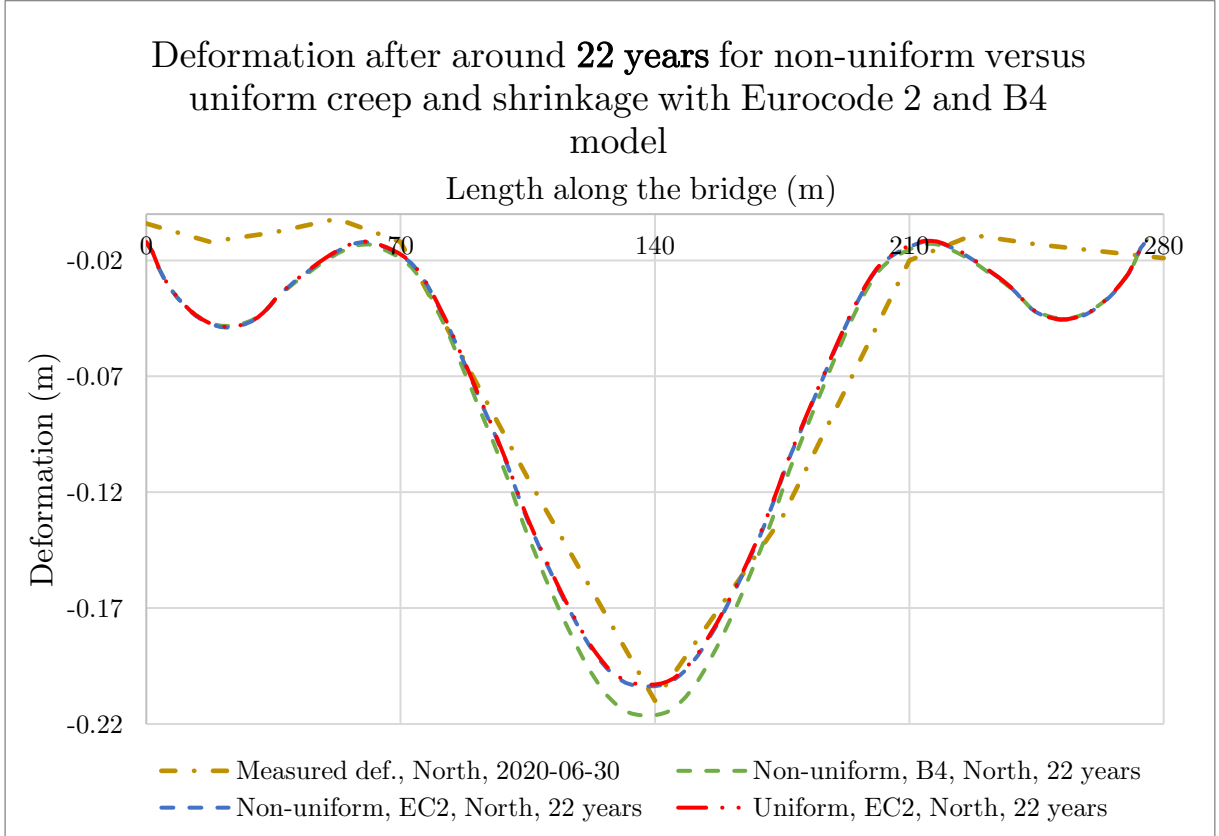


Figure 7.4: Deformation after around 22 years for non-uniform and uniform analysis with Eurocode 2, and non-uniform analysis with B4 model.

The deformation along the bridge span at the south edge after around 22 years is illustrated in Figure 7.5 for non-uniform and uniform analysis with Eurocode 2, and non-uniform analysis with the B4 model. The value of measured deformation at midspan was closer to the value calculated with the B4 model compared to Eurocode 2. The measured deformation at midspan was 0.190 m whereas the midspan deformation calculated with the B4 model was 0.187 m. The midspan deformation for Eurocode 2 was 0.174 m with the uniform and non-uniform approach.

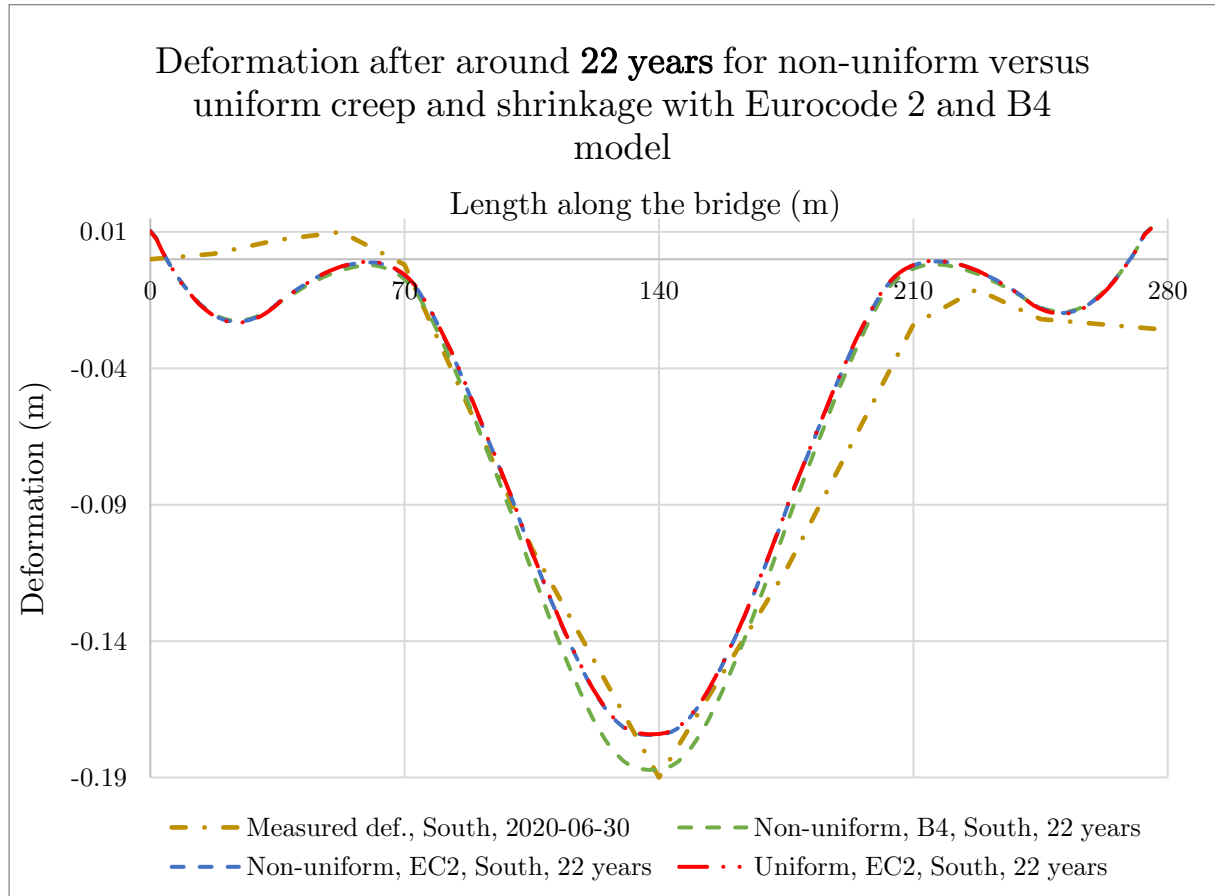


Figure 7.5: Deformation after around 22 years for non-uniform versus uniform creep and shrinkage with Eurocode 2 and B4 model.

The deformation was plotted along the north and south edge of the bridge span after 120 years, as illustrated in Figure 7.6. The north and south edge are illustrated in Figure 5.2. The results are compared between non-uniform and uniform analysis with Eurocode 2. Larger deformations were acquired at the north edge compared to the south edge. The deformations did not show a significant difference between the non-uniform and uniform analysis. The midspan on the northern edge had a deformation value of 0.208 m and 0.205 m for non-uniform and uniform analysis, respectively. The midspan on the southern edge had a deformation value of 0.179 m and 0.176 m for non-uniform and uniform analysis, respectively.

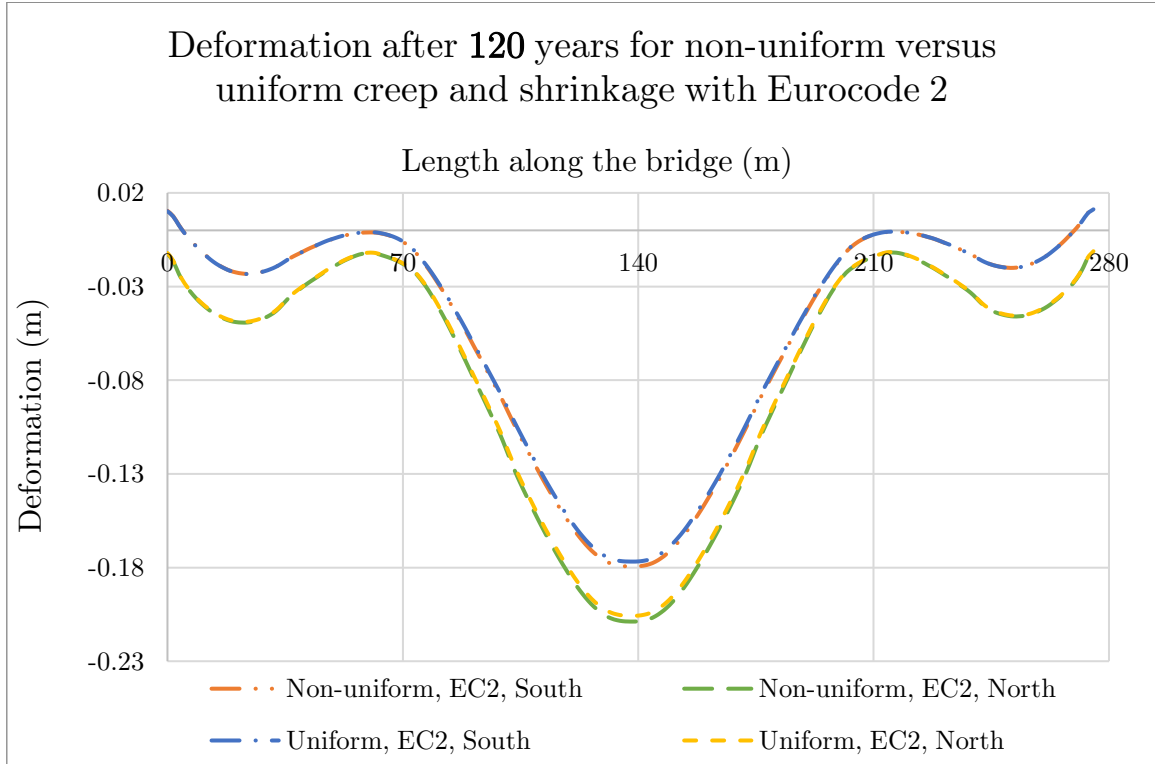


Figure 7.6: Deformation after 120 years for non-uniform versus uniform creep and shrinkage with Eurocode 2.

The deformation along the span at the north edge after 120 years was plotted in Figure 7.7 for non-uniform and uniform analysis with Eurocode 2, and non-uniform analysis with the B4 model. Larger deformations were acquired with the B4 model compared to Eurocode 2. The deformations did not show a significant difference between the non-uniform and uniform analysis with Eurocode 2. The midspan deformation value with Eurocode 2 was 0.208 m and 0.205 m for non-uniform and uniform analysis, respectively. The midspan deformation is 0.237 m with the B4 model.

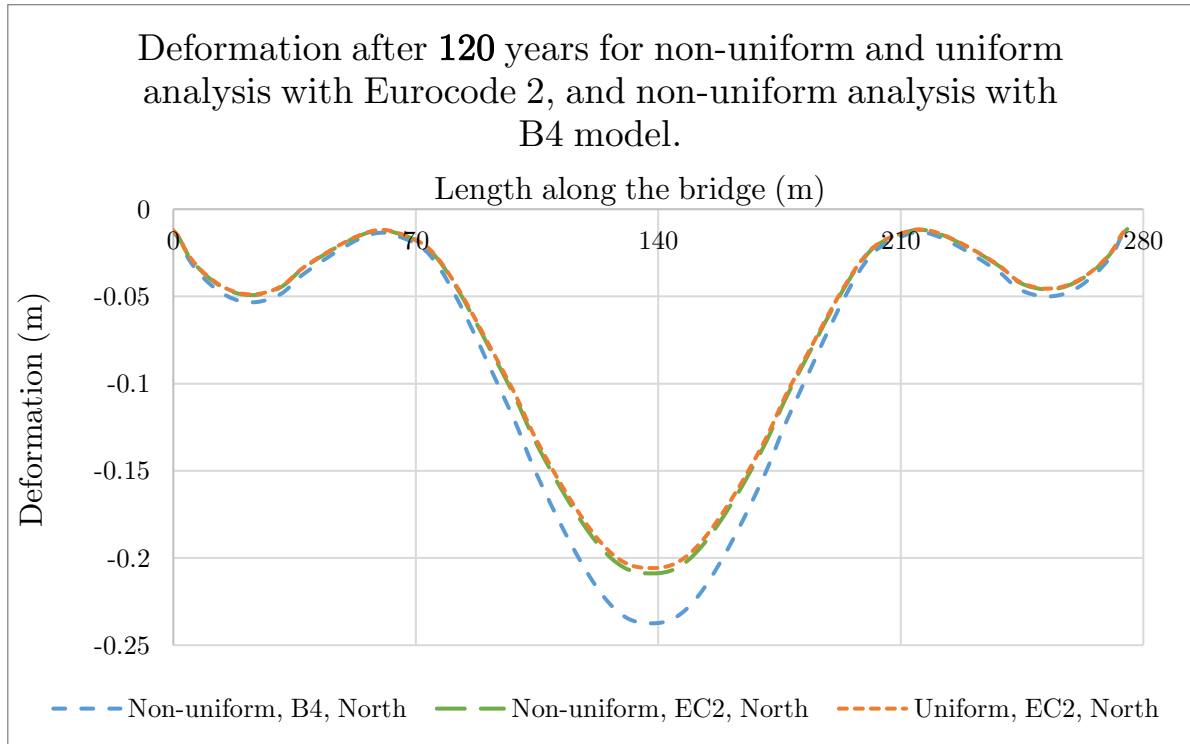


Figure 7.7: Deformation after 120 years for non-uniform and uniform analysis with Eurocode 2, and non-uniform analysis with B4 model.

7.2.2 Deformation over time at midspan

The deformation over time at midspan was plotted for 120 years, 22 years and 10 years at the north edge. The period of 120 years was chosen since that was the expected lifetime of the bridge. As mentioned in Chapter 7.1, the latest recorded deformation was in the year 2020 which is about 22 years after the Alvik bridge was constructed. Therefore, a period of 22 years was chosen. The period of 10 years was chosen to better investigate the difference in early deformation when comparing the results from Eurocode 2 with non-uniform and uniform analysis.

The deformation at midspan over 120 years is illustrated in Figure 7.8 for comparison between simulation results and measured values. The simulated results were compared between non-uniform and uniform analysis with Eurocode 2 and non-uniform analysis with the B4 model. The deformation obtained from Eurocode 2 stopped increasing after around 20 years, whereas the deformation continued to increase throughout the service life with the B4 model. The measured deformation also indicated increasing deformation up until 22 years which is the latest measured deformation value.

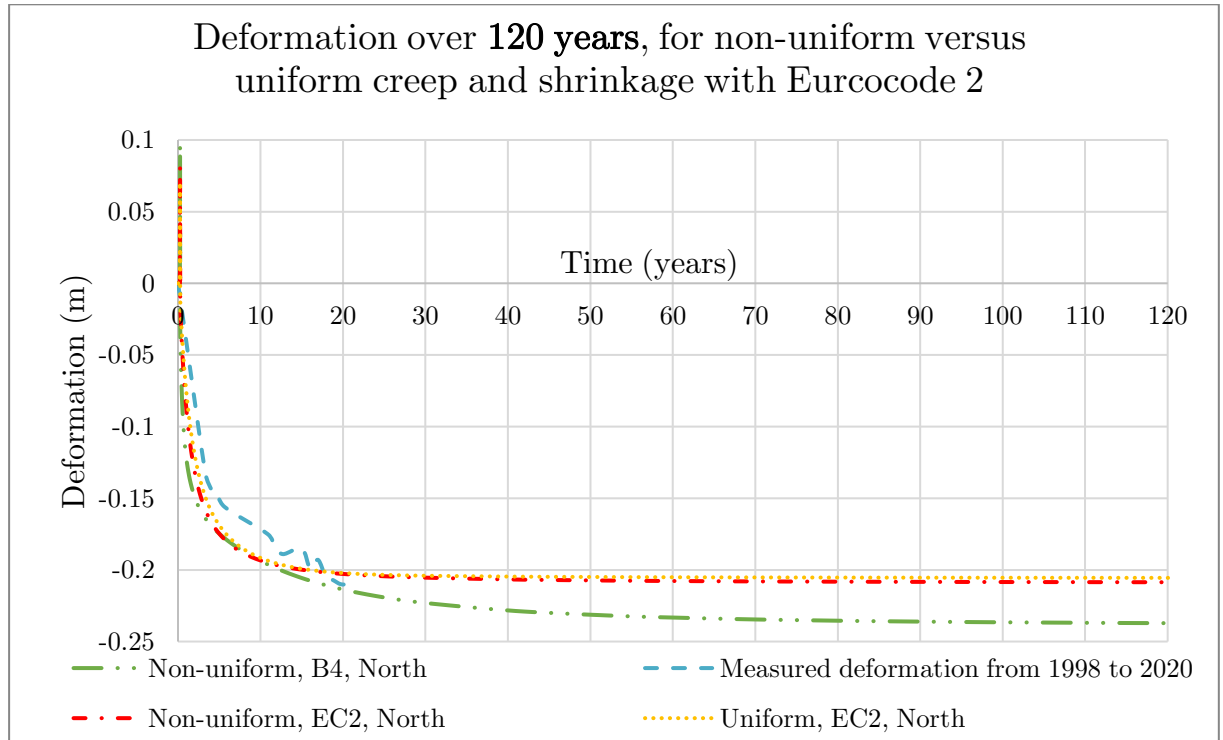


Figure 7.8: Deformation over 120 years, for non-uniform versus uniform creep and shrinkage with Eurocode 2 and B4 model.

The deformation at midspan over 22 years is illustrated in Figure 7.9 for comparison between simulation results and measured values. Similar to Figure 7.8, the simulated results were compared between non-uniform and uniform analysis with Eurocode 2 and non-uniform analysis with the B4 model. The deformation obtained from Eurocode 2 did not have a significant difference when using non-uniform or uniform analysis. The B4 model had larger early deformation compared to deformations obtained from Eurocode 2. The simulation deformation was in general larger in the early stage compared to the measured deformation. After about 18 years the measured deformation value remained in between the value obtained from the B4 model and Eurocode 2 and increased towards the values from the B4 model.

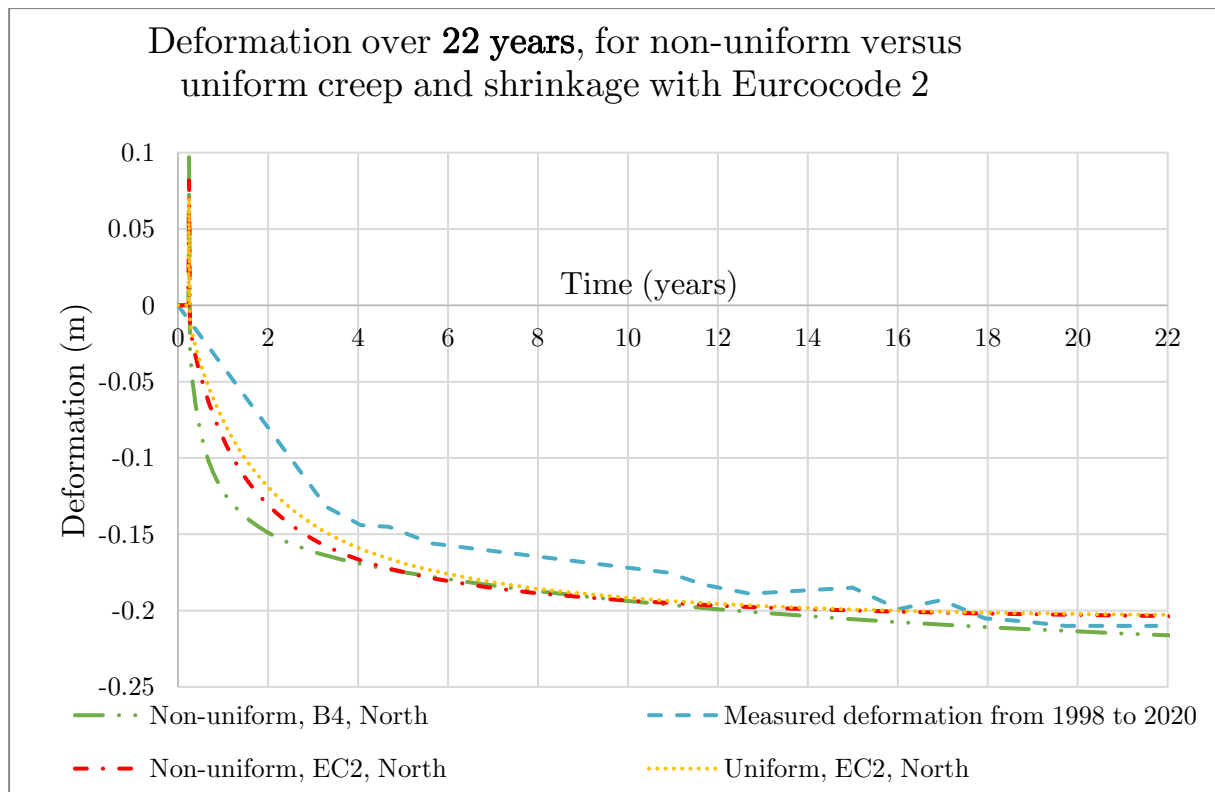


Figure 7.9: Deformation over 22 years, for non-uniform versus uniform creep and shrinkage with Eurocode 2.

The deformation over 10 years at midspan of the bridge is illustrated in Figure 7.10 for non-uniform and uniform analysis with Eurocode 2. The results showed that larger deformation was obtained with a non-uniform analysis compared to uniform analysis during the early years.

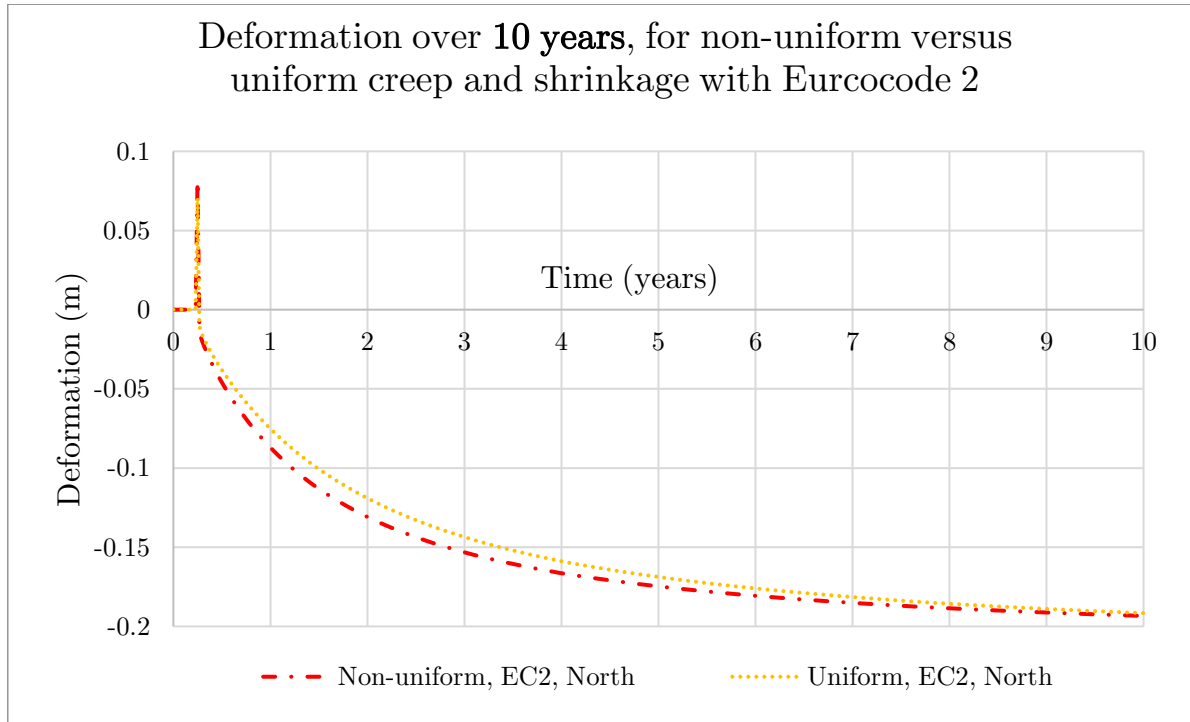


Figure 7.10: Deformation over 10 years, for non-uniform versus uniform creep and shrinkage with Eurocode 2.

7.2.3 Influence of creep versus shrinkage

To capture the influence of non-uniform versus uniform creep and shrinkage, deformation plots with solely creep versus solely shrinkage against total deformation were plotted. The effect of non-uniform versus uniform creep and shrinkage on deformation over the span at north edge after 120 years is illustrated in Figure 7.11 for non-uniform and uniform analysis with Eurocode 2, and non-uniform analysis with the B4 model. The results showed that no significant differences were obtained from Eurocode 2 with non-uniform and uniform analysis. The B4 model in general gave larger deformation compared to Eurocode 2. Shrinkage gave larger deformation in the B4 model compared to creep, whereas creep gave larger deformations compared to shrinkage in Eurocode 2.

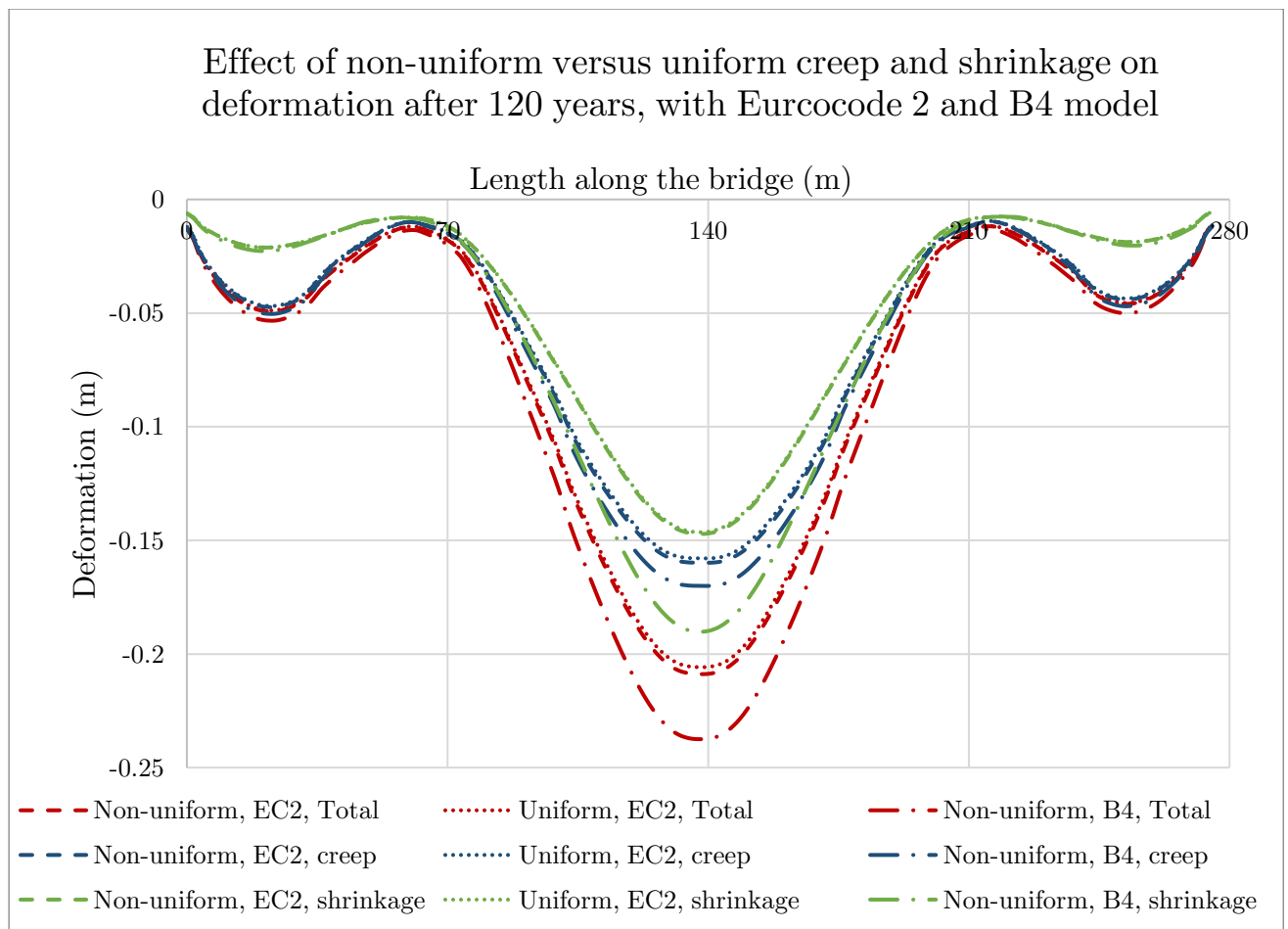


Figure 7.11: Effect of non-uniform versus uniform creep and shrinkage on deformation after 120 years, with B4 model.

7.3 Parameter study for non-uniform creep and shrinkage

7.3.1 Influence of relative humidity

The influence of relative humidity variation was plotted for non-uniform creep and shrinkage, along the span at the north edge, after 120 years. The deformations calculated with the B4 model and Eurocode 2 are illustrated in Figure 7.12 and Figure 7.13, respectively. Larger deformation was acquired with the B4 model compared to Eurocode 2, as well as when relative humidity was at 60 %. The higher the relative humidity, the smaller the deformation was.

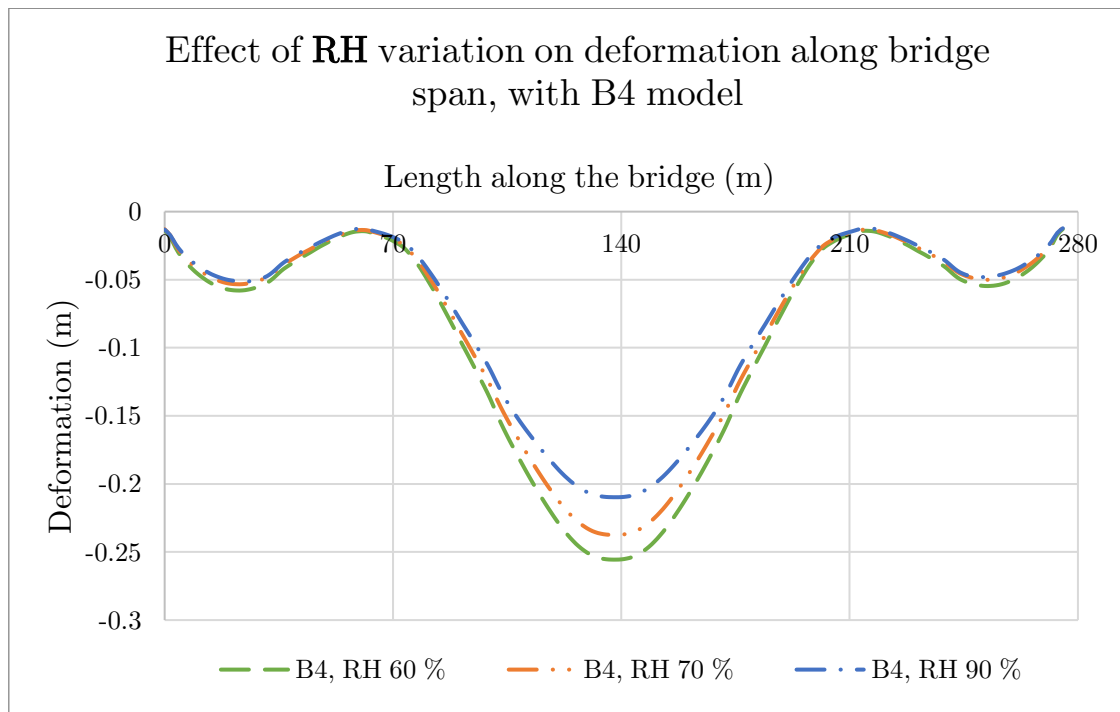


Figure 7.12: Effect of relative humidity variation on deformation along bridge span, with B4 model.

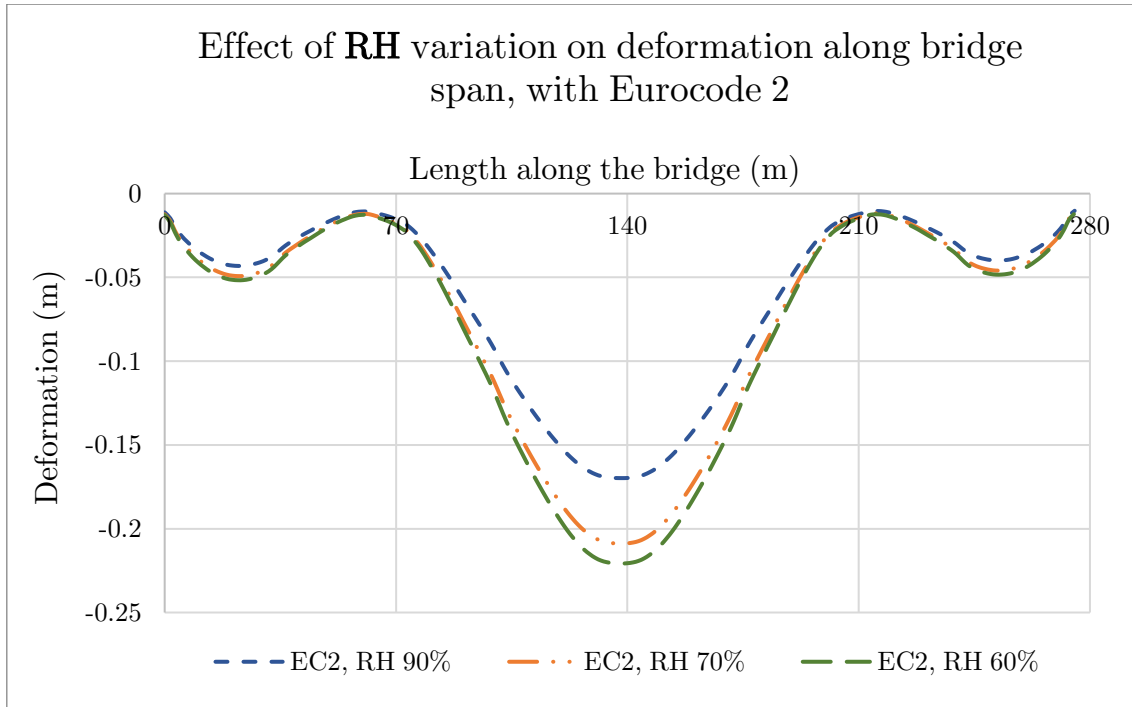


Figure 7.13: Effect of relative humidity variation on deformation along bridge span, with Eurocode 2.

The influence of relative humidity variation over 120 years was plotted for non-uniform creep and shrinkage, at midspan along the north edge of the bridge. The deformations over time, calculated with the B4 model and Eurocode 2 are illustrated in Figure 7.14 and Figure 7.15, respectively. Similar behaviour as the results obtained from Figure 7.12 and Figure 7.13 was found as the higher the relative humidity, the smaller the deformation was. Deformation with higher relative humidity also increased quicker compared to those with lower relative humidity.

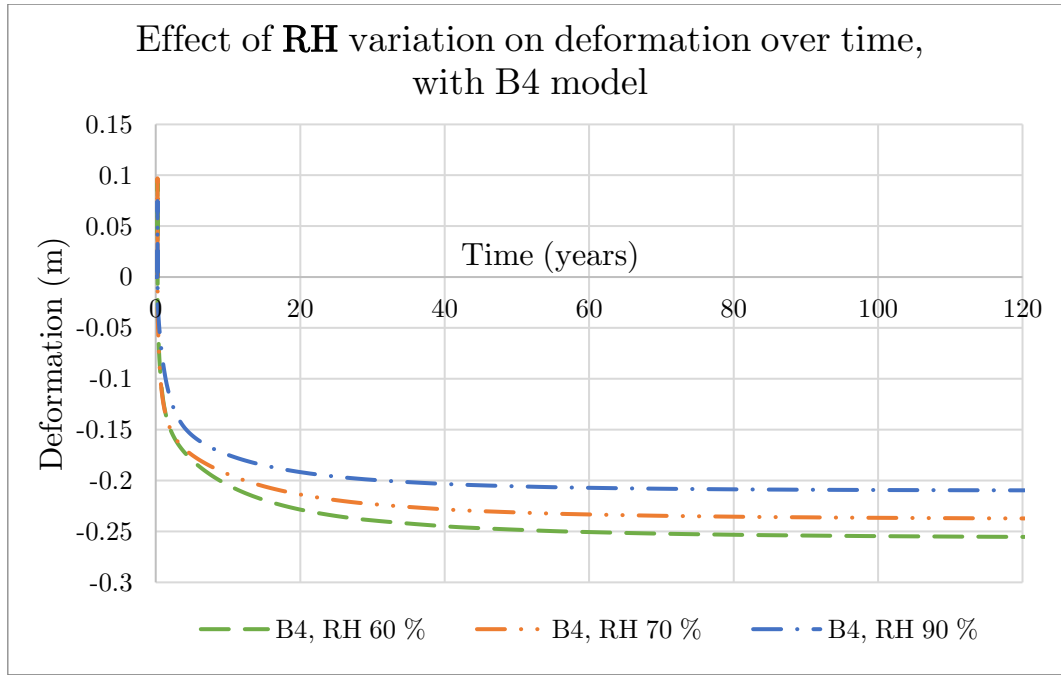


Figure 7.14: Effect of relative humidity variation on deformation over time, with B4 model.

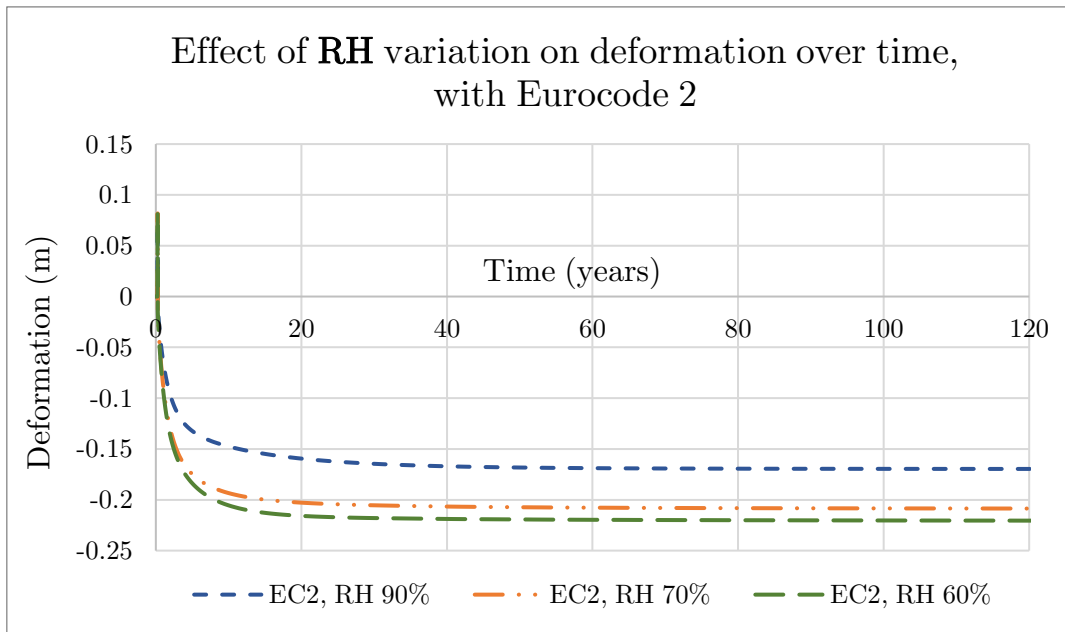


Figure 7.15: Effect of relative humidity variation on deformation over time, with Eurocode 2.

7.3.2 Influence of the water-cement ratio

The influence of the water-cement ratio was plotted for non-uniform creep and shrinkage along the span at the north edge after 120 years, as illustrated in Figure 7.16. No significant difference was found between the resulting deformation from the tested value of the water-cement ratio.

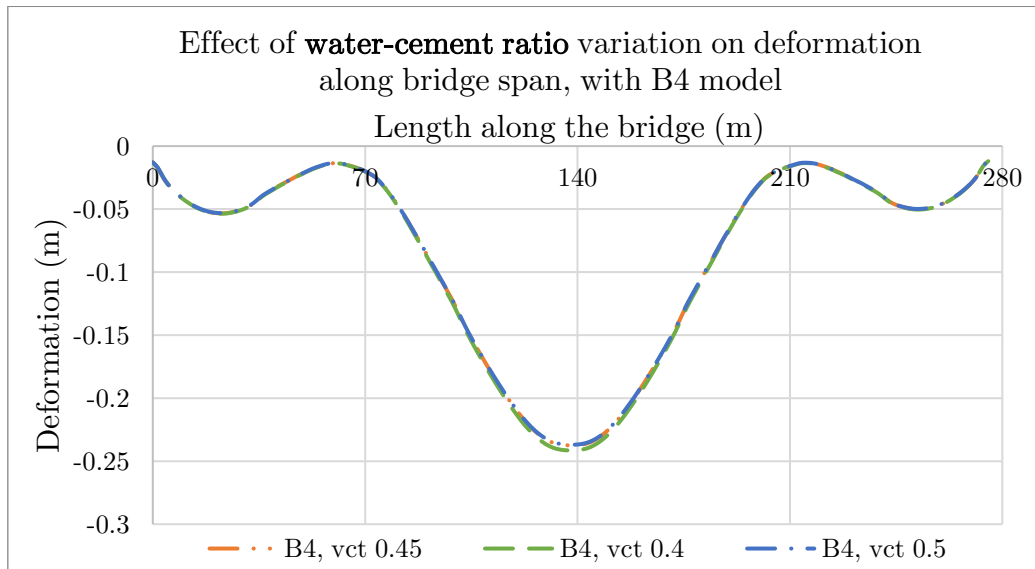


Figure 7.16: Effect of water-cement ratio variation on deformation along bridge span, with B4 model.

The influence of the water-cement ratio over 120 years was plotted for non-uniform creep and shrinkage, at midspan along the north edge of the bridge, as illustrated in Figure 7.17. Similar to Figure 7.16, no significant difference was found between the resulting deformation from the tested value of the water-cement ratio. A slightly larger deformation was obtained in the first 20 years with a water-cement ratio of 0.4.

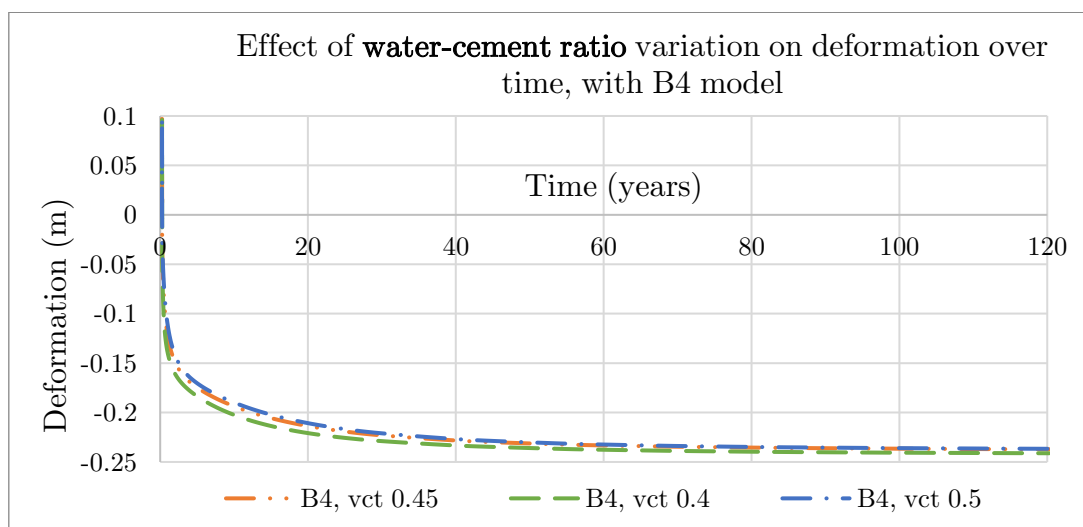


Figure 7.17: Effect of water-cement ratio variation on deformation over time, with B4 model.

7.3.3 Influence of ballast

The influence of ballast variation was plotted for non-uniform creep and shrinkage, along the span at the north edge after 120 years. The deformations calculated with the B4 model and Eurocode 2 are illustrated in Figure 7.18 and Figure 7.19, respectively. Larger deformation was acquired with the B4 model compared to Eurocode 2 as well as when the Ballast load was 11.8 kPa. The larger the ballast load the larger the deformations were.

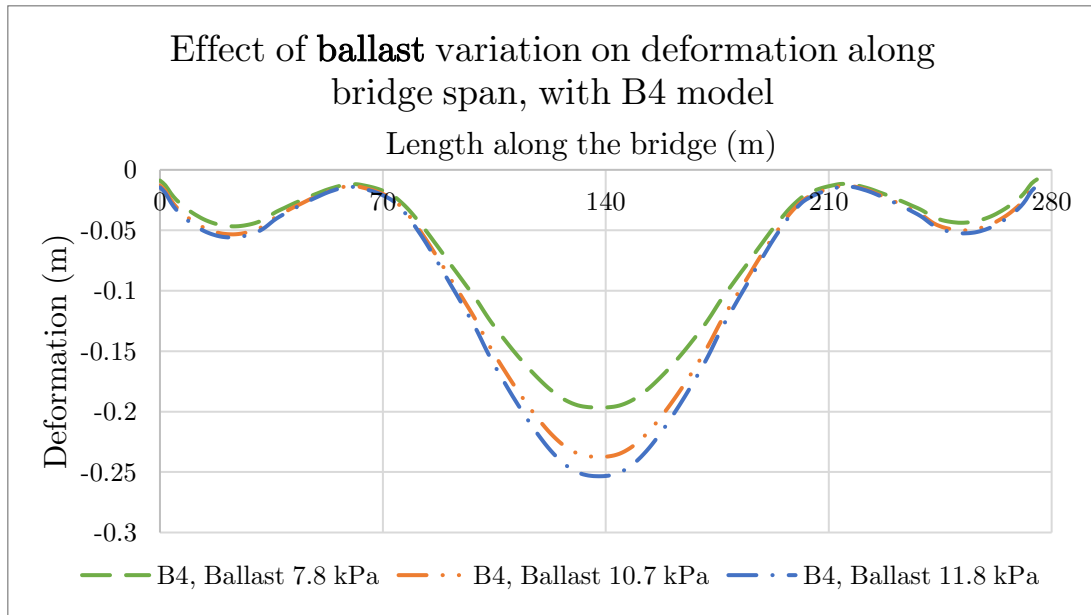


Figure 7.18: Effect of ballast variation on deformation along bridge span, with B4 model.

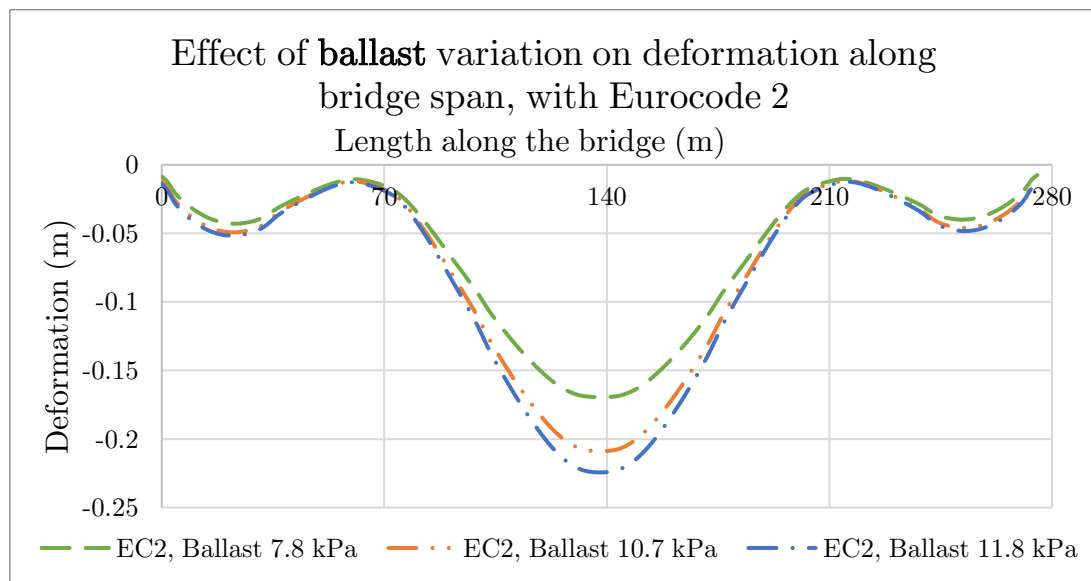


Figure 7.19: Effect of ballast variation on deformation along bridge span, with Eurocode 2.

The influence of ballast variation over 120 years was plotted for non-uniform creep and shrinkage, at midspan along the north edge of the bridge. The deformations over time, calculated with the B4 model and Eurocode 2 are illustrated in Figure 7.20 and Figure 7.21, respectively. Larger deformation was acquired with the B4 model compared to Eurocode 2 as well as when the Ballast load was 11.8 kPa. The larger the ballast load the larger the final deformation and deformation development was.

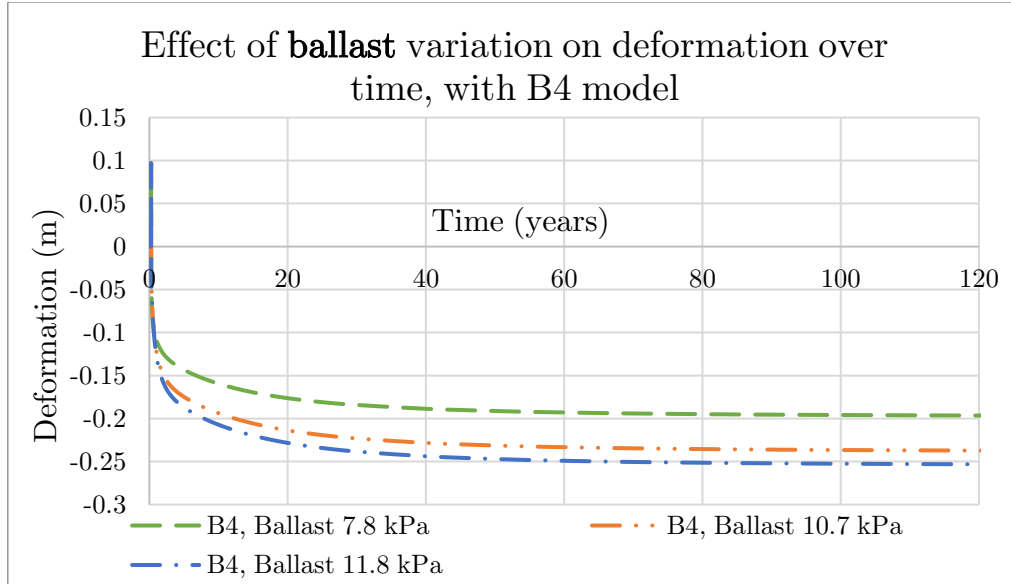


Figure 7.20: Effect of ballast variation on deformation over time, with B4 model.

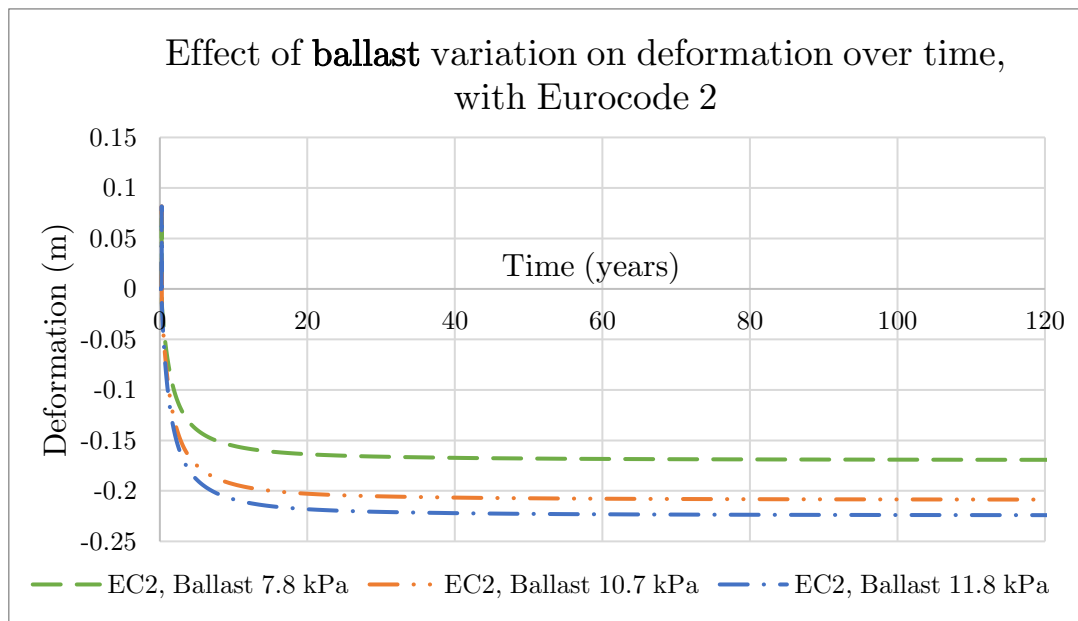


Figure 7.21: Effect of ballast variation on deformation over time, with Eurocode 2.

7.3.4 Influence of cross-section perimeter exposed to air

The influence of cross-section perimeter exposed to air was plotted for non-uniform and uniform creep and shrinkage with Eurocode 2 along the span at the north edge after 10 years, as illustrated in Figure 7.22. Larger deformations were obtained when the bridge deck was included in the perimeter exposed to air. Larger deformations were also obtained for calculation with non-uniform analysis.

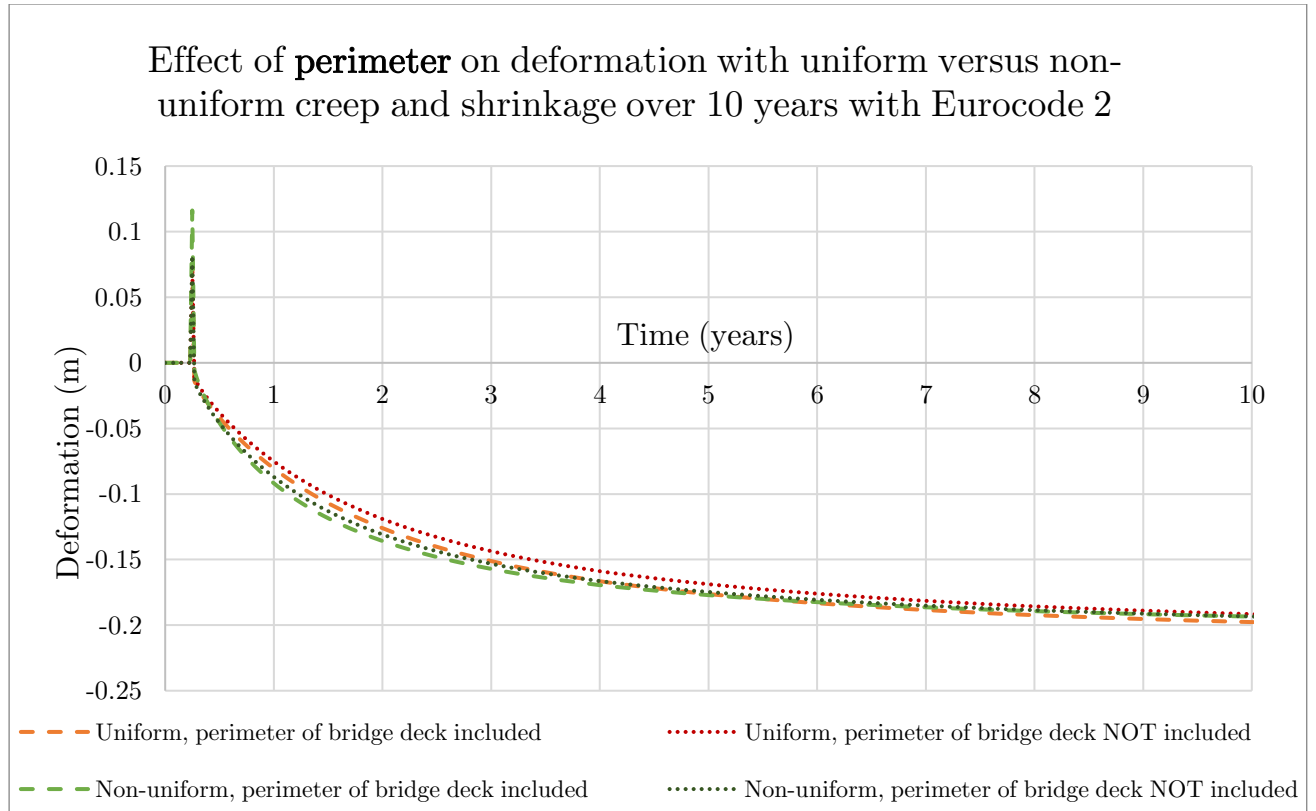


Figure 7.22: Effect of the perimeter on deformation with uniform- versus non-uniform creep and shrinkage over 10 years, with Eurocode 2.

7.4 Stress state

The stress state was plotted using Eurocode 2 with non-uniform and uniform analysis as well as the B4 model with non-uniform analysis, as illustrated in Figure 7.23. The stress state is shown after 3 years from which the first measurements were taken on the Alvik bridge. The purpose of this was to compare what difference the approaches have on the expected stress state and conclude its effect on cracking. The regions shown in red are where the tensile stress was higher than the design value of 3.2 MPa. The figure illustrates three simulation results. Model a) was with uniform analysis and Eurocode 2. Model b) was with non-uniform analysis and Eurocode 2. Model c) was with non-uniform analysis and the B4 model. The results showed that the largest stress was obtained with the B4 model compared to Eurocode 2. The stress was also higher for non-uniform

analysis using Eurocode 2 compared to uniform analysis. All three methods indicate areas that have tensile stress larger than the design value.

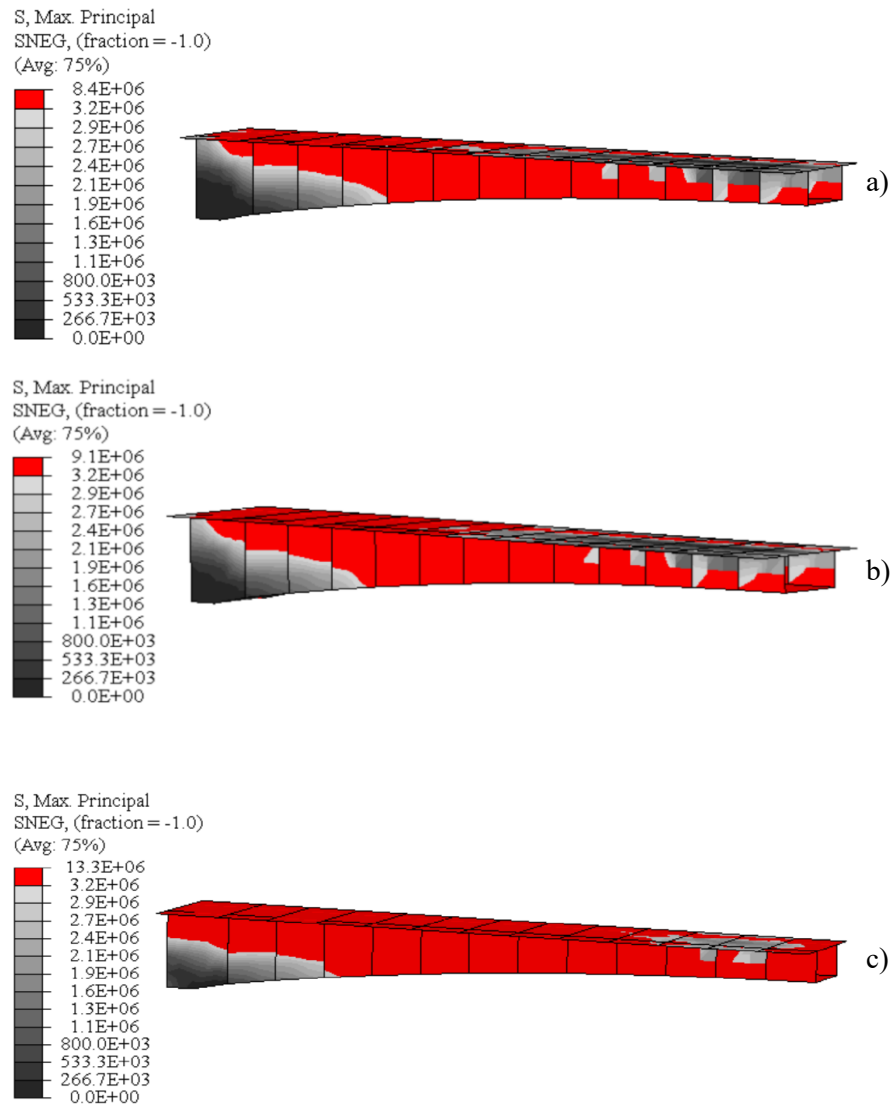


Figure 7.23: a) Tensile stress state. Everything above tensile stress of 3.2 MPa is marked red. a) uniform EC2, b) non-uniform EC2, c) non-uniform B4 model.

Chapter 8

Discussion and Conclusion

8.1 Effect of non-uniform versus uniform creep and shrinkage

The difference in deformations caused by non-uniform versus uniform creep and shrinkage was larger in the first ten years of the lifetime of the bridge. After ten years, the deformation values seemed to level out for non-uniform and uniform analysis. This indicated that noticeable differences between non-uniform and uniform analysis were obtained during the early stages of the total service life of the bridge. The results from the analysis indicated that the deformation values calculated with non-uniform and uniform analysis ultimately converged. This is illustrated in Figure 7.6, where no significant difference in deformation between non-uniform and uniform analysis was observed. The shrinkage rate for each part will ultimately reach the same value. The effect of non-linear creep was not large enough in the earlier deformations to lead to significantly larger long-term deformations, as illustrated in Figure 7.11.

The difference between calculations with uniform versus non-uniform analysis was not as significant as expected even in the first 10 years, compared to the analysis performed in the benchmark model for shrinkage. The difference in shrinkage results from the benchmark models indicated a significant difference between non-uniform and uniform analysis. This may depend on the relationship between thickness and perimeter exposed to air for each part. In the main analysis, it was assumed that the bridge deck was not exposed to air. This assumption meant that the top flange would only dry out on one side. Therefore, despite the relatively small thickness of the top flange, the shrinkage strain was not significantly larger than for the web or uniform cross-section. However, for the bottom flange and web, both sides of the parts, outside and inside, were assumed to be exposed to air. This assumption meant that a web of similar thickness as a top flange would have larger shrinkage strain since the web could dry out on all sides. The larger shrinkage rate for the web compared to the top and bottom flange could be an influencing factor for why non-uniform analysis resulted in larger deformations compared to uniform analysis.

The tensile stress state, after the first 3 years, which was when the first measurements were performed, as illustrated in Figure 7.23 shows that a larger tensile stress state was

obtained with calculations performed with non-uniform analysis compared to uniform. Tensile stress larger than the design value indicates a risk of cracking. The non-uniform analysis showed a larger stress state and a larger area where tensile stress was higher than the design value, compared to uniform analysis. For the owner of the bridge, the non-uniform analysis would be safer to use, as it is a more conservative approach for predicting the risk of cracking.

8.2 Difference in deformation behaviour between B4 model and Eurocode 2

The results indicated that larger deformations were obtained with the B4 model compared to Eurocode 2. A possible cause may be the definition of the perimeter in the B4 model versus Eurocode 2. Eurocode 2 defines the perimeter as the cross-section perimeter exposed to air. The B4 model defines the entire surface area, without considering exposure to air. This difference in defined perimeter resulted in a higher shrinkage strain rate for each part of the cross-section when calculating with the B4 model. Therefore, the larger difference in shrinkage strain rate resulted in larger deformations for the B4 model compared to Eurocode 2. The difference in creep coefficient between the B4 model and Eurocode 2 could be a reason for larger deformations with the B4 model. The creep coefficient for the B4 model reaches a final value of around 2.25, while Eurocode 2's corresponding value is around 2. Another important influencing factor for larger acquired deformations with the B4 model could be that the final shrinkage strain for the B4 model was a lot larger than Eurocode 2. The final shrinkage strain with the B4 model was a bit over 0.450 ‰, whereas Eurocode 2's corresponding value was around 0.300 ‰.

The calculated deformations behave differently over time with the B4 model and Eurocode 2. In the calculations based on Eurocode 2, the total deformation increases significantly for approximately the first ten years. After this, the deformation rate is reduced which results in slowly increasing deformation. With the B4 model, the deformations continue through the lifetime of the bridge, as illustrated in Figure 7.8. A possible explanation for why deformations continue in the model using the B4 model could be the difference in the convergence of the shrinkage strain rate. The shrinkage strain rate indicated convergence after around 30 000 days (80 years) for the B4 model, as illustrated in Figure 6.8. The shrinkage strain rate indicated convergence after around 10 000 days (30 years) for Eurocode 2, as illustrated in Figure 6.9. The B4 model's shrinkage strain rate converging slower could be the reason for deformation calculated with the B4 model not reaching a constant value until late in the bridge lifetime. When analysing the effect of creep and shrinkage, it was noticeable that calculations with B4 showed that shrinkage had a larger influence on deformations compared to creep. Unlike the calculations performed with Eurocode 2, where creep had a larger influence on the deformations compared to shrinkage. This could also be caused by the different definition of perimeter and surface for the different calculation models.

Another factor contributing to different results could be the input accuracy. When calculating with the B4 model, several different variables are needed in the calculation. The variables however are not always provided in detail by the design and construction

companies, which may lead to inaccurate assumptions of the variables. This was also highlighted in the benchmark model for the cube, where the aggregate type gave varying behaviour, as illustrated in Figure 4.6. Variables such as aggregate type and others within the B4 model must be properly considered when using the model to ensure accurate results.

The tensile stress state after the first 3 years, as illustrated in Figure 7.23, showed that a larger tensile stress state was obtained with calculations performed with the B4 model compared to Eurocode 2. Tensile stress larger than the design value indicates a risk of cracking. The B4 model analysis showed a larger stress state and a larger area where tensile stress was higher than the design value compared to Eurocode 2. A possible explanation for that could be that shrinkage has a more dominant influence on deformations compared to creep in the B4 model. Theory suggests that larger shrinkage results in larger stress, whereas larger creep results in smaller stress value. Therefore, for the owner of the bridge, the B4 model would be safer as it is more of a conservative approach for predicting the risk of cracking.

8.3 Influence of parameters on deformation

The deformation behaviour was similar for analysis performed with the B4 model and Eurocode 2, regarding relative humidity variation. Both models showed that higher relative humidity resulted in smaller deformations, whereas lower relative humidity resulted in larger deformations. This was expected, as the concrete should dry out quicker in drier ambient air.

Varying the water-cement ratio did not affect the deformations significantly. However, more detailed analysis with varying water-cement ratio should also consider that a lower water-cement ratio will lead to stiffer concrete with a higher value of strength. This was not considered in this thesis, which could have been an influencing factor (Ansell et.al, 2014)

The influence of the weight of the ballast was similar in calculation with the B4 model and Eurocode 2 where a larger load from the ballast resulted in larger deformations. An important factor to consider is that there is a significant difference in deformations when the ballast height is assumed as 0.45 m compared to 0.41 m. The difference is only 4 cm which indicates the importance of correct representation of the design loads in the structural drawings, as well as at construction sites. More detailed information should be provided on such a parameter due to its influence on the overall deformation.

Finally, larger deformations were obtained when the bridge deck was included in the perimeter in the analysis with Eurocode. The real-life situation may however be somewhere in between the analysis of including the bridge deck in the perimeter and not including it. The bridge deck is most likely not exposed to air where the asphalt mastic is placed. However, the bridge deck may be exposed to air where the ballast is placed.

8.4 Validity of numerical analysis

After 3 years, the measurements from the case study model showed that the deformation at midspan, at the northern edge was 13.2 cm, as illustrated in Figure 7.2. Figure 7.2 also shows that the deformation at midspan with the B4 model was 16.5 cm. However, with Eurocode 2 the deformation was 15.3 cm and 16.1 cm for uniform and non-uniform approach, respectively. The early difference between the measurement and the case study model may be due to an overestimation of the initial elastic deformation in the case study model. The measurements and results from the case study model were similar for the south edge at midspan after 3 years. The measurements showed deformation of 13.1 cm, as illustrated in Figure 7.3, also illustrates that deformation of around 14.2 cm was obtained with the B4 model, whereas Eurocode 2 gave values 13.0 cm and 13.1 cm for uniform and non-uniform analysis, respectively. The similarity of results may be due to more reliable estimation of the asphalt load, compared to the ballast load.

After 22 years, the deformation at midspan at the north edge was similar for the case study model and the measurements, see Figure 7.4. The measured deformation at midspan was 21.0 cm, whereas the deformation value was 21.6 cm for the B4 model. The deformation value with Eurocode 2 was 20.2 cm and 20.3 cm with a uniform and non-uniform approach, respectively. This may be due to the results in the case study model converging to more accurate deformations after the initial elastic deformation. The measurements along the south edge after 22 years resulted in a deformation of 19.0 cm. The deformation for the case study model along the south edge after 22 years resulted in 17.4 cm with Eurocode 2 and 18.7 cm with the B4 model, see Figure 7.5. Although both the B4 model and Eurocode 2 showed similar results to the measurements, the B4 model resulted in results more consistent with the measurements.

The simulated deformation was more accurate in the span between pier 4 and 5 compared to the span between pier 3-4 and 5-6. A possible explanation for that could be the boundary condition difference as well as an overestimation of certain loads. The simulated model overall had larger deformations along the north edge compared to the south edge which is congruent with the measurement observation. A larger eccentric load due to ballast was a direct cause since the north edge has ballast load whereas the south edge has asphalt load.

8.5 Further research

Results from the analysis showed that the variable for the length of the perimeter exposed to air was important. More information is required about which parts of the bridge deck are exposed to drying and which parts are protected from drying. More realistic simulations where the drying of concrete and detailed models based on multiphysics should also be researched. This type of simulation could be important for a better understanding of how non-uniform drying affects deformation behaviour.

Results from the study indicated that varying the ballast height corresponded with significant changes in short- and long-term deformations. It is therefore important to ensure that the ballast height at the construction site closely resembles the design height.

If the height of the ballast changes during the lifetime of the bridge, it should be reported, to provide an accurate prediction of the deformation behaviour.

Results from the study indicated that the B4 model could deliver accurate results for estimating deformations caused by non-uniform creep and shrinkage. However, more detailed information regarding the input variables, such as aggregate type, aggregate-cement ratio, etc. needs to be provided.

Possible further research could also be to perform analysis like the ones performed in this thesis on other bridges. This thesis has a case study of the Alvik bridge, but several other cantilever bridges could also be studied to see what behaviour they show.

This thesis did not consider the effect of cracking that happened on the Alvik bridge and the strengthening work that was performed. Detailed simulation considering cracking and strengthening could be interesting to research and compare with this study to see their effect on the deformation behaviour.

Bibliography

Ansell A., Hallgren M., Holmgren J., Lagerblad B. and Westerberg B. 2014. *Concrete Structures*. KTH Civil and Architectural Engineering. Stockholm. TRITA-BKN, report 143.

Bazant Z.P., Baweja S. 2001. Creep and Shrinkage Prediction Model for Analysis and Design of Concrete Structures: Model B3. ACI Concrete International ACI 23, Jan.2001, 38–39.

Bazant Z.P., Hubler M.H. and Wendner R. 2015. Model B4 for creep, drying shrinkage and autogenous shrinkage of normal and high-strength concretes with multi-decade applicability. *Materials and Structures* 48:753–770. doi: 10.1617/s11527-014-0485-2.

Bro och Stålkontroll. 2020. Avvägning - TVB VÄST, Alviks strand - Essingen, Alviksbron, över Oxhålet, Knr: 30-12512-1, Idnr-2: 51-0562.

Borbolla L. and Mazzola A. 2003. *Finite Element Simulation of the Crack Development in the Gröndal Bridge*. M.Sc., Chalmers University of Technology. Gothenburg. Department of Structural Engineering Master Thesis No. 03:1. Department of Structural Mechanics Master Thesis No. 03:3.

Canovic S. and Goncalves J. 2005. *Modelling of the response of the New Svinesund Bridge*. M.Sc., Chalmers University of Technology. Gothenburg. Master's Thesis 2005:39.

Dassault Systemes. (2020). SIMULIA User Assistance 2020: *Determination of viscoelastic material parameters*.
http://abaqus.sys.kth.se/v2020/English/DSSIMULIA_Established.htm?show=SIMACAEMATRefMap/simamat-c-timevisco.htm (Retrieved 2021-06-19).

Engström B. 2007. *Beräkning av betongkonstruktioner*. Institutionen för bygg- och miljöteknik, Avdelningen för konstruktionsteknik. Chalmers University of Technology. Gothenburg. Rapport 2007:13.

Ericsson L.E., Liljelund L., Sjöstrand M., Uusmann I., Modig S., Ärlebrant Å. and Högrell O. 2002. *Till statsrådet Lars-Erik Lövdén*. (SOU 2002:115).

Eurocode 1. 2002. *Eurocode 1: Actions on structures – Part 1-1: General actions – Densities, self-weight, imposed loads for buildings. SS-EN 1991-1-1:2002*. European Committee for Standardization, Brussels.

Eurocode 2. 2008. *Eurocode 2-9: Concrete bridges – Design and detailing rules. SS-EN 1992-2:2005*. European Committee for Standardization, Brussels.

Kelly P. 2013. *Solid mechanics part I: An introduction to solid mechanics*. Solid mechanics lecture notes, University of Auckland.

Krístek V., Bažant Z.P., Zich M. and Kohoutková A. 2006. Box Girder Bridge Deflections - Why is the initial trend deceptive?. *ACI Concrete International*. Vol. 28, No.1, pp.55-63.

Malm, R. 2016. GUIDELINE FOR FE ANALYSES OF CONCRETE DAMS. Energiforsk. REPORT 2016:270.

Malm R. 2020. *Långtidsdeformationer på Gröndalsbron*. Sweco, Uppdragsnummer: 15007223.

Malm, R. and Ansell, A. 2009. *Non-linear analyses of cracking in segmentally constructed concrete box-girder bridges*.

Malm R. and Sundquist H. 2010. Time-dependent analyses of segmentally constructed balanced cantilever bridges. *Engineering Structures*. 32 (2010) 1038–1045. doi:10.1016/j.engstruct.2009.12.030

Malm R., James G., and Sundquist H. (2006), *Monitoring and evaluation of shear crack initiation and propagation in webs of concrete box-girder sections*. The International Conference on Bridge Engineering – Challenges in the 21st Century, November 1-3, 2006, Hong Kong.

SBUF. No Date. *Förstärkning av broar med hjälp av kolfiberlaminat – resultat av efterföljande mätning med fiberoptiska sensorer*.
https://vpp.sbuf.se/Public/Documents/InfoSheets/PublishedInfoSheet/39f17687-f488-4ebc-ba38-ad32d85e3a21/13_13_0526.pdf (Retrieved 2021-06-19).

Silfwerbrand J. (ed.). 2017. *Betonghandbok. Material D. 1 Delmaterial samt färsk och hårdnande betong*. Solna: Svensk Byggtjänst.

SMHI. 2020. *Meteorologiska observationer - Relativ luftfuktighet timvärde*.
<https://www.smhi.se/data/utforskaren-oppna-data/se-acmf-meteorologiska-observationer-relativ-luftfuktighet-timvarde> (Retrieved 2021-06-19)

Takács, P.F. 2002. *Deformations in Concrete Cantilever Bridges: Observations and Theoretical Modelling. Doctoral Thesis*. The Norwegian University of Science and Technology.
<http://hdl.handle.net/11250/231135> (Retrieved 2021-04-14)

Trafikverket. 2019. *Krav – Krav Brobyggande*. TDOK 2016:0204

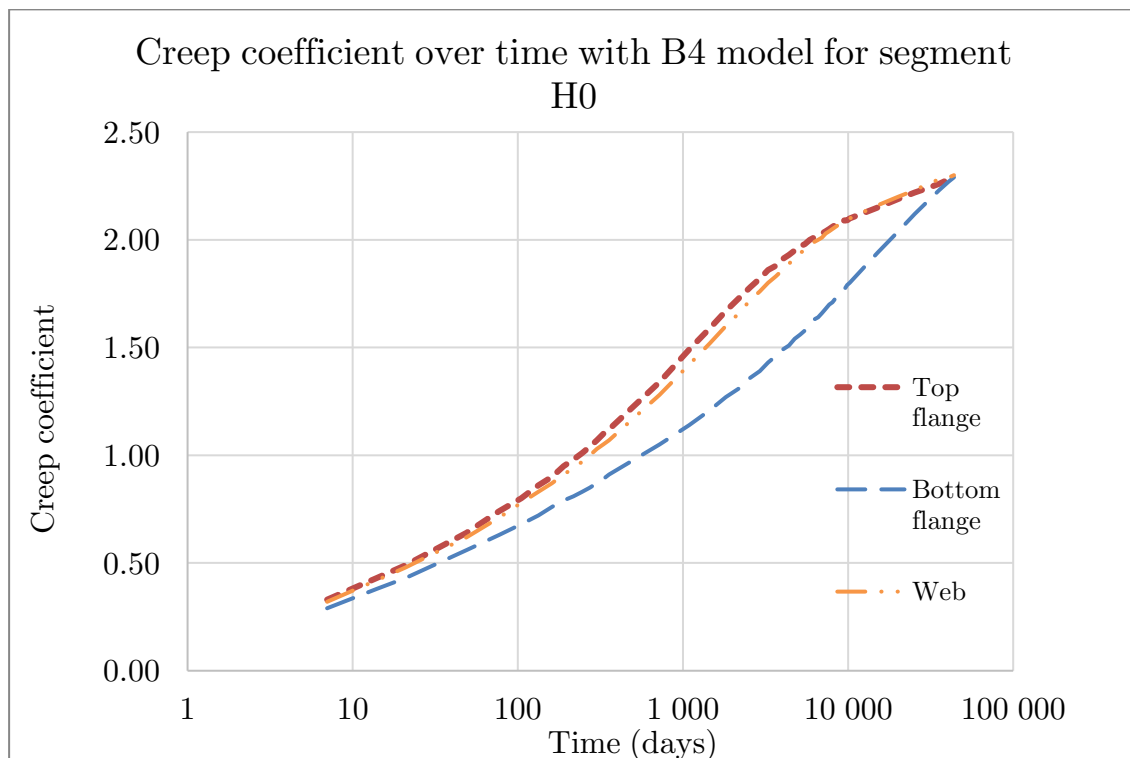
Weil G. 1959. *Influence des dimensions et des contraintes sur le retrait et le fluage du béton*. (1959) Bulletin RILEM, No. 3.

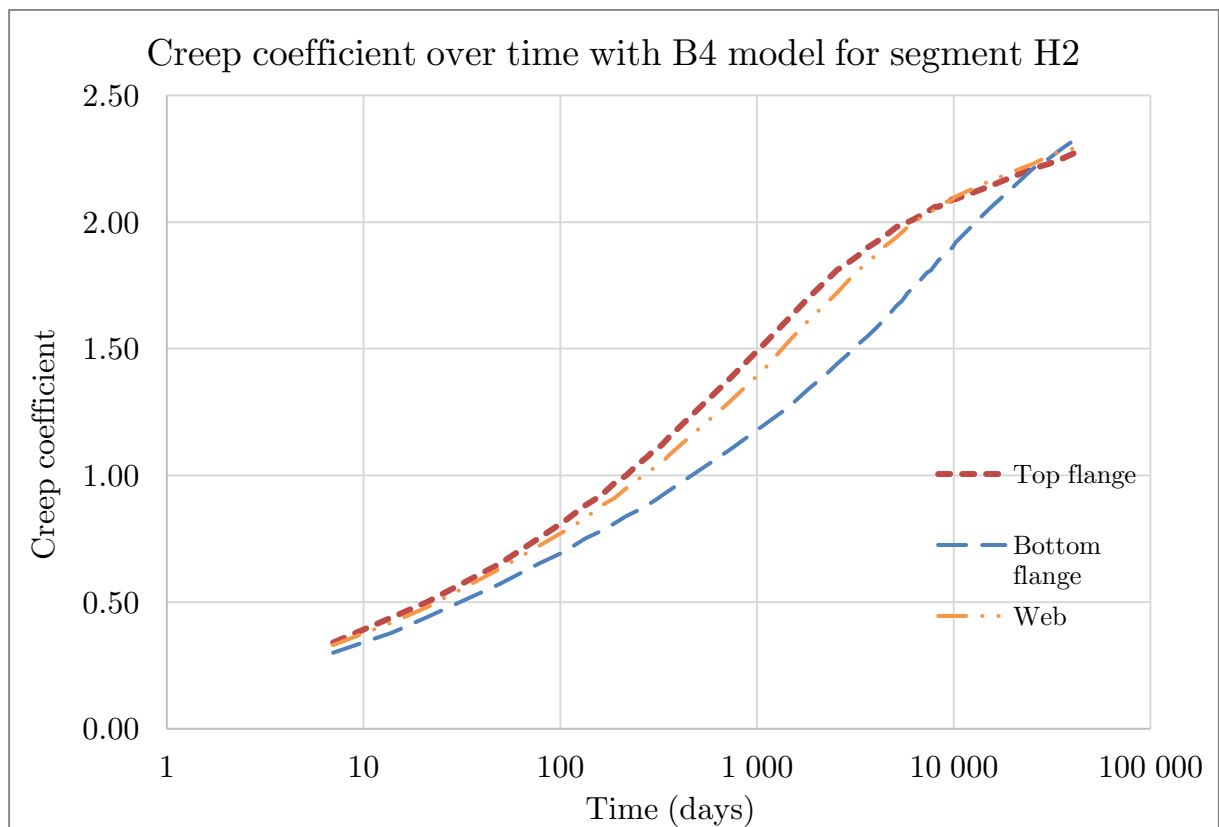
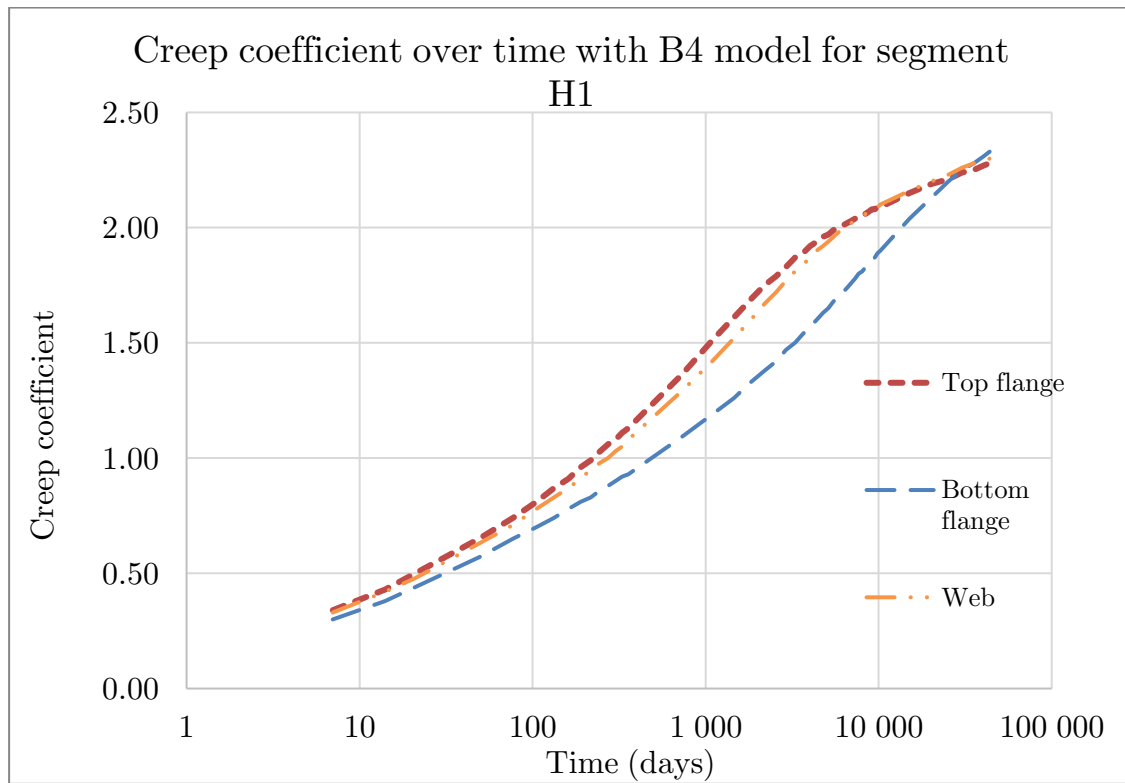
Zhuoya YUAN, Pui-Lam NG, Darius BAČINSKAS, Jinsheng DU. 2018. Analysis of non-uniform shrinkage effect in box girder sections for long-span continuous rigid frame bridge. *The Baltic Journal of Road and Bridge Engineering*. 13(2): 146-155.
<https://doi.org/10.7250/bjrbe.2018-13.409> (Retrieved 2021-04-14)

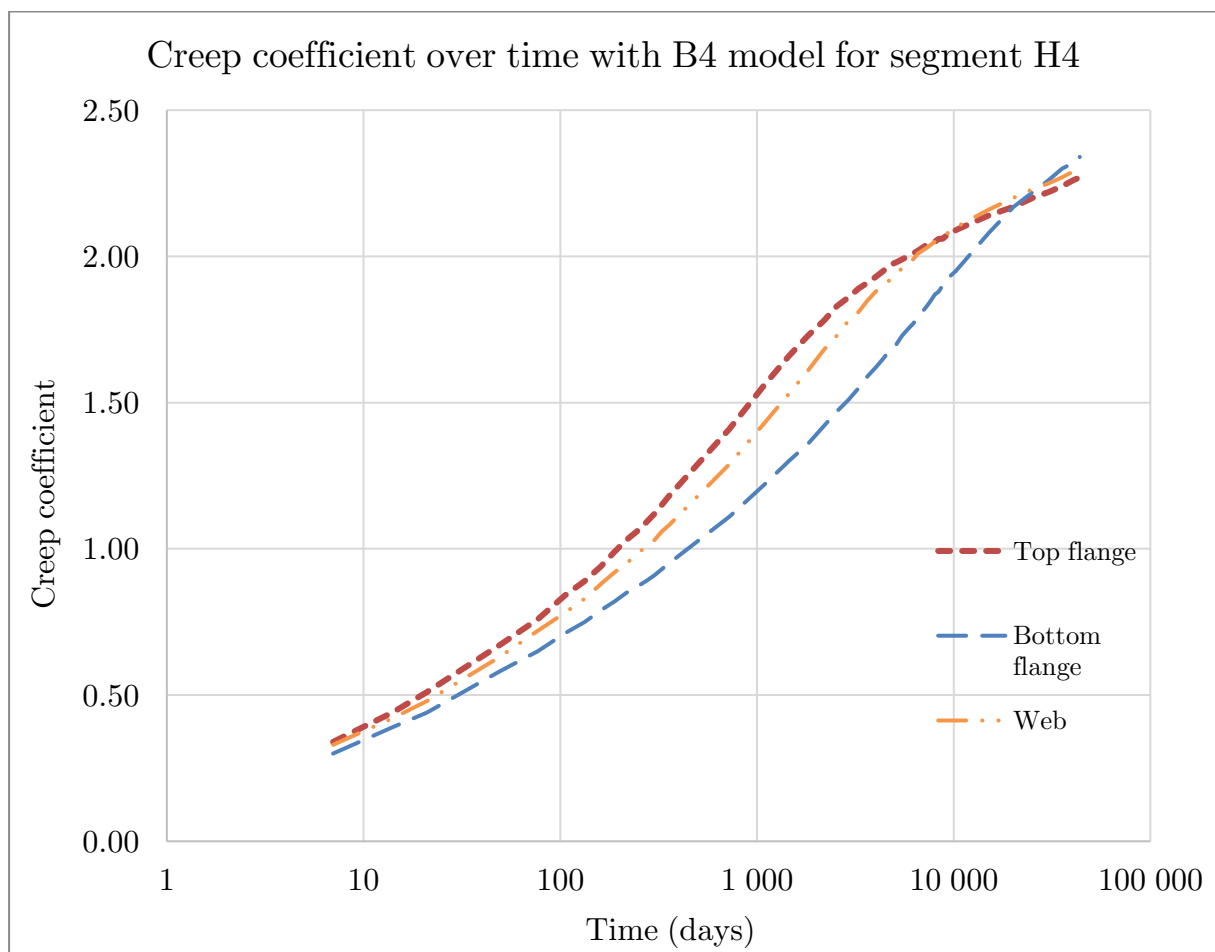
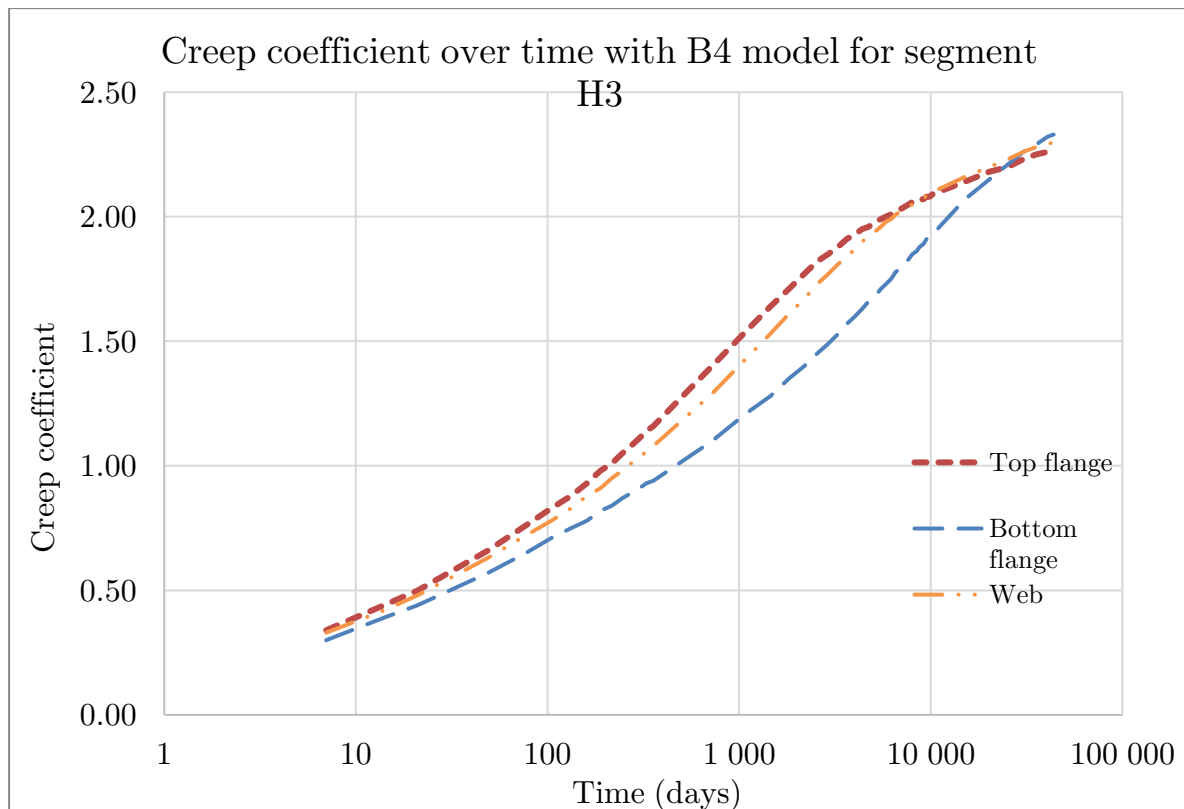
Appendix A

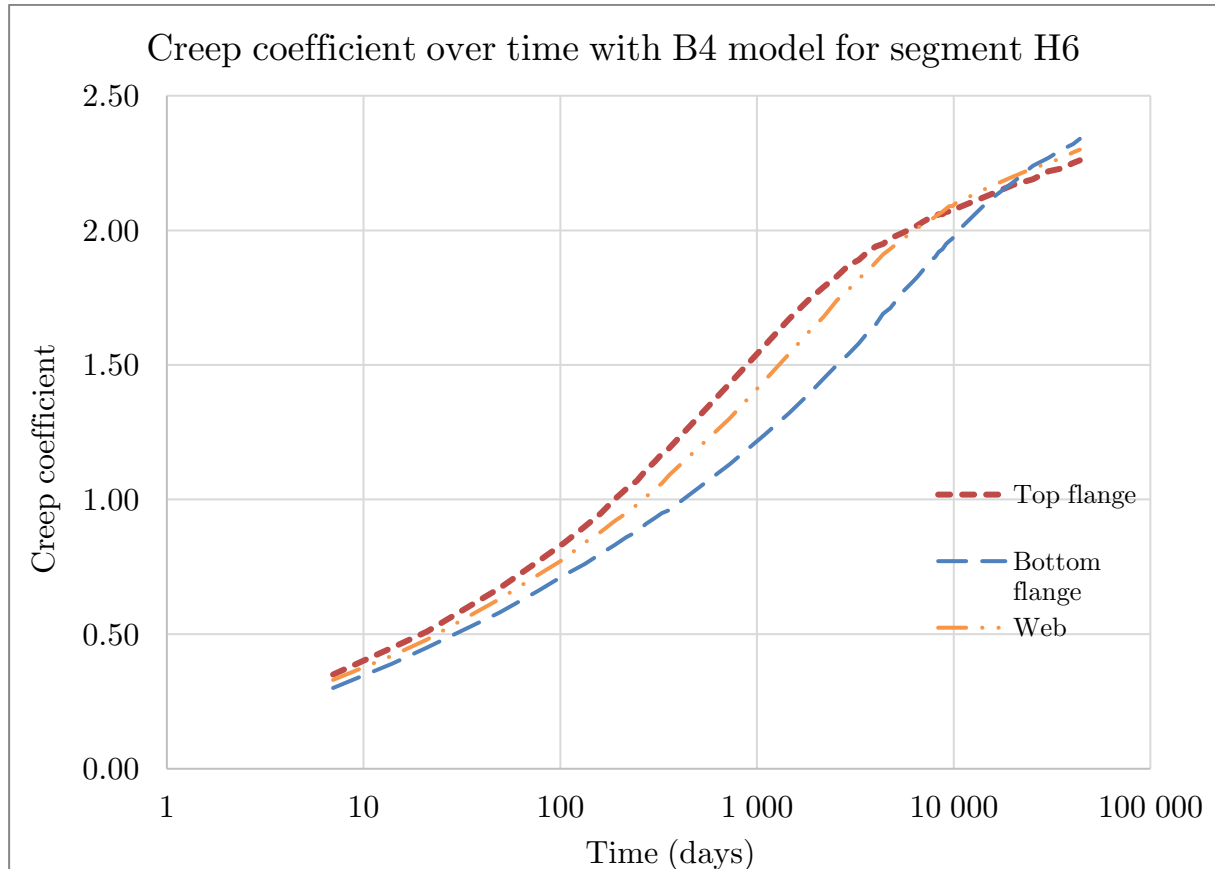
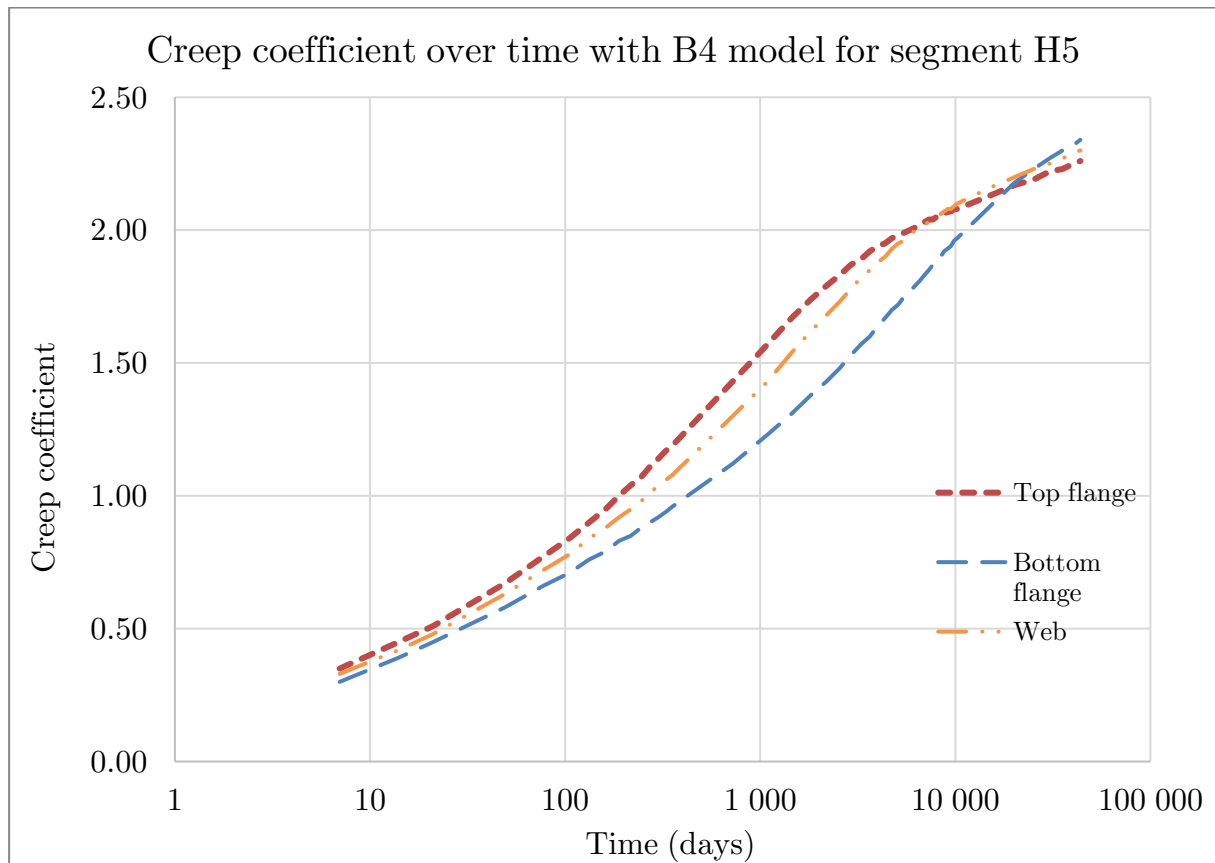
Material input

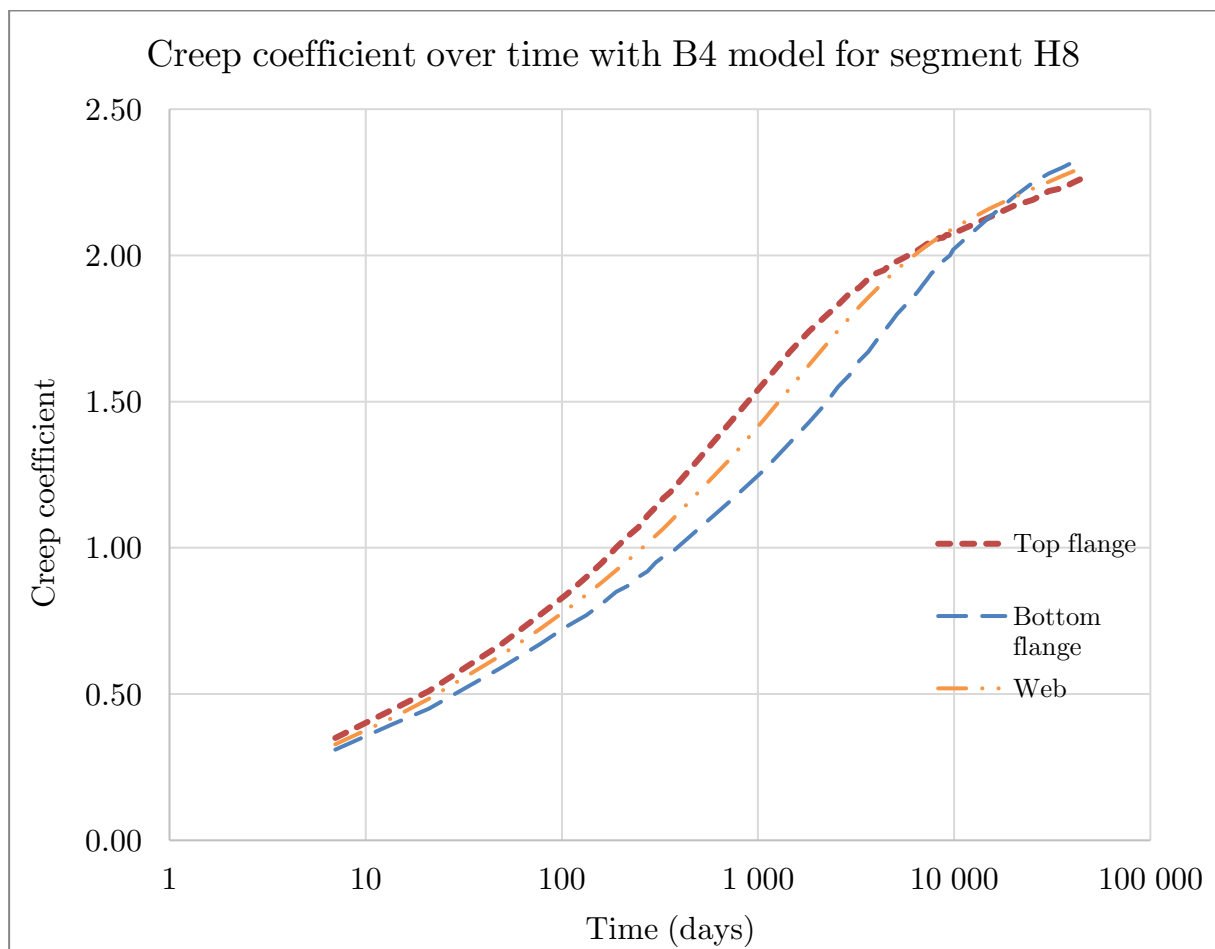
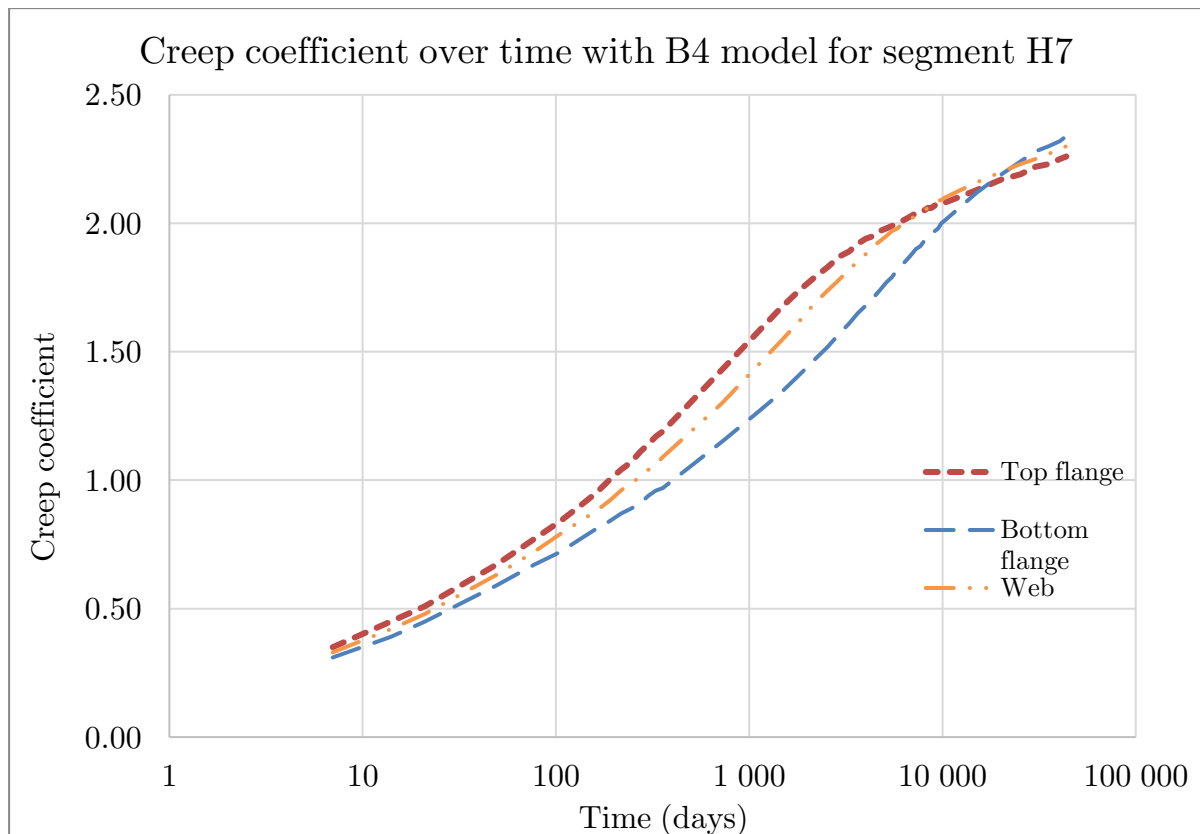
A.1 Creep coefficient variation for each segment

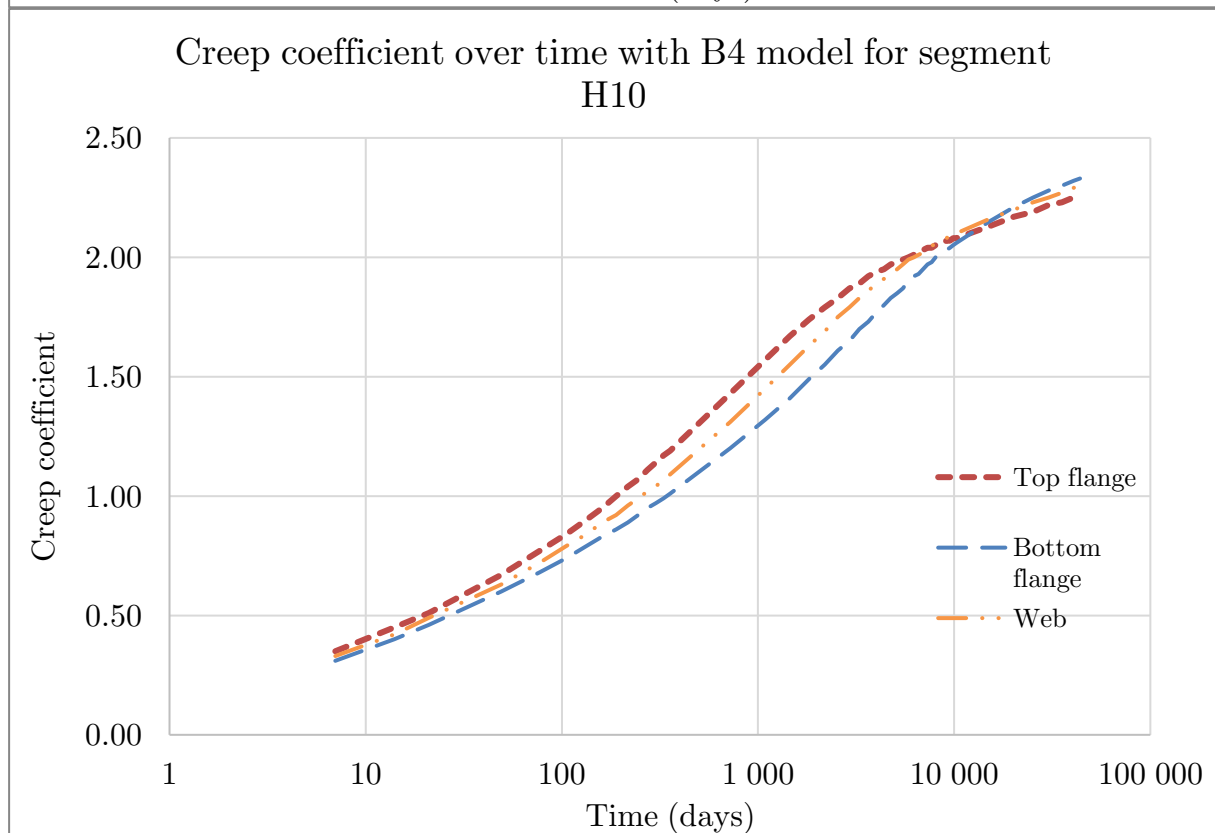
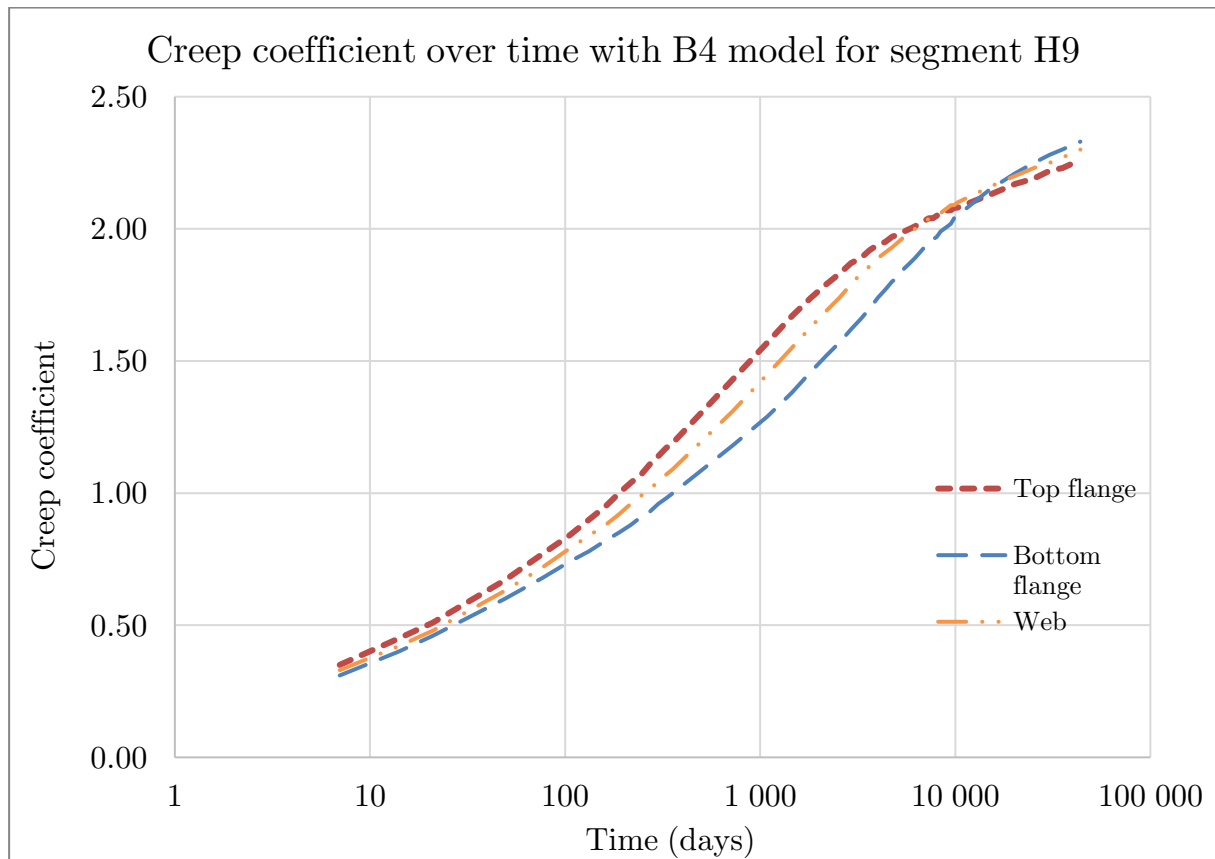


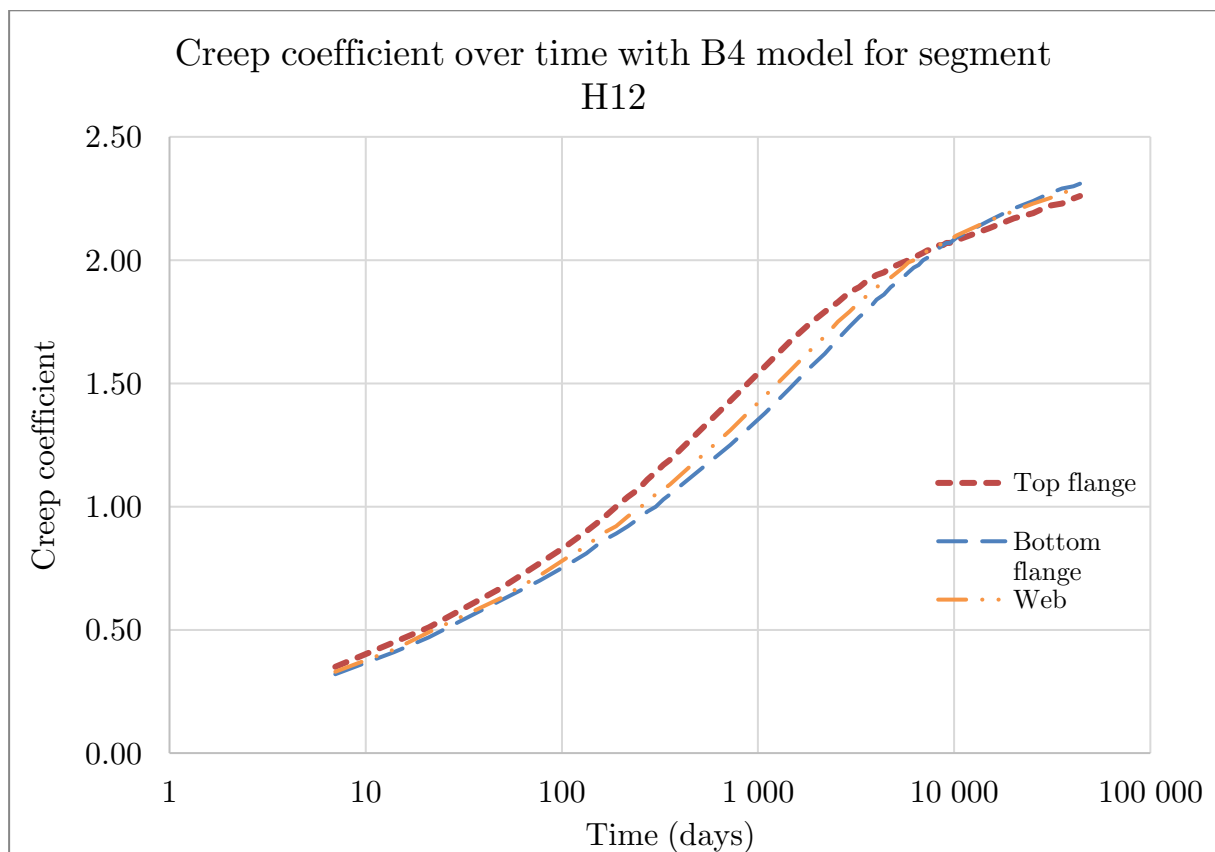
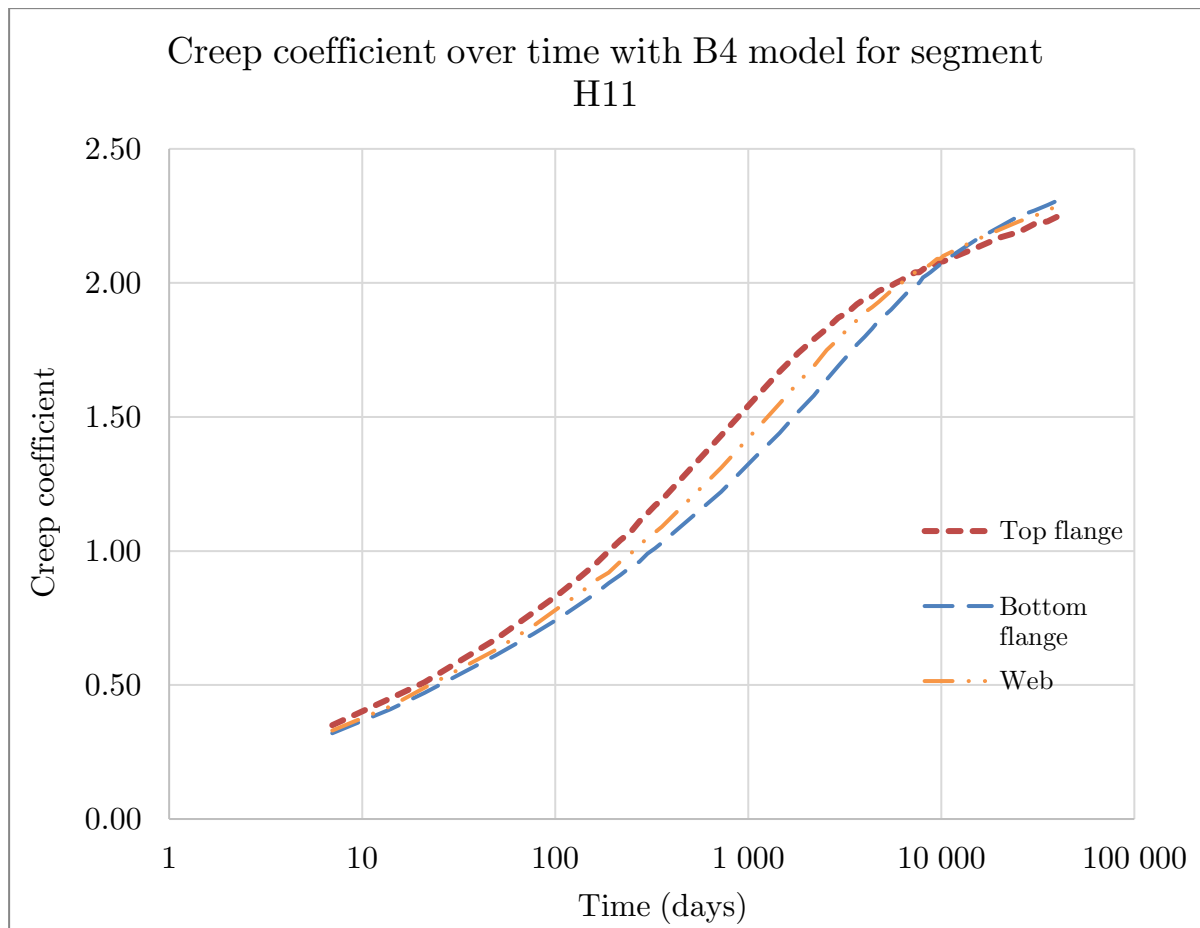


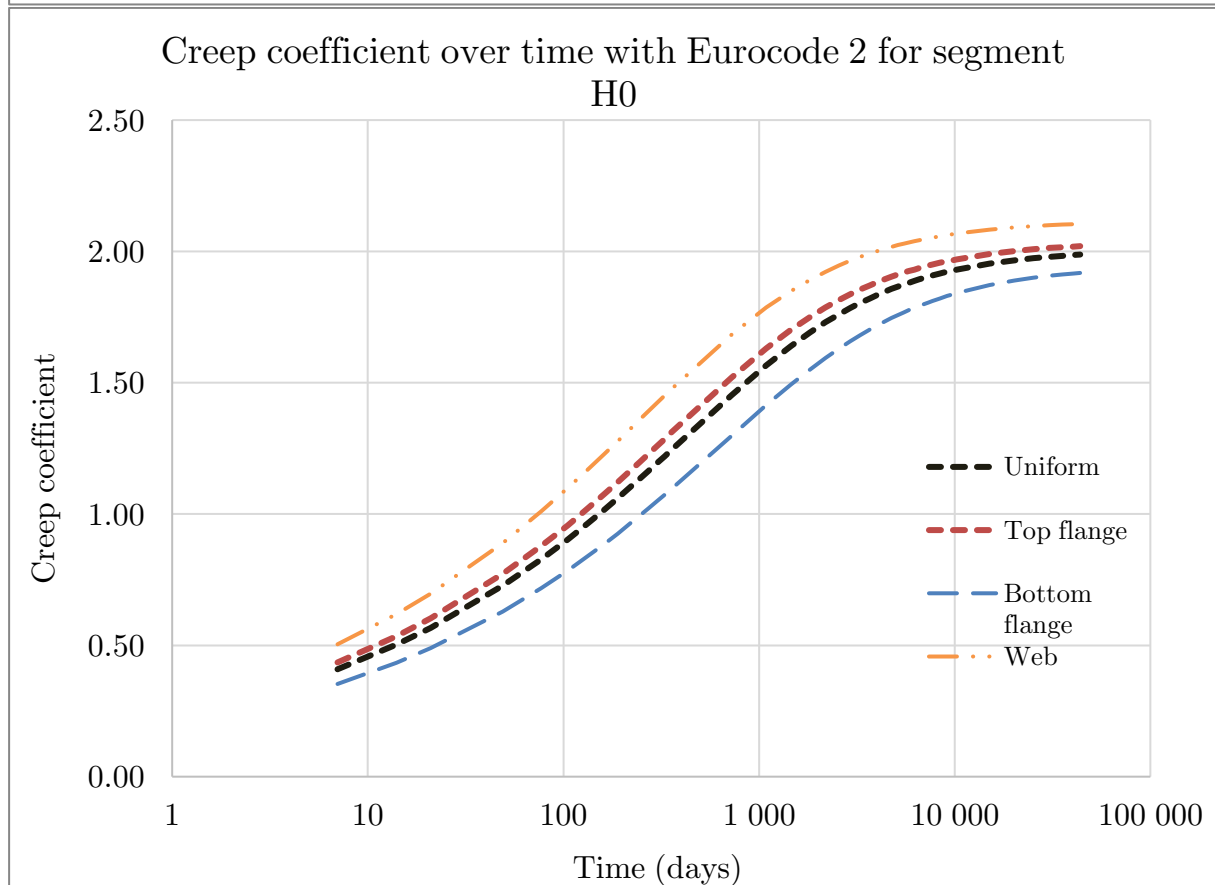
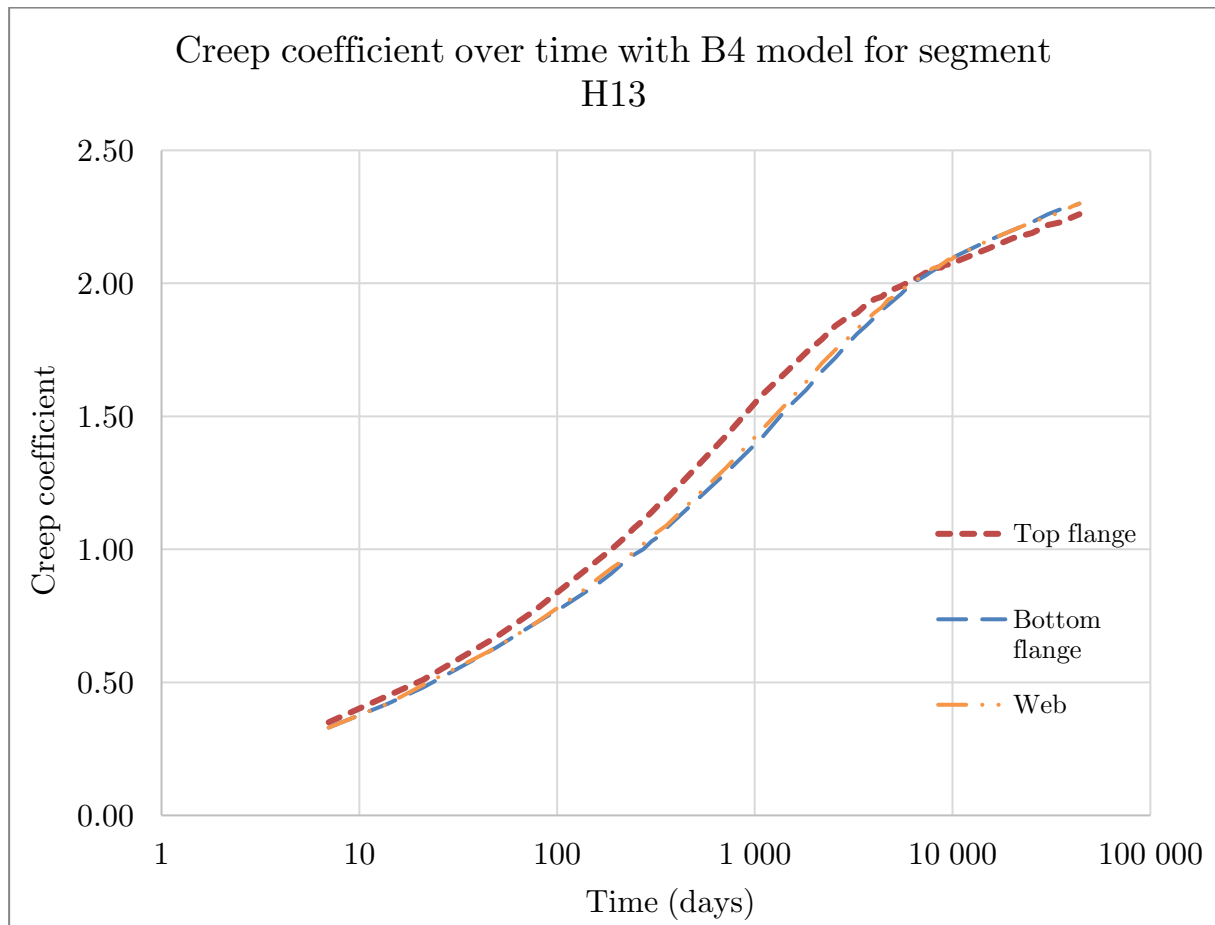


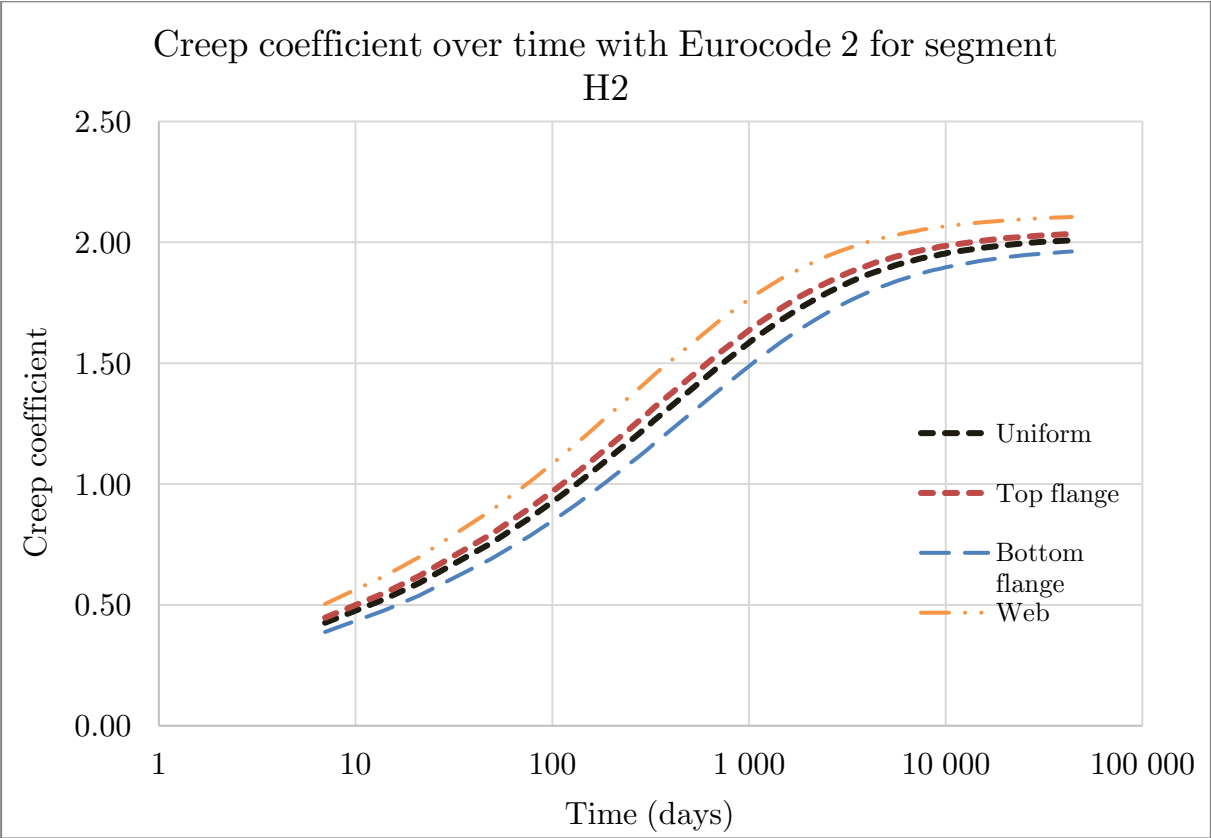
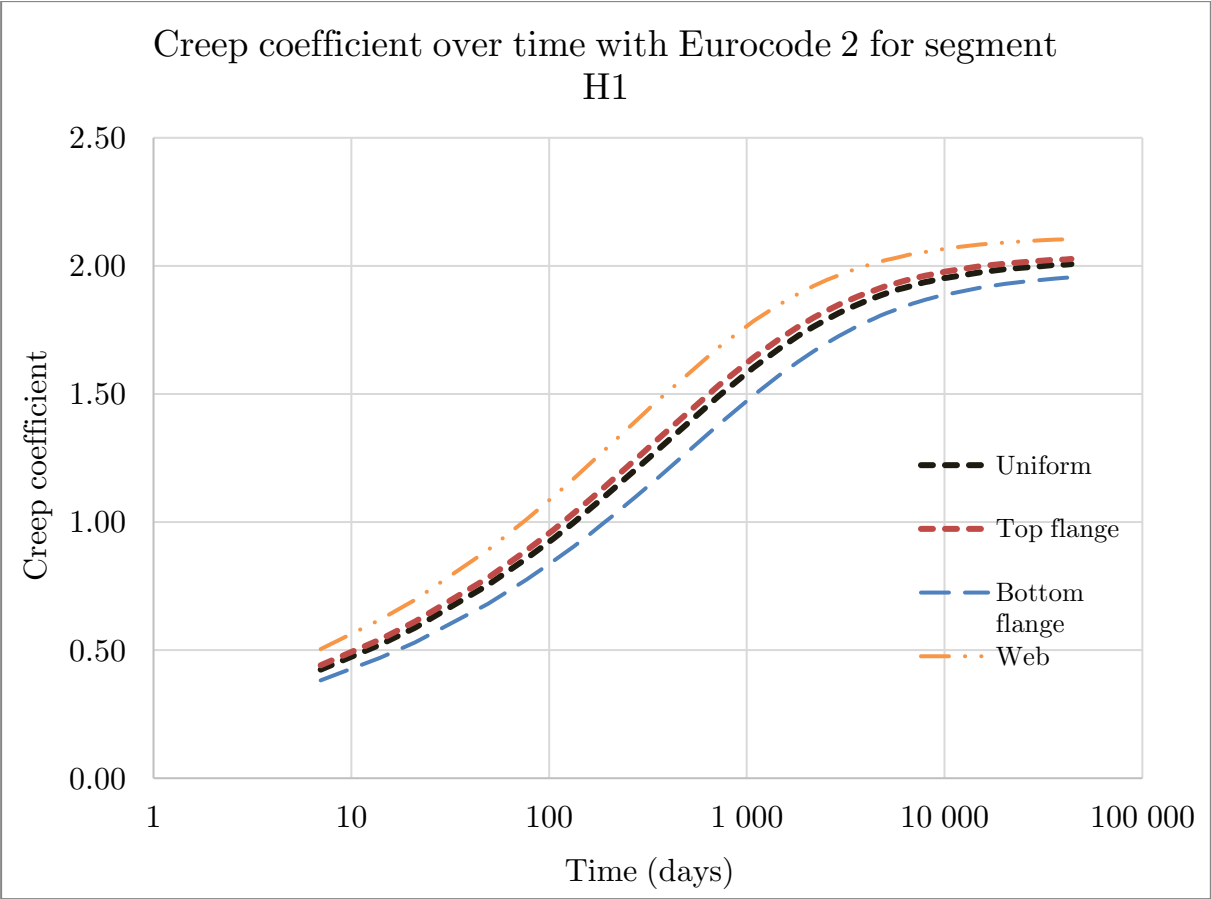


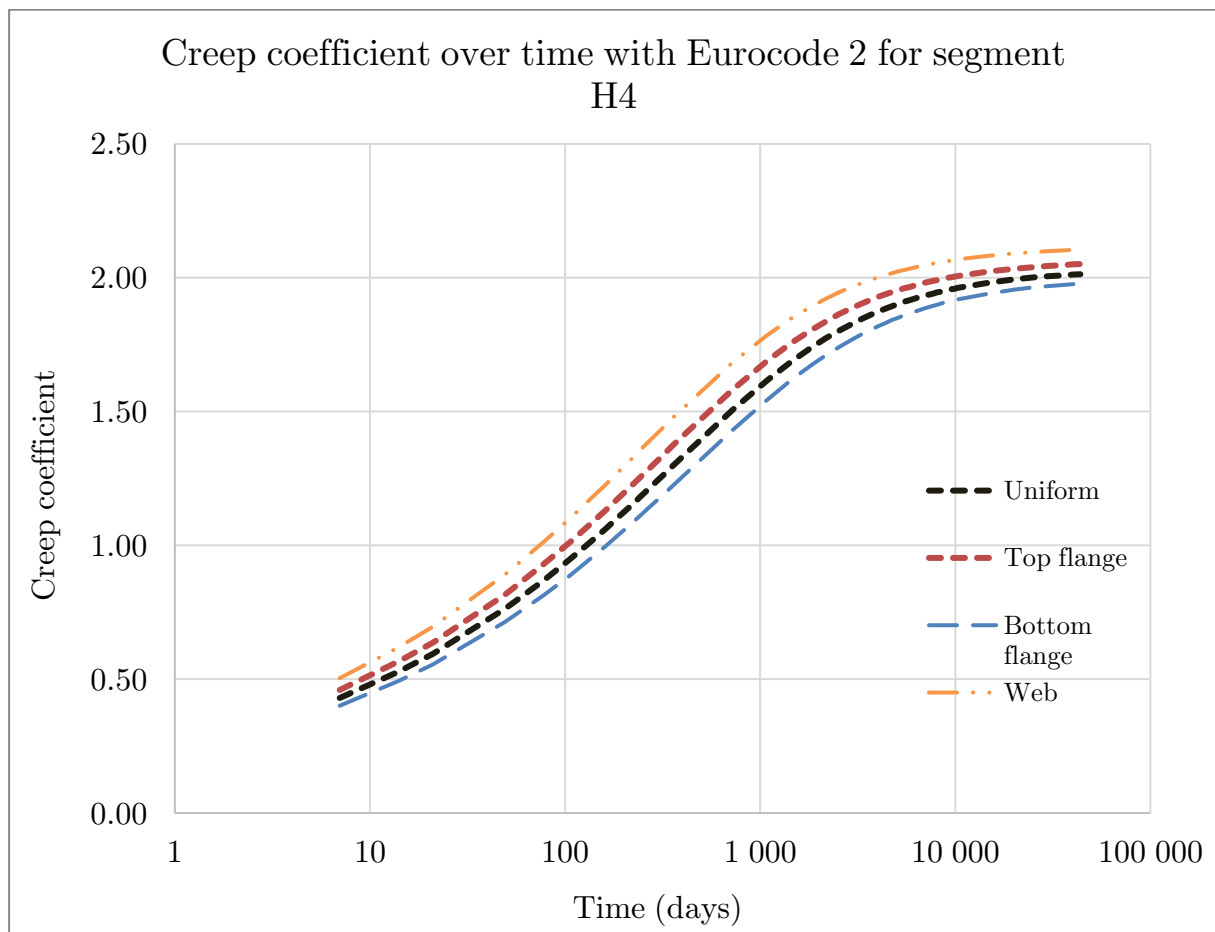
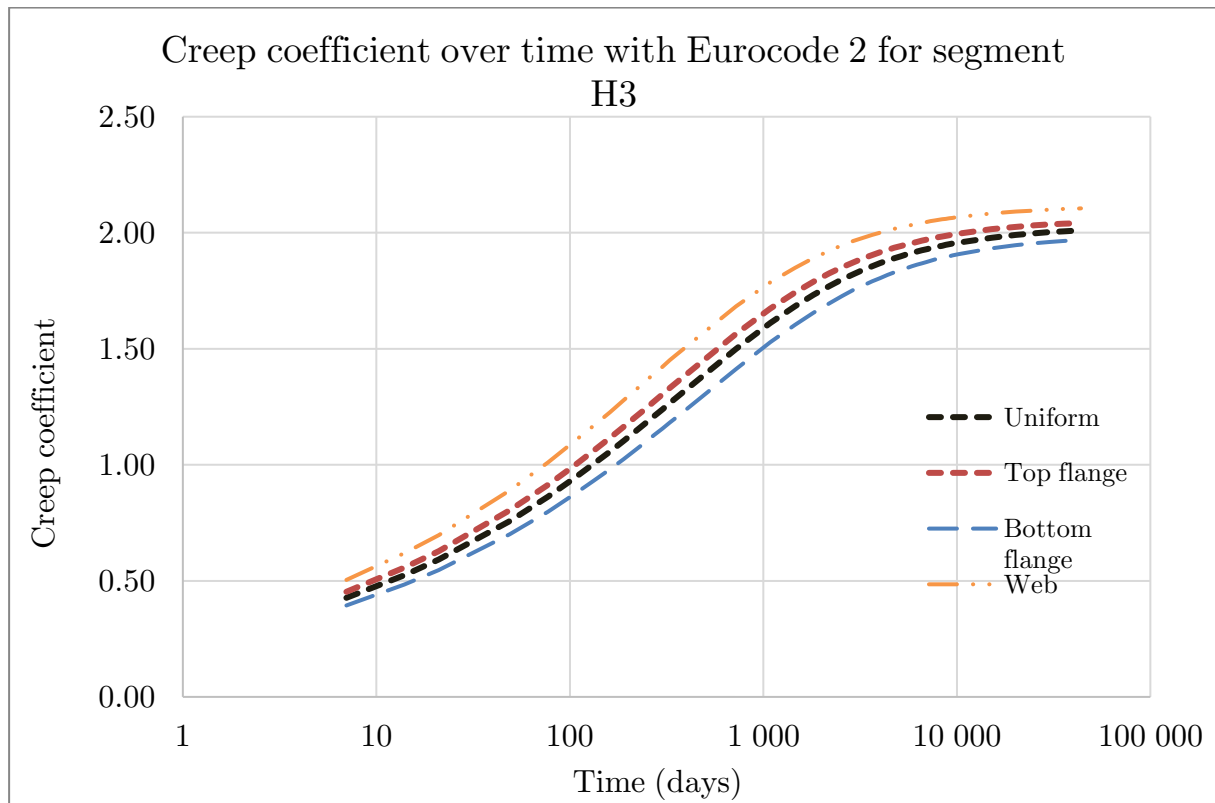


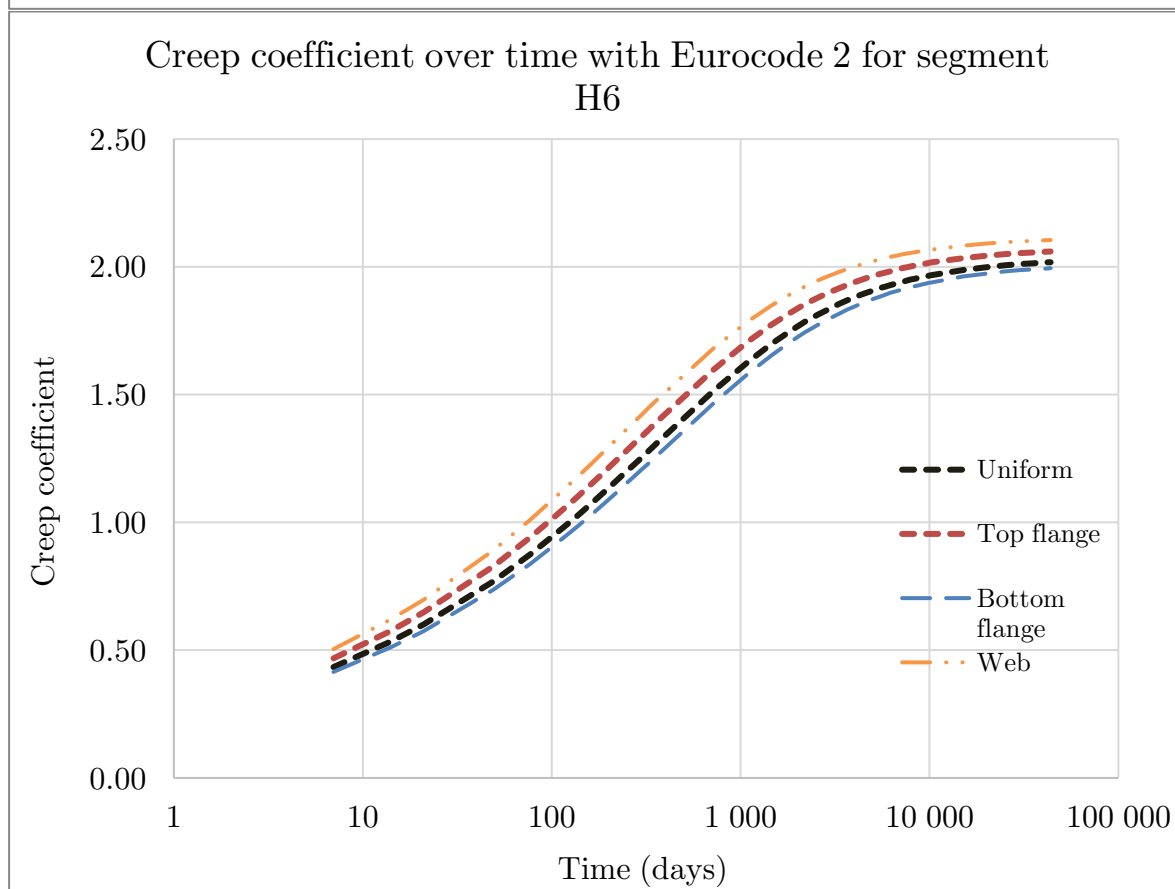
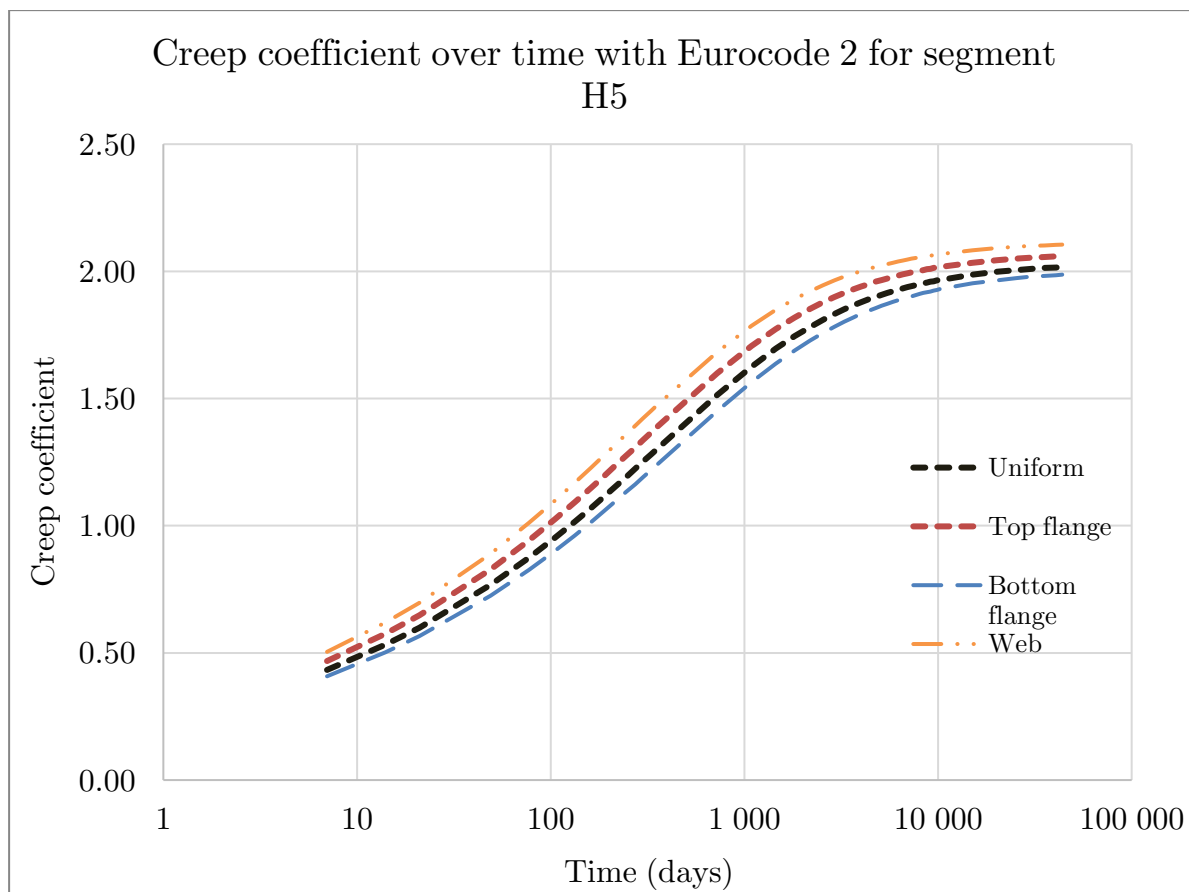


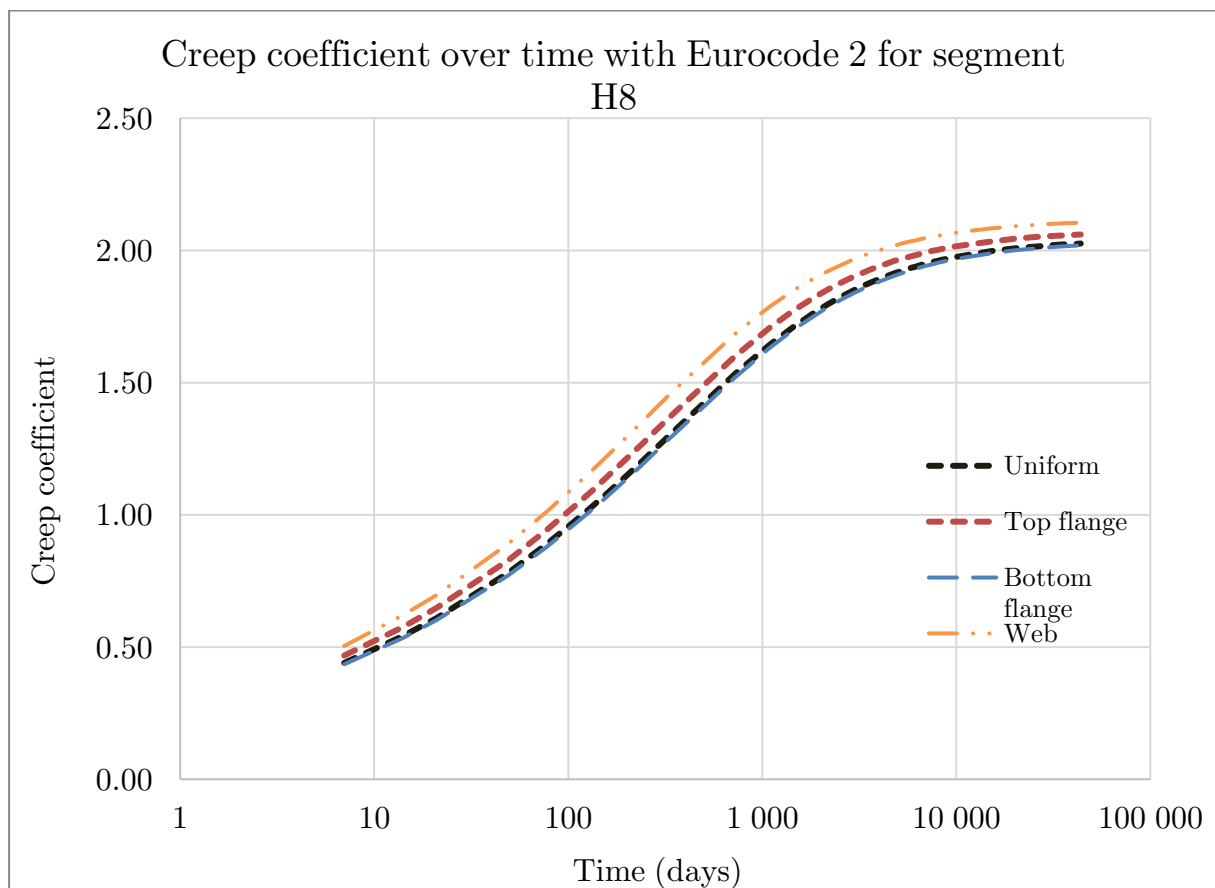
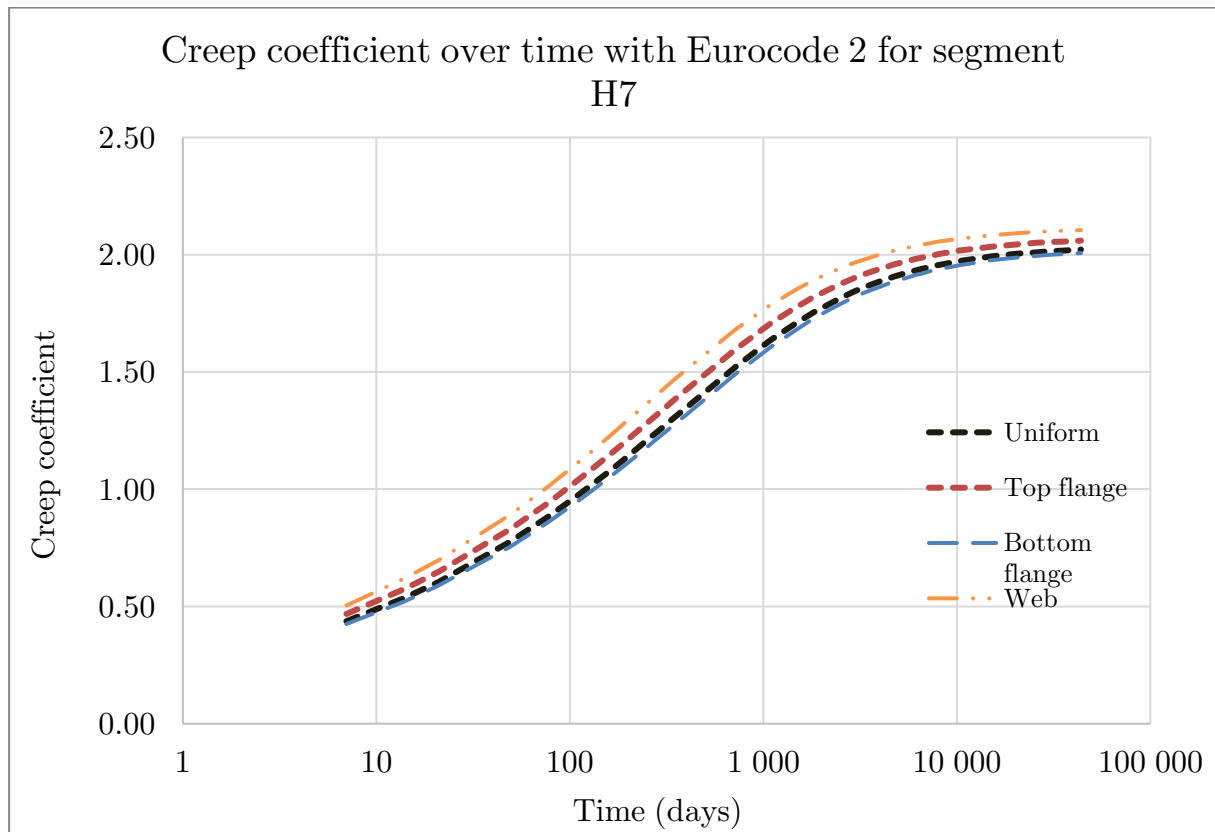


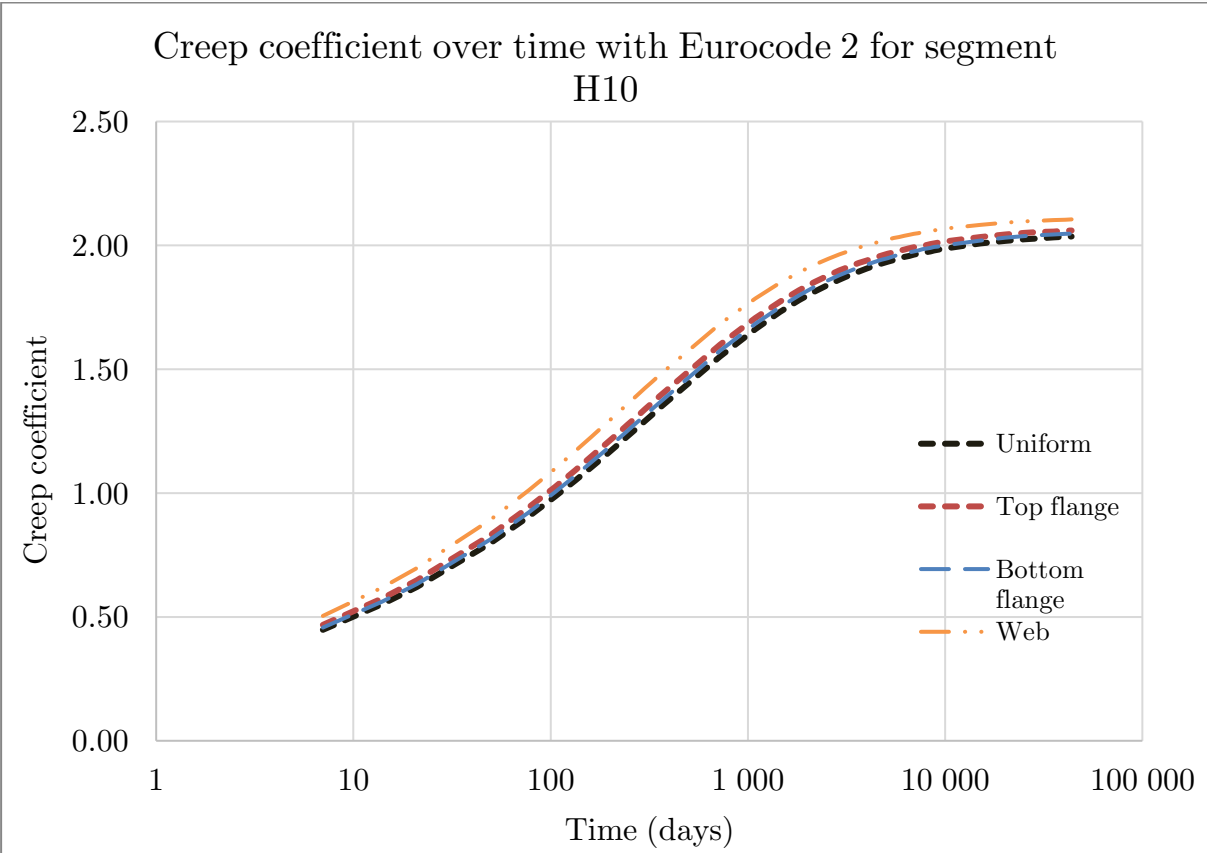
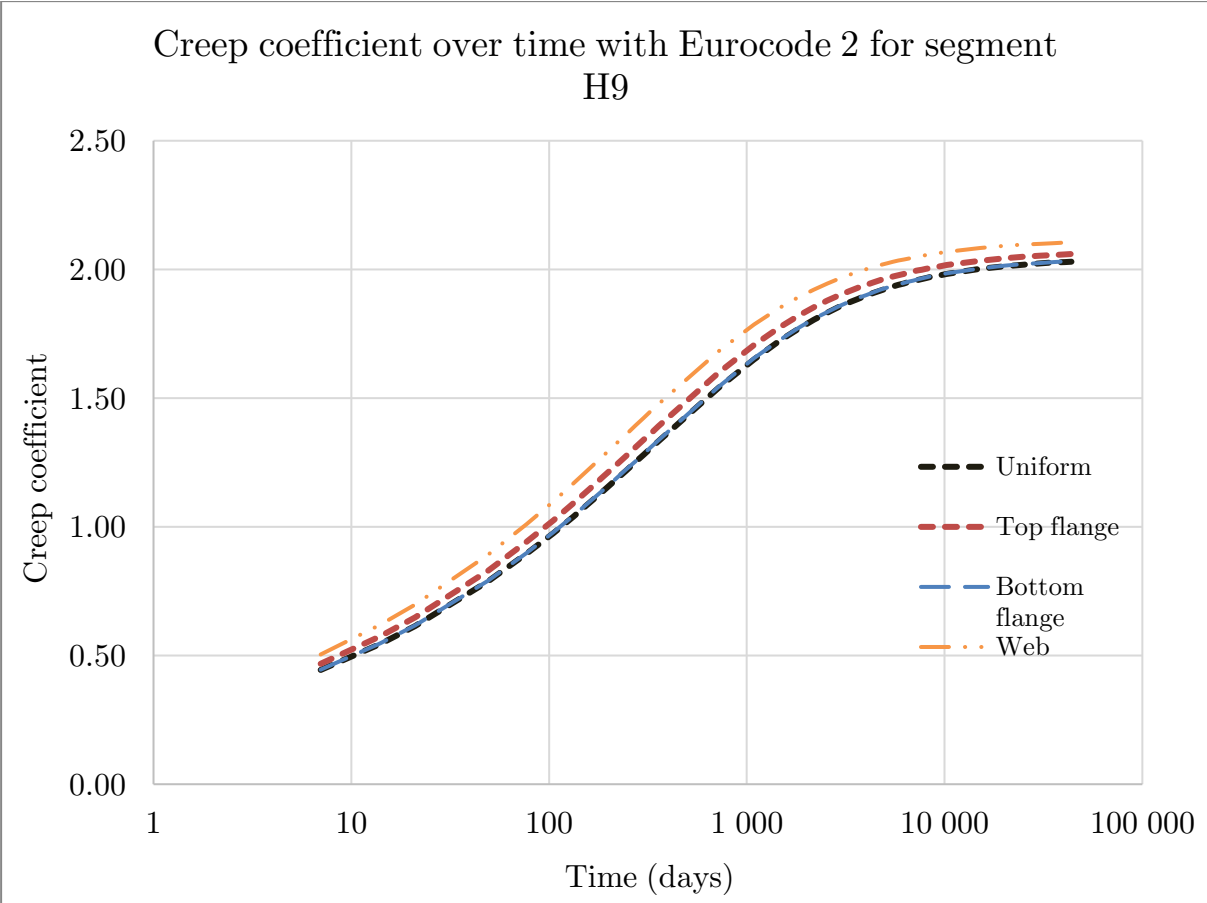


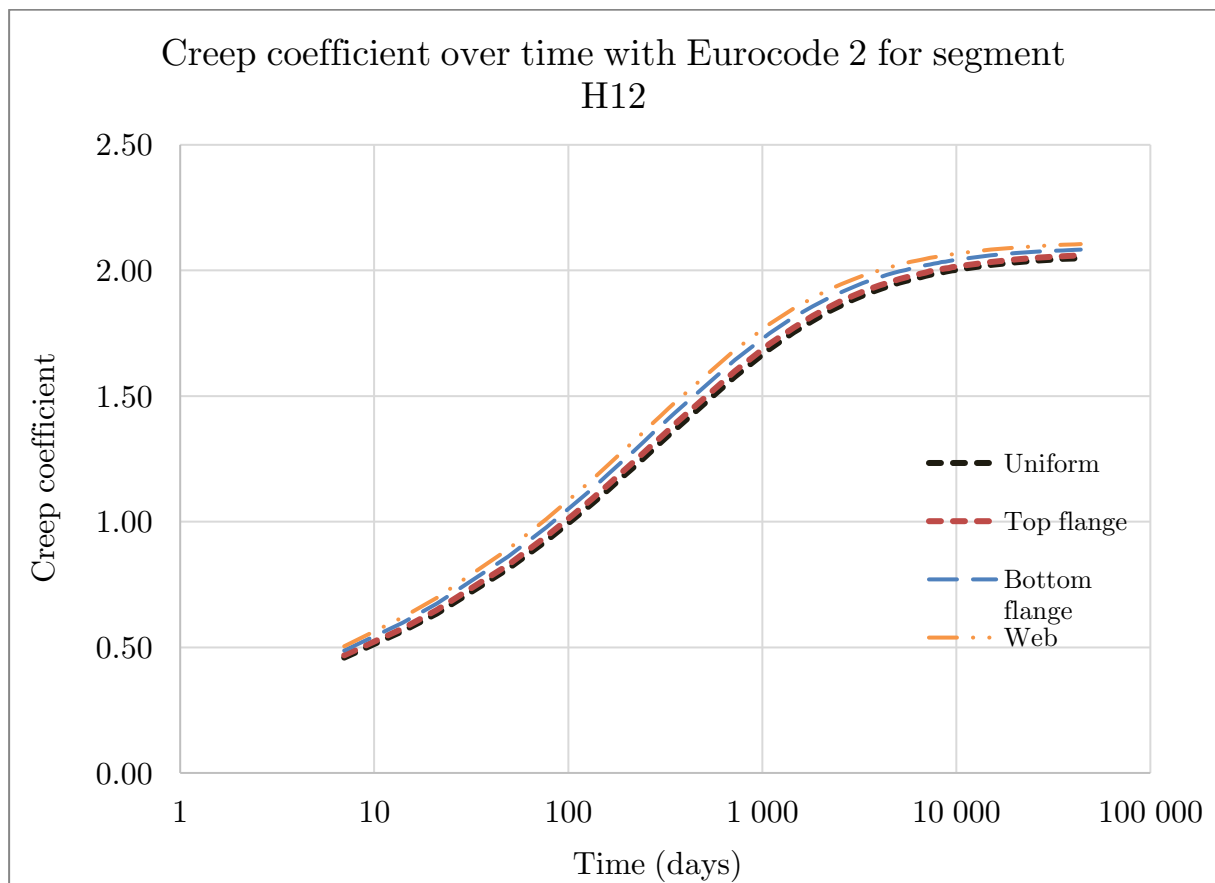
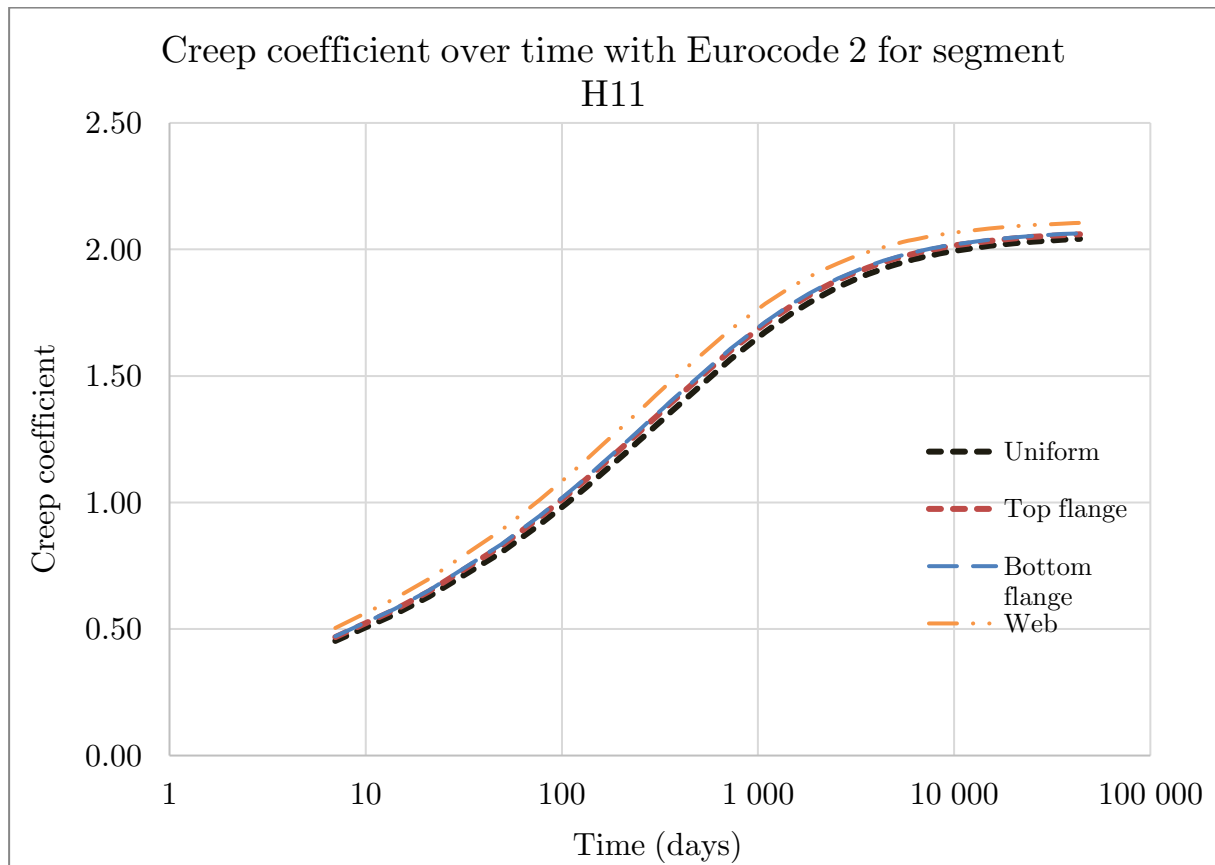


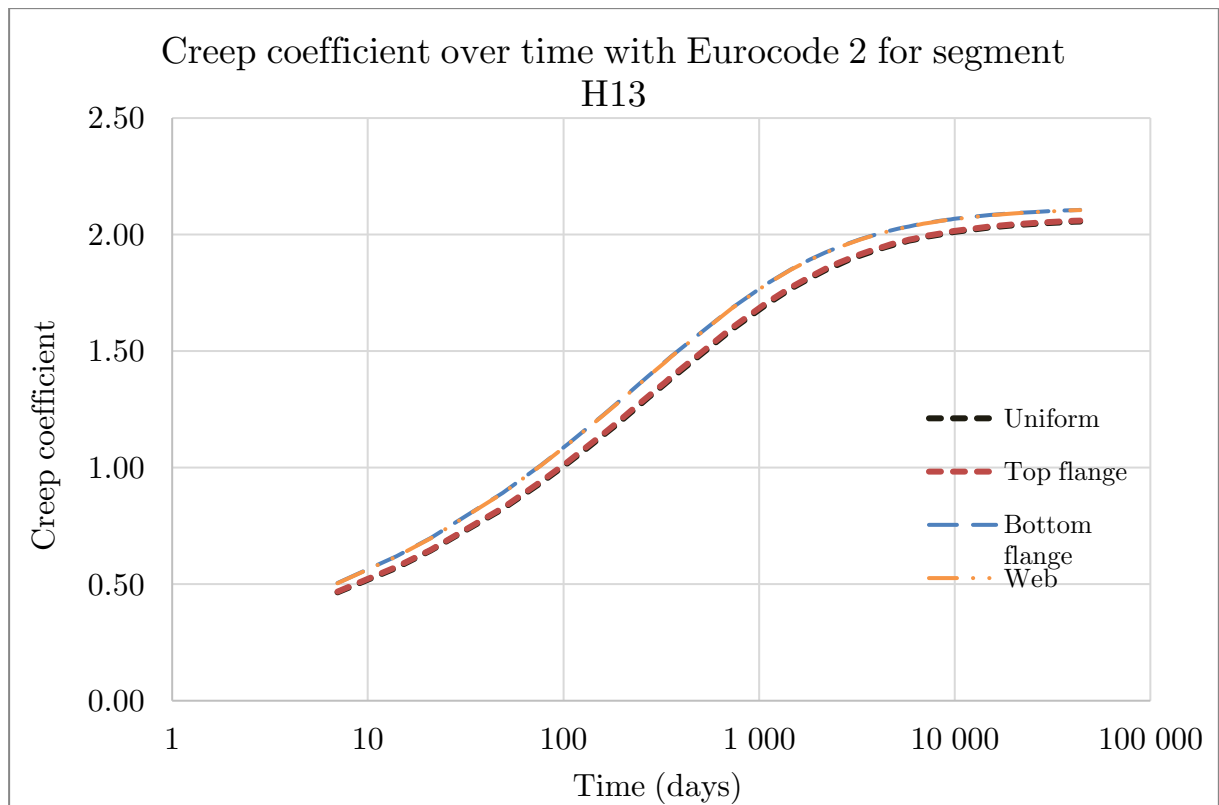




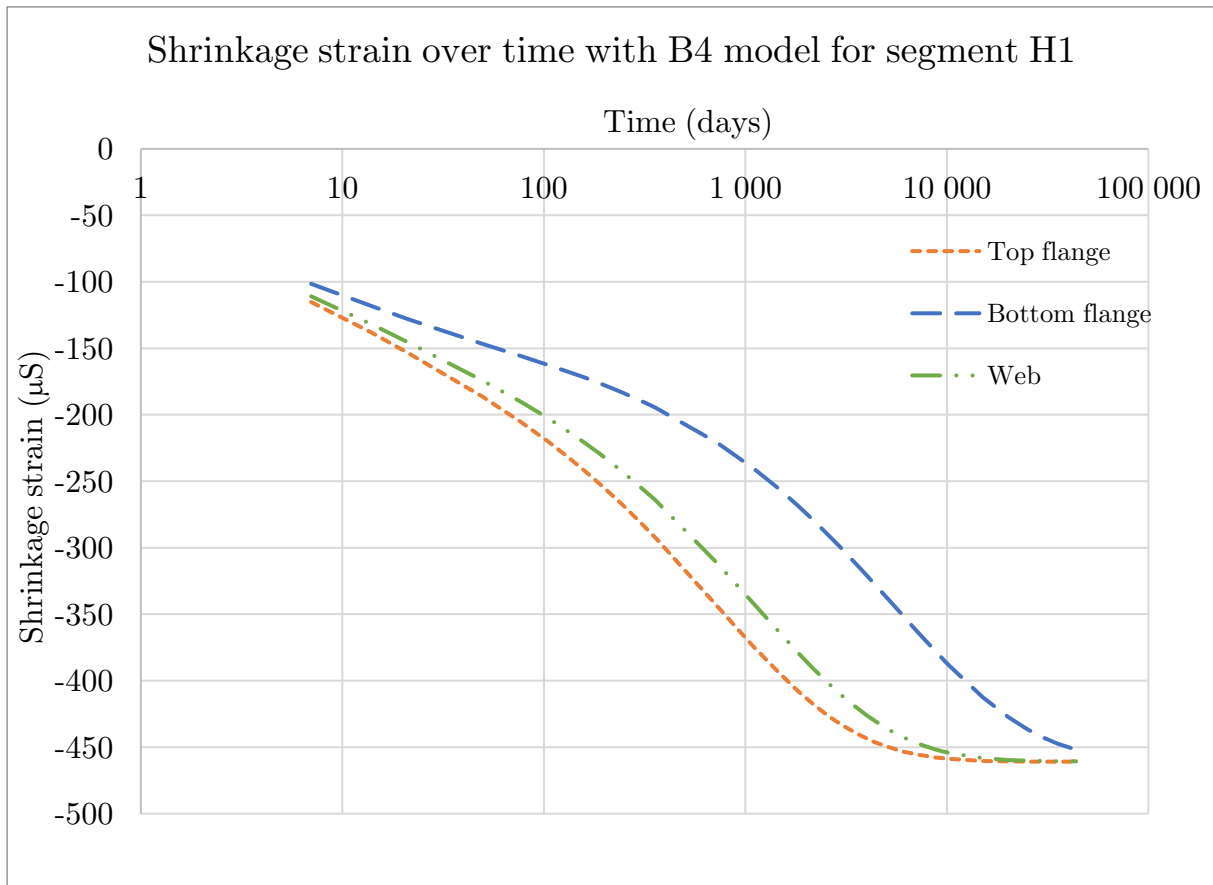
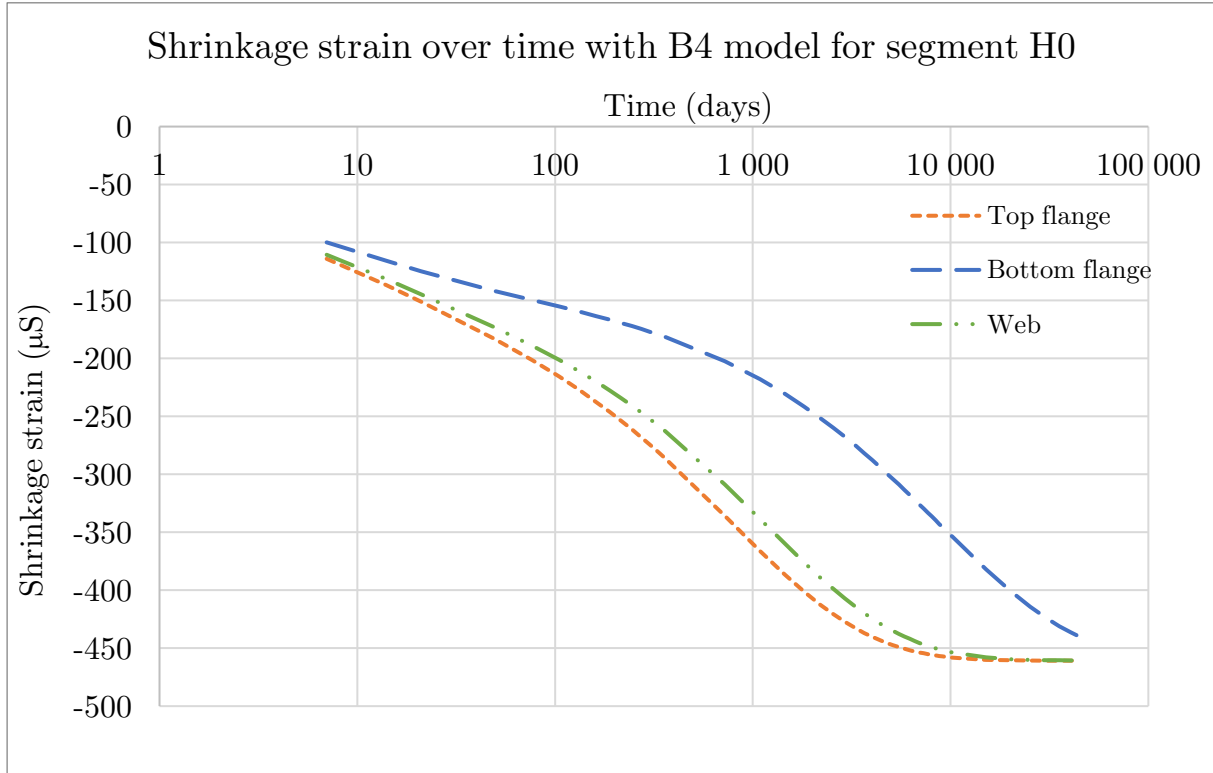


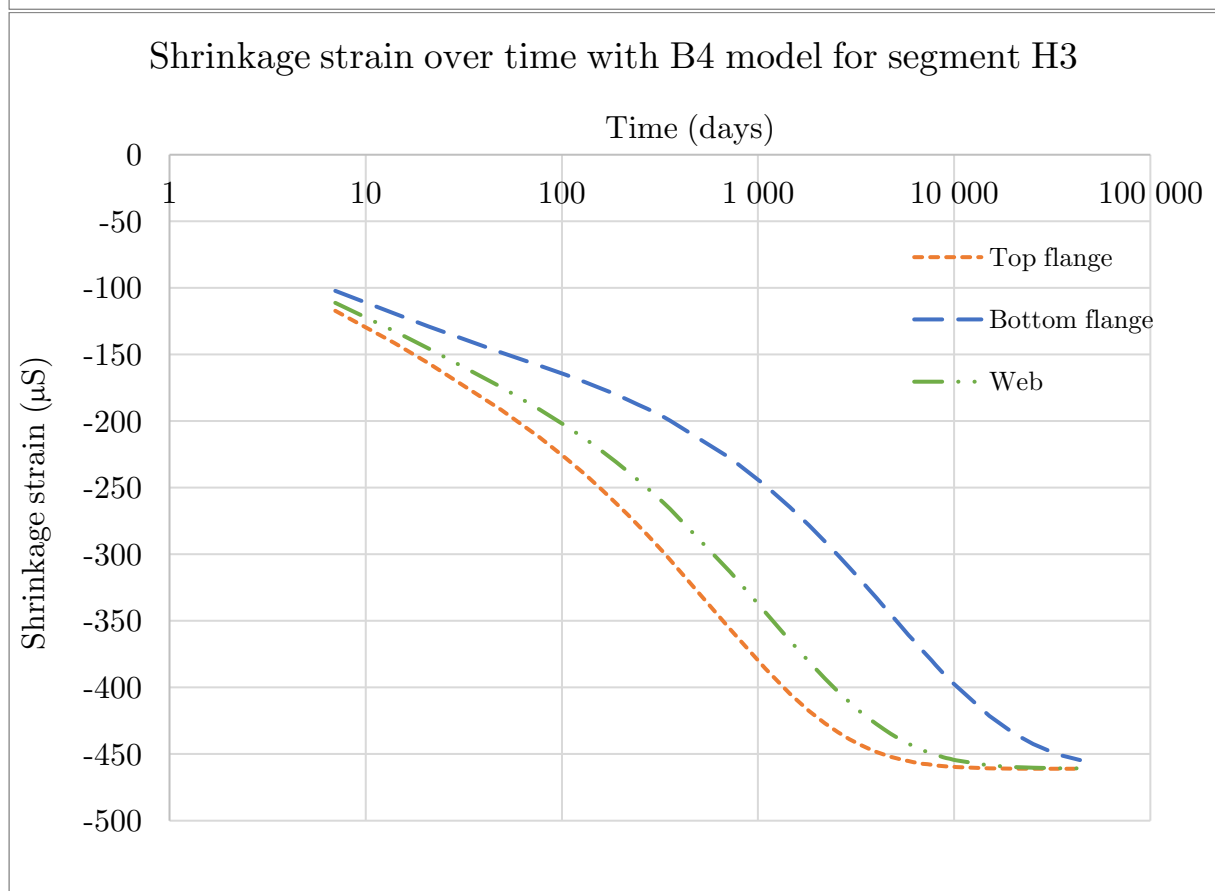
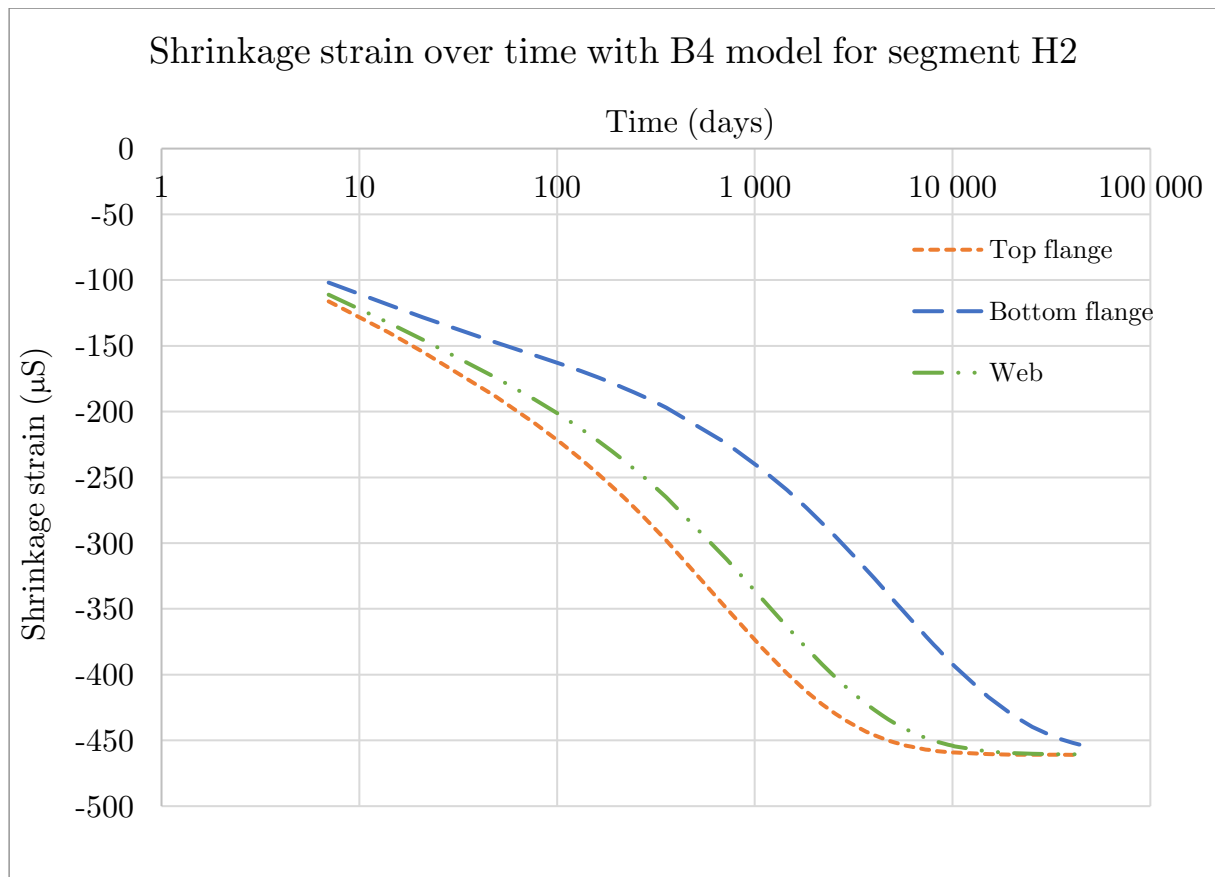


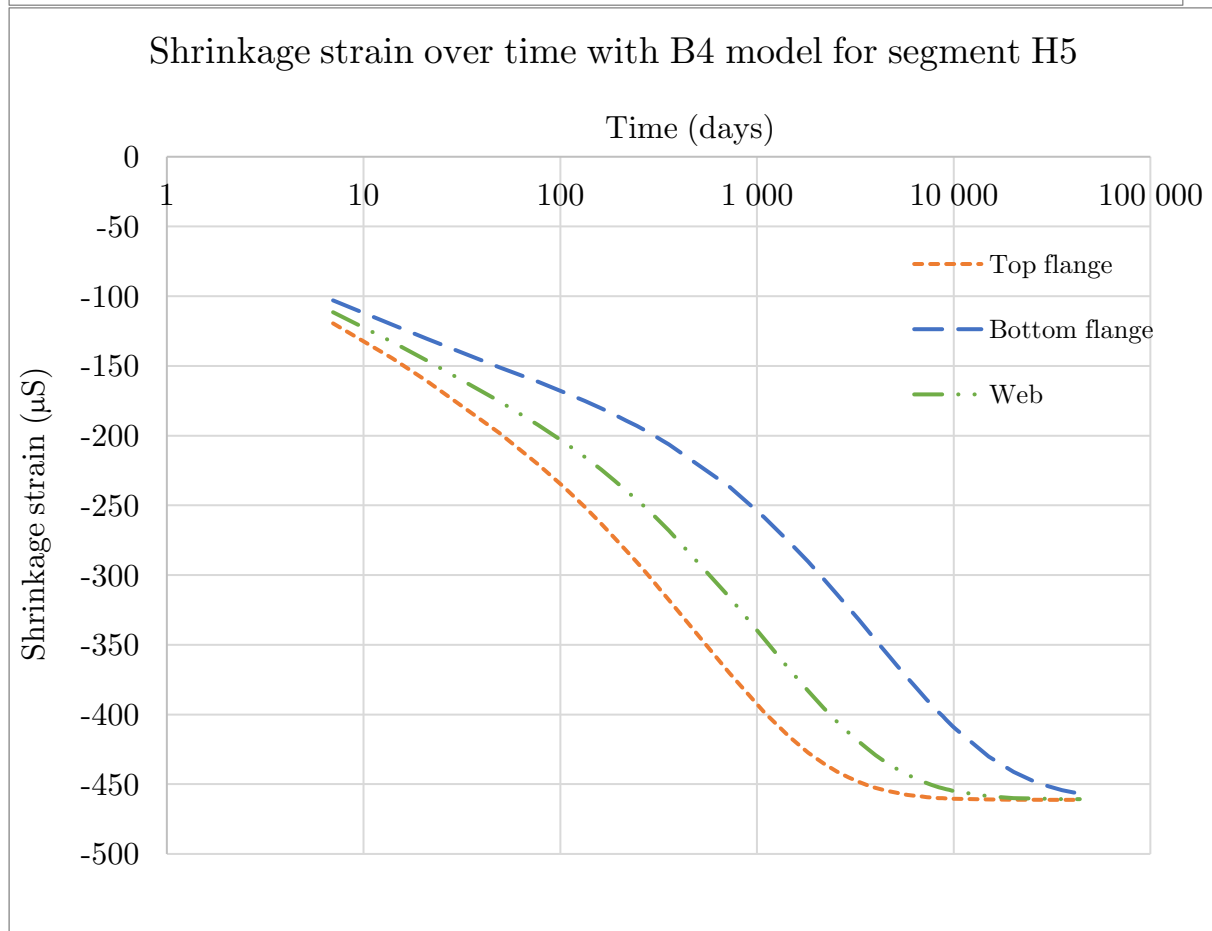
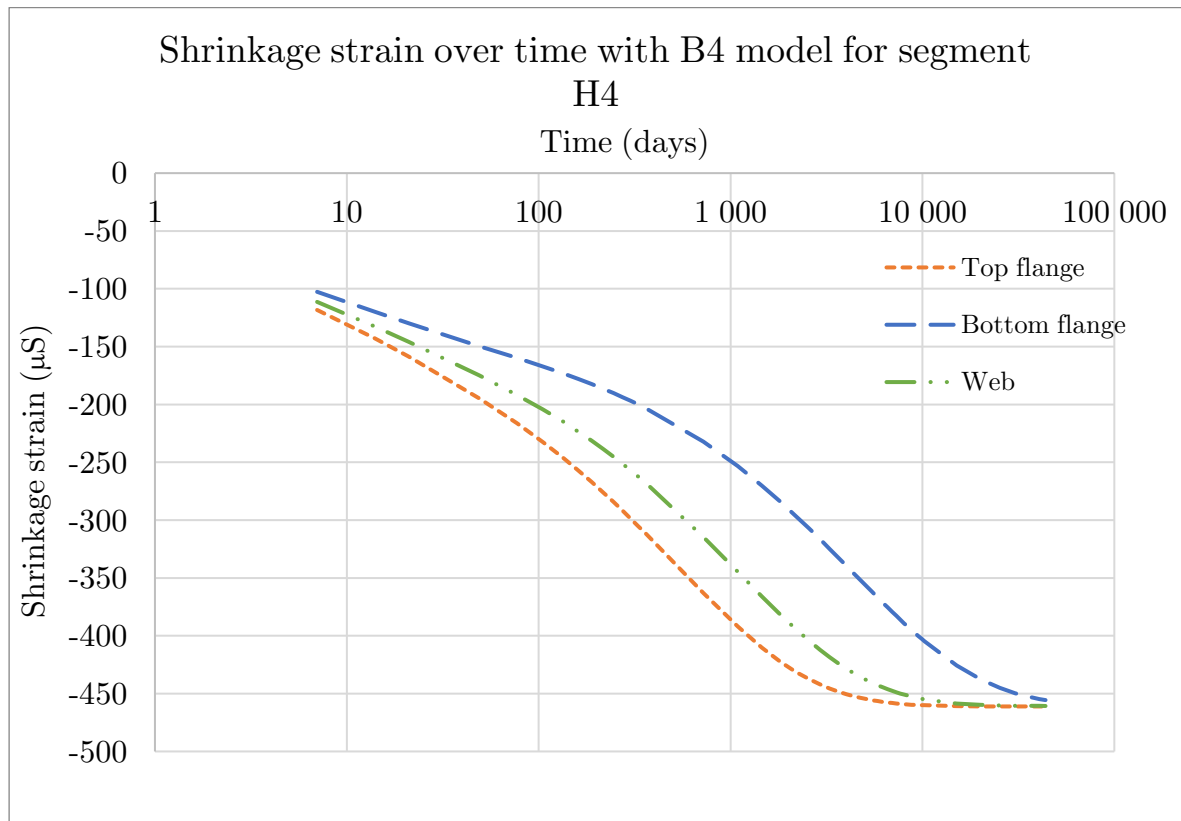


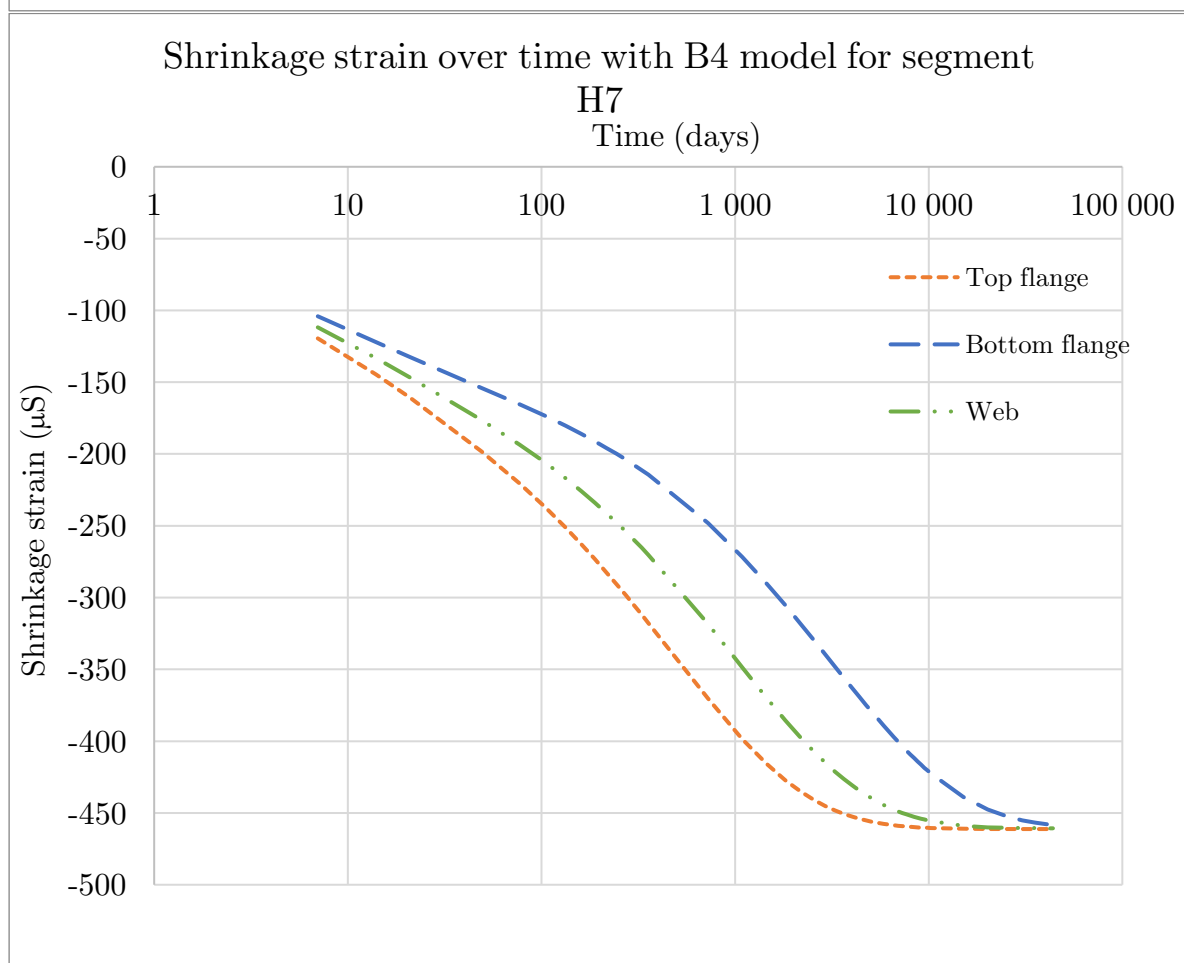
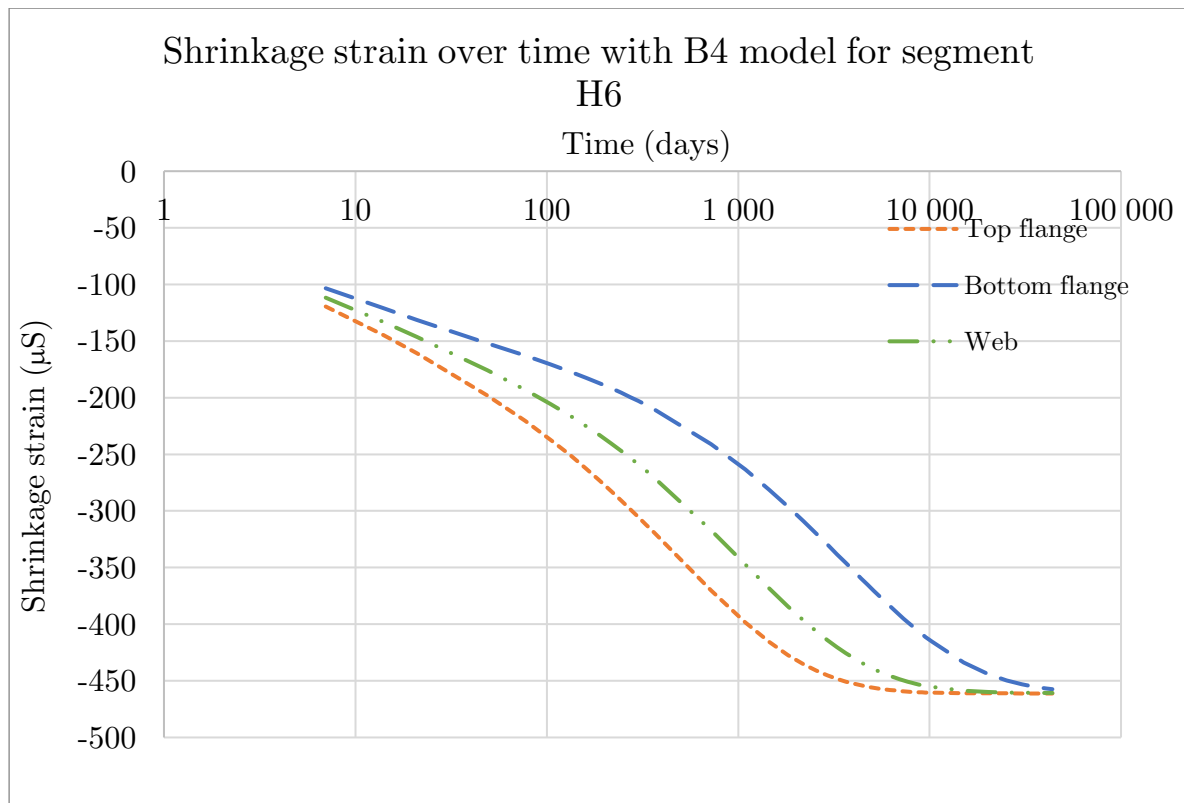


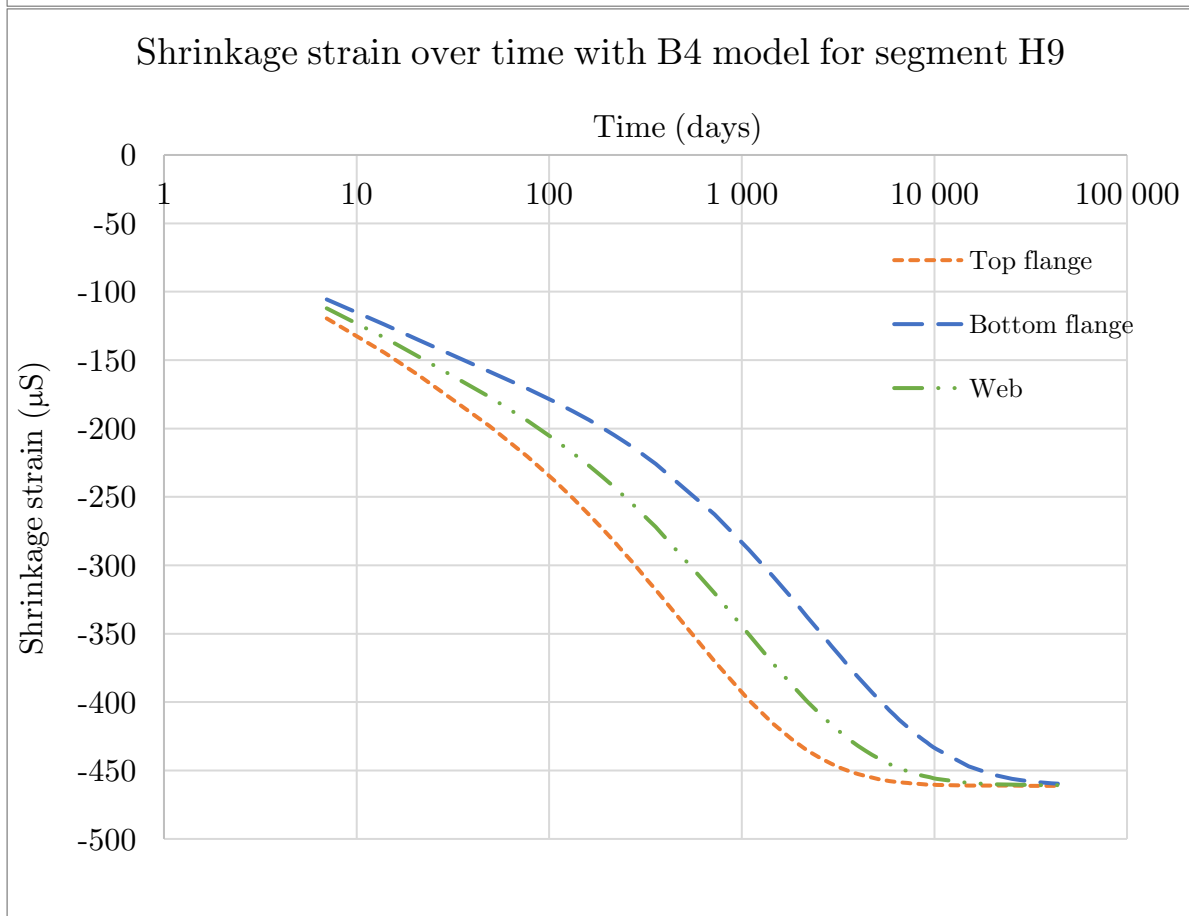
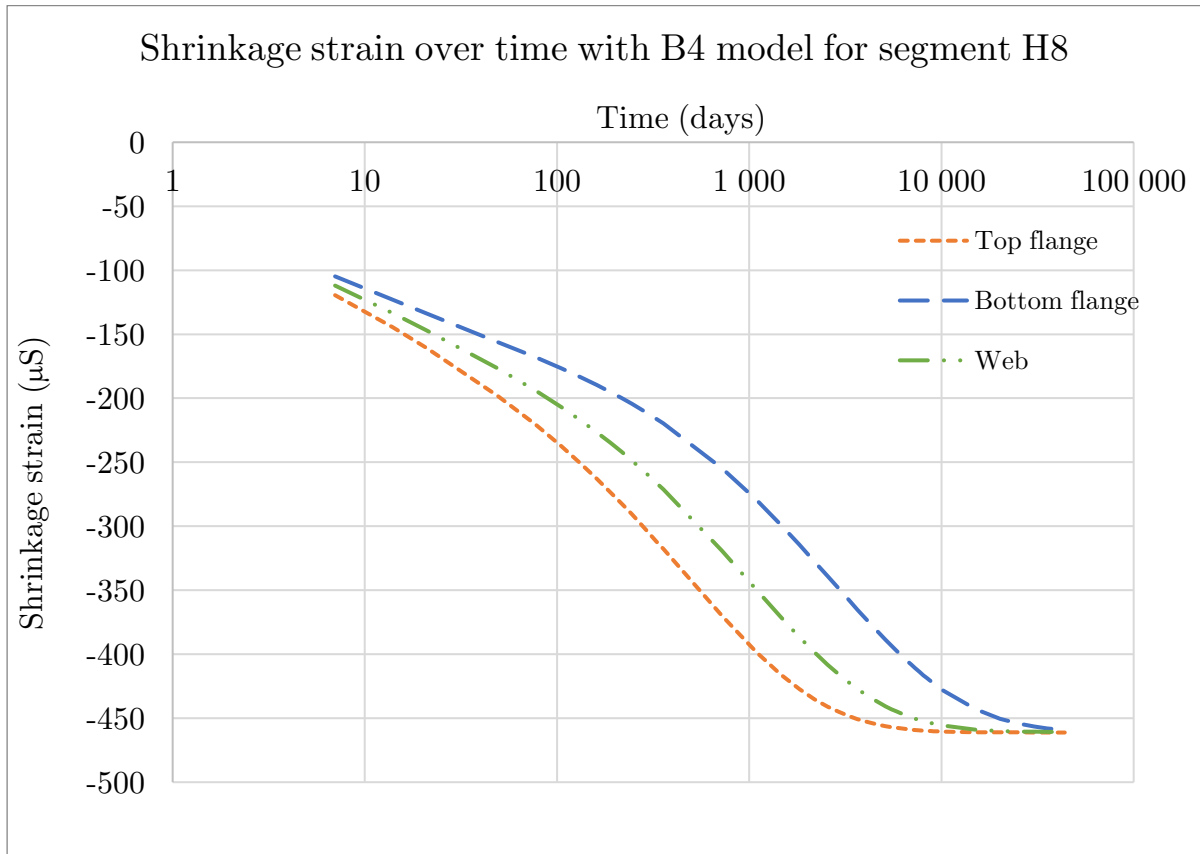
A.2 Shrinkage strain variation for each segment

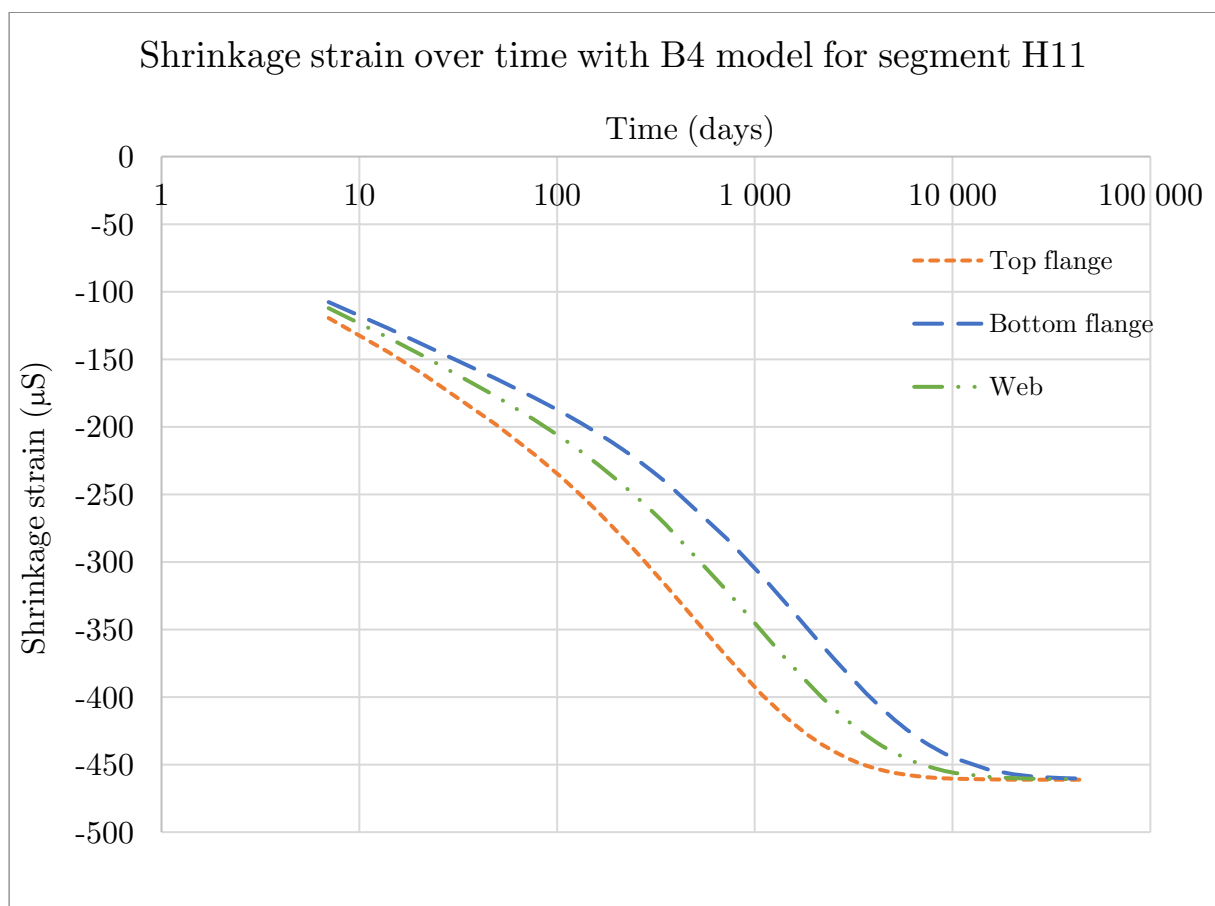
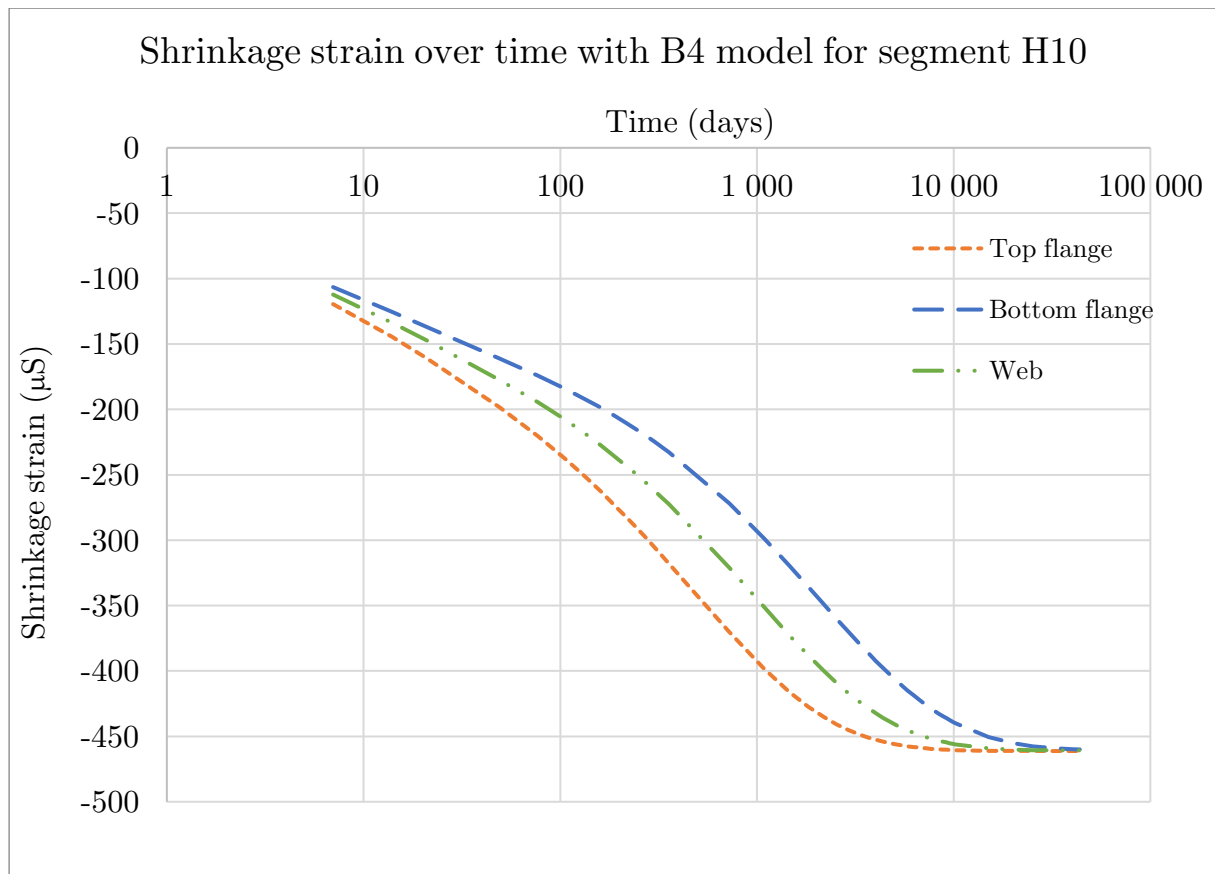


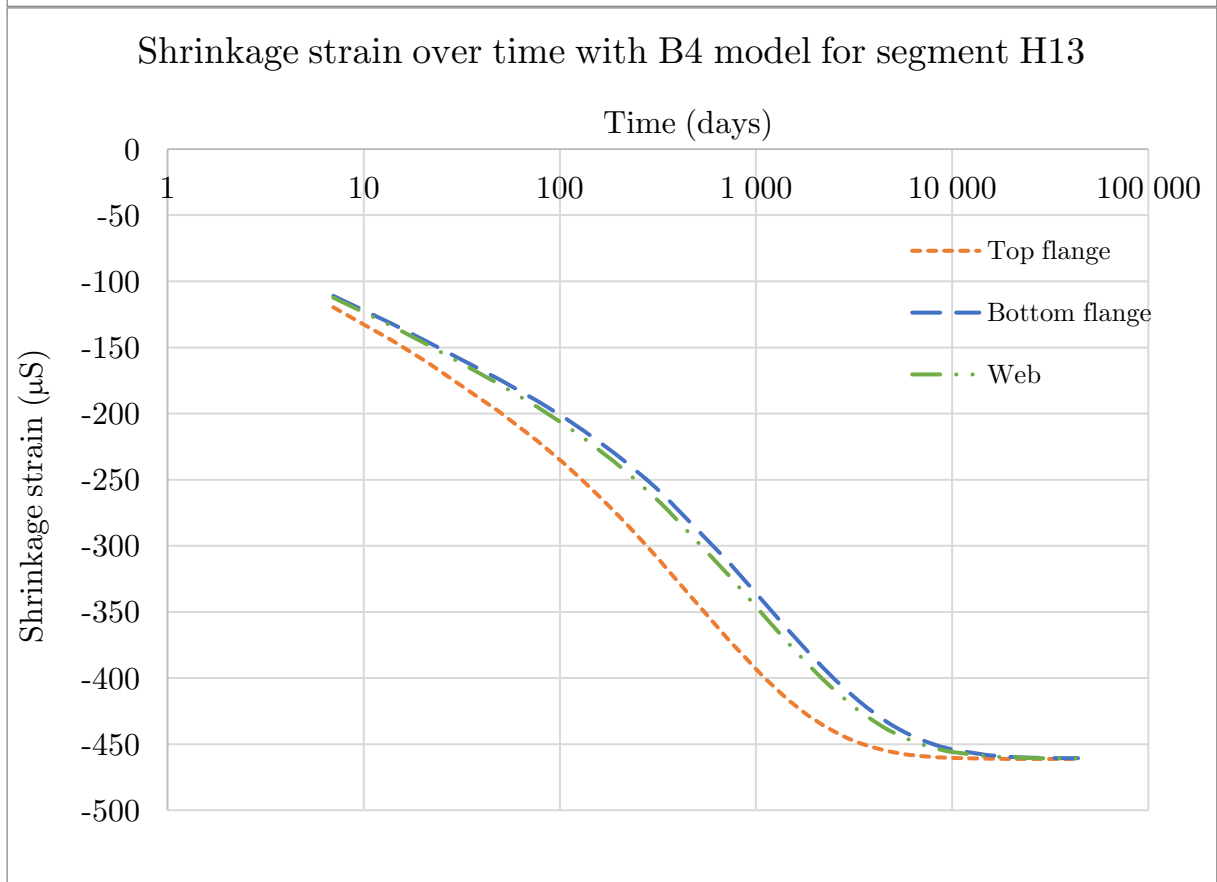
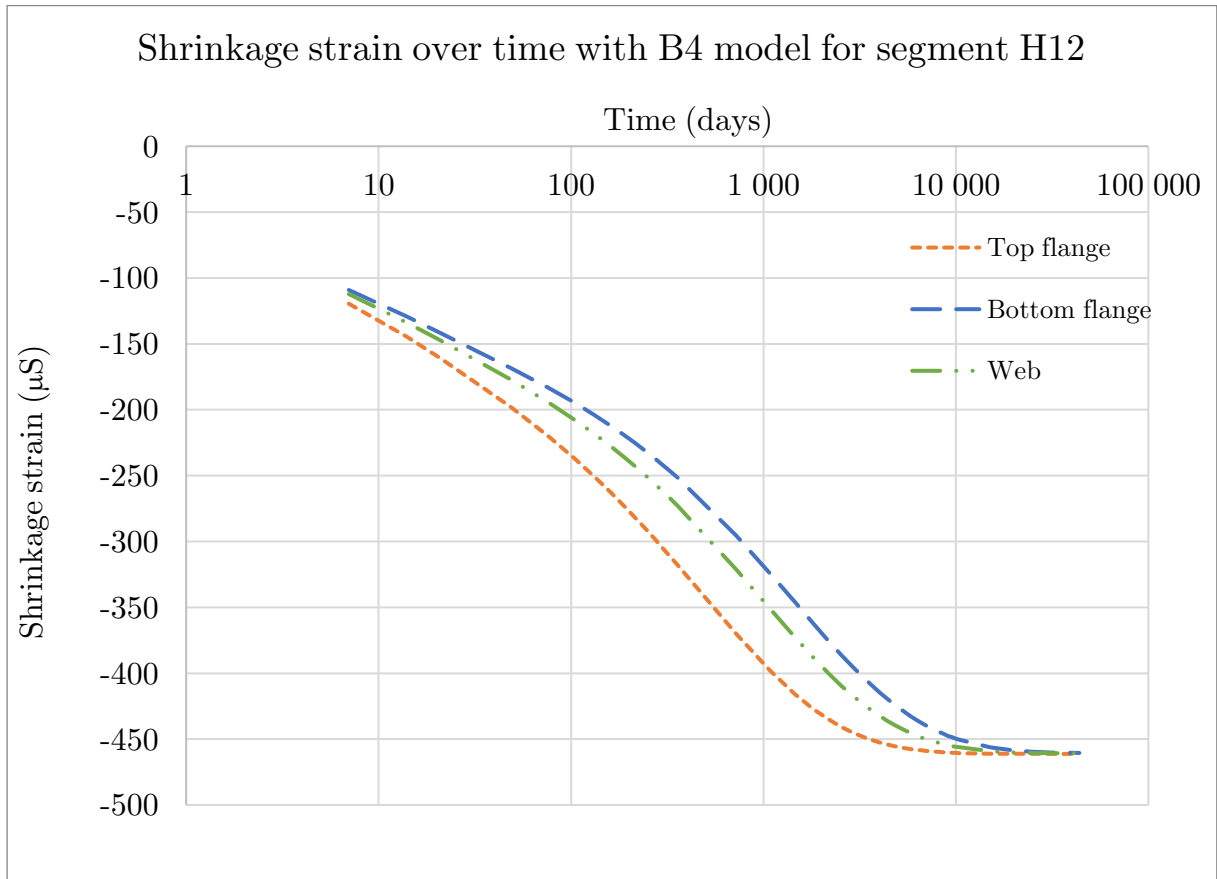


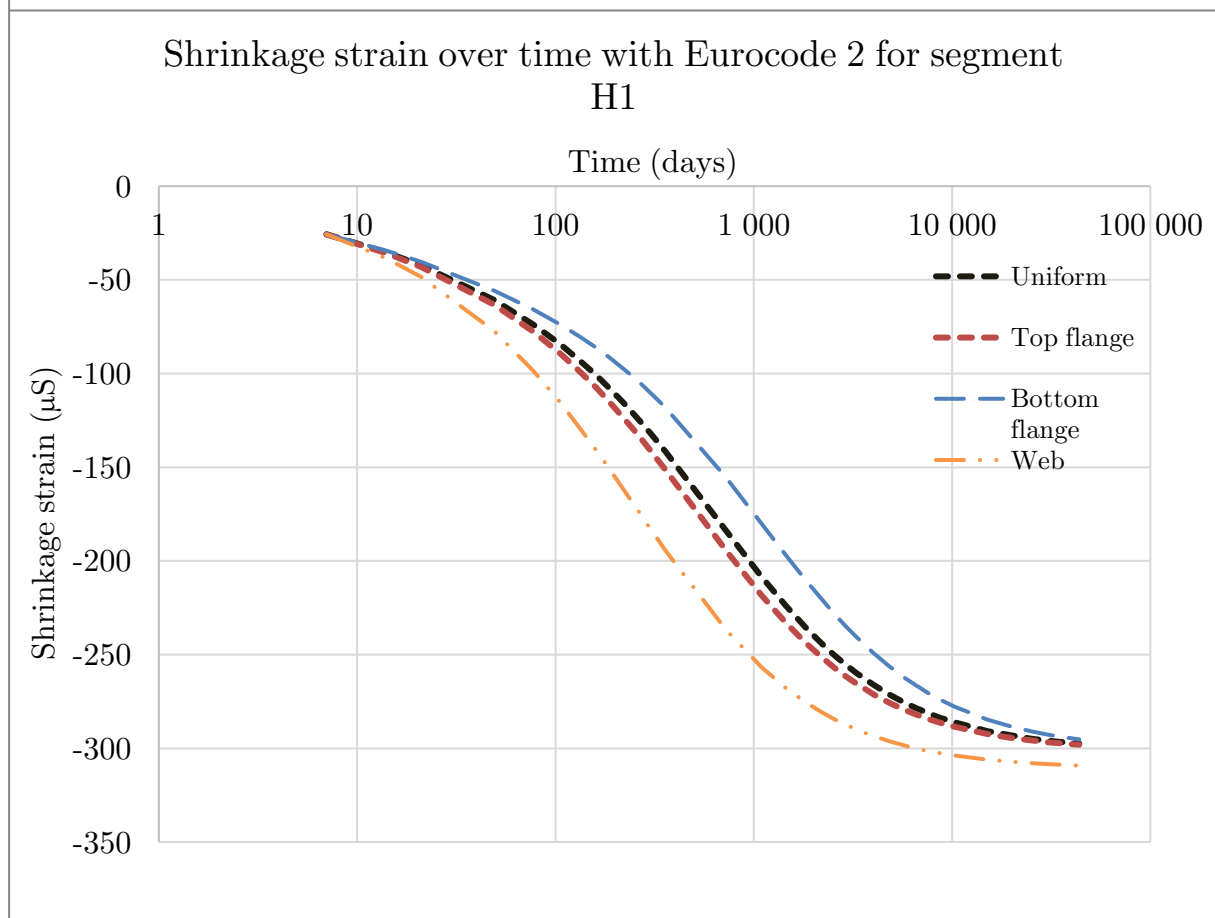
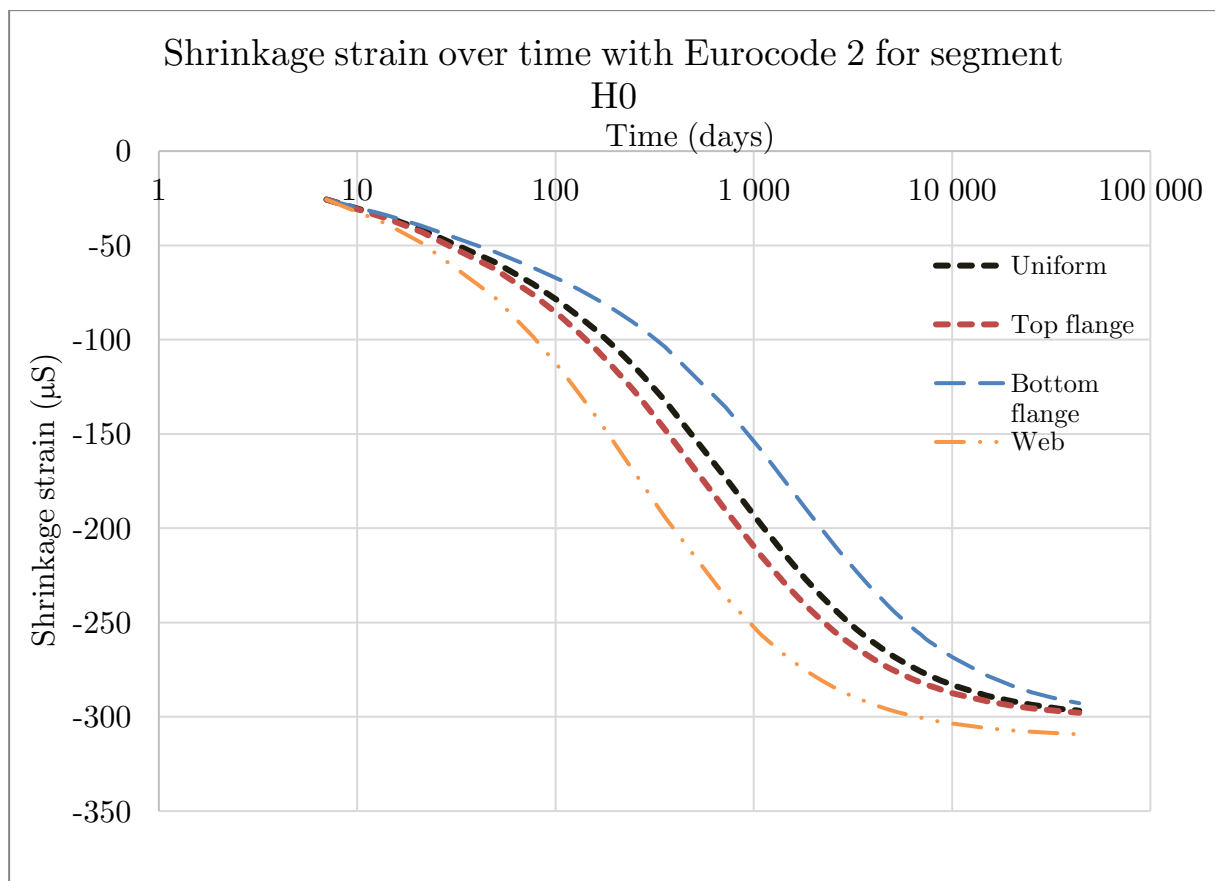


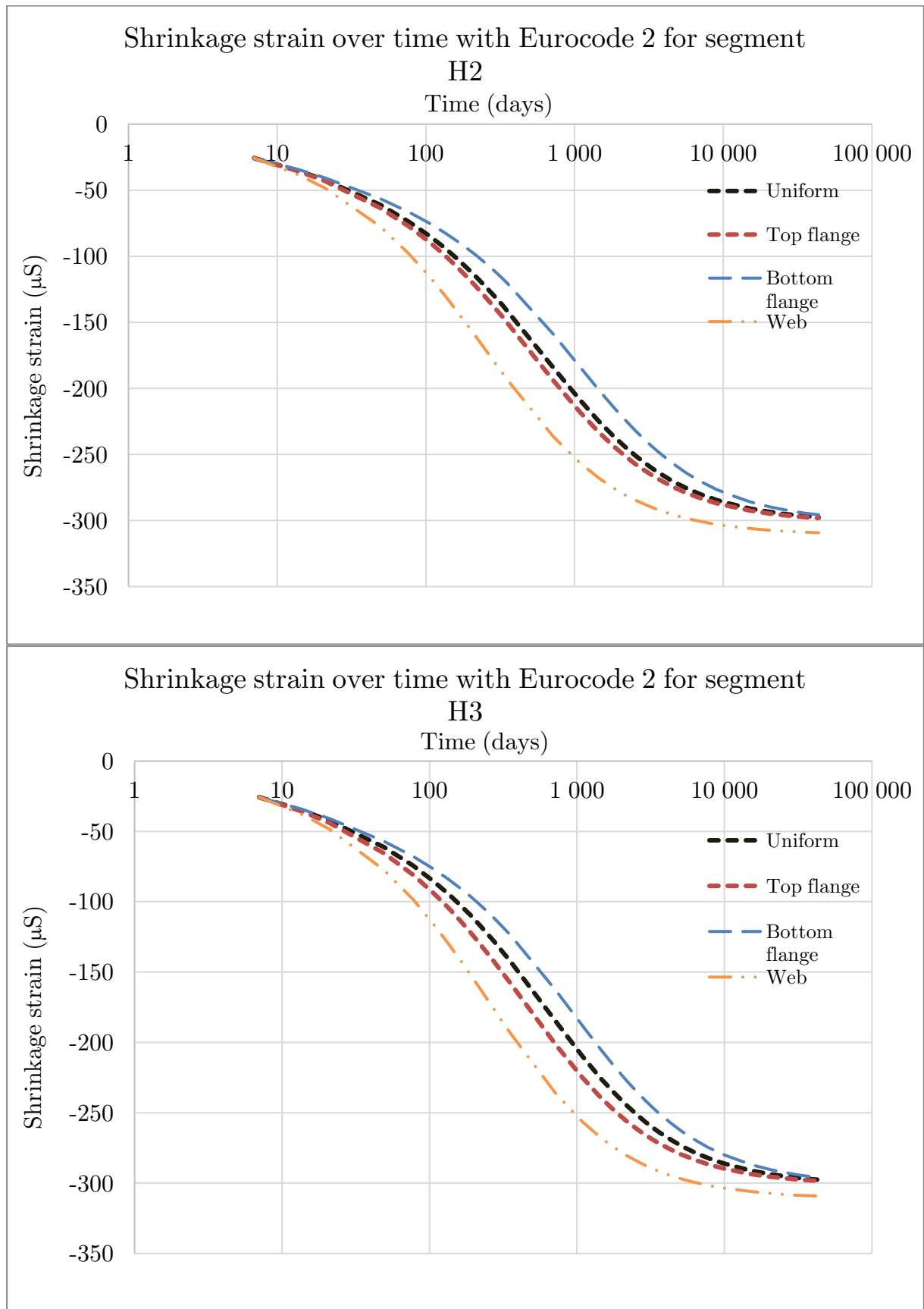


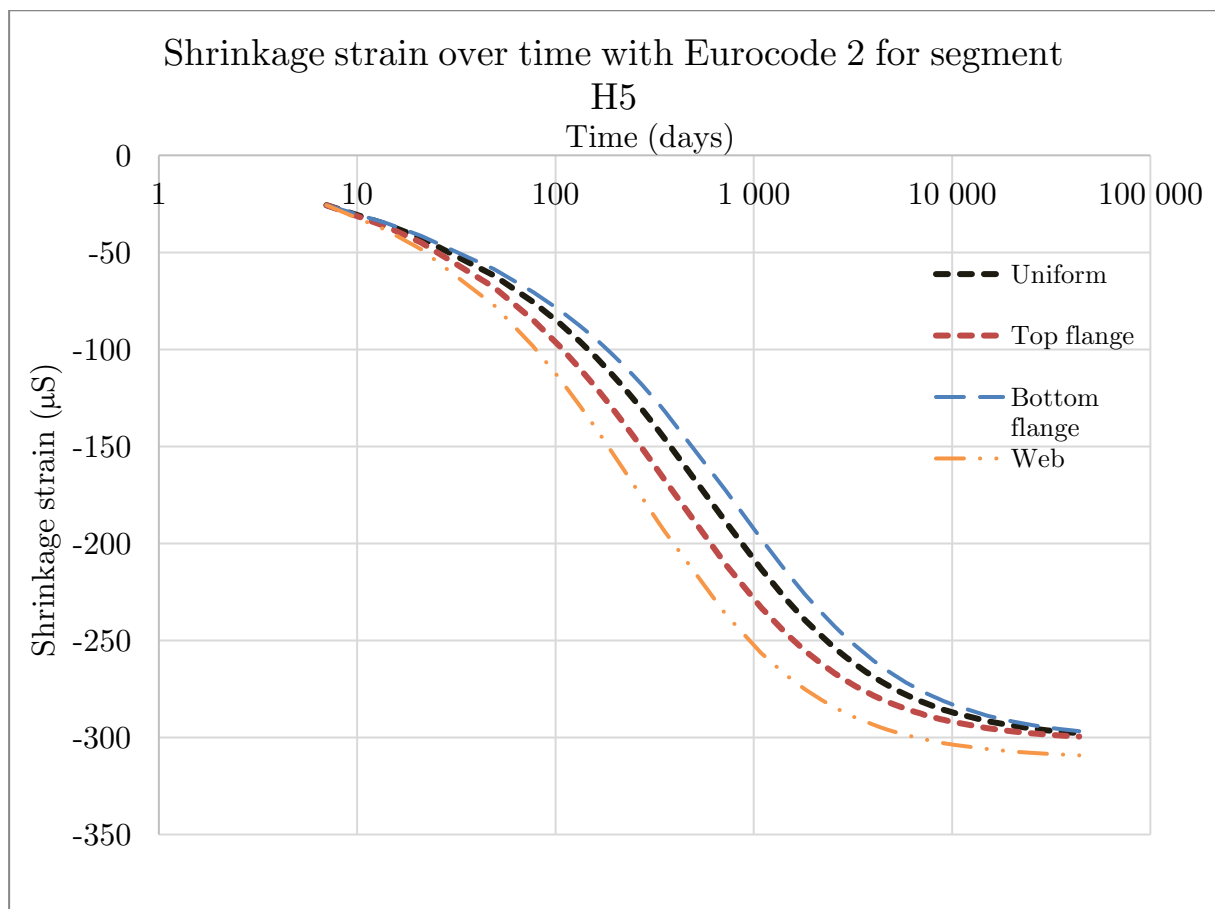
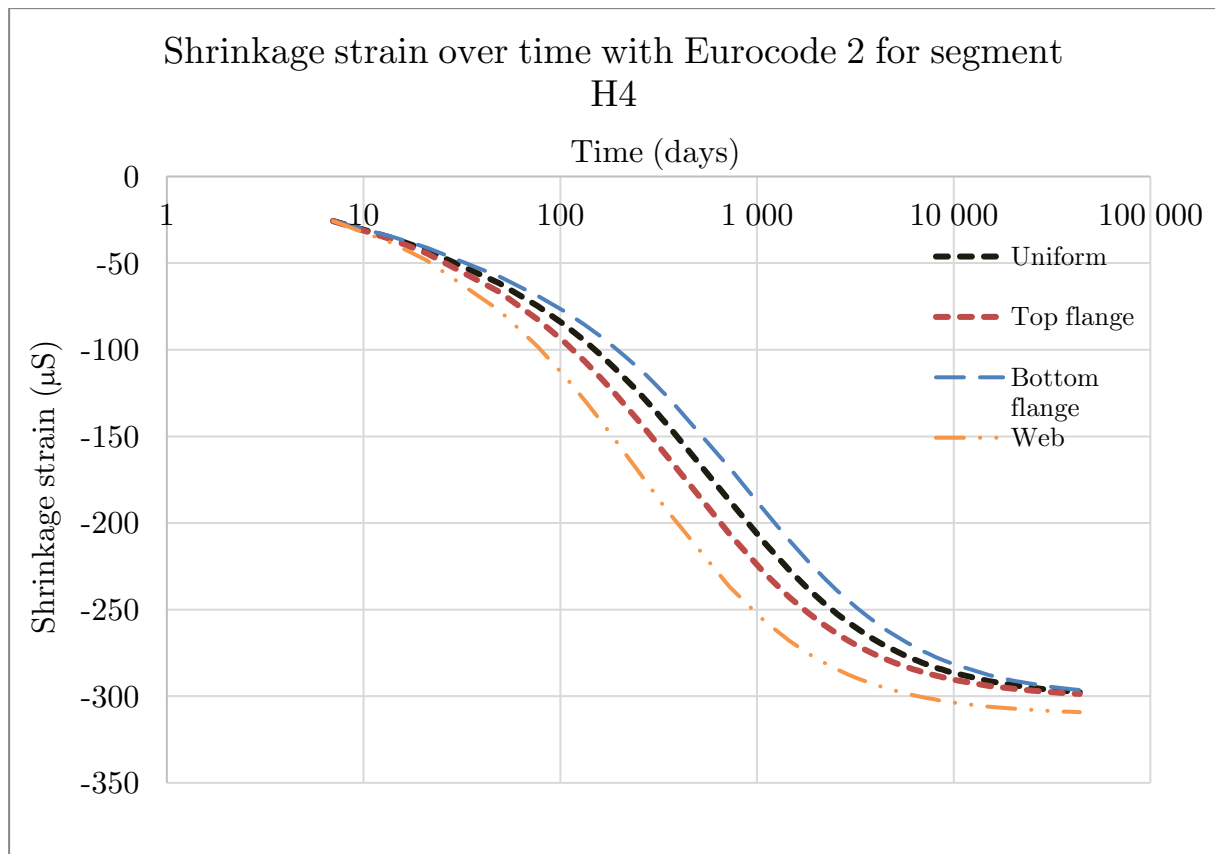


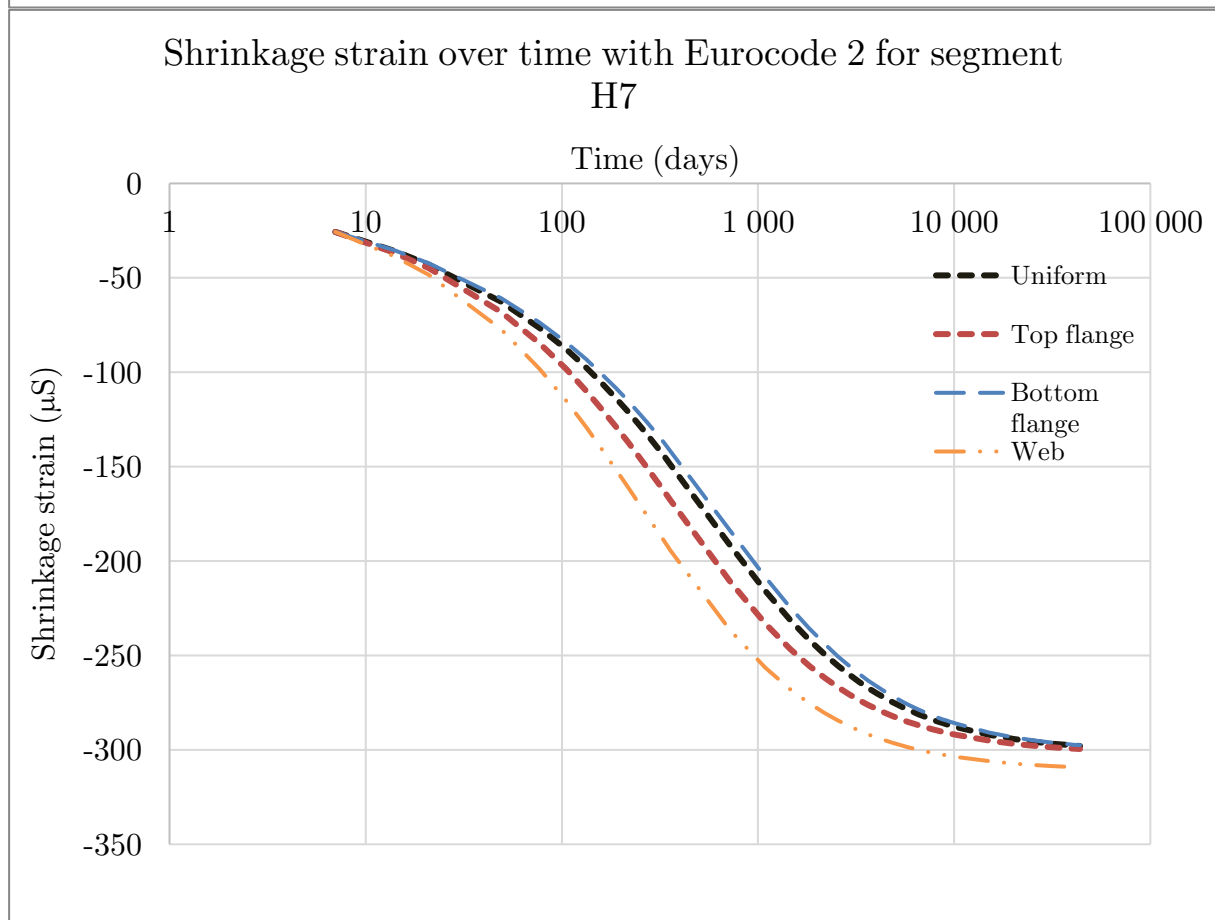
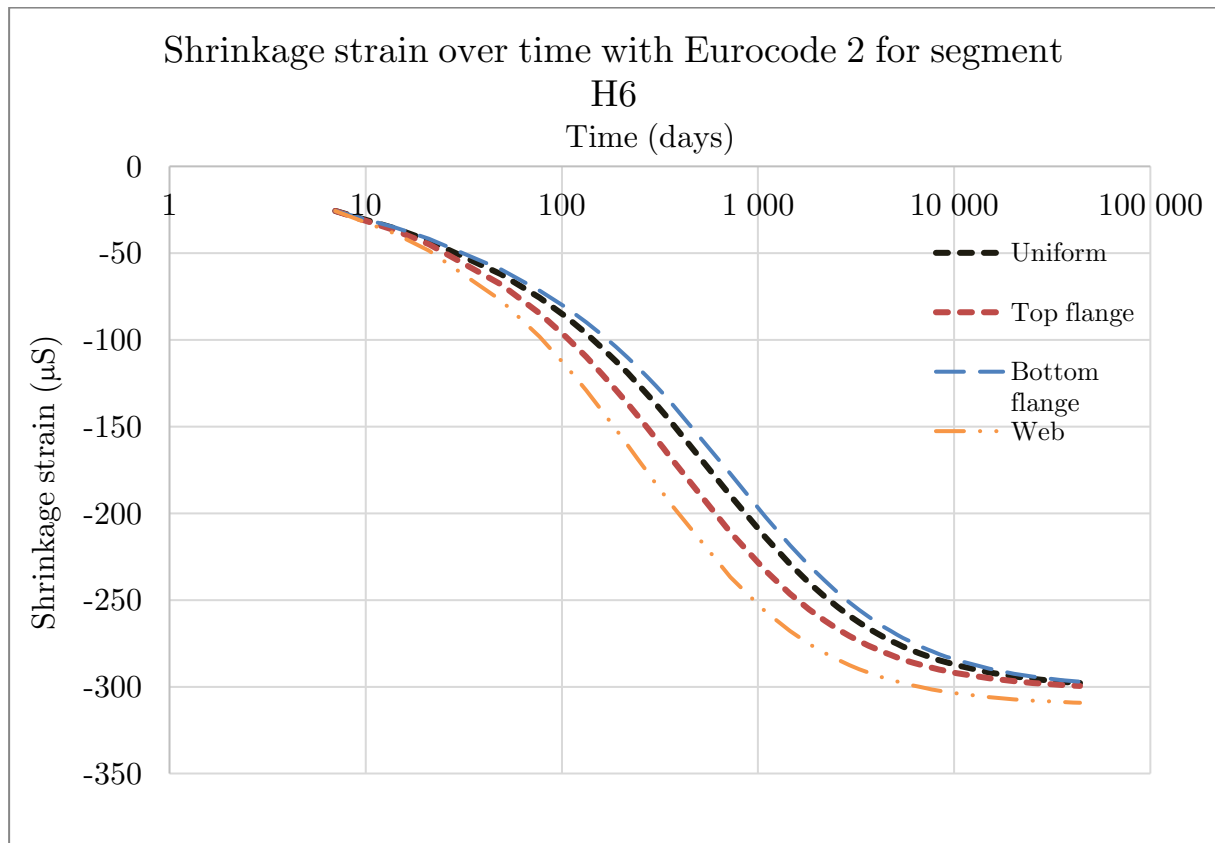


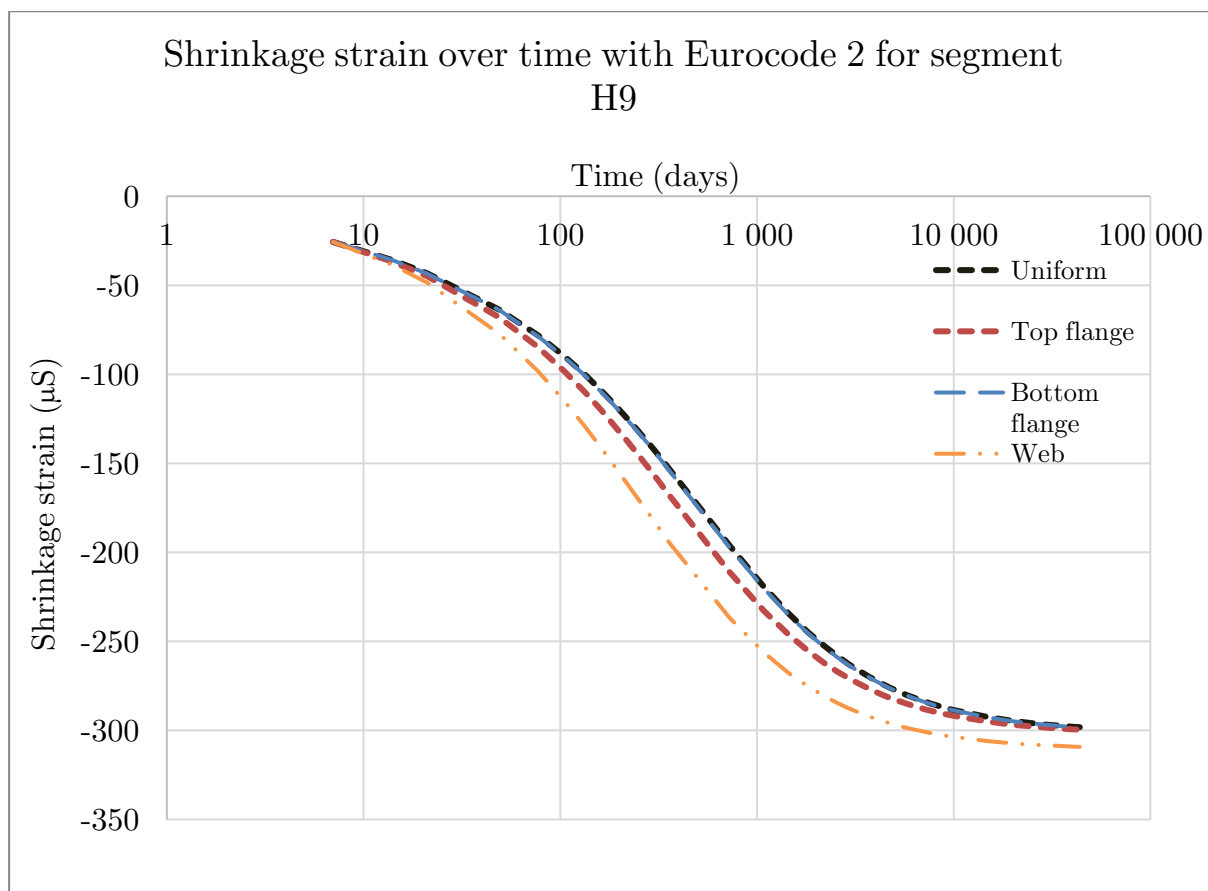
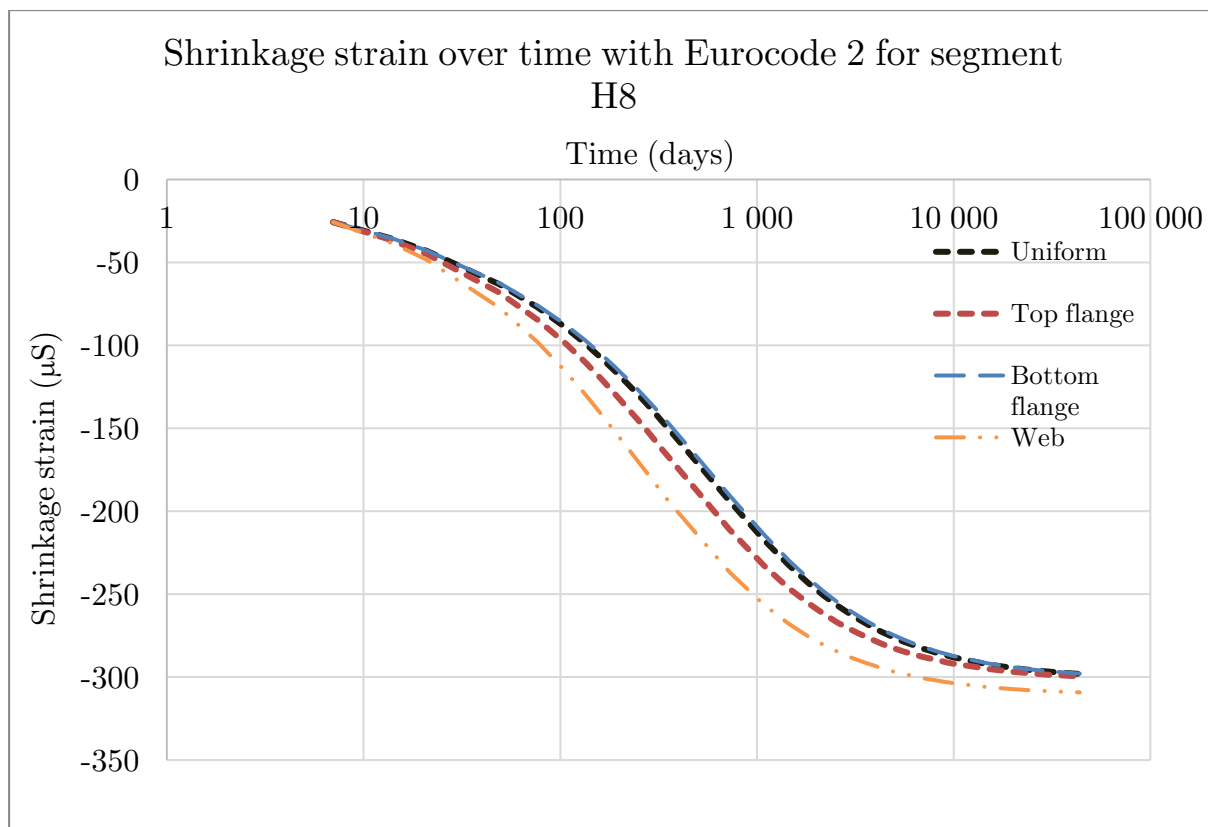


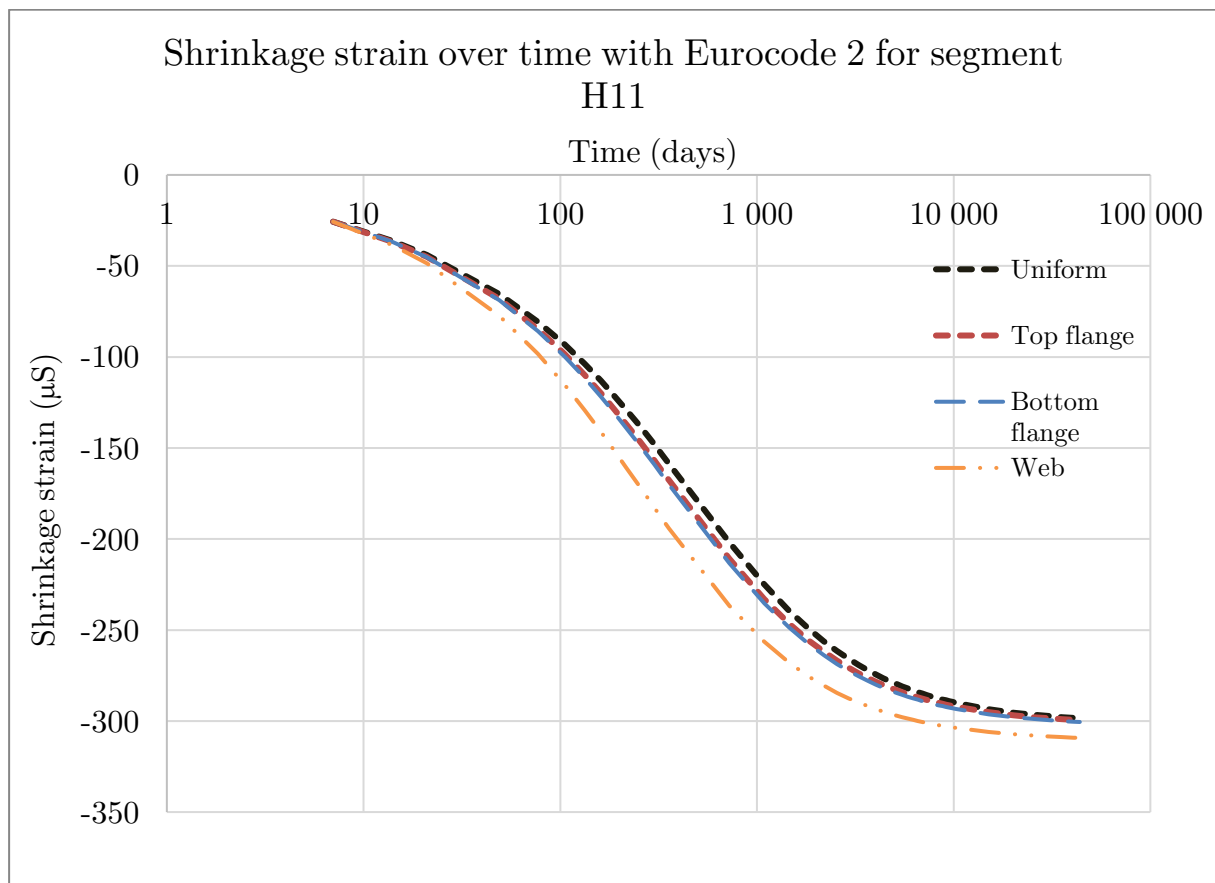
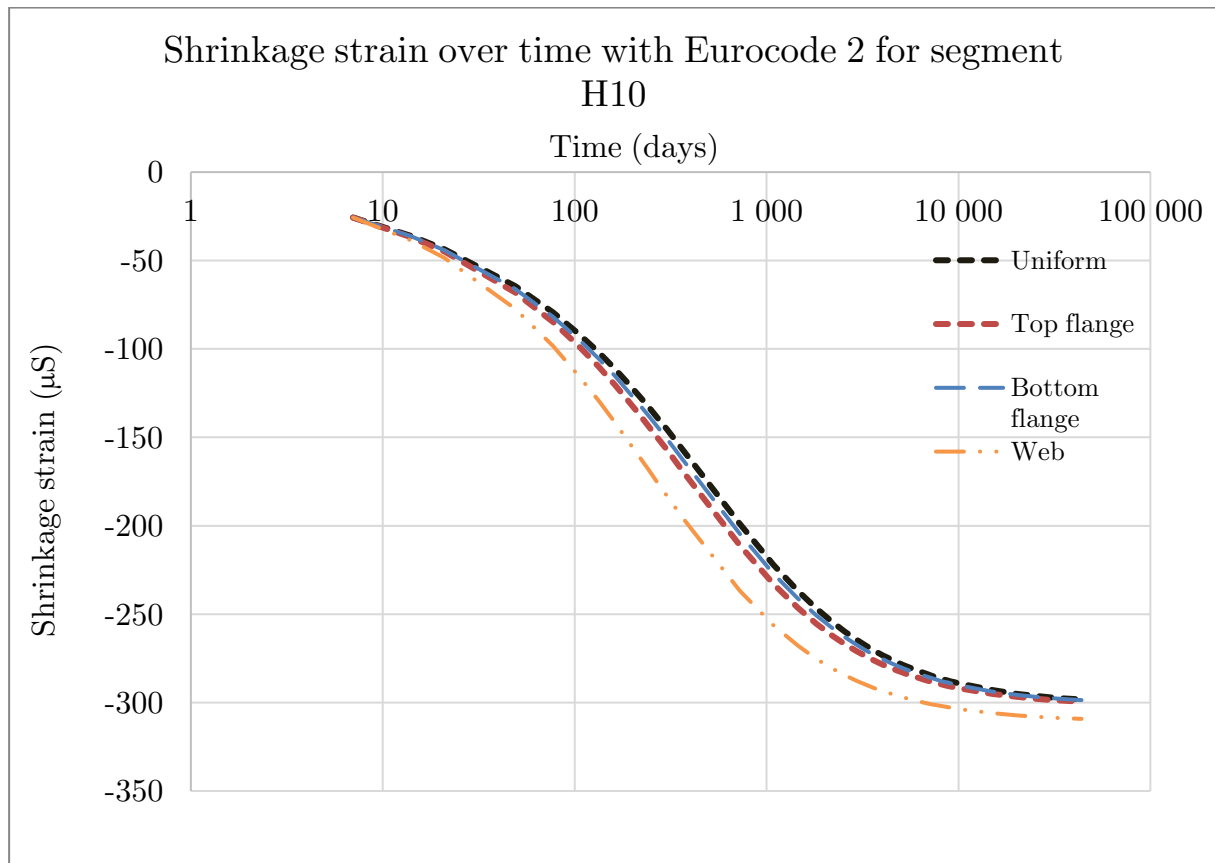


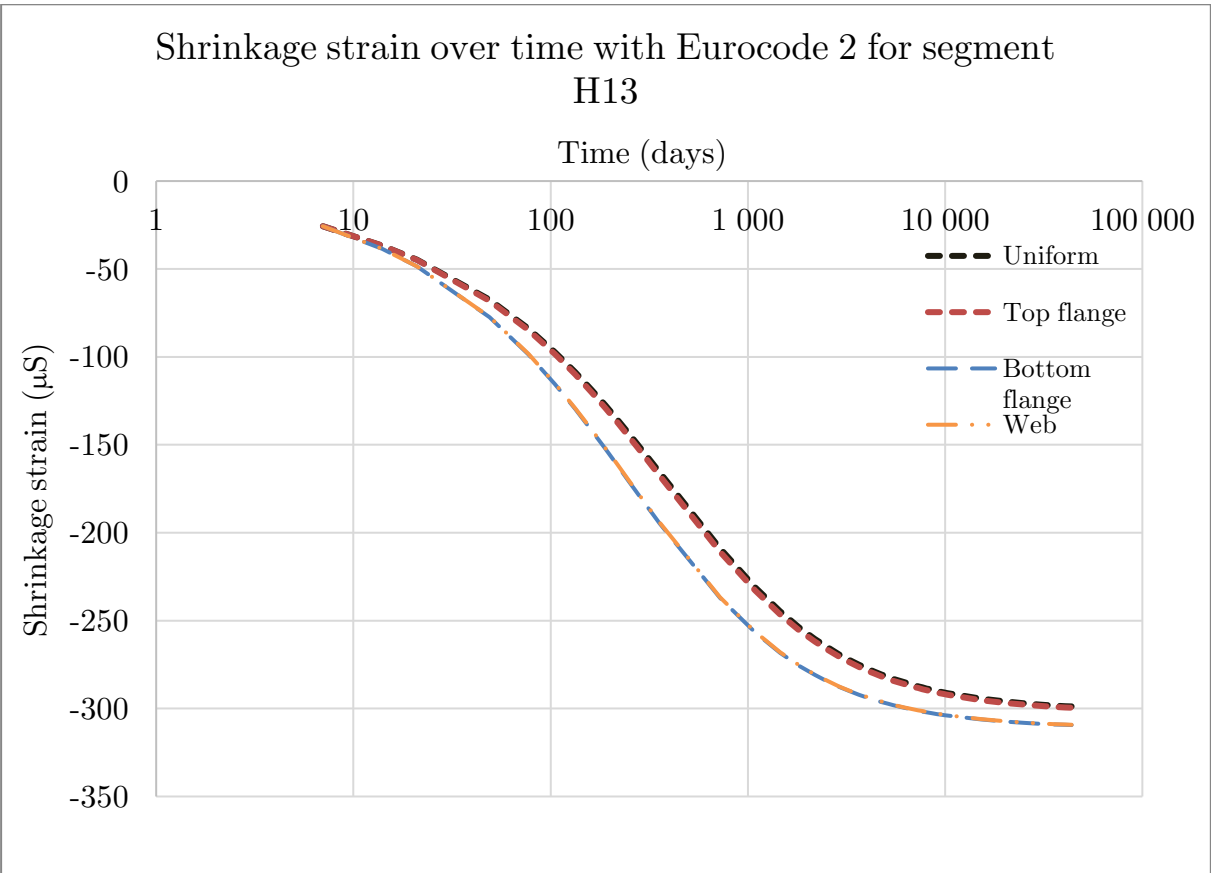
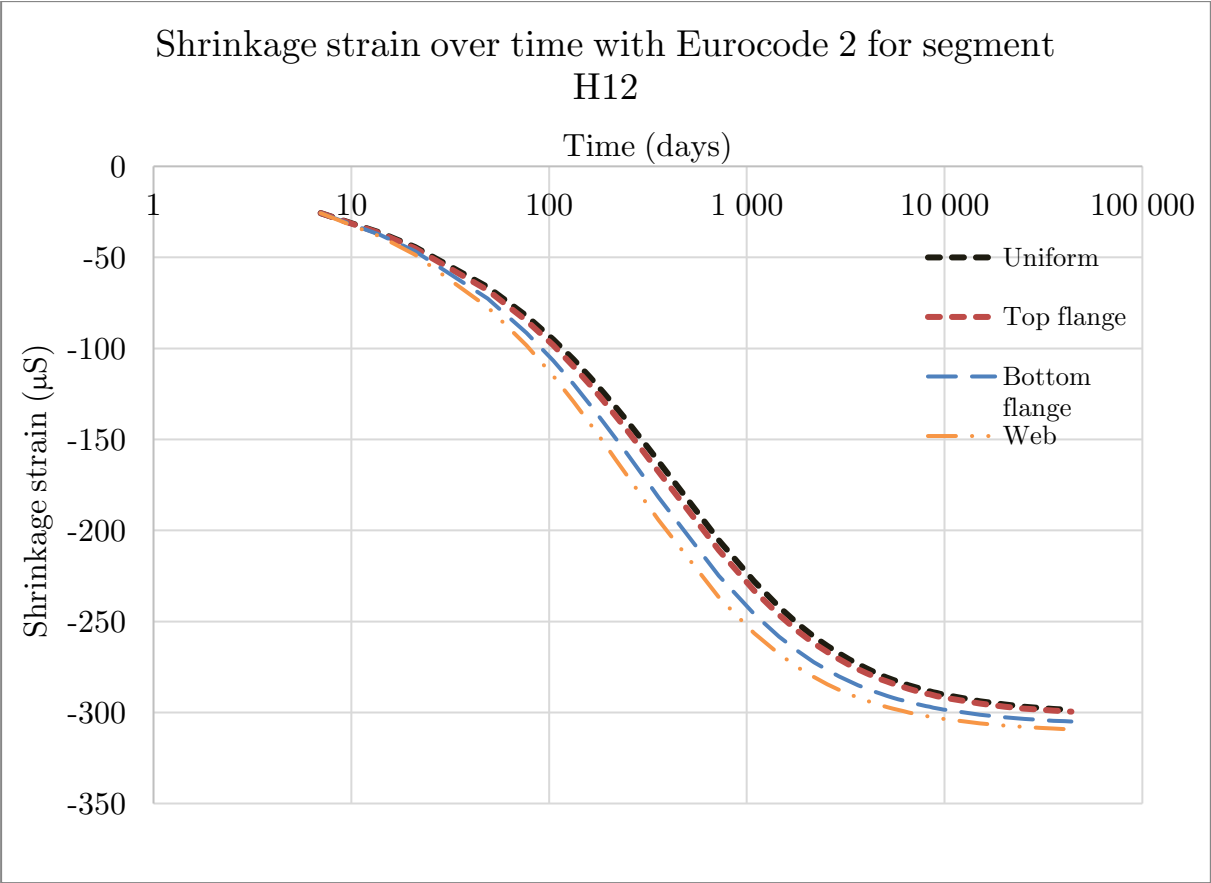












A.3 Relaxation data for tendons

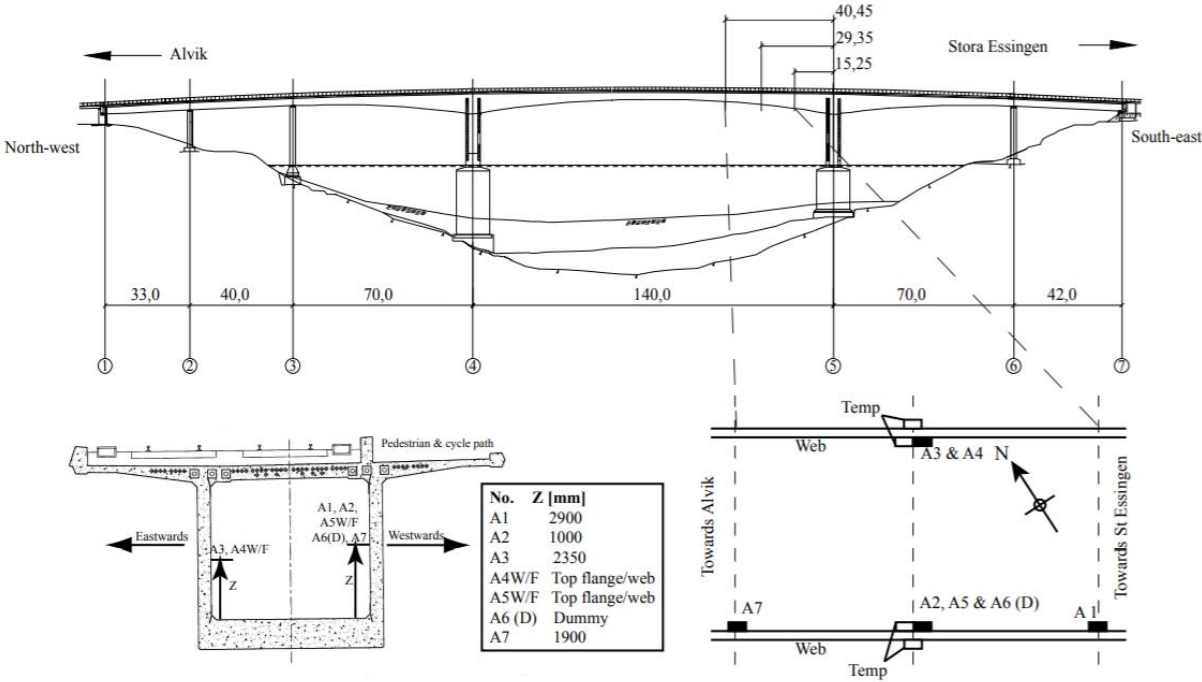
2242 kN	2294 kN	2345 kN	2377 kN	2312 kN
Normalized shear moduli, gR(t)	Normalized shear moduli, gR(t)	Normalized shear moduli, gR(t)	Normalized shear moduli, gR(t)	Normalized shear moduli, gR(t)
0,9990	0,9988	0,9987	0,9986	0,9988
0,9987	0,9985	0,9983	0,9982	0,9984
0,9985	0,9983	0,9981	0,9979	0,9982
0,9979	0,9977	0,9974	0,9972	0,9976
0,9976	0,9973	0,9970	0,9968	0,9972
0,9973	0,9970	0,9967	0,9964	0,9969
0,9970	0,9967	0,9964	0,9962	0,9966
0,9968	0,9965	0,9961	0,9959	0,9964
0,9966	0,9963	0,9959	0,9957	0,9962
0,9965	0,9961	0,9957	0,9955	0,9960
0,9963	0,9959	0,9956	0,9953	0,9958
0,9962	0,9958	0,9954	0,9951	0,9956
0,9960	0,9956	0,9952	0,9950	0,9955
0,9959	0,9955	0,9951	0,9948	0,9954
0,9958	0,9954	0,9950	0,9947	0,9952
0,9946	0,9941	0,9936	0,9932	0,9939
0,9937	0,9932	0,9926	0,9923	0,9930
0,9930	0,9925	0,9919	0,9915	0,9923
0,9925	0,9919	0,9912	0,9908	0,9916
0,9920	0,9913	0,9907	0,9902	0,9911
0,9915	0,9909	0,9902	0,9897	0,9906
0,9911	0,9904	0,9897	0,9893	0,9902
0,9907	0,9900	0,9893	0,9888	0,9898
0,9904	0,9897	0,9889	0,9884	0,9894
0,9900	0,9893	0,9886	0,9881	0,9890
0,9897	0,9890	0,9882	0,9877	0,9887
0,9894	0,9887	0,9879	0,9874	0,9884
0,9891	0,9884	0,9876	0,9871	0,9881
0,9889	0,9881	0,9873	0,9868	0,9878
0,9886	0,9878	0,9870	0,9865	0,9875

0,9883	0,9876	0,9867	0,9862	0,9873
0,9881	0,9873	0,9865	0,9859	0,9870
0,9879	0,9871	0,9862	0,9857	0,9868
0,9876	0,9868	0,9860	0,9854	0,9865
0,9874	0,9866	0,9858	0,9852	0,9863
0,9872	0,9864	0,9855	0,9850	0,9861
0,9870	0,9862	0,9853	0,9847	0,9859
0,9868	0,9860	0,9851	0,9845	0,9857
0,9866	0,9858	0,9849	0,9843	0,9854
0,9864	0,9856	0,9847	0,9841	0,9853
0,9863	0,9854	0,9845	0,9839	0,9851
0,9861	0,9852	0,9843	0,9837	0,9849
0,9840	0,9831	0,9821	0,9815	0,9827
0,9823	0,9813	0,9802	0,9796	0,9809
0,9808	0,9797	0,9787	0,9780	0,9794
0,9795	0,9784	0,9773	0,9766	0,9780
0,9783	0,9772	0,9761	0,9754	0,9768
0,9772	0,9761	0,9750	0,9742	0,9757
0,9766	0,9755	0,9743	0,9736	0,9751

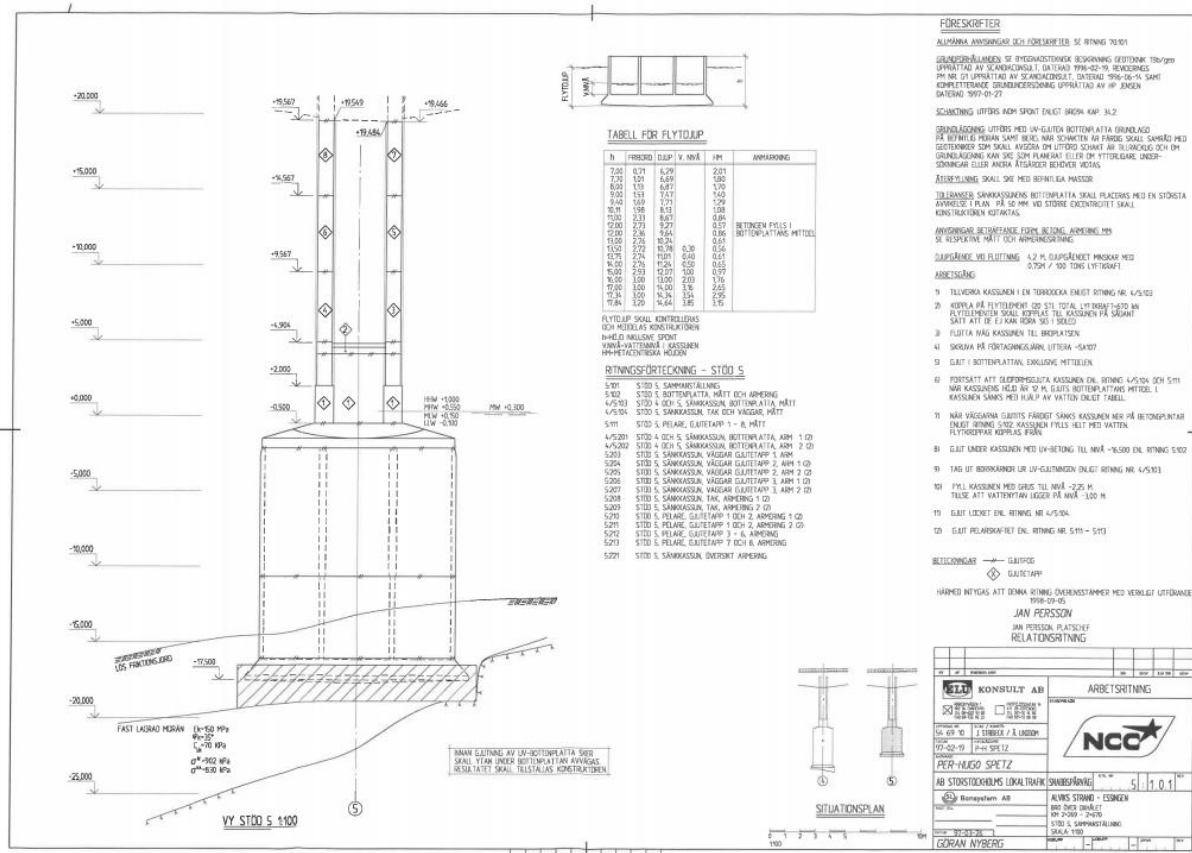
Appendix B

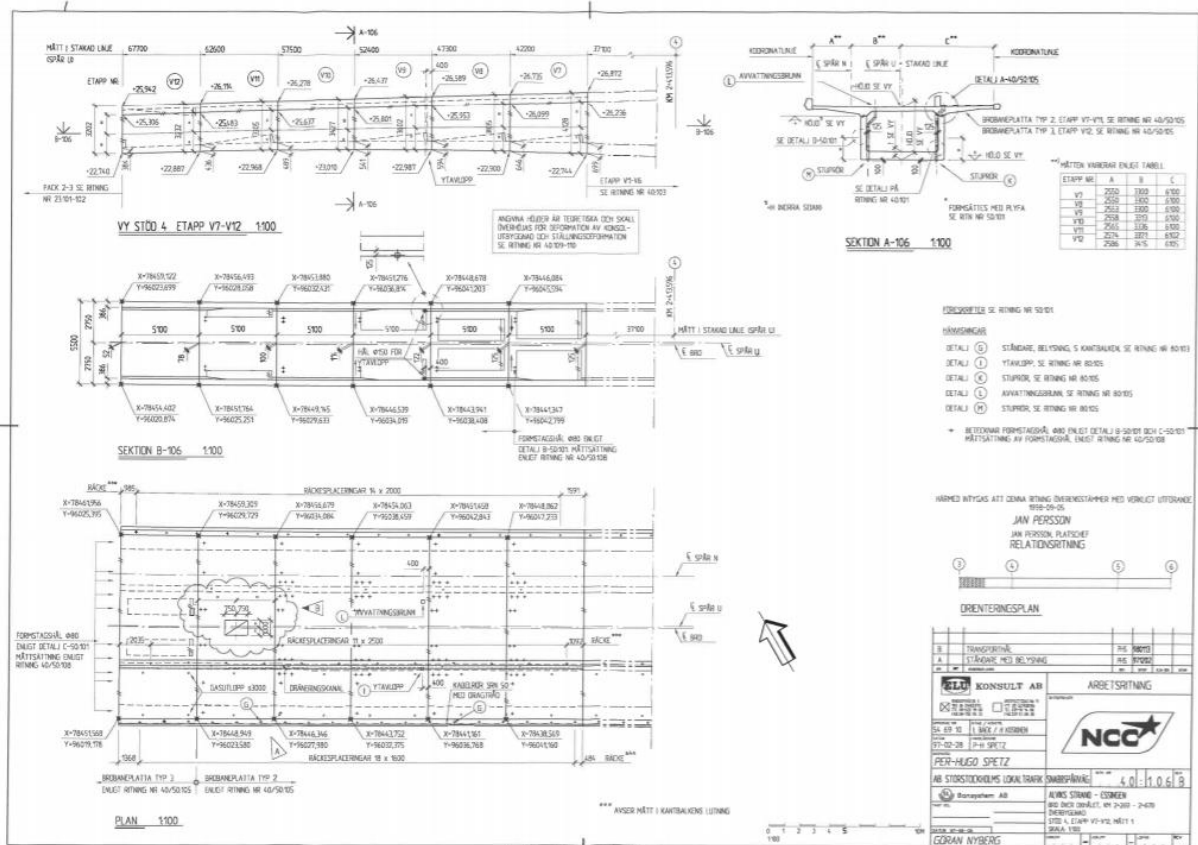
Drawings

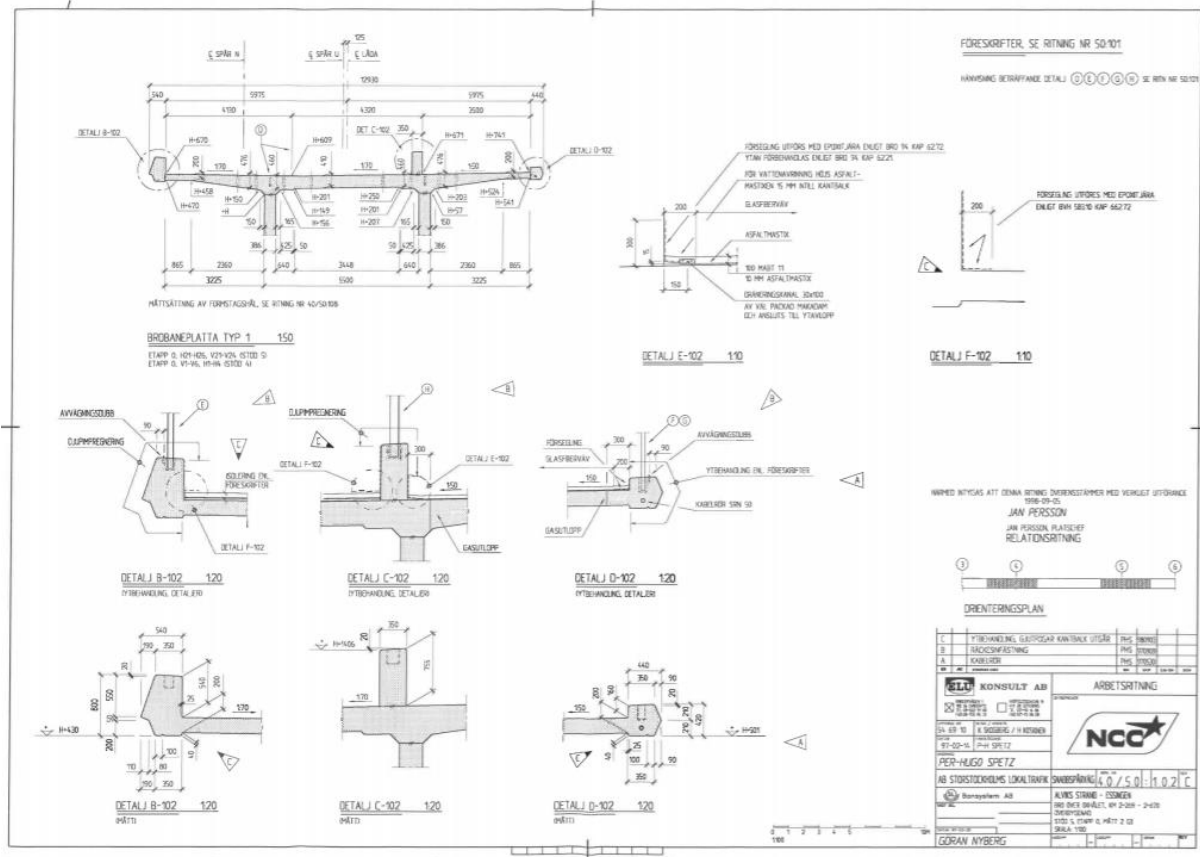
B.1 Instrumentation

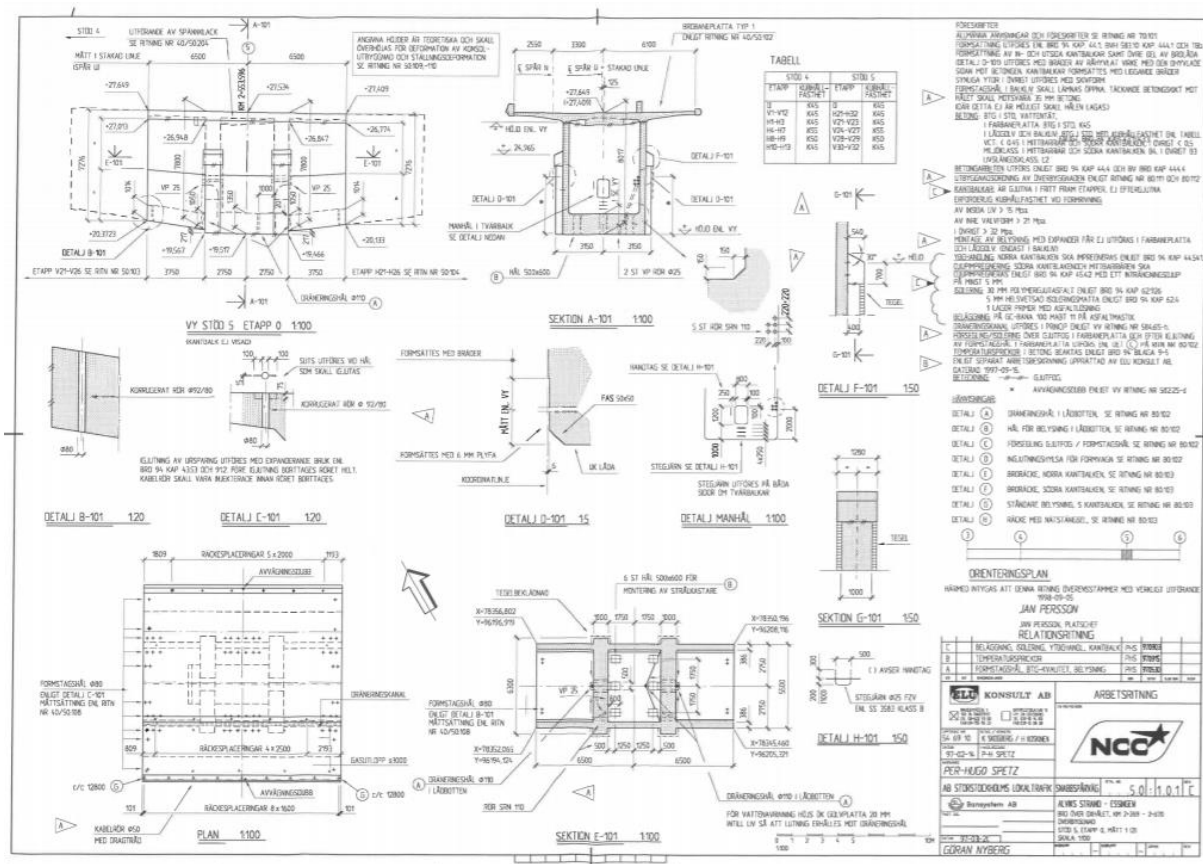


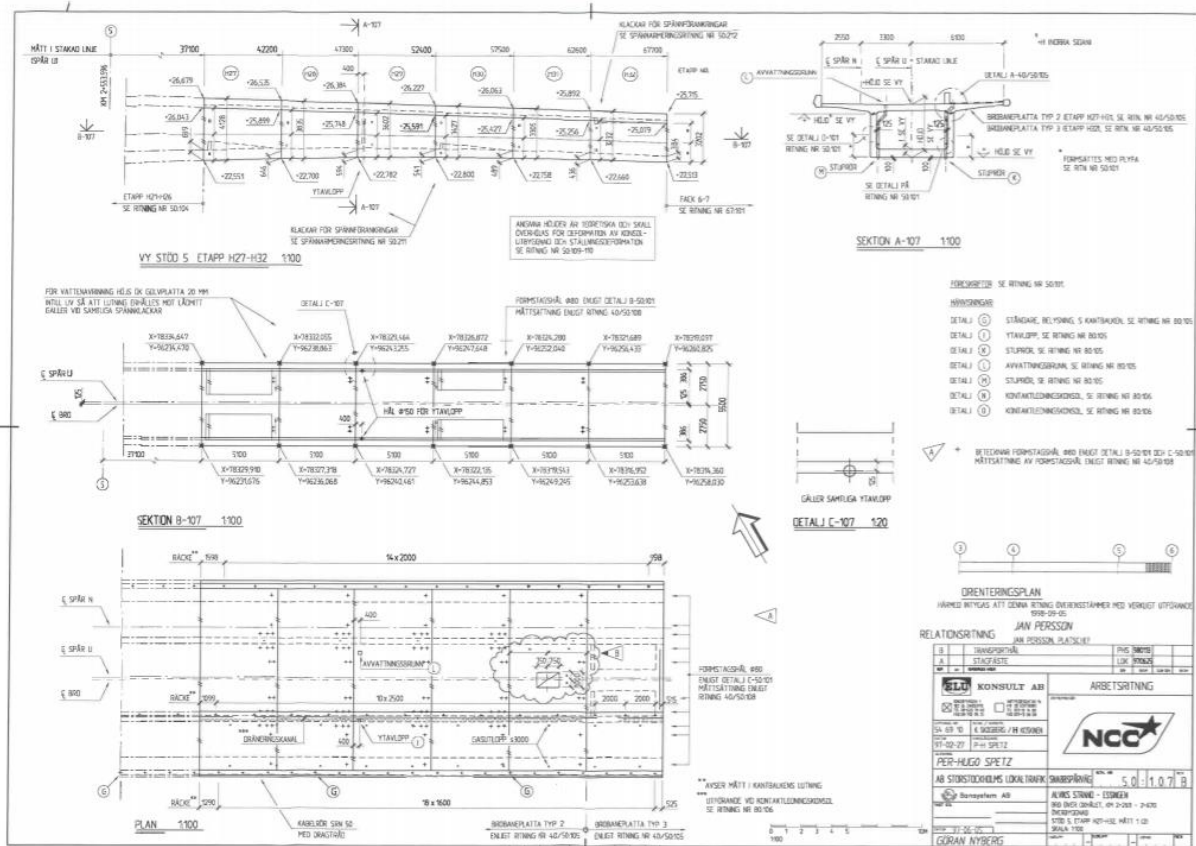
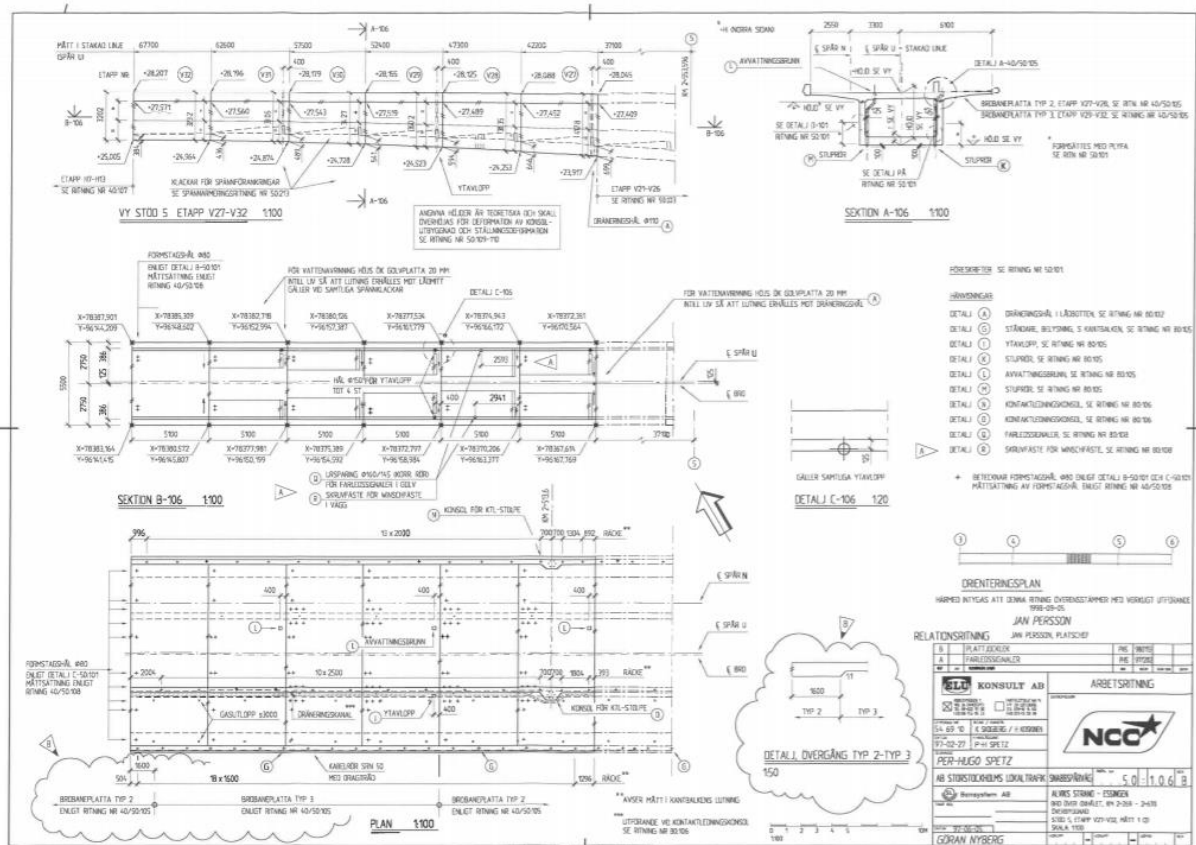
B.2 Structural Drawings











TRITA TRITA ABE-MBT-21382